The Pennsylvania State University

The Graduate School

Eberly College of Science

MODIFIED QUINONE ACCEPTORS IN PHOTOSYSTEM I

A Thesis in

Biochemistry, Microbiology, and Molecular Biology

by

Boris L. Zybailov

Submitted in Partial Fulfillment

of the Requirements

for the Degree of

Doctor of Philosophy

May 2003

We approve the thesis of Boris L. Zybailov. Date of Signature

_____ _____

John H. Golbeck

Professor of Biochemistry and Biophysics

Chair of Committee

Thesis Advisor

_____ _____

Don A. Bryant

Professor of Biochemistry and Molecular Biology

_____ _____

Squire Booker

Assistant Professor of Biochemistry and Molecular Biology

_____ _____

J. Martin Bollinger

Associate Professor of Biochemistry and Molecular Biology

_____ _____

Daniel A. Jones

Senior Scientist

_____ _____

Robert A. Schlegel

Professor of Biochemistry and Molecular Biology

Head of Department of Biochemistry and Molecular Biology

ABSTRACT

The function of the A_1 acceptor in cyanobacterial Photosystem I (PS I) complex was probed – using EPR and optical spectroscopies – by: i) interrupting phylloquinone biosynthesis; ii) replacing phylloquinone with foreign quinones; iii) introducing point mutations in amino acids within the A_1 quinone binding site.

Major findings include that: i) interruption of the *menA* (phytyl transferase) or *menB* (naphthoate synthase) genes in the phylloquinone biosynthetic pathway results in a functional PS I complex in which plastoquinone-9 replaces phylloquinone in the A_1 quinone binding site; ii) forward electron transfer from A_1 to F_X is endergonic in a PS I complex that contains plastoquinone-9; iii) plastoquinone-9 is loosely bound in *menA* and *menB* mutant PS I complexes, thus it is readily exchanged with both substituted and unsubstituted foreign quinones *in vitro*; iv) forward electron transfer in cyanobacterial PS I – as determined by studying the site-directed mutants W697F (PsaA) and W677 (PsaB), S692C (PsaA) and S672 (PsaB), and R694A (PsaA) and R674A (PsaB) – proceeds predominately through the PsaA-branch of cofactors.

Backward electron transfer from A_1^- to P_{700}^+ is biphasic, with lifetimes of ca. 10 µs and ca. 300 µs, in a PS I complex that contains plastoquinone-9. The slow kinetic phase disappears upon reduction with dithionite, indicating that the plastoquinone related to the slow phase has been reduced. However, the fast kinetic phase remains, indicating that the plastoquinone related to the fast kinetic phase has not been reduced. Therefore, these two plastoquinones differ in their midpoint potentials.

Supplementation of the growth medium of *menB* mutant cells with a set of unsubstituted quinones causes incorporation of phytylated quinone into the A_1 quinone

binding site. When the growth medium of *menA* mutant cells is supplemented in the same way, no such incorporation occurs and the A_1 quinone binding site remains occupied by plastoquinone-9. However, when either *menA* or *menB* mutant cells are grown with quinones that have long hydrophobic carbon chains (phylloquinone and menaquinone-8), these quinones occupy the A_1 quinone binding site at the expense of plastoquinone-9. Therefore, a long hydrophobic carbon chain is required for quinone incorporation into the A_1 quinone binding site *in vivo*.

TABLE OF CONTENTS ……Page

List of Figures

List of Tables

Abbreviations

A_0	primary electron acceptor of Photosystem I
A_1	secondary electron acceptor of Photosystem I
ATP	adenosine triphosphate
Car	carotenoid
^{T}Car	carotenoid triplet
Chl	chlorophyll
^{T}Chl	chlorophyll triplet
2-CH_3-1,4-NQ	2-methyl-1,4-naphthoquinone
DCPIP	2,6-dichlorphenol-indophenol
β-DM	n-dodecyl-β-D-maltoside
EPR	electron paramagnetic resonance
ENDOR	electron nuclear double resonance
ESE	electron spin echo
F_A	terminal acceptor of Photosystem I
F_B	terminal acceptor of Photosystem I
FeS	iron-sulfur
F_X	acceptor of Photosystem I preceeding F_A and F_B
HPLC	high performance liquid chromatography
MV	methyl viologen
MQ-8	menaquinone-8, vitamin K_2
1,4-NQ	1,4-naphthoquinone
NADP	nicotinamide adenine dinucleotide phosphate
P_{700}	primary electron donor of Photosystem I
PhQ	phylloquinone, vitamin K_1
PS I	Photosystem I
PS II	Photosystem II
Q	quinone

Q^-	semiquinone anion radical
SDS	sodium dodecyl sulfate
Tricine	N-[2-hydroxy-1,1-bis(hydroxymethyl)ethyl]glycine
Tris	tris(hydroxymethyl)aminoethane

Acknowledgments

I would like to thank my advisor Dr. John H. Golbeck for his patience and understanding. Without his guidance, this dissertation would not have been possible.

I want acknowledge all my collaborators who contributed to this work: Gaozhong Shen, Art van der Est, Ilya Vassiliev, Klauss Brettel, Robert Bittl, Stephan Zech, Christian Teutloff, Donald Bryant, Alexey Semenov, Mahir Mamedov, Oksana Gopta, Dietmar Stehlik, Bruce Diner, Parag Chitnis, Wu Xu, Daniel Jones, Wade Johnson and Yumiko Sakuragi.

My special thanks go to the Penn State undergraduate students who worked with me on this project: Derrick Kolling, Ester Shalome, Steve Beauparlant, Michael Harris and Haralambos Kaittanis.

Dedicated to my secondary school chemistry teacher, Korkina Raisa Andreevna

Chapter 1

General Introduction

ABSTRACT

In this introductory chapter, I define photosynthesis as an energy conversion system, discuss the functional organization of the photosynthetic machinery, and introduce reaction center types. Cyanobacterial Photosystem I (PS I) is discussed in detail. The arrangement of the electron carriers is described based on the latest structural information. Unresolved and controversial topics related to PS I are discussed and relevant issues are identified. The chapter ends with a brief review of the functional chemistry of the A_1 acceptor in PS I.

Photosynthesis: a high-efficient energy conversion system

Photosynthesis can be broadly defined as a process that converts energy of light into chemical bond energy. Energy-rich molecules are synthesized and are further employed in driving and regulating metabolism. The photosynthetic process typically involves generation of a transmembrane proton gradient via photon-driven charge-translocating enzymes coupled to ATP synthase (Fig. 1.1). Examples of this scheme are ubiquitous amongst the three branches of life. Photosynthetic eukaryotes include higher plants and algae; examples of photosynthetic bacteria are purple bacteria, green sulfur bacteria and cyanobacteria; archaeal phototrophy is common amongst halophiles (a well-known case is *Halobacterium salinarium*. As a rule, bacteria and eukaryotes use electron translocating molecular pumps (photosynthetic reaction centers), while archaea use proton translocating pumps (*e.g*. bacteriorhodopsin). Photosynthesis is an ancient metabolic process. The earliest organisms found in sedimentary rocks formed 3.5 billion years ago were, in fact, identified as close relatives of cyanobacteria. It is commonly accepted that the appearance of oxygenic photosynthesis caused dramatic atmospheric changes which involved the shift from a reductive to an oxidative atmosphere.

Oxygenic photosynthesis utilizes two different types of light-driven electron translocating reaction centers - Type I and Type II. The next section describes the mechanism of oxygenic photosynthesis.

Photosynthetic reaction centers; Photosynthesis in Cyanobacteria

In the early 1930s Emerson *et al*. (1932) demonstrated the presence of two types of photosystems that constitute the light reactions in plant photosynthesis. They were named Photosystem I and Photosystem II (PS I and PS II). Later it was shown that reaction centers in different types of photosynthetic bacteria are structurally related to either PS I or PS II, hence the more general terms, Type I and Type II reaction centers, were introduced. Type I reaction centers have [4Fe-4S] clusters as terminal acceptors, while Type II reaction centers have quinones as terminal acceptors. Typically, Type I reaction centers carry out one-electron translocations, and type II reaction centers carry out two-electron translocations. In the latter case the terminal quinone is loosely bound,

and upon sequential acceptance of two electrons and two protons, it leaves its site and diffuses into the quinone pool. Non-oxygenic photosynthetic organisms employ one of the two reaction center types. For example, purple bacteria use Type II reaction centers, while green sulfur bacteria and heliobacteria use Type I reaction centers. In their recent review, F. Baymann *et al*. (2001) hypothesize that the so-called Reaction Center I is the ancestral photosystem and PS II descended from Reaction Center I via gene duplication and gene splitting.

Oxygen-evolving photosynthetic organisms utilize both types of reaction centers. The organization of the photosynthetic apparatus in cyanobacteria, the simplest oxygenic phototroph, is shown in Fig. 1.2. The two photosystems are coupled through the plastoquinone pool, the cytochrome b_6f complex, and either plastocyanin or cytochrome c_6.

PS II performs light-catalyzed oxidation of water and reduces loosely bound plastoquinone-9 (see Yoder *et al*., 2002; Diner *et al*., 2001; Rhee 2001; Debus 2000). After absorption of a photon, an electron is transferred from the chlorophyll donor P_{680} to a pheophytin. The next step is the reduction of a plastoquinone-9 molecule, Q_A, which in turn reduces the second quinone Q_B. Oxidized P_{680} is then reduced by the redox-active tyrosine Z, which mediates electron flow from the manganese water-splitting complex. The net result is that the loosely bound plastoquinone Q_B is reduced to the quinol form for every 2 electrons transferred from water and every 2 photons absorbed. The manganese water-splitting complex is able to accumulate four oxidizing equivalents. Hence, stoichiometricaly, PS II action can be expressed by:

$$2H_2O \xrightarrow{PSII,light} 4H^+ + O_2 + 4e^-$$

Four electrons on the right side of the equation leave PS II in form of two plastoquinol molecules, and 'fresh' plastoquinone always arrives at the vacated site from the plastoquinone pool. Therefore - for every oxygen molecule evolved - there must be 4 photons absorbed, 4 electrons transferred and 2 plastoquinone-to-plastoquinol conversions.

Plastoquinol produced in PS II is further recycled by the cytochrome b_6f complex. Plastoquinol is oxidized at a special oxidation site. At this step the electron transfer pathway bifurcates: one electron goes through heme cofactors, b_L and b_H and reduces plastoquinone at the plastoquinone reduction site; the other electron proceeds to the Rieske FeS cluster followed by the transfer to a soluble carrier, either cytochrome c_{553} or plastocyanin depending on the environmental conditions (Zhang *et al*., 1992). The net action of the cytochrome b_6f complex is:

$$2PQH_2(o) + PQ(r) \xrightarrow{b_6 f} 2PQ(o) + PQH_2(r) + 2H^+ + 2e^-$$

Letters o and r denote quinol oxidation and quinone reduction sites, respectively. Therefore, for every 2 plastoquinols oxidized, one plastoquinone is reduced and 2 electrons are removed by the soluble carrier cytochrome c_{553}. Note that 2 protons are captured at the reduction site and 2 protons are released at the oxidation site. The released and captured protons are on opposite sides of membrane. The process described was proposed by Mitchell in 1976 and termed the "Q-cycle hypothesis" (Mitchel, 1976).

Cytochrome c_{553} has a relatively high reduction potential, and a weak oxidant needs to be used in order for electron flow to continue. This is achieved through PS I action. When a photon is absorbed by PS I, the excitation energy within the antenna is transferred to the primary electron donor, P_{700}. Excited P_{700} is oxidized by the primary electron acceptor A_0, and this initial charge separation is stabilized by the sequential electron transfer via redox-active cofactors, A_1, F_X, F_A and F_B (for reviews see Brettel and Leibl, 2001; Golbeck, 1993; Golbeck and Bryant, 1991). The terminal acceptor F_B is further oxidized by a soluble ferredoxin. Oxidized P_{700} is re-reduced by cytochrome c_{553}. As a net result, PS I performs light-mediated catalytical generation of the low-potential reductant (ferredoxin) by removing electron from the high-potential reductant (cytochrome c_{553}):

$$e^-(+400mV) \xrightarrow{PSI,light} e^-(-400mV)$$

During this process the reducing equivalent is transferred across the membrane and an electrochemical gradient is established. The result is that the lumenal side of the

membrane is more oxidizing and more acidic than the stromal side of the membrane. The potential energy of this gradient drives ATP synthesis**.**

PS I; Components of the electron transfer chain; Electron flow

A prolonged research effort has resulted in an X-ray crystal structure of PS I at a resolution of 2.5 Å (Jordan *et al*., 2001). The precise arrangement of the 12 subunits and the components of the electron transfer chain has been elucidated. Cyanobacterial PS I consists of 12 polypeptides, 96 chlorophyll *a* molecules, 13 ß-carotene molecules, two phylloquinone molecules and three [4Fe-4S] clusters. Two large subunits of about 83 kDa each (PsaA and PsaB) bind the following redox centers: P_{700} (chlorophyll *a/a'* dimer), A_0 (a monomeric chlorophyll *a*), A_1 (a phylloquinone) and F_X (a [4Fe-4S] cluster). Both of the terminal electron acceptors F_A and F_B (also [4Fe-4S] clusters) are coordinated by the PsaC subunit.

The cofactors potentially involved in electron transfer are arranged in two branches related by almost perfect C_2 symmetry (Fig. 1.3). These branches are located in the dimeric interface of PsaA/PsaB heterodimer. The cofactors primarily located either on PsaA or PsaB are called "PsaA-branch" and "PsaB-branch", respectively. Currently it is unclear whether one or both branches are active in the forward electron transfer. Experimental data in support of both hypotheses exist.

The unidirectional model is supported in the work of Yang *et al*. (1998), in which the authors employed a strategy of deletion mutagenesis. PS I complexes, with their subunits along the PsaA-branch (PsaE and PsaF) deleted, rendered the A_1 acceptor more susceptible to double reduction. In comparison, PS I complexes with similar deletions along the PsaB-branch showed no effect on quinone reduction. These findings led the authors to conclude that the PsaA-branch of cofactors is active in the forward electron transfer. In contrast, Guergova-kuras *et al*. (2001), favor a bidirectional model based on work with site-directed mutants in the A_1-binding site. This issue is discussed in more detail in the introduction to chapter 5.

The scheme of charge separation in PS I is shown in Fig. 1.4. Excitation of P_{700} leads to its singlet state $*P_{700}$; from which an electron is transfered to A_0 and then to A_1

on a picosecond time scale. From A_1 the electron is transferred to F_X and then to F_A and F_B on the nanosecond time scale (Brettel, 1997).

The primary acceptor A_0 is a low-potential chlorophyll *a* molecule that undergoes rapid reoxidation with a lifetime of 32±5 ps (Shuvalov *et al.*, 1976), leading to the reduction of phylloquinone to the semiphylloquinone form. This is faster, by three orders of magnitude, than the charge recombination between A_0^- and P_{700}^+, which has a lifetime of 30 ns to 50 ns (Sétif and Bottin, 1989).

Electron transfer from A_1 to F_X is biphasic, and is described by kinetic phases with 20 ns and 200 ns lifetimes (Luneberg *et al*., 1994). Forward electron transfer from A_1 to the iron-sulfur (FeS) clusters competes with charge recombination between A_1^- and P_{700}^+ (Xu, Q. *et al*., 1994). This reaction can be studied by prereducing the F_X, F_A and F_B acceptors. At cryogenic temperatures a backreaction with a lifetime of ca. 20 µs between A_1^- and P_{700}^+ directly populates the ground state of the P_{700}. At room temperature this charge recombination occurs with a lifetime of ca. 250 ns in the presence of prereduced iron acceptors and populates the P_{700} triplet ($^TP_{700}$) state. The $^TP_{700}$ relaxes to the ground state with a 3 µs to 5 µs lifetime (Sétif and Bottin, 1989).

It was suspected that these lifetimes could be influenced by the electrostatic interactions with the reduced FeS clusters, thus alternative methods that involved physical removal of the FeS clusters were developed. In the case in which the FeS clusters were removed, charge recombination kinetics is described by ca. 10 µs and 100 µs lifetimes (Brettel and Golbeck, 1995). The approach which involves selective inactivation of the terminal FeS centers is discussed in more detail in the introduction to chapter 3.

The A_1 acceptor of PS I

One of the general questions this thesis attempts to answer is what structural features of the quinone and its binding site constitute a functional A_1 acceptor. In this part of the introductory chapter, I review research of the past two decades on the structure and function of the A_1 acceptor in higher plants and cyanobacteria. Research efforts culminated in the solution of the X-ray crystal structure at a resolution sufficient to elucidate the precise location and orientation of the phylloquinone molecules in the PS I (Jordan *et al*., 2001). It is now established that phylloquinone (Vitamin K_1) functions as the A_1 acceptor; it accepts electrons from A_0 and passes them forward to the FeS clusters.

Sufficient experimental evidence in favor of phylloquinone being the A_1 acceptor in PS I was accumulated even before the detailed X-ray structure became available. This information was gathered by electron paramagnetic resonance (EPR) as well as optical and chromatographic methods, all of which pointed to the quinone nature of the A_1 acceptor. In this work we employ these non-crystallographic methods of study. Even though the structural information they provide is not as detailed, a significant amount of functional information on the dynamics of the electron flow can be gathered.

Phylloquinone (vitamin K_1) was discovered in plants by H. Dam in 1941, however its function remained unknown. In the early 1980's, its association with PS I was established (Interschick-Niebler, *et al.,* 1981; Takahashi, Y. *et al.,* 1985; Schoeder, H-U. and Lockau, W. 1986). Schoeder and Lockau showed specifically that there are two phylloquinones per P_{700}, and that they are associated with the PsaA/PsaB heterodimer. Using high performance liquid chromatography (HPLC) along with sodium dodecyl sulfate (SDS) page electrophoresis, the ratios of phylloquinones and plastoquinones per P_{700} were determined in membranes and PS I complexes. PS I complexes isolated from spinach were found to contain 1.8 phylloquinones and 0.2 plastoquinones per P_{700}. It was known from EPR and UV spectroscopy that the secondary acceptor of PS I (A_1) had quinone-like features (Thurnauer *et al*., 1985; Petersen *et al*., 1988; Mansfield *et al*., 1986; Brettel *et al.,* 1986). Extraction/reconstitution studies provided further evidence for the A_1 being phylloquinone (Itoh *et al,* 1987; Mansfield *et al.,* 1987; Biggins and Mathis, 1988). Biggins showed that a PS I complex was inactive in the reduction of nicotinamide

adenine dinucleotide phosphate (NADP) after removal of phylloquinone, but its function was restored after re-addition of phylloquinone. Similarly, the EPR spectrum associated with A_1 and the optical transients associated with $P_{700}^+ A_1^-$ recombination were restored upon addition of phylloquinone. For a comprehensive discussion on the reconstitution of the solvent-extracted PS I see Itoh *et al*. (2000).

Solvent extraction of PS I complexes has disadvantages that up to 85% of the 100 chlorophylls and all of the carotenoids are lost, and so it is uncertain whether or not the PS I complex has undergone structural changes as a result. In this thesis I present an alternative approach to study A_1 function by utilizing phylloquinone biosynthetic pathway mutants. When phylloquinone biosynthesis is interrupted, plastoquinone is recruited into the A_1 site and functions as the A_1 acceptor (chapters 2 and 3). The plastoquinone is rather loosely bound and can easily exchanged with foreign quinones, both *in vivo* and *in vitro* (chapter 4).

It is very likely that the two quinone molecules in PS I have different affinities for the binding sites on PsaA and PsaB. Malkin (1986) as well as Biggins and Mathis (1988) demonstrated that phylloquinones can be extracted sequentially using different solvents.

Additional clues come from a comparison of the quinone-binding sites on PsaA and PsaB, based on the atomic-resolution 2.5 Å X-ray crystal structure. Fig. 1.5 A depicts the PsaA quinone-binding site. The phylloquinone molecule is held in the site by π-π interactions with W697, an O-H-N hydrogen bond with L722, and by hydrophobic contacts of the phytyl chain with chlorophyll and β-carotenes. Hydrophobic interactions with PsaA residues are limited to the interactions of the phytyl chain with the side chain of L722 and to the 2-methyl group with the side chain of M688. The strength of the hydrophobic interaction between aliphatic groups can be estimated based on the distance between corresponding carbon atoms. A distance of 4 Å renders a strong interaction of the groups (one can take the C-H bond length as 1 Å and the van der Waals radius of a hydrogen as 1 Å). The entropic effect of water exclusion also plays a role in these interactions.

Fig. 1.5 B displays the PsaB quinone-binding site. Interactions of the phylloquinone head group with PsaB residues are very similar to interactions at the PsaA

quinone binding site. There are π-π interactions with W677; an O-H-N hydrogen bond with the amide group of L706; and hydrophobic interactions of the phytyl chain with the side chain of L706 and 2-methyl group with the side chain of M668. However, in contrast to the PsaA binding site, the phytyl chain of the quinone has more hydrophobic contacts with residues on PsaB, for example with W21 and I24 as shown in Fig. 1.5, B. As a result of these interactions, the phytyl chain is curved within the PsaB subunit. In light of this argument, we can predict that the quinone in PsaB is more strongly bound to the A_1 site than its counterpart in PsaA.

However, it is still not clear whether one or both of the phylloquinones are involved in forward electron transfer. This issue is addressed in chapter 5, where I focus on site-directed mutants in the quinone-binding pocket.

Collaborative work included in the Thesis

The study of quinone function in PS I has been a highly collaborative project, and a multidisciplinary approach was necessary to arrive at solutions to problems. All of the data are presented in the thesis so that reliable conclusions can be reached.

The mutant constructs were prepared for me by Parag Chitnis and Wade Johnson (*menB* and *menA* mutants of *Synechocystis* sp. PCC 6803); by Parag Chitnis and Wu Xu (site-directed phylloquinone-binding mutants); by Yumiko Sakuragi, Gaozhong Shen and Donald Bryant (*menB* and *rubA / menB* mutants of *Synechococcus* sp. PCC 7002).

Physiological studies of *rubA / menB* mutant cells cultures were performed in collaboration with Gaozhong Shen, Yumiko Sakuragi and Donald Bryant. Physiological studies of *menA* and *menB* mutant cells cultures were performed in collaboration with Wade Johnson and Parag Chitnis. Wade Johnson performed growth studies of the *menB* mutant cells in media supplemented with naphthoquinones. Supplementation by anthraquinones was done in cooperation with Ester Shalome and Gaozhong Shen. Identification of the quinone in the A_1 site in the mutant PS I complexes by mass spectrometry was performed in collaboration with Daniel Jones. Transient EPR experiments were performed in collaboration with Dietmar Stehlik and Art van der Est. Pulsed EPR experiments were done in collaboration with Robert Bittl. Measurements of

the transmembrane potentials in proteoliposomes were performed in collaboration with Mahir Mamedov and Alexey Semenov. Mahir Mamedov and Alexey Semenov also participated in the characterization of the *menB*$^-$ and *menA*$^-$ PS I complexes by visible spectroscopy. Optical measurements in the UV were done in coooperation with Bruce Diner. Most of the original *Igor Pro* code for the data handling and analysis was written by Ilya Vassiliev, who also built and maintained the spectrometers used in the optical experiments.

Experimental work performed exclusively by me included X- and Q-band continuous wave (CW) EPR spectroscopy, time-resolved X-band EPR measurements of the whole cells, flash-induced differential spectrophotometry in the visible and near-infrared (near-IR) regions, HPLC analysis of the quinone extracts, *in vitro* quinone replacements, inactivation of the terminal FeS clusters by chaotropic treatment, and studies of the *menB*$^-$ PS I complexes reduced with dithionite.

REFERENCES

Baymann F, Myriam Brugna, Ulrich Mühlenhoff, Wolfgang Nitschke (2001), *BBA* 1507 291-310

Biggins, J., and Mathis, P. (1988) *Biochemistry* **27**: 1494–500

Brettel, K. (1997) *Biochim. Biophys. Acta*. **1318**:322-373.

Brettel, K. and Golbeck, J. H. (1995) *Photosynthesis Research* **45**: 183-193

Brettel K. and Leibl W. (2001) *BBA-Bioenergetics* **1507** (1-3): 100-114

Brettel, K., Sétif, P. and Mathis, P. (1986) *FEBS Lett.* **203**: 220-224

Dam. H. (1941) *Adv. Enzymol*. **2**. 285-324

Debus R.J. (2000), *Met. Ions Biol. Syst*. **37**: 657-711

Diner B. A., Schlodder E., Nixon P. J., Coleman W. J., Rappaport F., Lavergne J., Vermaas W. F. J., Chisholm D. A. (2001), *Biochemistry*, **40** (31): 9265-9281

Emerson R., Arnold J. (1932), *Gen. Physiol.* **16:** 191-205

Golbeck, J. H. (1993) *PNAS* **90**(5): 1642-1646

Golbeck, J. H. Bryant, D. A. (1991) *Current Topics in Bioenergetics* **16**: 83-177

Guergova-Kuras M., Brent Boudreaus, Anne Joliot, Pierre Joliot, and Kevin Redding (2001) *PNAS*, **98**(8): 4437-4442.

Interschick-Niebler. E, and Lichtenthaler, H.K. (1981*) Z. Naturfrosch*. **36**c: 276-283

Itoh S, Iwaki M, I Ikegami, I. (2001) *Biochimica et Biophysics Acta* **45073** (2001) 1-24

Jones, R. M. (2001) *Current Biology* **11**(8): R318-R321

Jordan, P., Fromme, P., Witt, H. T., Klukas, O., Saenger, W., Krauβ, N. (2001), *Nature* **411**: 909

Lunerberg, J., Fromme, P., Jekow, P. and Schlodder, E. (1994) *FEBS Lett*. **338**:197-202

Malkin, R. (1986) *FEBS Lett*. **208**: 343–346

Mansfield, R.W. and Evans, M. C. W. (1986) *FEBS Lett.* **203**: 225-229

Mitchel P. (1976) *J. Theor. Biol.* **62**:327-367

Petersen, J., Stehlik. D., Gast. P. and Thurnauer, M. C. (1988) *Photosynth. Res*. **14**, 15-29

Rhee K. H. (2001) *Annu. Rev. Bioph. Biom.* **30**: 307-328

Schoeder, H-U. and Lockau, W. (1986) *FEBS Lett.* **199**: 23-27

Sétif, P. and Bottin, H. (1989*) Biochemistry* **28**: 2689-2697

Shuvalov, (1976) *Biochim. Biophys. Acta* **430**: 113-121

Shuvalov, V. A., Nuijs, A.M., van Gorkom, H.J., Smith, H. W. J., and Duysens, L. N. M. (1986) *Biochim. Biophys. Acta* **850**: 319-323.

Takahashi, Y., Hirota, K. and Katoh, S. (1985) *Photosynth. Res*. **6**: 183-192

Thurnauer, M. C. and Gast. P. (1985) *Photobiochem. Photobiophys*. **9**: 29-38

Yang, F., Shen, G. Z., Schluchter, W. M., Zybailov, B. L., Ganago, A. O., Vassiliev, I. R., Bryant, D. A. and Golbeck, J. H. (1998) *Journal of Physical Chemistry* B **102**: 8288-8299.

Xu Q., Jung Y. S, Chitnis V. P., Guikema J. A., Golbeck J. H., Chitnis P. R. (1994), *J. Biol. Chem*. **2693**: 21512-21518

Yoder L. M., Cole A. G., Sension R. J. (2002) *JACS* **124** (25): 7459-7471

Zhang, L., McSpadden, B., Oakrasi, H. B., and Whitmarsh, J. (1992) *Journal of Biol. Chem*. **267**: 19054-19059

FIGURE LEGENDS

Figure 1.1 General scheme of the photosynthetic energy conversion. A charge translocating molecular pump is coupled to the ATP synthase.

Figure 1.2 Photosynthetic machinery of cyanobacteria (adapted from Jones, R. M. 2001)

Figure 1.3 Electron transfer cofactors in PS I. Electron carriers preceding F_X are symmetrically arranged in two chains in the interface of PsaA/PsaB heterodimer. FeS cluster F_X is ligated by four cysteines, two cysteines from each of PsaA and PsaB. Terminal electron acceptors F_A and F_B are harbored by PsaC subunit of PS I.

Figure 1.4 Energy diagram of the electron flow in PS I. Solid arrows represent forward electron transfer, broken arrows represent charge recombination. Lifetimes for the known processes are shown.

Figure 1.5 PsaA and PsaB phylloquinone binding sites. *A*, phylloquinone binding site in PsaA. *B*, phylloquinone binding site in PsaB. Phylloquinone molecules are depicted in pink color. Water molecules are depicted as blue dots (PDB entry: 1JB0)

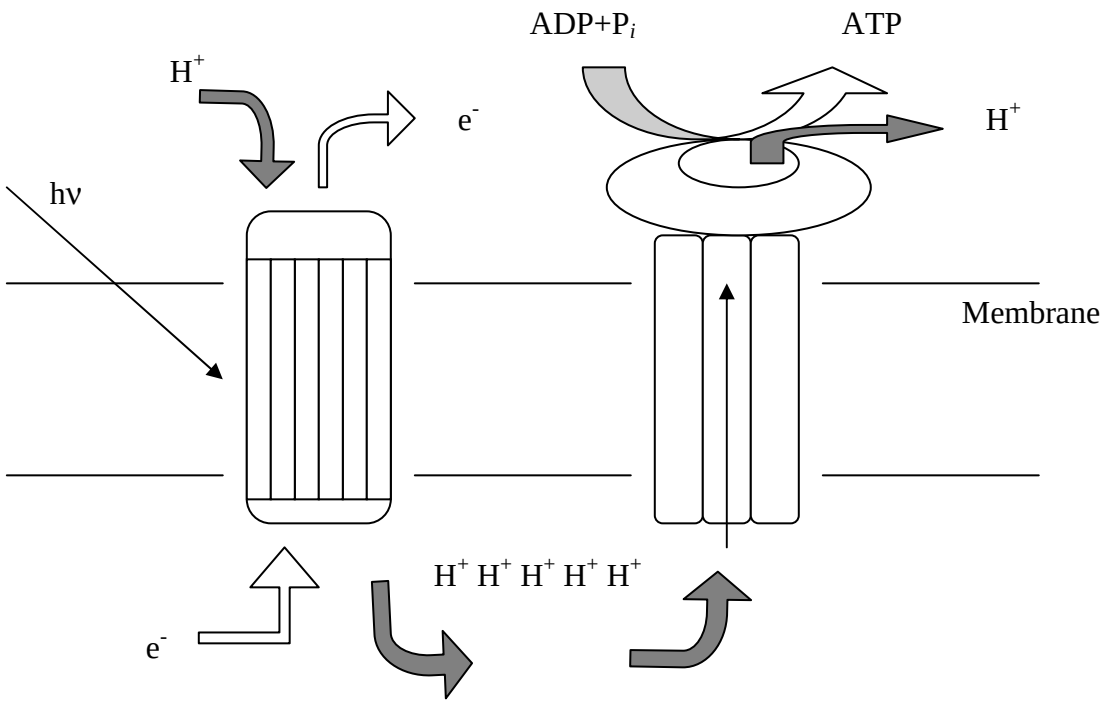
charge translocation system
ATP synthesis
ADP+P$_i$
ATP
H$^+$
e$^-$
H$^+$
hν
Membrane
H$^+$ H$^+$ H$^+$ H$^+$ H$^+$
e$^-$

Figure 1.1

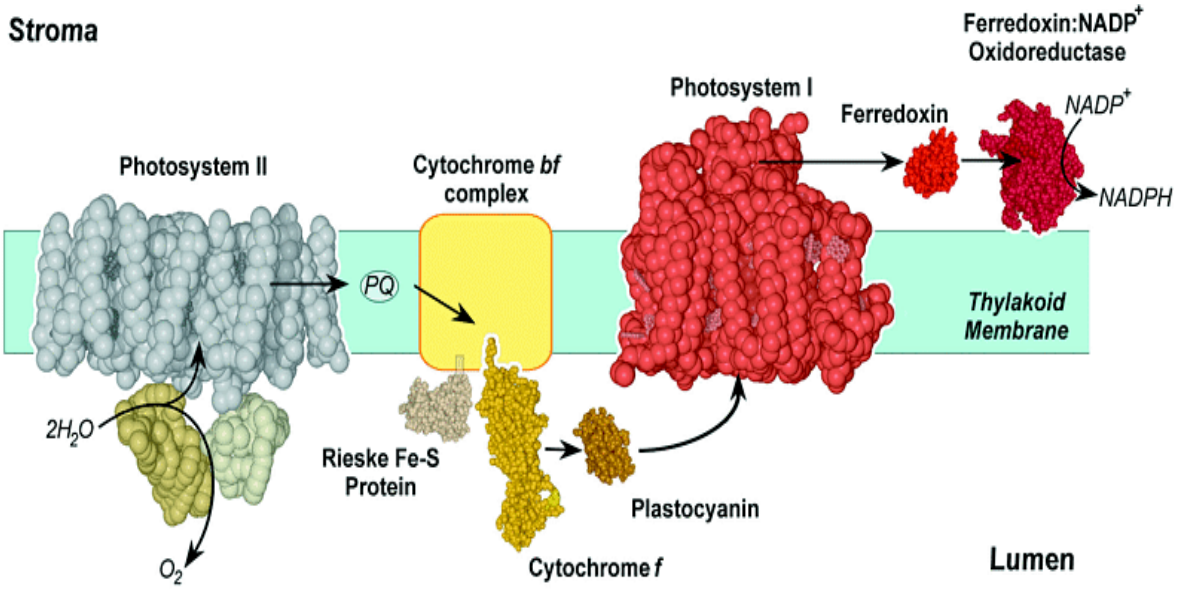

(adapted from Jones, R. M. 2001)

Figure 1.2

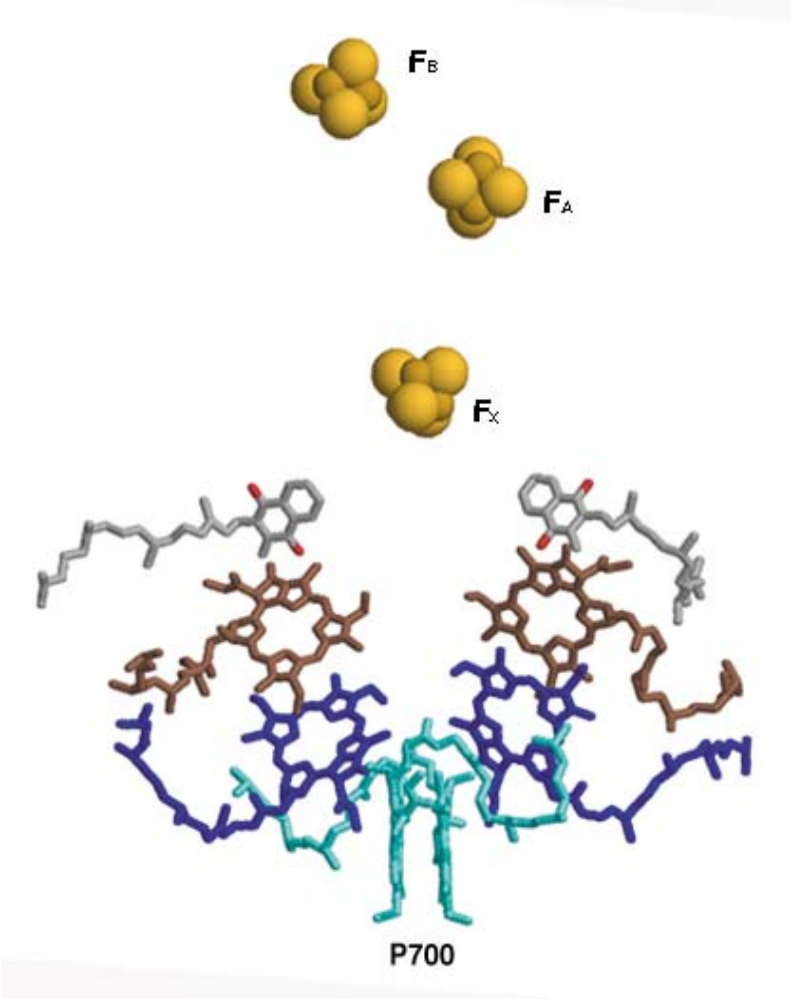

Figure 1.3

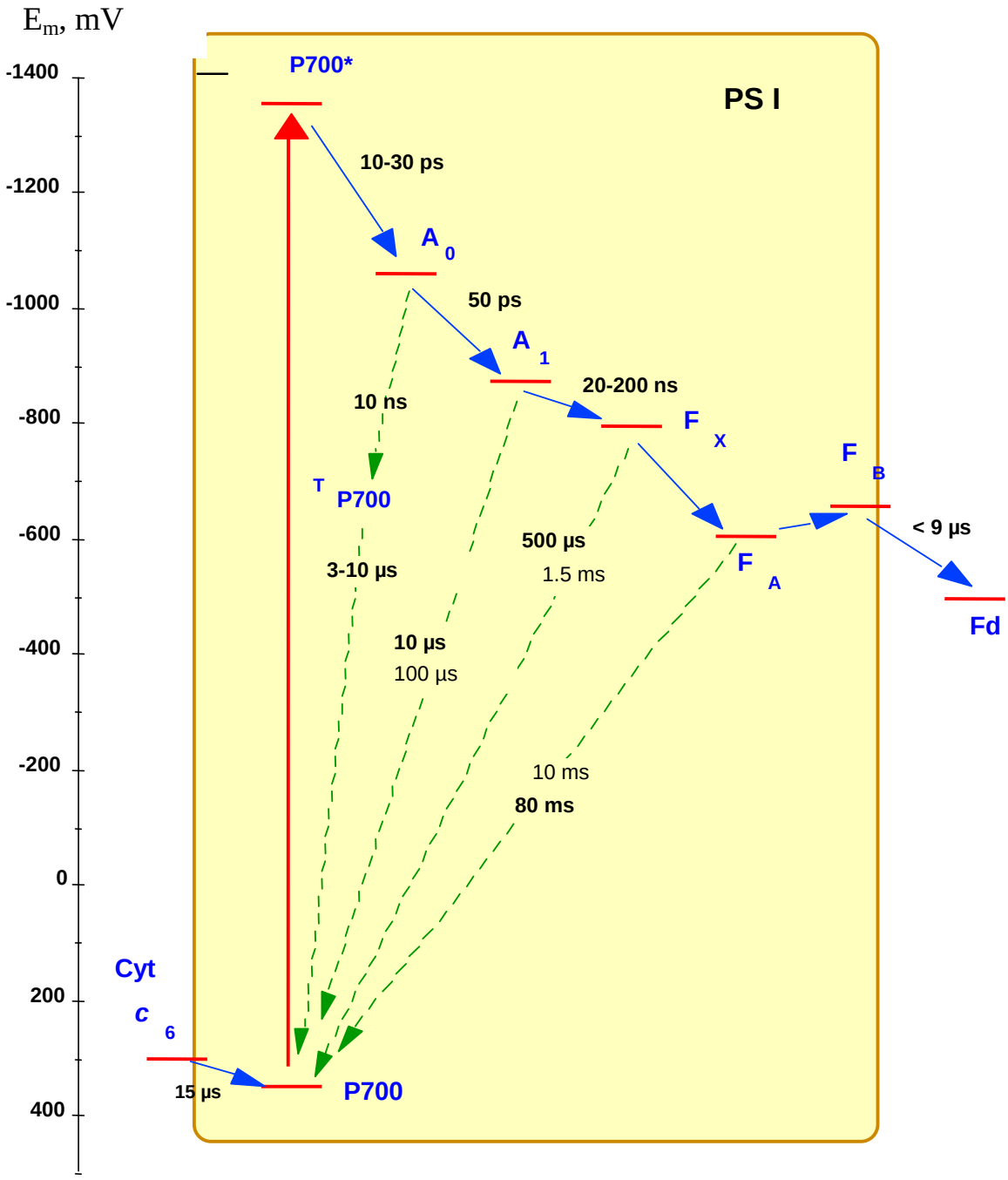
E$_m$, mV
-1400
-1200
-1000
-800
-600
-400
-200
0
200
400
P700*
PS I
10-30 ps
A 0
50 ps
A 1
20-200 ns
F X
F B
F A
Fd
< 9 µs
10 ns
T P700
3-10 µs
500 µs
1.5 ms
10 µs
100 µs
10 ms
80 ms
Cyt c 6
15 µs
P700

Figure 1.4

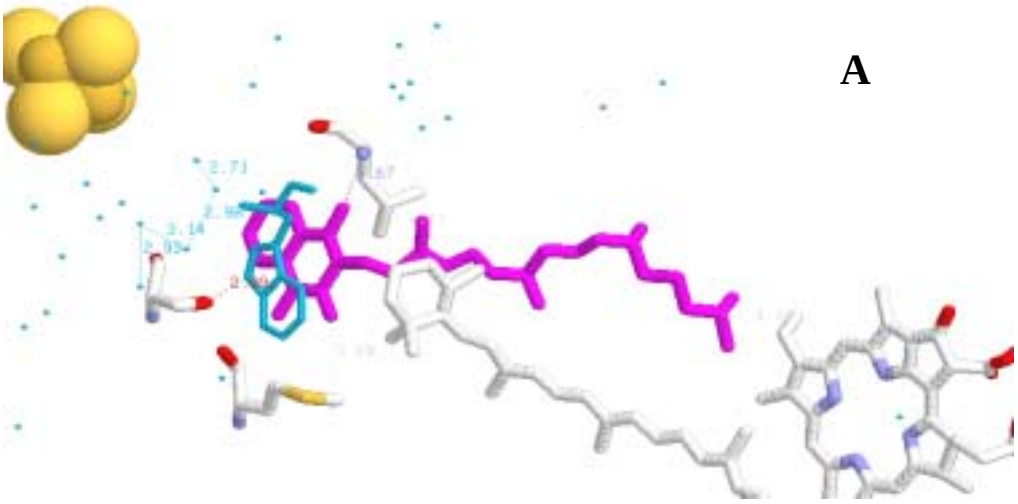

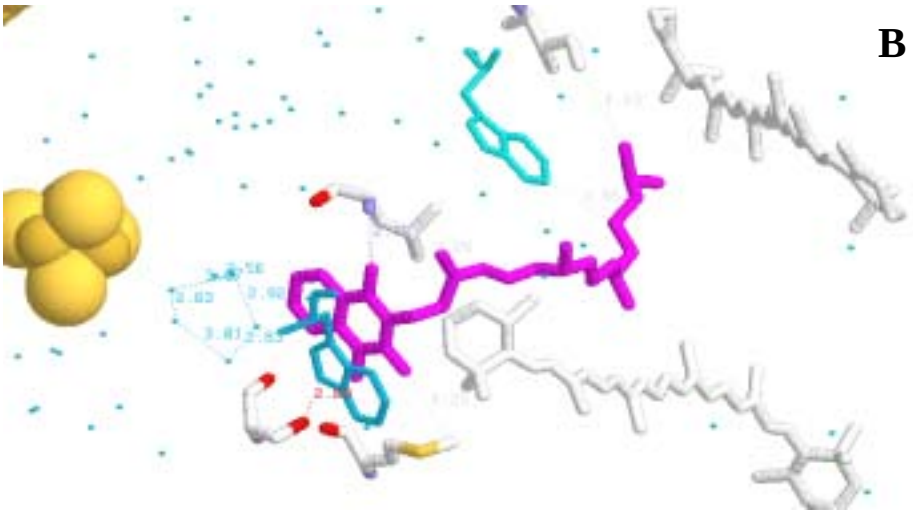

Figure 1.5

Chapter 2

Recruitment of Plastoquinone-9 into the A_1 Site of Photosystem I

[Published in part, as papers:

Johnson, T. W., Shen, G. Z., Zybailov, B., Kolling, D., Reategui, R., Beauparlant, S., Vassiliev, I. R., Bryant, D. A., Jones, A. D., Golbeck, J. H. and Chitnis, P. R. Recruitment of a foreign quinone into the A(1) site of photosystem I. I. GENETIC AND PHYSIOLOGICAL CHARACTERIZATION OF PHYLLOQUINONE BIOSYNTHETIC PATHWAY MUTANTS IN *Synechocystis* sp. PCC 6803 (2000) *J. Biol. Chem.* **275**: 8523-8530

Zybailov, B., A. van der Est, S. Zech, C. Teutloff, T. W. Johnson, G. Shen, R. Bittl, D. Stehlik, P. R. Chitnis, and J. H. Golbeck, Recruitment of a foreign quinone into the A_1 site of photosystem I. II. STRUCTURAL AND FUNCTIONAL CHARACTERIZATION OF PHYLLOQUINONE BIOSYNTHETIC PATHWAY MUTANTS BY EPR AND ENDOR, *J. Biol. Chem.*, **275**: 8531-8539

Semenov A. Y., Vassiliev I. R., van der Est A., Mamedov M. D., Zybailov B., Shen G., Stehlik D., Diner B. A., Chitnis P. R., and Golbeck J. H., Recruitment of a foreign quinone into the A_1 site of photosystem I. III ALTERED KINETICS OF ELECTRON TRANSFER IN PHYLLOQUINONE BIOSYNTHETIC PATHWAY MUTANTS STUDIED BY TIME-RESOLVED OPTICAL, EPR. AND ELECTROMETRIC TECHNIQUES (2000) *J. Biol. Chem.* **275**: 23429-23438]

ABSTRACT

In this chapter I describe the *menB* and *menA* phylloquinone biosynthetic pathway mutants, and I show that plastoquinone-9 (instead of phylloquinone) functions as the A_1 acceptor in PS I. The biosynthetic pathway mutants of *Synechocystis* sp. PCC 6803 grow photoautotrophically under low light intensities and support high rates of electron transfer from cytochrome c_6 to flavodoxin. HPLC analysis of PS I complexes show that plastoquinone-9 is present in the *menA* and *menB* mutants, but not in the wild type. Room temperature CW EPR measurements at 9.4 GHz of whole cells of the mutants show transient appearance and disappearance of an organic radical with the *g*-value and anisotropy characteristic of a quinone. The CW EPR spectrum of the photoaccumulated Q^- radical measured at 34 GHz, and the electron spin-polarized transient EPR spectra of the radical pair $P_{700}^+ Q^-$ measured at 9.4, 34 and 94 GHz, show three prominent features: (i) Q^- has a larger *g*-anisotropy than phylloquinone; (ii) Q^- does not display the prominent methyl hyperfine couplings attributed the 2-methyl group of phylloquinone; (iii) the orientation of Q^- in the A_1 site, as derived from the spin polarization, is within experimental error that of phylloquinone in the wild type. Electron spin echo (ESE) modulation experiments on $P_{700}^+ Q^-$ show that the dipolar coupling in the radical pair is also the same as in wild-type PS I, *i.e.*, the distance between P_{700}^+ and Q^- (25.3 ± 0.3 Å) is the same as that between P_{700}^+ and A_1^- in the wild type. Pulsed electron nuclear double resonance (ENDOR) studies show two spectral features that can be interpreted as arising from a nearly axially symmetric hyperfine coupling, which is tentatively assigned to two methyl groups on Q.

In total, these results show that the foreign quinone Q: (i) occupies the A_1 pocket much as phylloquinone does; (ii) functions in accepting an electron from A_0^- and in efficiently passing the electron forward to the FeS clusters; (iii) has spectroscopic characteristics consistent with its identity as plastoquinone-9. A global multiexponential analysis of time-resolved optical spectra in the blue region shows the following three kinetic components: (i) a 3-ms lifetime, in the absence of methyl viologen, that represents charge recombination between P_{700}^+ and an FeS^- cluster; (ii) a 750-µs lifetime that

represents electron donation from an FeS^- cluster to methyl viologen; and (iii) a ca. 15-µs lifetime that represents an electrochromic shift of a carotenoid pigment. Room temperature direct detection transient EPR studies of forward electron transfer show a spectrum of $P_{700}^+ Q^-$ during the lifetime of the spin polarization and give no evidence of a significant population of $P_{700}^- FeS^-$ for $\tau < 3$ µs. The UV difference spectrum measured 5 µs after a flash shows a maximum at 315 nm, a crossover at 280 nm, and a minimum at 255 nm as well as a shoulder at 290 nm to 295 nm all of which are characteristic of the plastoquinone-9 anion radical. Kinetic measurements that monitor Q at 315 nm show a major phase of forward electron transfer to the FeS clusters with a lifetime of 15 µs - which matches the electrochromic shift at 485 nm of the carotenoid - as well as a minor phase with a lifetime of 250 µs. Electrometric measurements show similar biphasic kinetics. The slower kinetic phase can be detected using time-resolved EPR spectroscopy and has the characteristic spectrum of a semiquinone anion radical. I estimate the redox potential of plastoquinone-9 in the A_1 site to be more oxidizing than phylloquinone, so that electron transfer from Q to F_X is thermodynamically unfavorable in the *menA* and *menB* mutants.

The initial biochemical characterization and physiological studies were done in collaboration with Gaozhong Shen and Wade Johnson. The transient EPR experiments were done in collaboration with Dietmar Stehlik, and the pulsed EPR experiments were done in collaboration with Robert Bittl. The electrometric measurements of the transmembrane potential were performed in collaboration with Mahir Mamedov and Alexey Semenov. Identification of quinone species in the mutant PS I complexes by mass spectrometry was performed in collaboration with Daniel Jones.

INTRODUCTION

Light induced charge separation in photosynthetic reaction centers proceeds via a common multistep electron transfer process to a stabilized, charge-separated radical pair state $P^+ Q^-$, consisting of an oxidized chlorophyll donor and a reduced quinone acceptor. Two types of reaction centers can be distinguished according to the electron acceptors and electron transfer pathways subsequent to the quinone acceptor. A series of FeS clusters with electron transfer essentially perpendicular to the membrane characterize Type I reaction centers (PS I, green sulfur bacteria, heliobacteria), whereas a second quinone acceptor Q_B and electron transfer parallel to the membrane from the first quinone acceptor Q_A characterize Type II reaction centers (PS II and the reaction centers of purple bacteria). The first quinone is therefore the interface either between electron transfer involving organic cofactors and electron transfer involving FeS clusters (Type I), or between pure electron transfer and coupled electron and proton transfer involving a second organic cofactor (Type II). Their widely varying midpoint potentials, their ability to be an electron-only or an electron-and-proton carrier, and their function as a bound or mobile electron (and proton) carrier are the primary reasons to study and compare the available structural and functional properties of quinones in their native binding sites.

Compared with the binding sites for Q_A and Q_B in bacterial reaction centers, the binding sites for phylloquinone in PS I are poorly understood. Transient EPR studies of the radical pair $P^+ A_1^-$ (Stehlik *et al.,* 1989; van der Est *et al.,* 1997) show that phylloquinone is oriented with its carbonyl bonds parallel to the vector joining P_{700}^+ and A_1^-. Measurement of the dipolar coupling between the P_{700}^+ and A_1^- radical pair shows the distance between these two radicals to be 25.4 ± 0.3 Å (Zech *et al.,* 1996; Dzuba *et al.,* 1997; Bittl *et al.,* 1997). Transient EPR studies of $P^+ A_1^-$ in single crystals of PS I provide an angular range for the orientation of phylloquinone (Kamlowski *et al.,* 1998) which is consistent with a spin echo study (Bittl *et al.,* 1997). These studies show that the dipolar coupling axis and the quinone carbonyl bonds make an angle of 27±5 degrees with the crystallographic *c*-axis (membrane normal). Nearly the same orientation has

been determined from EPR studies of photoaccumulated A_1^- in oriented membranes (MacMillan *et al.,* 1997).

The orientation of the other axis in the quinone plane is less certain. For photoaccumulated A_1^- in oriented membranes, the quinone plane is nearly perpendicular to the membrane (76 degrees) (MacMillan, 1997). Recent transient Q-band EPR of $P_{700}^+A_1^-$ in PS I single crystals (Zech, 1999) determine an angle of 55 ± 20 degrees between the quinone plane and the plane containing the carbonyl bond direction and the crystalline *c*-axis (membrane normal), which is in good agreement with the most recent X-ray structure (Jordan *et al.,* 2001).

The spectroscopic distance and orientation information was crucial in allowing the identification of two regions in the electron density map that likely correspond to the quinones. One of the two quinones could be located on the initial 4 Å electron density map of PS I complexes from *Synechococcus elongatus* (Schubert *et al.,* 1997), but a refined electron density map has since allowed the second quinone to be located (Klukas *et al.,* 1999). The modeling of the A_1 binding pocket, which was initially derived from the ENDOR and spin echo studies, places phylloquinone near the loop connecting the *m* (*m*') transmembrane and *n* (*n*') surface helices of PsaA/B heterodimer in the PS I reaction center, with a parallel arrangement to a W residue located at the beginning of the *n* (*n*') helix as a likely contribution to A_1 binding (Kamlowski *et al.,* 1998). The current X-ray structure of PS I confirms these predictions (Jordan *et al.,* 2001).

A variety of benzoquinones, naphthoquinones and anthraquinones can replace phylloquinone after solvent extraction, and these substitute quinones are capable of accepting electrons from A_0 (Takahashi, 1985; Ikegami, 1987; Biggins, 1990; Iwaki, 1991). 2-methyl-3-decyl-1,4-naphthoquinone, 2-methyl-3-$(isoprenyl)_2$-1,4-naphthoquinone, and 2-methyl-3-$(isoprenyl)_4$-1,4-naphthoquinone are the only quinones that appear to be capable of passing electrons forward to F_X. This implies that the 2-methyl group and/or the 3-phytyl side chain of phylloquinone are required for correct interaction with a hydrophobic domain of the A_1 site (Biggins, 1988; Biggins, 1990). The proper orientation of the head group may be the critical factor in the ability of the quinone to transfer an electron to F_X (Sieckman *et al.,* 1991; van der Est *et al.,* 1995), or

an appropriate redox potential may be the only requirement for a quinone to function in electron transfer from A_0 to F_X (Itoh and Iwaki, 1991; Iwaki and Itoh, 1994). The discrepancy between the two schools of thought could result from differences due to the chemical treatments used to extract the phylloquinone and to introduce a foreign quinone in PS I. In view of this problem, I sought an entirely new approach to remove phylloquinone from the A_1 site.

My approach was to study mutants in which the phylloquinone biosynthesis pathway was interrupted (Johnson *et al*, 2001). The *menA* gene product (naphthoate synthase) and the *menB* gene product (phytyl transferase) were proposed to be directly involved in the biosynthesis of phylloquinone and were therefore targeted for insetional inactivation. The goal was to disallow the biosynthesis of phylloquinone and produce an empty A_1 site, which could then be reconstituted with a variety of quinones. Instead, it was found that photoautotrophic growth under low light intensities and steady-state rates of flavodoxin reduction were relatively unaffected by the absence of phylloquinone. To account for these results, I proposed that the A_1 site was not empty, but that a foreign quinone had been recruited into the A_1 sites of the *menA* and *menB* mutants. In this chapter I provide evidence for the presence of a functional quinone in the *menA* and *menB* mutant strains of *Synechocystis* sp. PCC 6803. From its EPR spectroscopic properties, structural characteristics are derived that are consistent with identifying the foreign quinone as plastoquinone-9 (Fig. 2.3).

I further explore the functional consequences of the presence of plastoquinone-9 in the A_1 site. Plastoquinone-9 and phylloquinone have different one-electron reduction potentials in dimethylformamide, and therefore they are likely to possess different reduction potentials - and hence different kinetic properties - in the A_1 site. The kinetics of forward electron transfer from A_1^- to the FeS clusters in wild-type PS I have been well documented using transient EPR spectroscopy and time-resolved UV spectroscopy. Both methods are consistent in showing a forward electron transfer time of ca. 280 ns in spinach and cyanobacterial PS I complexes (Brettel 1988; Bock *et al.*, 1989; Sétif and Brettel, 1993; van der Est *et al.,* 1994). Photovoltage measurements of the oriented cyanobacterial PS I complexes reveal an electrogenic phase with a forward electron

transfer time similar to that ascribed to the A_1^- to F_X transition (Leibl *et al.,* 1995). Optical studies reveal an additional component with a forward electron transfer time of ca. 10 ns in detergent-treated samples, but not in whole cells (Brettel, 1988). In the absence of detergent, the fast phase represents only 30% of the total contribution, leading to the possibility that in native membranes the forward transfer time is the same in spinach and cyanobacteria.

Since electron transfer rates are sensitive to changes in Gibbs free energy, as well as to alterations in distances and reorganization energies among donor and acceptor pairs, the replacement of phylloquinone by plastoquinone-9 is expected to translate into a change in the rate of electron transfer through A_1. However, the reorganization energy is not expected to differ significantly, given that the replacement quinones are structurally similar to phylloquinone. I find that the rate of forward electron transfer from Q^- to F_X is slowed by a factor of 100 to 1000 compared with that of the wild type. The forward electron transfer kinetics allows us to measure a light induced difference spectrum of Q^- minus Q in the UV. Based on the behavior of plastoquinone-9 and phylloquinone in organic solvents, and based on rate versus free energy relationships derived from electron transfer theory, I estimate the redox potential of plastoquinone-9 in the A_1 site.

MATERIALS AND METHODS

Growth of Synechocystis sp. PCC 6803

Wild-type *Synechocystis* sp. PCC 6803 cells were grown in medium BG-11 (Rippka *et al.,* 1979). The *menA* and *menB* mutant strains of *Synechocystis* sp. PCC 6803 were grown in medium BG-11-TES supplemented with 5 mM glucose and the appropriate antibiotic. Agar plates for the growth of mutant strains were kept at low light intensity (2 to 5 $\mu E\ m^{-2}\ s^{-1}$). Liquid cultures of wild-type and mutant strains were grown under reduced light conditions (10 to 20 $\mu E\ m^{-2}\ s^{-1}$) in the presence of 5 mM glucose (Johnson *et al.,* 2000). Cell growth in liquid cultures was monitored by measuring the absorbance at 730 nm using a Cary-14 spectrophotometer that had been modified for computerized data acquisition by On-Line Instruments, Inc. (Bogart, GA). Cells from liquid starter cultures in the late exponential phase of growth (A730 = 0.8 to 1.2) were harvested by centrifugation and were washed once with BG-11 medium. For growth experiments, all cultures were adjusted to the same initial cell density (A730 = 0.1) and bubbled with air as described (Shen *et al.,* 1993).

Growth of Synechocystis sp. PCC 6803 in D_2O

Unlike wild-type *Synechococcus* sp. PCC 7002 (Klughammer *et al.,* 1997; Yang *et al.,* 1998; Klughammer *et al.,* 1999), wild-type *Synechocystis* sp. PCC 6803 does not immediately grow in a culture medium in which H_2O is replaced with D_2O. Instead, we found it necessary to adapt the cultures to gradually increasing D_2O concentrations. The cells were initially grown in BG11 medium containing 35% D_2O under normal light intensity (40 to 60 $\mu E\ m^{-2}\ s^{-1}$). At late exponential phase (A730, 0.75 to 1.0), the cells were pelleted and reinoculated to A730 = 0.1 in a BG11 solution containing 40% D_2O; the excess cells were frozen in 50/50% (v/v) water/glycerol and retained. This process was repeated by increasing the D_2O concentration by 5% increments to 90% D_2O, and lastly by a 2% increment to 92% D_2O, the maximum that allowed growth. Above 50% D_2O, the cells were inoculated twice at a set D_2O percentage to ensure the stability of the cultures. Cells above 50% D_2O grew at approximately half the rate of H_2O grown cells

when fully adapted. Cells grown in cultures of ≥500 ml were shaken slowly in a 3-liter flat-bottomed Erlenmeyer flask. The flask was slowly purged, but not bubbled, with sterile, dry air to reduce the depletion of D_2O by evaporation. Cells grown at 92% D_2O could be streaked onto a BG-11 agar plate containing 100% H_2O for storage and still retain the ability to grow in D_2O liquid cultures. To initiate growth of D_2O -adapted cells that had been stored on plates, the cells were inoculated in a medium with 75% D_2O, grown to late exponential phase, and then reinoculated in a medium with 92% D_2O. The *menB* mutant cells could grow in BG11 medium only up to 55% D_2O (*menA* cells were not studied). At concentrations higher than 55%, the *menB* mutant cells maintained a green color but did not divide.

Isolation of Thylakoid Membranes and PS I Complexes

Thylakoid membranes were prepared from cells in the late exponential growth phase as described by Shen *et al.*, (1993). Cells were broken by two passages through a French pressure cell at 20,000 lb in^{-2} at 4 °C. The thylakoid membranes were pelleted by centrifugation at 50,000 × *g* for 45 min. The thylakoid membranes were resuspended in buffer (50 mM HEPES/ NaOH, pH 8.0, 5 mM $MgCl_2$, 10 mM $CaCl_2$, 0.5% (v/v) dimethyl sulfoxide, and 15% (v/v) glycerol) for storage, or resuspended in 50 mM Tris/HCl, pH 8.0, for further PS I complex preparations. For the isolation of PS I complexes, thylakoid membranes were solubilized in 1% (w/v) *n*-dodecyl-β-D-maltoside (β-DM) for 2 to 4 h at 4 °C. The trimeric and monomeric PS I complexes were separated by centrifugation on 5 to 20% (w/v) sucrose gradients with 0.03% β-DM in 50 mM Tris at pH 8.0. Further purification was achieved by a second centrifugation on sucrose gradients in 50 mM Tris at pH 8.0 in the absence of β-DM at 10 ml min^{-1} (Johnson, 2000).

Analysis of Phylloquinone Using HPLC-UV/Vis and Mass Spectrometry

Membranes containing 0.1 mg of chlorophyll ml^{-1} were centrifuged at 1000 × *g* for 60 min, and the supernatant was removed. The membrane pigments were sequentially

extracted with 1 ml of methanol, 1 ml of 1:1 (v/v) methanol:acetone, and 1 ml of acetone, and the three extracts were combined. The resulting solution was concentrated by vacuum at 10 °C in the dark to approximately 0.8 mg chlorophyll ml^{-1}. Chromatography with UV/Vis detection was performed on an ISCO dual pump HPLC system (Lincoln, NE). The pumps were operated by ISCO Chemresearch version 2.4.4 software, UV/Vis detection was performed with an ISCO V4 absorbance detector set at 255 nm, and data collection and processing were done using JCL6000 version 26 software (Jones Chromatography Limited, Mid-Glamorgan, UK). HPLC separations were also monitored with photodiode array UV/visible detection using a Hewlett-Packard (Palo Alto, CA) model 1100 quaternary pump and model G1316A photodiode array detector. Sample injections (20 ml) were made on a 4.6-mm x 25-cm Ultrasphere C18 column (4.6 mm x 250 mm) with 5 mm packing (Beckman Instruments, Palo Alto, CA), using gradient elution (solvent A, methanol; solvent B, isopropanol; 100% A from 0 to 10 min to 3% A/97% B at 30 min, hold until 40 min) at 0.5 ml min-1. A solution of phylloquinone (40 mM) was prepared in absolute ethanol and kept at -20 °C as a standard for calibration. Extracts were also analyzed by LC/MS using a Perceptive Biosystems Mariner time-of-flight mass spectrometer with electrospray ionization in negative mode with a needle potential of -3500 V and a nozzle potential of -80 V. A postcolumn flow splitter delivered column eluent to the electrospray ion source at 10 µl min^{-1}. Gas chromatography/MS analyses were performed using a Hewlett-Packard 5972 mass spectrometer coupled to a Hewlett-Packard 5890 gas chromatograph. Splitless injections of 1.0 µl were made onto a 30-m DB-5 column (J & W Scientific, Folsom, CA) using helium (35 cm s^{-1}) as the carrier gas. The column was programmed from 100 °C to 300 °C at a rate of 6°C min^{-1}. Data were acquired in full scanning mode and using selected ion monitoring of m/z 450 for trace detection of phylloquinone.

X-band CW EPR Spectroscopy

Whole-cell EPR experiments were carried out using a Bruker ER300E spectrometer equipped with a TM110 cavity. Mutant and wild-type cells of *Synechocystis* sp. PCC 6803 were grown photomixotrophically to early exponential phase, collected by

centrifugation at room temperature and resuspended in growth medium to 0.4 mg of chlorophyll ml^{-1}. The protocol for studying the time-dependent kinetics of P_{700}^{+} and A_1^{-} is a modification of the method described by Klughammer *et al*. in 1997 and 1999. Viable cells were placed in a 10-ml reservoir that was incorporated into a closed circuit with an aqueous flat cell by means of tubing and a microprocessor-controlled peristaltic pump (ISCO WIZ) to an aqueous flat cell (Wilmad WG-813- Q). The reservoir, tubing, and TM110 cavity were maintained in complete darkness to ensure that the cells were dark-adapted. A 200-watt mercury-xenon lamp provided controlled illumination by use of a Uni-Blitz shutter and shutter driver/timer (model T132). The EPR computer was programmed to begin data acquisition at t = 0, open the shutter at t = 0.2 s, close the shutter at t = 2.7 s, and pump a fresh sample into the flat cell at t = 4.0 s. This protocol was repeated 20 times at 10-s intervals at a given magnetic field to obtain data with an adequate signal to noise ratio. The magnetic field was stepped 0.5 G, and the process was repeated until data had been obtained at 54 magnetic field settings. The data were downloaded to a Power Macintosh G3 computer and plotted as three-dimensional and two-dimensional data sets using Transform 2.0 (Spyglass, Inc.).

Q-band CW EPR Spectroscopy

Photoaccumulation experiments at Q-band (34 GHz) were carried out using a Bruker ESR300E spectrometer equipped with an ER 5106 QT-W1 resonator with a port for in-cavity illumination. Cryogenic temperatures were maintained with an ER4118CV liquid nitrogen cryostat and controlled with an ER4121 temperature control unit. The microwave frequency was measured with a Hewlett-Packard 5352B frequency counter, and the magnetic field was measured with a Bruker ER035M NMR gaussmeter. The magnetic field was calibrated by γ,γ-bisdiphenylene-β-phenylallyl complexed 1:1 with benzene.

Photoaccumulation protocols on wild type and mutant PS I complexes were carried out in a manner similar to that described in (Yang *et al.,* 1998). Prior to the measurement, the pH of the sample was adjusted to 10.0 with glycine buffer, and sodium dithionite was added to a final concentration of 50 mM. After incubation for 20 min in

the dark, the sample was placed into the resonator, the temperature adjusted to 205 K, and a background spectrum was recorded. The sample was illuminated with a 20-mW He-Ne laser at 630 nm for 40 min, the laser was turned off, and the light-induced spectrum was recorded. The spectra reported represent the difference between the two measurements. EPR spectral simulations were carried out on a Power Macintosh G3 computer using a Windows 3.1 emulator (Soft Windows 3.0, Insignia Solutions, Santa Clara, CA) and SimFonia software (Bruker Analytik), and then they were imported into *Igor Pro* (Wavemetrics, Inc.).

Time-resolved CW EPR Spectroscopy

EPR spectral changes shown in Fig. 2.10 B were measured using a Bruker ESP 300E spectrometer equipped with a TM110 cylindrical resonator (Bruker ER4103). A frequency-doubled Nd-YAG laser (Spectra Physics DCL) provided the excitation flash at a wavelength of 532 nm and an energy of 14 mJ. The computer was configured to capture and average the data and to flash the laser at 10-s intervals. The data represent an average of 64 flashes. The flat cell (Wilmad WG-813-Q) contained the PS I complexes isolated from the *menA* or *menB* mutants at 0.4 mg of chlorophyll ml^{-1}, 25 mM Tris-HCl, pH 8.3, 10 mM sodium ascorbate, 4 mM of 2,6-dichlorphenol-indophenol (DCPIP), and 0.03% w/v β-DM.

Time-resolved EPR and ENDOR Spectroscopy

All samples contained 1 mM sodium ascorbate and 50 mM phenazine methosulfate as external redox agents and were frozen in the dark for the low temperature experiments. The W-band (94 GHz) transient EPR spectra were measured using a Bruker E680 spectrometer. Illumination was accomplished with a frequency-doubled Nd-YAG laser using an optical fiber fed into the sample capillary and terminated directly above the PS I sample. Q-band (35 GHz) transient EPR spectra were measured in the set-up described earlier (van der Est *et al.*, 1998), except that a Bruker ER 056 QMV microwave bridge equipped with a home-built cylindrical resonator and an Oxford CF935 liquid helium cryostat was used. The transient and pulsed X-band EPR measurements were

performed using the experimental setup described in (Bittl *et al*., 1997). Two microwave (mw) pulses with a variable pulse spacing τ, were applied to the radical pair $P_{700}^{+}Q^{-}$ at a time t, following the laser flash. ESE amplitude modulation curves were obtained by recording the amplitude of the echo detected at time $T \approx \tau$ after the second mw pulse as a function of τ. The mw pulse lengths were set to 8 ns for the first pulse and 16 ns for the second pulse, resulting in flip angles of about 65 and 130°, respectively, with a microwave field B_1 = 0.8 mT. The external magnetic field B0 and the detection time T were adjusted to yield maximum out-of-phase echo intensity. The echo modulation was recorded at 512 points with 8-ns increments in t, and 64 traces were averaged to increase the signal-to-noise ratio. Pulsed ENDOR studies of the $P_{700}^{+}Q^{-}$ state were performed using the same experimental setup as for the pulsed EPR experiments, using a Bruker ESP360D-P ENDOR accessory, a Bruker ER4118X-MD-5W1-EN ENDOR resonator, and an ENI A500 radiofrequency amplifier. The pulse sequence was, according to Davies-ENDOR, π(mw) - π (radiofrequency) - $\pi/2$(mw) - π (mw) - echo, with identical lengths of the two microwave π pulses.

Optical Kinetic Spectroscopy in the Near-IR Region

Optical absorbance changes in the near-IR were measured using a laboratory-built spectrophotometer (Vassiliev *et al.*, 1997). To ensure resolution of kinetics in the microseconds time domain, the high frequency roll-off amplifier described in the original specifications was not used, but instead the signal was fed directly into the plug-in (11A33 differential comparator, 100-MHz bandwidth) of the Tektronix DSA601 oscilloscope. The sample cuvette contained the PS I complexes isolated from the *menA* or *menB* mutants at 50 mg chlorophyll ml^{-1} in 25 mM Tris/HCl, pH 8.3, 10 mM sodium ascorbate, 4 mM DCPIP, and 0.04% w/v β-DM.

Optical Kinetic Spectroscopy in the Visible Region

Optical absorbance changes in the visible region were measured using a laboratory-built spectrometer consisting of a 400-watt tungsten-halogen source (Oriel), a

1⁄4 -meter monochromator (Jarrell Ash model 82-410) prior to the sample cuvette (to select a measuring wavelength), a sample compartment for a 1 3 1-cm fluorescence (4-sided clear) cuvette, a second 1⁄4 -meter monochromator (Jarrell Ash model 82-410) after the sample cuvette (to reject the flash and fluorescence artifacts), and a PIN-10 photodiode detector (United Detector Technology). Suitable lenses were placed to focus the light onto the monochromator slits and to provide a collimated beam through the sample cuvette. The photocurrent was converted to a voltage with a 30,000-ohm resistor; the voltage was amplified using a model 100 amplifier (EG & G) set to a DC bandwidth of 100 kHz; the signal was digitized using a Model 4094A digital oscilloscope (Nicolet Instruments, Madison, WI). This was interfaced via an IEEE-488 bus using a GPIB-TNT board (National Instruments, Austin, TX) in a Power Macintosh 7100/88 computer. The data were transferred to the computer and stored as binary files using LabView 4.1 (National Instruments, Austin, TX) and further processed in *Igor Pro* (Wavemetrics, Inc., Lake Oswego, OR). Actinic flashes were supplied using a frequency-doubled Nd-YAG laser (Spectra Physics) operating at 532 nm with a flash energy of 1.4 mJ. Each kinetic trace represents 16 averages within the digital oscilloscope. The sample cuvette (10 x 10-mm) contained 3.0 ml of PS I complex at 10 µg chlorophyll ml^{-1} suspended in 25 mM Tris, pH 8.3 with 0.04% w/v β-DM, 10 mM sodium ascorbate, and 4 µM DCPIP.

Optical Kinetic Spectroscopy in the UV Region

Optical studies in the UV (240 nm to 340 nm) were conducted using a pulse-probe spectrometer described in Diner (1998). The monochromator slit was fixed at 4 mm, equivalent to a bandwidth of 8 nm. Measurements in the UV were performed using a xenon flashlamp as the actinic source filtered by a Schott and a Kodak Wratten 34 filters. The photodiodes were protected by Corion Solar Blind UV-transmitting filters. The optical path length of the sample cuvette was 1 cm. Each data point represents the average of eight measurements, taken with a flash spacing of 20 s to allow complete reduction of P_{700}^{+} by the external donor. A background measurement was taken similarly, except that the sample was shielded from the detecting flash to allow for correction of the actinic flash artifact. The absorbance change reported represents the difference between

the two measurements. The sample cuvette contained the PS I complexes isolated from the *menB* mutant at 10 µg chlorophyll ml^{-1}, 25 mM Tris/HCl, pH 8.3, 10 mM sodium ascorbate, 4 mM DCPIP, and 0.03% β-DM.

Electron Spin Polarized Transient EPR Spectroscopy (Direct Detection)

Room temperature transient EPR experiments were carried out using a setup described in detail elsewhere (van der Est *et al.,* 1998). The samples were pumped continuously through a flat cell mounted in a Varian rectangular resonator equipped with a rough-surfaced glass window that scatters the laser light to provide a more even distribution of light intensity in the cell. Time/magnetic field data sets were collected using direct detection by measuring light-induced transients at fixed magnetic field positions over an appropriate spectral region. Decay-associated spectra were then generated by fitting the transients with a kinetic function and plotting the amplitude(s) against the magnetic field as discussed (Bock *et al.,* 1989; van der Est *et al.,* 1994).

Transient EPR Spectroscopy with Field Modulation Detection

The same setup and conditions were also used to collect time time/field data sets shown in Fig. 2.16 but in this case with field modulation and lock-in detection. By using direct detection, the decay of the spin polarization limits the accessible time range to times shorter than a few microseconds. By using field modulation, the spectrometer has a rise time of ca. 50 µs but a much higher sensitivity so that slow forward electron transfer and charge recombination can be monitored.

Photovoltage Measurements

Measurements of transmembrane electric potential difference generation by PS I-containing proteoliposomes adsorbed onto the surface of azolectin-impregnated collodion film were done at room temperature as described elsewhere (Mamedov *et al.,* 1996). The instrument rise-time was 200 ns. Saturating light flashes were provided by a frequency-doubled Quantel Nd:YAG laser (532 nm; pulse half-width, 15 ns; flash energy, 20 mJ).

Analysis of Kinetic Data

The multiexponential fits of optical and EPR kinetics were performed by the Marquardt algorithm in Igor Pro version 3.14 (Wavemetrics Inc., Lake Oswego, OR) on a G3/300 Macintosh computer. For global analysis of kinetics in the visible region (Fig. 2.11), individual kinetics were analyzed first assuming the presence of either three components or two components and a base line. The results of these analyses were then used for fitting the whole set of data to global lifetimes, and the best solution was chosen based on the analysis of χ^2, standard errors of the parameters, and the residuals of the fits.

RESULTS

Absence of Phylloquinone in the menA and menB Mutant Strains

The phylloquinone content of the PS I complexes was determined using HPLC with photodiode array UV-visible detection. As shown in Fig. 2.3 A, multiple peaks are present in the 254-nm chromatogram of the solvent extracts from PS I complexes of wild-type cells. By co-injecting standards and interpreting the UV-visible spectra, chlorophyll *a* was identified at 24.7 and 27.0 min (the former is missing the phytyl tail), a polar carotenoid (probably monohydroxylated but otherwise uncharacterized) was identified at 28.4 min, and β-carotene was identified at 37.0 min. Phylloquinone was identified by co-elution at 29.7 min with an authentic phylloquinone standard (Fig. 2.3 A, *top* inset) as well as by its UV-visible spectrum (Fig. 2.3, *bottom* inset). As shown in Figure 2.3 B, virtually identical chromatograms were obtained for solvent extracts of PS I complexes from the *menA* and *menB* mutants, except that the phylloquinone peak at 29.7 min is missing. Gas chromatography/MS is capable of separating and detecting nonpolar benzoquinones, ubiquinones and naphthoquinones, provided their molecular masses are less than about 600 Da. Using total ion current for detection, the crude solvent extract from wild-type PS I complexes showed a peak with a retention time of approximately 8 min, which matched that of authentic phylloquinone. The molecular ion at m/z = 450 confirmed the identification of this molecule as phylloquinone. Sensitive selected-ion-monitoring analyses did not find a detectable amount of phylloquinone in solvent extracts of PS I complexes isolated from either the *menA* or *menB* strains. The limit of detection using selected ion-monitoring was determined from the calibration curve to correspond to approximately 0.1% of the wild-type level. Because there are approximately 100 chlorophyll per P_{700} in cyanobacterial PS I complexes, the *menA* and *menB* mutant strains thus contain $\leq$0.02 phylloquinones per P_{700}.

Presence of Plastoquinone-9 in the menA and menB Mutant

Through the EPR measurements of the whole *menB* and *menA* cells, as well as of the photoaccumulated PS I complexes (these results are discussed further below), we

found that a quinone other than phylloquinone functions as a A_1 acceptor in the mutant PS I complexes. To determine the identity of this quinone, solvent extracts of PS I complexes from the *menA* and *menB* mutants were analyzed by HPLC using photodiode array UV-visible detection. The search was initially complicated by the absence of new peaks in chromatograms. We therefore sought evidence of a new component co-eluting with another pigment, by comparing the UV-visible spectra of peaks in chromatograms of the *menA* and *menB* mutants with the corresponding peaks for the wild type.

The only significant difference was in a component that co-eluted with β-carotene at 37 min. The difference spectrum of the components eluting at 37 min showed a strong absorbance near 254 nm that was lacking in the wild type (Fig. 2.3 B, *bottom* inset). This is the spectral region in which the biologically occurring benzoquinones, ubiquinones, and naphthoquinones absorb strongly but in which β-carotene has relatively weak absorbance. It was noted that the UV spectrum of the coeluting component was similar to plastoquinone-9, a quinone that is present in thylakoid membranes at a 10-fold higher concentration than phylloquinone (Grane *et al*., 1960). Indeed, it was found that authentic plastoquinone-9 coelutes with, and has a UV spectrum that matches, the peak at 37 min (Fig. 2. 3 B, *top* inset). Sensitive selected-ion-monitoring analyses of the HPLC eluate at the mass of plastoquinone-9 (*m/z* 748) showed a peak at this retention time. We consistently found levels of plastoquinone-9 in trimeric PS I complexes from the *menA* and *menB* mutants similar to those of phylloquinone in PS I complexes from the wild type. In contrast, no plastoquinone-9, or a very small amount was found in PS I complexes from the wild type. Full scan HPLC/MS analyses of the mutants showed that none of the other peaks showed molecular ions of related naphthoquinones (such as biosynthetic precursors of phylloquinone).

In Vivo Detection of a Quinone in the A_1 Site by X-band EPR

The semiquinone anion radical of A_1 can be observed transiently in whole cells of *Synechococcus* sp. PCC 7002 as a light-induced resonance centered at g = 2.0049 and with a peak-to-peak linewidth of 10 G (Klughammer and Pace, 1997; Klughammer *et al.*, 1999). The ability to detect a quinone radical *in vivo* at room temperature thus provides a

useful method to determine whether a quinone is present or absent in the A_1 binding site of the *menA* and *menB* mutants. When whole *menA* cells of *Synechocystis* sp. PCC 6803 are dark-adapted and illuminated for 2.5 s, a plot of time versus magnetic field versus amplitude depicts two independent radicals undergoing time-dependent and nearly reciprocal patterns of oxidation and reduction (Fig. 2.4). Whole cells of the *menB* mutant show a similar time course (data not shown). The radical attributed to P_{700}^+ is the highly symmetrical resonance with maxima and minima at 3482 and 3490 G, and the radical attributed to a foreign quinone, termed Q^-, is the anisotropic resonance visible around 3475 G as the low field shoulder (Fig. 2.4, arrow). The time course is caused by a transient rate limitation in the utilization of NADPH, which causes electrons to back up, reducing, in sequence, F_A, F_B, F_X, and finally the quinone in the A_1 site. At a certain point in time, the rate limitation is relieved, the reduced acceptors pass their electrons forward, and P_{700}^+ once again is allowed to accumulate due to the availability of oxidized acceptors beyond A_0. Were the foreign quinone Q^- not able to pass electrons forward in the *menA* and *menB* mutants, then both the quinone and P_{700} would remain reduced in the light. The resonances from P_{700}^+ and Q^- can be better distinguished when the plot is oriented so that the time axis is normal to the plane of the paper. In this depiction, the P_{700}^+ radical that develops on initial illumination is identified in Fig. 2.5 (top, dotted line) as the highly symmetrical resonance centered at g = 2.0023 with peak-to-peak linewidth of 7.8 G. The spectrum of Q^- denoted by the arrow in Fig. 2.4 is the highly anisotropic resonance in Fig. 2.5 (top, solid line), with a crossover at g = 2.0042 and peak-to-peak linewidth of 10.5 G. On cessation of illumination, the highly symmetrical resonance in Fig. 2.5 (top, dashed line) is derived again from P_{700}^+. The kinetics of P_{700}^+ and Q^- can be resolved by measuring the former at the Q^- zero crossing point of 3484.5 G, and the latter at the P_{700}^+ zero crossing point of 3475 G. After an initial instrument-limited rise, P_{700}^+ undergoes a time-dependent decay that is roughly mirrored as a rise in Q^- (Fig. 2.5, *bottom*). After reaching a maximum at 0.5 s of illumination, the slower decay of Q^- is roughly mirrored as a reciprocal rise in P_{700}^+. Measurements made at 3486 G, which is on the low field shoulder of the 10.5 G-wide Q^- radical, and for which the contribution from P_{700}^+ is negligible, confirm the kinetic measurement made at 3475 G (zero crossing point

of P_{700}^+ at g = 2.00232). The relevance of this analysis to the *menA* and *menB* mutants is 2-fold: (i) the *g*-value and *g*-anisotropy of the transiently produced Q^- is consistent with its identification as a semiquinone anion radical, and (ii) the transiently produced radical shows that Q is capable of not only accepting electrons from A_0^- via P_{700}^+ but also of discharging electrons by forward electron transfer after a suitable period of adaptation. Hence, the foreign quinone Q is dynamic and participates in forward electron transfer to the FeS clusters under physiological conditions.

CW EPR Spectroscopy at Q-band of Photoaccumulated A_1

The *g*-anisotropy derived from high field CW EPR studies of photoaccumulated PS I complexes contains information about the degree of aromaticity of the semiquinone anion radical. To extract the *g*-tensor, the EPR spectrum of the photoaccumulated Q^- radical in the wild type and in the *menA* and *menB* mutants was measured at 34 GHz (Q-band), a frequency in which the nuclear-electron hyperfine couplings no longer dominate the spectrum. Fig. 2.6 (solid line) shows the spectrum of wild-type PS I complexes isolated from *Synechocystis* sp. PCC 6803 grown in H_2O. At 34 GHz, the field-dependent *g*-anisotropy dominates the spectrum of A_1^- (Thurnauer and Gast, 1985), allowing the turning points of g_{xx} = 2.0062 and g_{zz} = 2.0021 to be partially resolved. The g_{yy} component of the tensor is obscured by the four hyperfine lines resulting from the high spin density at the carbon position 2 of the phyllosemiquinone radical with the methyl group attached.

To better resolve the *g*-anisotropy, PS I complexes were isolated from *Synechocystis* sp. PCC 6803 grown in 92% D_2O, the highest concentration that permitted growth. As shown in Fig. 2.6 (*solid* line), the suppression of the hyperfine couplings results in a narrowing of the line widths of the *g*-components, with the consequence that g_{xx}, g_{yy}, and g_{zz} are almost completely resolved. Satisfactory simulation of the spectrum is obtained with the *g*-tensor principal values g_{xx} = 2.0062, g_{yy} = 2.0051, and g_{zz} = 2.0022 and line widths of 2.4, 3.7, and 2.4 G, respectively. This is in good agreement with previous determinations of the A_1 *g*-tensor from 34 GHz (Q-band) studies of deuterated PS I complexes from *Synechococcus* sp. PCC 7002 (Fan Yang *et al.*, 1998), from 95 GHz

(W-band) studies of in non-deuterated PS I complexes from *Synechococcus lividus* (van der Est *et al.*,. 1997), and from 283 GHz studies of non-deuterated PS I complexes from *Synechocystis* sp. PCC 6803 membrane fragments (MacMillan *et al.*, 1997). Because the simulated spectrum (Fig. 2.6, *dashed* line) matches the experimental spectrum quite well, in the high field region, the amount of contaminating A_0^- or P_{700}^+ appears to be minimal in the deuterated sample.

The nondeuterated spectrum was simulated (Fig. 2.6, *dashed* line) using the *g*-tensor extracted from the deuterated A_1^- spectrum and a hyperfine A-tensor with principal values of 9.0, 12.9, and 9.0 MHz (Rigby *et al.*, 1996). The major deviations from the simulated spectrum appear principally in the mid- and high field regions, therefore they show a minor contribution from A_0^- and/or P_{700}^+. The Q-band EPR spectra of photoaccumulated Q^- in PS I complexes isolated from the *menB* and *menA* mutants of *Synechocystis* sp. PCC 6803 grown in H_2O are shown in Fig. 2.6 (*solid* lines). In both mutants, the four prominent hyperfine lines are missing, and the *g*-tensor of Q^- appears more anisotropic than that of A_1^- in the wild type. Attempts to simulate the spectrum of Q^- were complicated by a large contamination with a second radical, probably A_0^- and/or P_{700}^+. Using the g-tensor for Q^- extracted from transient EPR studies (see below), the spectrum was accurately represented by principal values g_{xx} = 2.0067, g_{yy} = 2.0051, and g_{zz} = 2.0022, with an error of 2 in the last digit, and line widths of 6 G for each value (Fig. 2.6, *dotted* line). The difference between the actual and simulated spectrum of Q^- yields a roughly symmetrical radical with a g-value of approximately 2.0030 and a line width of approximately 12 G to 15 G, which identifies the contaminating radical as A_0^-. Any distortion of the experimental spectrum of Q^- would therefore occur in the midfield and high field portions of the spectrum, leaving the g_{xx} resonance of Q^- unaffected.

Because the g_{zz} component of the tensor is almost invariant for Q^-, A_0^-, and P_{700}^+, the deduced *g*-anisotropy of Q^- should not be influenced by contamination of the spectrum with A_0 or P_{700}^+. Hence, the larger *g*-anisotropy of Q^-, along with the conspicuous absence of prominent hyperfine couplings, agrees with the assessment that a quinone different from phylloquinone has been photoaccumulated in the *menA* and *menB* mutants. Indeed, the larger *g*-anisotropy (also seen in the transient spin-polarized EPR

spectra; see Fig. 2.7) can be further rationalized in terms of differences in the delocalization of unpaired electron density over plastoquinone-9 and phylloquinone. Because benzoquinone derivatives (such as plastoquinone-9) have a single aromatic ring, while naphthoquinone derivatives (such as phylloquinone) have two aromatic rings, benzoquinone derivatives exhibit higher spin density on their carbonyl oxygens and larger *g*-anisotropies. Thus, with plastoquinone-9 incorporated into the A_1 site, an increase in the *g*-anisotropy compared with wild-type PS I is to be expected.

Time-resolved EPR Spectroscopy at X-, Q-, and W-bands

The spin polarization patterns derived from transient EPR spectra of the functional radical pair state P_{700}^{+} Q^{-} contain information about the relative orientation of the species involved and about the influence of the protein environment and electron transfer kinetics on the magnetic properties and spin dynamics. For wild-type PS I in frozen solution, spectra of the state $P_{700}^{+}A_1^{-}$ are observed from the fraction of the complexes in which cyclic electron transfer to A_1 takes place. At temperatures below 200 K, this fraction accounts for about 1/3 of the centers, whereas stable charge separation between P_{700} and F_A /F_B occurs in the remaining 2/3 (see Brettel, 1997 for review).

In Fig. 2.7 spin-polarized transient EPR spectra of PS I complexes from the *menA* and *menB* mutants are compared with the wild type at X-, Q-, and W-bands (9, 35, and 94 GHz, respectively). The spectra of the two mutants are depicted as solid curves, and those of the wild type are depicted as dashed curves. In the spectrum of the wild type the low-field features are due to A_1^{-}, whereas the high-field region is dominated by P_{700}^{+}. For the mutants, the high-field sides of the spectra are very similar to the corresponding wild-type spectra, whereas there is a clear shift of the features on the low-field side, particularly at the W-band. The partially resolved hyperfine couplings to the methyl group in position 2 of the phylloquinone (Fig. 2.3), discussed above, also result in the feature on the central absorptive maximum of the spin-polarized X-band and Q-band spectra of the wild type (Fig. 2.7 *dashed* lines). Again, these features are absent in the spectra of the *menA* and *menB* mutants (*solid* lines). In general, the overall spectral width increases as the micro-wave frequency is increased, i.e. in proceeding from X-band (Fig.

2.7, *bottom*) to W-band (Figures. 2.7, *top*), because the components of the quinone *g*-tensor are more highly resolved at higher field/frequency. The features on the low field side of the transient EPR spectra are shifted downfield compared with the wild type, and the magnitude of the shift increases with increasing microwave frequency. This behavior is in agreement with the CW EPR finding at Q-band (Fig. 2.6), that Q in the *menA* and *menB* mutants has a larger *g*-anisotropy than phylloquinone. It also demonstrates that Q is actively involved in the electron transfer and is not simply a low quantum yield trap.

The emissive and absorptive components (Fig. 2.7, E and A, respectively) of the high field and low field regions of the spectra have equal intensity because the radical pair P_{700}^{+} A_1^{-} is generated from a singlet precursor on a picosecond time scale. If the lifetime of the precursor is sufficiently long that appreciable singlet-triplet mixing takes place, i.e. longer than about 0.5 ns, net polarization develops on each of the radicals (Hore, 1996; Kandrashkin *et al.*, 1998; Tang *et al.*, 1996). No net polarization of this type is visible in the spectra of the *menA* and *menB* mutants; thus it can be concluded that the electron transfer to Q occurs on a time scale less than roughly 0.5 ns.

If the A_1 site in the mutants were vacant or forward electron transfer were slow, charge recombination from A_0 would generate a spin-polarized EPR spectrum of $^{T}P_{700}$ (Budil and Thurnauer, 1991; Rutherford and Sétif, 1990; Seickman *et al.*, 1993). Thus, the observation of a weakly coupled radical pair spectrum with no significant contribution from the triplet state of the donor $^{T}P_{700}$ shows that efficient forward electron transfer past A_0 occurs in the mutants. This observation also suggests that the A_1 binding site is fully occupied.

For wild-type PS I, simulations of the polarization patterns of P^{+} A_1^{-} (Stehlik *et al.*, 1989; van der Est *et al.*, 1997; Kamlowski, Zech *e. al.*, 1998; van der Est *et al.*, 1998) show that A_1 is oriented such that the carbonyl bonds of the phylloquinone head group are parallel to the vector joining P_{700}^{+} and A_1^{-}. Qualitatively, this orientation of the quinone is reflected in the emissive feature on the low field edge of the spectra shown in Fig. 2.7 (*dashed* lines). For the mutants, simulations using the same parameters as found for wild-type PS I (van der Est, 1998), but with a value of $g_{xx} = 2.0067$ for the acceptor, gives excellent agreement with the experimental polarization patterns at all three

microwave frequencies. Thus it can be concluded that the acceptor in the mutants is oriented in a similar fashion, *i.e*. with its C=O bonds directed toward P_{700}.

It is important to note that when just the headgroup, *i.e.* naphthoquinone, is substituted for phylloquinone in PS I, its orientation changes, so that its C=O bonds are now oriented perpendicular to the P_{700}—A_1 connecting vector (Sickman *et al.,* 1991; van der Est *et al.,* 1995; Zech *et al.,* 1997). Nevertheless, it is bound to the same A_1 binding site as phylloquinone in the wild type (Zech *et al.,* 1997). Because the main difference between naphthoquinone and phylloquinone is the presence of the isoprenoid side chain in phylloquinone, it is likely that Q is a quinone with a side chain that is appropriate to lead to the same orientation as phylloquinone.

Pulsed EPR Spectroscopy

The EPR results presented above show that an acceptor with a quinone-like *g*-tensor is involved in the electron transfer in the *menA* and *menB* mutants. However, without an accurate determination of the distance between the donor and acceptor, the data do not show unambiguously that the acceptor is bound at the A_1 site. Recently, ESE experiments have been used to determine the distance between P_{700}^+ and A_1^- in wild-type PS I (Zech *et al.,* 1996; Dzuba *et al.,* 1997; Bittl *et al.,* 1997) and to demonstrate that the distance remains the same for a number of nonnative quinones used in phylloquinone extraction/substitution experiments (Dzuba *et al*., 1997; Zech *et al.,* 1997). The ESE of a weakly coupled spin-correlated radical pair is phase shifted by 90° compared with that of a single radical and shows deep amplitude modulations as a function of the pulse spacing (Salikhov *et al*., 1992). The modulation frequency is selectively determined by the spin-spin coupling, the dipolar part of which yields the distance between the radicals.

The out-of-phase ESE amplitude modulation curves from the mutants and wild-type PS I are compared in Fig. 2.8. The solid curves are from the mutants *menA* (Fig. 2.8, *top*) and *menB* (Fig. 2.8, *bottom*), whereas the result for the wild type is shown for reference as a dashed curve. Comparison of the echo modulation curves shows that the dominant frequency components from both mutants and the wild type are virtually identical. The values for the dipolar and exchange coupling parameters can be determined

quantitatively by comparison of the experimental echo modulations with numerical simulations calculated using the correlated coupled radical pair model. An important feature of such simulations is that the anisotropies of the g-tensor and hyperfine splittings do not influence the out-of-phase echo modulation significantly, so they can be safely ignored (Bittl *et al.,* 1997; Dzuba, 1998; Timmel *et al.,* 1998). Simulation of the ESE modulation curves in Fig. 2.8 yields dipolar coupling constants, D = –172 ± 4 mT for both mutant samples. This value is identical within error to that (D = –170 ± 4 mT) obtained for the wild type (Zech *et al.,* 1997). In all three samples, the isotropic exchange coupling is extremely weak, and only an upper limit of J = 1.0 ± 0.8 mT can be given. This small value is consistent with the simulation of the transient EPR spectra (van der Est *et al.,* 1997).

Using a simple point-dipole model, the measured dipolar coupling constant corresponds to a distance of 25.3 ± 0.3 Å between P_{700}^{+} and Q^{-} in the mutants, which is the same within error as the distance of 25.4 ± 0.3 Å established between P_{700}^{+} and A_1^{-} in several preparations of wild-type PS I (Zech *et al.,* 1996, Dzuba *et al.,* 1997; Bittl *et al.,* 1997, Zech *et al.,* 1997). Thus, it can be concluded that the recruited quinone acceptor in the mutants is indeed bound to the A_1 site. This corresponds to the results obtained by quinone substitution experiments (Dzuba *et al.,* 1997; Zech *et al.,* 1997), in which the same A_1 site has been shown to be occupied in all cases.

Pulsed ENDOR Spectroscopy

CW EPR spectroscopy used in photoaccumulation and transient studies is capable of resolving the *g*-tensor at higher fields/frequencies and thereby providing information on the aromaticity of the foreign quinone in the A_1 site. However, ENDOR spectroscopy on the P_{700}^{+} Q^{-} state is able to resolve hyperfine interactions that can provide additional information on the specific interactions of the foreign quinone in its binding site. Fig. 2.9 shows the pulsed ENDOR spectra of the P_{700}^{+} Q^{-} state in *menA* (top) and *menB* (middle) and, for comparison, the P_{700}^{+} A_1^{-} state in wild-type PS I complexes from *Synechococcus elongatus* (bottom). The first observation is that spectm ra of PS I complexes isolated fro*menA* and *menB* are identical within the available signal-to-noise ratio. The second is

that spectra are drastically different from the P_{700}^{+} A_1^{-} spectrum observed in *S. elongatus*. This is shown by the clearly resolved lines of an (almost) axially symmetric tensor in the range of 8.6 MHz to 10.6 MHz and 18.9 MHz to 20.9 MHz in the wild-type PS I complex. These lines are assigned to the 2-CH_3 group of phylloquinone, with $A_{\|}$ = 12.8 MHz and $A_{\perp}$ = 9.0 MHz (Rigby *et al.,* 1996).

The pulsed ENDOR studies in both the light-induced (transient) P_{700}^{+} A_1^{-} state and on photoaccumulated A_1^{-} agree (Bittl *et al.,* 1998), thereby bolstering confidence in the ability of the latter to measure the quinone in the active A_1 site. It is clear that this pair of lines is missing in PS I complexes isolated from the *menA* and *menB* mutants (Fig. 2.9). Instead, two pairs of lines of similar shape arise in the spectra of PS I complexes isolated from *menA* and *menB* due to an axially symmetric hyperfine coupling tensor. These line pairs, in the ranges (i) 9.6 MHz to 11.4 MHz and 18.0 MHz to 19.8 MHz and (ii) 12.0 MHz to 13.4 MHz and 16.2 MHz to 17.5 MHz correspond to coupling tensors with (i) $A_{\|}$ = 9.8 6 0.2 MHz, $A_{\perp}$ = 6.8 ± 0.2 MHz and (ii) $A_{\|}$ = 5.7 ± 0.2 MHz, $A_{\perp}$ = 2.8 ± 0.2 MHz. The similar shape of the two sets of lines and their similarity to the corresponding shape in the PS I spectrum hints at their assignment to two inequivalent methyl groups in the recruited quinone.

Both sets of hyperfine couplings are smaller than those of the 2-CH_3 group of phylloquinone in wild-type PS I, and they differ significantly from each other, indicating substantial asymmetry in the spin density distribution of the recruited quinone. Finally, the ENDOR spectra of the PS I complexes isolated from *menA* and *menB* mutants in Fig. 2.9 show clear spectral wings extending out to 8.3 MHz and 21.1 MHz, respectively. They exhibit the opposite sign in signal intensity compared with the inner signal contributions assigned above to two methyl groups. This opposite sign is most readily associated with an opposite relative sign of the respective hyperfine couplings. This suggests the assignment of the outer wings in the ENDOR spectrum to the H atom of an aromatic C-H fragment in the recruited quinone.

Two pairs of ENDOR lines have been assigned to two CH_3 groups (Fig. 2.9), which indeed occur as substituents of plastoquinone-9 (see Fig. 2.3). For the two CH_3 groups, different hyperfine couplings have been observed for plastoquinone-9 radical

anions in liquid and in frozen alcoholic solution, as well as for the reduced primary acceptor Q_A^- in PS II (MacMillan *et al.,* 1995). The inequivalence of the CH_3 groups was largest in frozen alcoholic solution, which showed two hyperfine coupling tensors of $A_{\|}$ = 8.58 MHz, $A_{\perp}$ = 5.29 MHz and $A_{\|}$ = 6.68 MHz, $A_{\perp}$ = 3.70 MHz, respectively. The difference of the two CH_3 tensors found for the recruited quinone Q^- is even larger, with $A_{\|}$ = 9.8 MHz, $A_{\perp}$ = 6.8 MHz and $A_{\|}$ = 5.7 MHz, $A_{\perp}$ = 2.8 MHz, respectively. Despite the increased inequivalence of these positions, the sum of their average hyperfine couplings with 11.1 MHz for plastoquinone-9 in frozen alcoholic solution and 11.6 MHz for Q^- is very similar, supporting our assignment.

The inequivalence of the -CH_3 couplings in Q^- indicates a rather strong asymmetry in the spin density distribution of plastoquinone-9 in the A_1 binding site. This finding is further supported by the largest coupling of the α-proton, with A_{extr} = –12.8 MHz assigned to the spectral wings with negative intensity in Fig. 2.9. The corresponding tensor component was reported as A_{extr} = –9.0 MHz (and thus significantly smaller) for the plastoquinone-9 radical anion in frozen alcoholic solution (MacMillan *et al.,* 1995). A similar increase of the hyperfine coupling of the -CH_3 group in the corresponding position 2 of phylloquinone is observed between semiphylloquinone in frozen alcoholic solution and semiphylloquinone in wild-type PS I. The average CH_3 hyperfine coupling for phylloquinone increases from 7.9 MHz in frozen solution to 10.2 MHz for A_1^- (Rigby *et al.,* 1996). Assuming an equivalent spin density increase at carbon positions 2 and 6 of the recruited Q, the larger of the two CH_3 hyperfine coupling tensors of Q^- is assigned to the group attached to ring position 6 and the smaller CH_3 coupling tensor to the group attached to position 5, respectively.

P_{700}^+ Recombination Kinetics, Optical and EPR Spectroscopy.

In PS I complexes isolated from the wild type with β-DM, the reduction of P_{700}^+ is multiphasic after a saturating flash (Vassiliev *et al.,* 1997). When measured by optical spectroscopy in the near-IR, and in the absence of external electron acceptors, the majority of P_{700}^+ is reduced with lifetimes of ca. 86 ms and 12 ms in ca. 10:1 ratio (minor microsecond kinetic phases are present due to backreactions from earlier acceptors in

damaged reaction centers). There also exists a long-lived kinetic phase of P_{700}^+ reduction due to direct reduction of P_{700}^+ by reduced DCPIP; this represents ca. 20% of the total absorbance change. In PS I complexes isolated from the *menB* mutant, the reduction of P_{700}^+ is also multiphasic after a saturating flash (Fig. 2.1 A). When measured in the absence of external electron acceptors, P_{700}^+ is reduced with lifetimes of ca. 2.6 ms and 7 ms in a 0.63:0.37 ratio (minor microsecond kinetic phases are similarly present due to backreactions from earlier acceptors in damaged reaction centers).

There also exists a minor long-lived kinetic phase of P_{700}^+ reduction due to direct reduction of P_{700}^+ by reduced DCPIP; this represents 7% of the total absorbance change. The PS I complexes from the *menA* mutant showed nearly identical kinetics. When measured in the same reaction medium using time-resolved EPR spectroscopy with field modulation detection (Fig. 2.10 B), the majority of P_{700}^+ in the PS I complexes from the *menB* mutant is reduced with a lifetime of 3.2 ms, a value in good agreement with the optical study. Since the signal-to-noise ratio limits the precision of these measurements, the single kinetic phase found in the EPR measurement may correspond to a convolution of the 2.6-ms and 7-ms lifetimes found in the optical experiment.

The EPR study also shows a long-lived kinetic phase of P_{700}^+ reduction that corresponds to ca. 13% of the total spin concentration. The study of the PS I complexes from the *menA* mutant showed similar kinetics. Considering only the 3.2-ms kinetic phase, the charge recombination of the electron acceptor(s) with P_{700}^+ is ca. 25 times faster in the PS I complexes from the *menA* and *menB* mutants than in the wild type.

Global Multiexponential Analysis of Optical Spectra in the Blue Region.

Fig. 2.11 A depicts spectra obtained in the blue region by global multiexponential analysis of kinetics, in the absence of methyl viologen, in PS I complexes from the *menB* mutant. Three discrete kinetic components are present. The component fitted to the slowest kinetic phase approximated by a base line (*checked* boxes), corresponds to the spectrum (P_{700}^+ minus P_{700}) and represents a population of P_{700}^+ reduced by the external electron donor, DCPIP. In these reaction centers, the electron has already escaped from FeS^- to an external acceptor, probably molecular oxygen. The 3.2-ms kinetic phase (solid

squares) corresponds to the spectrum of (P_{700}^+ FeS^- minus P_{700} FeS) and represents a close match to the kinetics of P_{700}^+ relaxation measured optically and by EPR (Figs. 2.10, A and B). The third kinetic phase is the 13-ms kinetic event (solid circles), which will be discussed in detail later. Fig. 2.11 B depicts spectra obtained by global multiexponential analysis of kinetics in the presence of methyl viologen. As in the absence of methyl viologen, three discrete kinetic components are present. The component fitted to the slowest kinetic phase (open squares) corresponds to the spectrum of (P_{700}^+ minus P_{700}); it represents the entire population of P_{700} reduced by the external electron donor, DCPIP. The spectrum of the 18-µs component (open circles) resembles that of the 13-µs component in the absence of methyl viologen (this component will be discussed later). An additional third component, with a lifetime of 744 µs (solid diamonds), is present with a broad bleaching from 400 nm to 500 nm characteristic of an S to Fe charge-transfer transition and corresponds to the spectrum of FeS^- minus FeS. It is not possible to identify unambiguously the FeS cluster giving rise to this absorbance change, because the difference spectra (oxidized minus reduced state) of F_X, F_B, and F_A are nearly identical. However, the electron is likely in equilibrium between F_A and F_B, and the kinetics likely represents the forward electron donation from the terminal electron acceptor F_B^- to methyl viologen.

The larger absorbance change of the 3.2-ms phase in the absence of methyl viologen (Fig. 2.11 A) compared with the slow phase in the presence of methyl viologen (Fig. 2.11 B) is derived from the additional contribution of a reduced electron acceptor. Assuming that the spectrum of the 3.2-ms component in the absence of methyl viologen corresponds to the absorbance changes brought about by P_{700}^+ plus a reduced acceptor, whereas the spectrum of the slow kinetic component in the presence of methyl viologen corresponds to the absorbance changes of P_{700}^+ alone, the difference will correspond to the spectrum of the reduced acceptor. The resulting spectrum, presented in Fig. 2.11 C, is similar to that of the 744-µs kinetic phase in the presence of methyl viologen (Fig. 2.11 B, *solid diamonds*); it shows a broad bleaching from 400 nm to 500 nm characteristic of an S $\rightarrow$ Fe charge-transfer transition. The amplitude of the absorbance change is lower than in Fig. 2.11 B (*solid diamonds*) because a fraction of the reaction centers has already

lost the electron from the FeS clusters. The electron that back reacts with P_{700}^+ with a 3.2-ms lifetime is therefore located in a FeS cluster, although for reasons mentioned above, it is not possible to differentiate between F_B and F_A. The PS I complexes from the *menA* mutant showed similar results.

Forward Electron Transfer; Decay of the Electron Spin Polarized EPR Signal from P_{700}^+ A_1^-

An attempt was made to measure the forward electron transfer from Q^- to the FeS clusters in the PS I complexes from the *menA* and *menB* mutants, by accumulating time/field transient EPR data sets at 9 GHz (X-band) in PS I complexes isolated with β-DM. Fig. 2.12 shows spectra extracted from the data sets by fitting the individual transients as described in van der Est (1994). Fig. 2.13 shows selected transients corresponding to the field position marked in Fig. 2.12 by the arrow. For the wild type (Fig. 2.12, *top*, and Fig. 2.13, *top*), the onset of the laser flash results in the appearance of an E/A/E polarization pattern within the rise time of the spectrometer due to the generation of the spin-polarized radical pair P_{700}^+ A_1^- (Bock *et al.*, 1989; van der Est, 1994). At the field position chosen for the transients in Fig. 2.12, this radical pair makes the absorptive contribution to the top trace. This spectrum decays, with a time constant of ca. 280 ns, to the emissive spectrum due to P_{700}^+ $(FeS)^-$ shown in Fig. 2.12, *top*. In the corresponding transient in Fig. 2.13 (*top*), the electron transfer results in a transition from an absorptive contribution at early time to an emissive contribution at later times.

It was shown that in samples devoid of F_A and F_B, the late signal is retained, indicating that the electron transfer proceeds via F_X (van der Est *et al*., 1994). However, it is not possible to identify unambiguously the FeS cluster involved in the radical pair giving the emissive spectrum in intact samples, because its contribution is spread over a large spectral range and because of fast relaxation at room temperature (see Kandrashkin *et al*., 1998 for discussion). The subsequent decay of the emissive spectrum, with a time constant of 1.5 ms, represents the relaxation of the spin-polarized signal. This represents the limit on the time resolution of the spin polarization method.

For the PS I complexes from the *menA* (Figs. 2.12, *middle,* and 2.13, *middle*) and *menB* (Figs. 2.12, *bottom,* and 2.13, *bottom*) mutants, the onset of the laser flash results in the appearance of a spectrum that is assigned to the P_{700}^{+} Q^{-} state, where Q is identified as plastoquinone-9 in the A_1 site. This spectrum does not show any singlet-triplet mixing in the precursor state, and its rise time is governed by the response time of the spectrometer. Thus, it is concluded that electron transfer to Q occurs on a time scale of less than ca. 0.5 ns.

Compared with the wild type, the spectrum of P_{700}^{+} Q^{-} decays more slowly than that of P_{700}^{+} A_1^{-}, and there is no indication of P_{700}^{+} FeS^{-} during the 1.5- µs decay of the spin polarization pattern. Thus, a conservative lower limit of 2 µs to 3 µs on the lifetime of P_{700}^{+} Q^{-} can be placed. This result indicates that electron transfer from A_1^{-} to F_X is slowed by a factor of at least 10, from ca. 280 ns in the wild-type PS I complexes to $\geq$ 2-3 µs in the PS I complexes from the *menA* and *menB* mutants; one kinetic phase will be shown to be ca. 300 µs when measured directly in the field modulation transient EPR experiment which is described further below.

Forward Electron Transfer, Optical Absorbance Changes in the Near-UV

It is possible to accurately measure forward electron transfer from Q^{-} to the FeS clusters in the UV using a flash-detection, pump-probe spectrophotometer (Joliot *et al.,* 1980). Absorption changes in the PS I complexes from the *menA* mutant were found to range from 245 nm to 330 nm at time points 5 µs, 100 µs, and 5 ms after an actinic flash. The light-minus-dark difference spectrum, recorded 5 µs after the flash, shows a maximum at 310 nm, a cross-over at 280 nm, and a minimum of 255 nm, as well as a shoulder at 290 nm to 295 nm (Fig. 2.14 A, *circles*). The difference spectra at both 100 µs (Fig. 2. 14 A, *squares*) and 5 µs (Fig. 2.14 A, *triangles*) after the flash resemble the spectrum at 5 µs, implying that all kinetic phases are derived from the same species.

This spectrum is strikingly similar to the semiplastoquinone-9 minus plastoquinone-9 difference spectrum in methanol (Fig. 2.14 B, *checked circles*), which shows a maximum at 315 nm, a crossover at 280 nm and a minimum of 255 nm, as well as a shoulder at 280 nm to 300 nm (Benasson *et al.,* 1973). The reader should note that

the absolute value of the absorbance change of the trough on the short wavelength (blue) side is larger than the absolute value of the absorbance change of the peak on the long wave-length side in both the Q^-/Q (Fig. 2.14 A, *circles*) and the plastoquinone anion radical minus plastoquinone-9 (Fig. 2.14 B, *checked circles*) difference spectra. The spectrum of Q^- minus Q is also strikingly similar to the Q_A^- minus Q_A difference spectrum in deoxycholate- isolated PS II complexes (van Gorkom, 1974), except that the latter is shifted to the red about 15 nm (Fig. 2.14 B, *checked squares*).

It is noteworthy that the spectrum in Figure 2.14 A does not resemble that of wild-type PS I, in which the flash-induced difference spectrum (with phylloquinone in the A_1 site) shows a peak centered at 380 nm and a crossover of ca. 325 nm (Brettel, 1988). It is also interesting that the Q^- minus Q difference spectrum differs from the protonated semiplatoquinone-9 minus plastoquinone-9 difference spectrum, in which the peak occurs at 295 nm, and in which the absolute value of the extinction coefficient at 250 nm is over twice that at 300 nm (Benasson *et al.,* 1973). This indicates that the plastoquinone radical in the A_1 site remains unprotonated during its measured lifetime. The light-minus-dark difference spectrum of Q^- minus Q therefore supports the assignment of Q as plastoquinone-9 in the A_1 site.

The kinetics of the absorbance change at the 310 nm maximum of the *menA* mutant are depicted in Fig. 2.15 A. The decay kinetics are (at least) biphasic, and the lifetime of the fast phase is estimated to be 17.6 µs. The slow phase is difficult to fit precisely due to the limited number of data points. Nevertheless, the extrapolated absorbance at the onset of the flash indicates that ca. 60% of Q^- decays within 100 µs. If one assumes that 100 chlorophyll molecules are associated with each PS I monomer, then at concentration of 10 µg chlorophyll ml^{-1}, the P_{700} concentration in this sample would be 112 nM. The flash-induced absorption change of Q^- minus Q at the peak maximum of 315 nm (Fig. 2.14 A, *circles*) would correspond to 0.94 mOD measured 5 ms after the flash.

The differential extinction coefficient of semiplastoquinone-9 minus platoquinone-9 at the peak in the UV is reported as 13,000 M^{-1} cm^{-1} in solution (Benasson *et al.,* 1973), and this value has also been used for Q_A in PS II (van Gorkom,

1974). By using this value and the absorption difference at the onset of the flash gives a total of 72 nM of Q undergoing light-induced reduction. Assuming an equimolar concentration of plastoquinone-9 in the A_1 site with P_{700}, this would correspond to 64% of the redox-active Q.

However, the difference spectrum is recorded 5 µs after the flash, and given that the lifetime of the fast kinetic phase is 17.6 µs, the absorption change of Q^- /Q at the onset of the flash can be estimated as 1.04 mOD. Hence 80 nM, or 71% of the redoxactive Q, is associated with forward electron transfer. This estimation suffers from uncertainty in the extinction coefficient of plastoquinone-9 in the A_1 site and is the estimate of the absorbance at the onset of the flash. Nevertheless, the calculation shows that the majority of electrons that are transferred from A_0^- to the FeS clusters are mediated by plastoquinone-9. This rules out a significant electron bypass of the quinone at room temperature in the PS I complexes from the *menA* and *menB* mutants.

Forward Electron Transfer Kinetics; Electrochromic Band-shift at 490 nm

The global multiexponential analysis of the flash-induced changes in the absorption spectra of PS I complexes from the *menB* mutant revealed a 13- µs kinetic event in the absence of methyl viologen, with a derivative-shaped spectrum centered at 460 nm (Fig. 2.11 A, *solid circles* connected with *dotted* line). This spectrum is characteristic of the electrochromic shift of a pigment that occurs in response to electron transfer. The same electrochromic shift can be seen in the presence of methyl viologen, except that the extracted lifetime is 18 µs and the amplitude is higher (Figure 2.2 B, *open circles* with dotted line). The longer lifetime may be instrument-related; to obtain a reasonable signal-to-noise ratio, the rise time (1/e) of the amplifier was limited to 10 µs, which would tend to cause underestimation of the initial amplitude in Fig. 2.11 A.

The electrochromic shift also shows a slower kinetic phase in the absence (Fig. 2.15 B) and presence (data not shown) of methyl viologen. The kinetics in the near-millisecond time domain are complicated by absorbance changes at 490 nm due to the decay of P_{700}^+, and no further attempt was made to separate their relative

contributions. Similar kinetic phases were measured in the PS I complexes from the *menA* mutant (data not shown).

In wild-type PS I complexes, the light-minus-dark difference spectrum shows a positive-going absorption band from 440 nm to 500 nm, with a shape that resembles the red shift of a pigment centered at about 470 nm (Brettel, 1988). A similar set of absorption changes were recently measured in mutant cells of *Chlorella sorokiniana* that lack PS II (Joliot, P., and Joliot, A., 1999). These features in the wild type were attributed to an electrochromic red shift of an absorption band of a carotenoid that is induced by A_1^-. Similarly, the spectrum of the ca. 18-µs component measured in PS I complexes from the *menB* mutant most probably represents an electrochromic bandshift due induced by Q^- on a nearby carotenoid. The kinetics of the flash-induced carotenoid bandshift therefore represents an indirect, but reliable, method to measure the oxidation kinetics of the semiplastoquinone in the visible region.

Photovoltage Measurements on PS I Complexes in Proteoliposomes

Excitation of oriented PS I complexes with a single turnover flash leads to the generation of a transmembrane electric potential difference from which the forward electron transfer rates and dielectrically weighted transmembrane distances can be measured (Leibl *et al.,* 1995; Mamedov *et al.,* 1996; Mamedova *et al.,* 1999). PS I complexes were incorporated into proteoliposomes, and the flash-induced response corresponded to the negative charging of the proteoliposome interior.

For wild-type PS I in the absence of an external electron donor to P_{700}^+, the photoelectric response due to charge separation between P_{700} and the terminal electron acceptors, F_A /F_B, occurs within the ca. 0.2 µs rise time of the instrument (Vassiliev *et al.,* 1997). Thus, the 20- and 200-ns kinetic phases of forward electron transfer between A_1 and F_X in wild-type PS I are not resolved using our instrumentation. However, for PS I complexes isolated from the *menB* mutant (Fig. 2.15 C, inset) and *menA* mutant (data not shown), the photoelectric response shows an instrument-limited rise followed by a slower rise in the submillisecond time range.

Decomposition of these kinetics, presented in Fig. 2.15 C, reveals components with lifetimes of ca. 11.4 µs and 306 µs, and equal relative contributions (ca. 10%) to the overall photoelectric response. The decomposition also includes an offset that represents a longer-lived component in the low millisecond time range. The lifetime of the fast kinetic phase is in reasonable agreement with the measurements of Q^- oxidation at 315 nm and the carotenoid bandshift at 485 nm.

The slow kinetic phase is also probably related to the oxidation of Q^-, although the optical data at 315 and 485 nm are compromised by the presence of millisecond-lifetime P_{700}^+ minus P_{700} changes at these wavelengths. These two components are assigned to vectorial electron transfer from Q^- forward to the FeS clusters in the PS I complexes from the *menA* and *menB* mutants. The data points contributing to the 11.4-µs phase are overwhelmed by the large spike at early time, which is probably due to dielectric relaxation of the sample following the charge separation (Vassiliev *et al.*, 1997). Elimination of this artifact is difficult, and as a result there is a fairly large error associated with the lifetime and amplitude of the faster of the two phases.

Forward Electron Transfer, Field Modulation Transient EPR

If the slow kinetic phase that extends into the hundreds of microseconds time range represents the oxidation of Q^-, then the semiquinone anion radical should be detectable at these times using conventional time-resolved EPR spectroscopy (i.e. using field modulation detection). Fig. 2.16 shows the results of an analysis of a room temperature field modulation transient EPR experiment. Fig 2.16, *top,* compares boxcar spectra of PS I complexes from the *menA* mutant at two times with the decay-associated spectrum of the 32-ms major kinetic phase in the wild type. At late times of ca. 5 ms after the laser flash, the *menA* mutant and the wild type give the same spectrum, because the electron is on one of the FeS clusters (see Fig 2.11 B). At early times of ca. 100 µs to 200 µs after the laser flash, the zero crossing in the spectrum of the mutants is clearly shifted to lower field because of the contribution from Q^-.

The *g* anisotropy and crossover of this radical are similar to that obtained in dark-adapted whole cells of the *menA* mutant after exposure to white light; they can be

attributed to a semiquinone anion radical (Figs. 2.4 and 2.5). Fig. 2.16, *bottom*, shows a fit at the field position marked with an arrow in Fig. 2.16, *top*. From this fit, an electron transfer lifetime of ca. 300 µs and a recombination lifetime of ca. 5 ms can be extracted. The identification of a slow kinetic phase with the decay of Q^- is consistent with the presence of the Q^-/Q difference spectrum measured in the UV 100 µs after the flash (Fig. 2.14 A, *squares*).

DISCUSSION

The main finding of this chapter is that when phylloquinone biosynthesis is interrupted, a foreign quinone is incorporated into the A_1 site of PS I. When the interrupted genes are *menB* (naphthoate synthase) or *menA* (phytyl transferase), the foreign quinone is shown to be plastoquinone-9. The incorporated quinone functions as an efficient electron transfer cofactor within PS I, accepting electrons from A_0 and passing them forward to F_X.

The asymmetric spin density distribution found for Q^- in the mutants, and for phylloquinone in wild-type PS I, is consistent with an increased spin density at ring position 2, *i.e.,* between the carbonyl group in position 1 and the hydrocarbon chain in position 3 (see Fig. 2.3). This asymmetric spin density is exactly opposite that for Q_A^- in bacterial reaction center (see Lubitz and Feher, 1999 for a review). Here, a decrease in spin density is observed for the corresponding position 2. The latter is attributed to a stronger H-bond to the carbonyl in position 1 (chain in position 3). This is also concluded from the structure of bacterial reaction center, which shows strong H-bonding to the carbonyl in position 1 of Q_A from the H residue in the *d*-helix, which also ligates the nonheme iron. A weaker backbone H-bond is suggested for the other carbonyl bond of Q_A.

If the opposite spin density distribution observed for A_1 in PS I compared with Q_A in bacterial reaction center is attributed to inequivalent H-bonds to the quinone carbonyls, then the preferential H-bond has to be inverted between PS I and the bacterial reaction center. The present PS I structure (Jordan *et al.,* 2001) supports the difference in H-bonding to A_1 compared with Q_A in purple bacterial reaction center. There is a direct correspondence between the transmembrane helices in PS I and in the bacterial reaction center, but there are significant differences in the quinone binding region. The *m*-helix of PS I ends earlier toward the stromal side compared with the corresponding *d*-helix of the bacterial reaction center. Moreover there is no H residue in the PsaA/B primary sequence in this region. Hence, the strong H-bond donor for Q_A in the bacterial reaction center has no analog in PS I. This may also be one of the reasons for the significantly different

orientation and position of A_1 relative to the rest of PS I (Kamlowski *et al.,* 1998). On the other hand, there is a possibility for H-bonding to the other carbonyl group of phylloquinone in the A_1 binding site via an I residue, a proposal which is supported by the PS I structure (Fig. 2.18). Similar conclusions were reached on the basis of spin density functional calculations (O'Malley, 1998, 1999). O'Malley was able to quantitatively explain the observed spin densities for Q_A in the purple bacterial reaction center (O'Malley, 1998) versus A_1 in PS I by assuming a preferential strong H-bond to one of the carbonyl groups and to the opposite one in each of the respective quinone acceptors. Experimental evidence is provided here that the same direction of asymmetric spin density distribution (and correspondingly the same H-bonding pattern) is observed for plastoquinone-9 recruited in the A_1 site as for phylloquinone in wild-type PS I. Further comparison can be made to the asymmetric spin density distribution observed for plastoquinone-9, both in solution and as Q_A in PS II. It is interesting to note that an asymmetric spin density distribution has been calculated for plastoquinone-9 in isotropic solution (O'Malley, 1998), presumably as a result of the inherent asymmetry of the substituents (see Fig. 2.3). Indeed, a substantial anisotropy has been observed for plastoquinone-9 in frozen solution (MacMillan, *et al.,* 1995). Compared with this intrinsic asymmetry for plastoquinone-9 in solution, the asymmetry is found in this work to increase for plastoquinone-9 recruited as Q in PS I mutants and, in contrast, to decrease for plastoquinone- 9 as Q_A in PS II (MacMillan, *et al.,* 1995). The latter is consistent with the assumption of an asymmetric H-bonding similar to that established for purple bacterial reaction center, see Lubitz and Feher, 1999. As a consequence, preferential H-bonding appears to operate in all mentioned reaction centers. Interestingly, the stronger H-bond concerns opposite carbonyl groups (with respect to the common ring numbering used in Fig. 2.3) for quinones in the A_1 site of PS I versus quinones in the Q_A site of PS II and purple bacterial reaction center. The results raise a number of interesting issues concerning the nature of the A_1 binding site. First, the fact that the A_1 site is occupied in the absence of phylloquinone means that under normal conditions there must be strong competition in favor of phylloquinone as compared with plastoquinone-9, both of which are presumed to be present during the biosynthesis and assembly of PS I. Thus,

the binding affinity of phylloquinone must be higher. Given the relatively high concentration of plastoquinone-9 in the membrane, the difference in the binding constants must be quite substantial. One reason for a higher affinity could be structural constraints, *i.e.* the binding site could be designed to accommodate phylloquinone better than plastoquinone-9. Evidence to support this idea comes from quinone exchange experiments which showed that parameters such as hydrophobicity influence the binding affinity of quinones to PS I (Iwaki and Itoh, 1991; Rustandi *et al*., 1992). The structure of the respective quinones may also play a role. The binding of duroquinone (2,3,5,6-tetramethyl-benzoquinone) is weaker than predicted by its hydrophobicity (Itoh and Iwaki, 1991), and out-of-phase ESE experiments on PS I containing duroquinone suggested a wider distribution of P_{700}^{+} Q^{-} distances than for P_{700}^{+} Q^{-} in the wild-type PS I. This could be an indication that the poorer binding is due to steric effects (Sieckman *et al.,* 1991). However, the spin polarization patterns of the mutants show that any increase in steric hindrance for plastoquinone-9 as compared with phylloquinone is not accompanied by a different orientation of the two acceptors. Another possible explanation for different binding affinities of phylloquinone and plastoquinone-9 has been given by Zheng and Dismukes (Zheng, Dismukes, 1996). For the quinones with a CH_3 group at position 2, such as ubiquinone-10 and phylloquinone, the side chain at position 3 is attached perpendicularly to the quinone head group plane (dihedral angle (C_2 -C_3, C_β -C_γ) about 90°), whereas for quinones with a hydrogen at position 2, the side chain is in plane with the head group in the ground state (dihedral angle (C_2 -C_3, C_β -C_γ) about 0°). A difference in energy separation between ground state and excited state for opposite side chain to head group conformation of about 25 kJ/mol was estimated, yielding a greater than 10-fold excess of the ground state versus excited state population at room temperature. An optimized protein structure for the respective quinone ground state conformations has been proposed by Zheng and Dismukes (Zheng, Dismukes, 1996) as a possible explanation for the low efficiency of substitution of ubiquinone-10 with plastoquinone-9 in bacterial reaction centers (Okamura *et al.,* 1975) and plastoquinone-9 by ubiquinone-9 in PS II (Diner *et al.,* 1988). Because phylloquinone has the same

ground state configuration as ubiquinone-10, this argument would also explain the selectivity of PS I for phylloquinone.

Yet another explanation of the PS I selectivity for the phylloquinone comes from considering the structural constraints imposed by the length and flexibility of the isoprenyl carbon chain. Plastoquinone-9 has a longer and more rigid isoprenoid chain than phylloquinone (Fig. 2.3), and its compaction into the hydrophobic pocket may include rearrangement of the antenna chlorophylls and carotenoids as well as changes in the position of the hydrophobic amino-acid side-chains.

The results from time-resolved optical, electrometric and CW and transient EPR techniques show that, despite the altered forward and back electron transfer kinetics, plastoquinone-9 functions as an efficient electron cofactor in PS I. To accomplish forward electron transfer, it is necessary that the midpoint potential of the cofactor in the A_1 site be sufficiently reducing to transfer electrons to the FeS clusters at a rate that outcompetes the inherent backreaction of reduced plastoquinone-9 with P_{700}^+. The midpoint potential of Q^-/Q can be estimated using two approaches: a comparison of the redox properties of plastoquinone-9 and phylloquinone in organic solvents, and a consideration of rate versus free energy relationships from electron transfer theory.

Phylloquinone has a reported $E_{1/2}$ of -465 mV versus NHE in dimethylformamide (DMF) (Prince *et al.*, 1983), whereas plastoquinone-9 has a reported $E_{1/2}$ of -369 mV (versus NHE) in DMF (Prince *et al.*, 1986). If the A_1 site has a polarity similar to that of DMF, then plastoquinone-9 would be 96 mV more oxidizing than native phylloquinone in the A_1 site. However, this is only a crude estimate, and it should be possible to refine this value using the concept of "acceptor number." Jaworski and colleagues (Jaworski *et al.*, 1979) showed that the redox potential of a quinone undergoing the first electron reduction in organic solvent is related to the electrophilic properties of the solvent. This work was based on a formulation by Gutman (Gutman, 1976) of an acceptor number, a dimensionless number that expresses the acceptor properties of a given solvent relative to that of $SbCl_5$. The central idea is that $E_{1/2}$ values of different quinones show smaller differences from one another in solvents with low acceptor numbers and higher

differences from one another in solvents with high acceptor numbers. This solvent effect is quantitatively described by empirical Equation 1:

$$E_{1/2} = E^{0}_{1/2} + \alpha(AN) \qquad \text{(Eq.1)}$$

where α is the slope (i.e. the sensitivity to the solvent effect based on Lewis acidity); AN is the acceptor number (which ranges from 0 in hexane to 100 in $SbCl_5$, the reference solvents; benzene is 8.2, DMF is 16, and water is 54.8), and $E_{1/2}{}^{0}$ is the intercept (the value of $E_{1/2}$ corresponding to a solvent with AN = 0). An important point is that the semiquinone radical is destabilized in solvents with low acceptor numbers, which leads to a lower redox potential for the first electron reduction. Itoh and co-workers (Iwaki and Itoh, 1994) applied Gutman's ideas to a study of re-placement quinone head groups (lacking the phytyl tail) in PS I and estimated the acceptor number for the A_1 site to be 4.0, which is similar to the acceptor number for diethyl ether of 3.9. By assuming that the redox potential of a given quinone in organic solvent is strictly linearly related to the $E_{1/2}$ value in the A_1 site, the following Equation 2 was derived (Iwaki and Itoh, 1994):

$$E_m = 0.69E_{1/2}(DMF) - 433mV \qquad \text{(Eq. 2)}$$

where $E_{1/2}$ is the redox potential in DMF and E_m is the redox potential in the A_1 site. Given that phylloquinone has an $E_{1/2}$ of - 465 mV (versus NHE) in DMF (Prince *et al.*, 1983), the E_m of phylloquinone in the A_1 site is -754 mV. Given that plastoquinone-9 has an $E_{1/2}$ of -369 mV versus NHE in DMF (Prince *et al.*, 1986), the E_m of plastoquinone-9 in the A_1 site is -687 mV. Accordingly, the redox potential of plastoquinone-9 in the A_1 site is 67 mV more oxidizing than phylloquinone. Equation 2 was derived assuming that the added quinones are capable of passing the electrons forward to the FeS clusters. However, since there remains a lingering uncertainty over whether added quinones without phytyl tails are properly oriented so as to accommodate forward electron transfer from A_1^- to the FeS clusters (Biggins and Mathis, 1988, Biggins, 1990; Rustandi *et al.*, 1992), an independent approach to the determination of the midpoint potential of plastoquinone-9 in the A_1 site was sought.

According to (Moser *et al.,* 1992; Moser and Dutton, 1992), the rate of intraprotein electron transfer between two electron carriers with distance R can be described by following Equation 3:

$$\log k = 15 - 0.6R - 3.1(\Delta G^0 + \lambda)^2 / \lambda \qquad \text{(Eq. 3)}$$

where R is the edge-to-edge distance in Å; ΔG^0 is the standard reaction free energy in eV, and λ is the reorganization energy in eV. Any change - whether in the reorganization energy, the distance (including the orientation), or the redox potential of the quinone in the A_1 site - will have an effect on the rate constant of electron transfer. For the purpose of this argument, it is assumed that there is no change in the reorganization energy caused by substitution of similar molecules in the A_1 site, *i.e.,* a dimethylbenzoquinone for a naphthoquinone. Results of the pulsed EPR spectroscopy (Fig. 2.8) indicate that the distance between the plastoquinone-9 anion radical and P_{700}^+ in the *menA* and *menB* mutants is nearly identical to the distance between the phylloquinone anion radical and P_{700}^+ in the wild type. Hence, any alteration in the rate constant of electron transfer will be governed primarily by the difference in the redox potential between phylloquinone and plastoquinone-9. The rate relationship in Equation 4 is equivalent to that in Equation 3.

$$k_{exergonic} = 10^{(15-0.6R-3.1(\Delta G^0+\lambda)^2/\lambda)} \qquad \text{(Eq. 4)}$$

The equilibrium constant K_{eq} between Q and F_X is defined in Equation 5 as follows:

$$K_{eq} = k_{forward}/k_{reverse} \text{ (Eq. 5)} \qquad \text{(Eq. 5)}$$

The equilibrium constant K_{eq} is related to Gibbs free energy according to Equation 6.

$$K_{eq} = 10^{-\Delta G/\,0.059} \qquad \text{(Eq. 6)}$$

Hence, the reverse electron transfer rate, $k_{reverse}$, can be expressed in Equation 7 as follows:

$$k_{endergonic} = 10^{(15-0.6R-3.1(\Delta G^0+\lambda)^2/\lambda-\Delta G/0.059)} \qquad \text{(Eq. 7)}$$

Equation 4 is used to specify the rate of forward electron transfer in an exergonic reaction and Equation 7 is used to specify the rate of forward electron transfer in an endergonic reaction. The averaged edge-to-edge distance between Q_K (the two identified quinones in the X-ray crystal structure) and F_X is reported to be 11.3 Å (Klukas *et al.,*

1999). A reorganization energy of 0.7 eV is commonly used for photosynthetic electron transfer reactions (Moser *et al.,* 1992), although a value of 1.0 eV was recently estimated for the reorganization energy of electron transfer between A_1 and F_X from the temperature dependence (Schlodder *et al.,* 1998). The value of $k_{exergonic}$ will therefore depend on the difference in Gibbs free energy between the quinone and the F_X iron-sulfur cluster. This calculation requires accurate knowledge of redox potentials for both cofactors. The $E_{1/2}(Q/Q^-)$ of phylloquinone in wild-type PS I has not been measured directly. However, a value of -810 mV versus NHE has been derived from calculations based on the kinetics of electric field-induced electron transfer rates (Vos and Gorkom, 1988), and a value of less than or equal to -800 mV versus NHE has been calculated based on the $^TP_{700}$ yield (Sétif *et al.,* 1990). As mentioned earlier, the considerably higher value of -754 mV has been deduced from the measured $E_{1/2}$ values of phylloquinone and plastoquinone-9 in DMF and an application of Gutman's acceptor number of 4.0 for the A_1 site. The $E_{1/2}$ (F_X/F_X^-) of phylloquinone in wild-type PS I has been measured directly; an $E_{1/2}$ of -705 mV was found for F_X/F_X^- in PS I complexes by electrochemical poising and EPR measurement (Chamorovsky and Cammack, 1982). However, this approach suffers from the uncertainty that the midpoint potential of F_X was determined in the presence of a reduced F_A and F_B and may be overestimated due to the electrostatic effect of nearly reduced acceptors. A considerably higher $E_{1/2}$ of -670 mV has been measured in P_{700}-F_X cores that lack PsaC and, hence any electrostatic influence from the F_A and F_B clusters. Recently, an equilibrium constant of 73.5 was determined between F_X and F_A in P_{700}-F_X cores by analysis of the backreaction kinetics, which indicates that F_X may be 110 mV more electronegative than F_A (Shinkarev *et al.,* 2000). Since the $E_{1/2}$ of F_A has been measured to be -520 to -540 mV, the $E_{1/2}$ of F_X should be -630 to -650 mV. However, these approaches suffer from an uncertainty whether there is any effect on the midpoint potential of F_X from the removal of PsaC, due either to structural changes or to alterations in solvent accessibility of the FeS cluster.

Table 2.1 shows a matrix of the predicted values of the forward rate constant, $k_{exergonic}$, for the three published values of the midpoint potential of A_1^-/A_1, the three published values of the midpoint potential of F_X^-/F_X, and the two published values of the

reorganization energy. Assuming a reorganization energy of 0.7 eV, the averaged rate constant of optimum forward electron transfer should be 223 ± 99 ns. This value is similar to the ca. 280-ns lifetime of A_1^- measured in wild-type PS I complexes (Brettel, 1988; Bock *et al.,* 1989; Sétif and Brettel, 1993; van der Est *et al.,* 1994; Leibl *et al.,* 1995). If a reorganization energy of 1.0 eV is used instead, the averaged rate of optimum forward electron transfer is 1.83 µs, a value considerably slower than that observed experimentally. The measured lifetime of Q^- in the PS I complexes from the *menA* and *menB* mutants was next used to back-calculate the redox potential for Q^- /Q. Given that the major kinetic phase of forward electron transfer from Q^- in the PS I complexes from the *menA* and *menB* mutants has a lifetime of ce 15 µs (Figs 2.15, A–C), careful consideration of Equations 4 and 7 shows that electron transfer must be endergonic between A_1 and F_X to accommodate this rate. Table II lists a matrix of the predicted values for the increase in Gibbs free energy between A_1 and F_X and the calculated redox potential for Q^- /Q, for the three values of the midpoint potential of F_X^- /F_X, and the two values of the reorganization energy. This results implies that, regardless of whether the reorganization energy is 0.7 or 1.0 eV, electron transfer between A_1 and F_X is endergonic by 12 mV to 95 mV. If we accept a value of -705 mV for the F_X^- /F_X redox couple and a reorganization energy of 0.7, then plastoquinone-9 in the A_1 site of the PS I complexes from the *menA* and *menB* mutants will have a midpoint potential of -610 mV. A value of -670 mV for the F_X^- /F_X redox couple leads to a midpoint potential of -575 mV for plastoquinone-9 in the A_1 site, a value which is nearly isopotential with the F_B iron-sulfur cluster.

Although the value obtained using electron transfer theory provides an interesting exercise, this approach cannot be used for precise estimation; the uncertainties approach an order of magnitude for the energy and the rate constant. Given the additional uncertainties in the midpoint potentials of the components, in the precise value of the reorganization energies when phylloquinone and plastoquinone-9 occupy the A_1 site, and in the exact edge-to-edge distance between the quinone and the FeS cluster, the estimated values must be used with caution. Nevertheless, these considerations support the appraisal based on the redox behavior of plastoquinone-9 and phylloquinone in organic

solvents; *i.e.,* they suggest that the midpoint potential of Q is more oxidizing than that of F_X (Fig. 2.17). If so, then we must ask how a thermodynamically unfavorable reaction can be reconciled with the high quantum yield of electron transfer observed in the steady-state measurements (Johnson *et al.,* 2000) and with the efficient reduction of F_A /F_B observed by optical and EPR spectroscopy (Johnson *et al.,* 2000). The important factor here is that, even with an endergonic electron transfer step between A_1 and F_X, overall net electron transfer is exergonic between A_1^- and F_A /F_B (Fig. 2.8). A drop in the quantum yield and an inefficiency in F_A /F_B reduction would be expected only if electron transfer between A_1^- and F_X were sufficiently slow that the inherent backreaction between A_1^- and P_{700}^+ would dominate. There is no evidence for a backreaction between Q^- and P_{700}^+ when the terminal FeS clusters F_A and F_B are oxidized and available for electron transfer (data not shown). A similar instance of an unfavorable electron transfer with an overall negative change in the free Gibbs energy has been postulated for the electron transfer stage from F_X via F_A and F_B to ferredoxin (Diaz-Quintana *et al.,* 1998; Vassiliev *et al.,* 1998; Golbeck, 1999).

The calculated values in Table 2.2 will now be compared with the experimental data. The issue is whether the reduction of F_A /F_B on a single turnover flash (Fig. 2.10) corresponds to the amount expected on the basis of chlorophyll concentration. In the following analysis, the term FeS refers to the FeS cluster that accepts the electron on a single-turnover flash, without specifying its identity as F_A or F_B. Assuming that 100 chlorophyll molecules are associated with each PS I monomer, then at a concentration of 10 mg chlorophyll ml^{-1}, the concentration of P_{700}, F_A, and F_B in this sample is 112 nM. The flash-induced absorption change due to FeS^- in this sample, determined by global analysis of kinetics in the blue (Fig. 2.2 B, *solid diamonds*), corresponds to 1.4 mOD. Given the extinction coefficient for P_{430} at 430 nm is 13,000 M^{-1} cm^{-1} (Franke *et al.,* 1995), a total of 108 nM of FeS undergoes light-induced reduction. The flash-induced absorption change due to FeS^- in this sample, determined by difference in the absence and presence of methyl viologen (Fig. 2.11 C), corresponds to 1.1 mOD (however, this is known to be an underestimate; see "Results"). Here, a total of 84.6 nM of FeS undergoes light-induced reduction. Taking the midpoint potential of F_A to be -530 mV and the

amount of F_A reduced to be between 76 and 96%, a straightforward application of the Nernst equation indicates that the midpoint potential of Q must be more reducing than -559 to -611 mV to account for the high quantum yield of FeS reduction on a single turnover flash (for simplification, the equilibrium between F_A and F_B has been ignored). These values are in reasonable agreement with those determined by applying electron transfer theory (Table 2.2).

SUMMARY

These studies show that, upon interruption of the *menB* and *menA* genes in the phylloquinone biosynthesis pathway, a foreign quinone is recruited into PS I complexes that functions as an efficient electron transfer cofactor. Employing various spectroscopic methods, this quinone is identified as plastoquinone-9. Multiple approaches show that when plastoquinone-9 occupies the A_1 site, electron transfer between Q^- and F_X is endergonic.

REFERENCES

Benasson, R., and Land, E. J. (1973) *Biochim. Biophys. Acta* **325**, 175–181

Biggins, J., and Mathis, P. (1988) *Biochemistry* **27**, 1494–500

Biggins, J. (1990) *Biochemistry* **29**, 7259–7264

Bittl, R., and Zech, S. G. (1997) *J. Phys. Chem. B.* **101**, 1429–1436

Bittl, R., Zech, S. G., Teutloff, C., Krabben, L., and Lubitz, W. (1998) in *Photosynthesis: Mechanisms and Effects* (Garab, G., ed) Vol. I, pp. 607–610, Kluwer, Dordrecht, The Netherlands

Bock, C. H., Van der Est, A. J., Brettel, K., and Stehlik, D. (1989) *FEBS Lett.* **247**, 91-96

Brettel, K. (1988) *FEBS Lett.* **239**, 93–98

Brettel, K. (1997) *Biochim. Biophys. Acta* **1318**, 322–373

Bryant, R. D., and Golbeck, J. H. (1998) *J. Phys. Chem. B.* **102**, 8288–8299

Budil, D. E., and Thurnauer, M. C. (1991) *Biochim. Biophys. Acta* **1057**, 1–41

Chamorovsky, S. K., and Cammack, R. (1982) *Photobiochem. Photobiophys*. **4**, 195–200

Diaz-Quintana, A., Leibl, W., Bottin, H., and Sétif, P. (1998) *Biochemistry* **37**, 3429–3439

Diner, B. A., deVitry, C., and Popot, J. L. (1988) *Biochim. Biophys. Acta* **934**, 47–54

Diner, B. A. (1998) in *Photosynthesis: Molecular Biology of Energy Capture* (Mcintosh, L., ed) Vol. 297, pp. 337–360, Academic Press Inc., San Diego

Dzuba, S. A., Hara, H., Kawamori, A., Iwaki, M., Itoh, S., and Tsvetkov, Y. D. (1997) *Chem. Phys. Lett*. **264**, 238–244

Dzuba, S. A. (1998) *Chem. Phys. Lett*. **278**, 333–340

Franke, J. E., Ciesla, L., and Warden, J. T. (1995) in *Proc. of the 10th International Photosynthesis Congress*, Montpelier, France, August 20–25, 1995 (Mathis, P., ed) Vol. **2**, pp. 75–78, Kluwer Academic Publishers, Dordrecht, Netherlands

Golbeck, J. H. (1999) *Photosynth. Res.* **61**, 107–144

Crane, F., Ehrlich, B., and Kegel, L. P. (1960) *Biochem. Biophys. Res. Commun.* **3**, 37–41

Gutman, V. (1976) *Coord. Chem. Revs.* **18**, 225–255

Hanley, J., Deligiannakis, Y., MacMillan, F., Bottin, H., and Rutherford, A. W. (1997) *Biochemistry* **36**, 11543–11549

Hore, P. J. (1996) *Mol. Phys*. **89**, 1195–1202

Itoh, S., and Iwaki, M. (1991) *Biochemistry* **30**, 5340–5346

Iwaki, M., and Itoh, S. (1991) *Biochemistry* **30**, 5347–5352

Iwaki, M., and Itoh, S. (1994) *Plant Cell Physiol*. **35**, 983–993

Jaworski, J. S., Lesniewska, E., and Kalinowski, M. K. (1979) *J. Electroanal. Chem*. **105**, 329–334

Joliot, P., Be´ al, D., and Frilley, B. (1980) *J. Chim. Phys*. **77**, 209–259

Joliot, P., and Joliot, A. (1999) *Biochemistry* **38**, 11130–11136

Johnson, T. W., Shen, G., Zybailov, B., Kolling, D., Reategui, R., Beauparlant, S., Vassiliev, I. R., Bryant, D. A., Jones, A. D., Golbeck, J. H., and Chitnis, P. R. (2000) *J. Biol. Chem*., **275**, 8523–8530

JordanP, Fromme P, Witt H. T., Klukas O, Saenger W, Krauβ N. 2001 Nature **411**, 909

Kamlowski, A., Zech, S. G., Fromme, P., Bittl, R., Lubitz, W., and Stehlik, D. (1998) *J. Phys. Chem. B.* **102**, 8266–8277

Kamlowski, A., Altenberg-Greulich, B., van der Est, A., Zech, S. G., Bittl, R., Fromme, P., Lubitz, W., and Stehlik, D. (1998) *J. Phys. Chem. B.* **102**, 8278–8287

Kandrashkin, Y. E., Salikhov, K., van der Est, A., and Stehlik, D. (1998) *Appl. Magn. Res*. **15**, 417–447

Klughammer, C., and Pace, R. J. (1997) *Biochim. Biophys. Acta* **1318**, 133–144

Klughammer, C., Klughammer, B., and Pace, R. (1999) *Biochemistry* **38**,

3726–3732

Klukas, O., Schubert, W. D., Jordan, P., Krauß, N., Fromme, P., Witt, H. T., and Saenger, W. (1999) *J. Biol. Chem* **274**, 7361–7367

Leibl, W., Toupance, B., and Breton, J. (1995) *Biochemistry* **34**, 10237–10244

Lubitz, W., and Feher, G. (1999) *Appl. Magn. Reson*. **17**, 1–48
MacMillan, F., Lendzian, F., Renger, G., and Lubitz, W. (1995*) Biochemistry* 34, 8144-8156

MacMillan, F., Hanley, J., van der Weerd, L., Knupling, M., Un, S., and Rutherford, A. W. (1997) *Biochemistry* **36**, 9297–9303

Mamedov, M. D., Gadzhieva, R. M., Gourovskaya, K. N., Drachev, L. A., and Semenov, A. Y. (1996) *J. Bioenerg. Biomembr*. **28**, 517–522

Mamedova, A. A., Mamedov, M. D., Gourovskaya, K. N., Vassiliev, I. R., Golbeck, J. H., and Semenov, A. Y. (1999) *FEBS Lett.* **462**, 421–424

Moser, C. C., Keske, J. M., Warncke, K., Farid, R. S., and Dutton, P. L. (1992) *Nature* **355**, 796–802

Moser, C., and Dutton, P. (1992) *Biochim. Biophys. Acta* **1101**, 171–176

Okamura, M. Y., Isaacson, R. A., and Feher, G. (1975) *Proc. Natl. Acad. Sci. U. S. A.* **72**, 3491–3495

O'Malley, P. J. (1998) *Chem. Phys. Lett*. **285**, 99–104

O'Malley, P. J. (1999) *Biochim. Biophys. Acta* **1411**, 101–113

O'Malley, P. J. (1998) *J. Am. Chem. Soc*. **120**, 5093–5097

Parrett, K. G., Mehari, T., Warren, P. G., and Golbeck, J. H. (1989*) Biochim. Biophys. Acta* **973**, 324–332

Prince, R. C., Dutton, P. L., and Bruce, J. M. (1983) *FEBS Lett*. **160**, 273–276

Prince, R. C., Lloyd-Williams, P., Bruce, J. M., and Dutton, P. L. (1986) *Methods Enzymol*. **125**, 109–119

Rigby, S. E. J., Evans, M. C. W., and Heathcote, P. (1996) Biochemistry 35, 6651–6656

Rippka, R., Deruelles, J., Waterbury, J. B., Herdman, M., and Stanier, R. Y. (1979) *J. Gen. Microbiol*. **111**, 1–61

Rustandi, R., Snyder, S., Biggins, J., Norris, J., and Thurnauer, M. (1992) *Biochim. Biophys. Acta* **1101**, 311–320

Rutherford, A. W., and Sétif, P. (1990) *Biochim. Biophys. Acta* **1019**, 128–132

Salikhov, K. M., Kandrashkin, Y., and Salikhov, A. K. (1992) *Appl. Magn. Res.* **3**, 199–216

Sétif, P., Bottin, H., and Brettel, K. (1990) in *Proceedings of the 8 th International Conference on Photosynthesis, Stockholm, Sweden, August 6–11*, 1989 (Baltscheffsky, M., ed) Vol. **2**, pp. 539–546, Kluwer Academic Publishers
Group, Dordrecht, Netherlands

Sharma, V., Hudspeth, M. E., and Meganathan, R. (1996*) Gene* **168**, 43–48

Shen, G. Z., Eaton-Rye, J. J., and Vermaas, W. F. J. (1993) *Biochemistry* **32**, 5109–5115

Shinkarev, V., Vassiliev, I., and Golbeck, J. H. (2000) *Biophys. J.* **78**, 263–272

Schlodder, E., Falkenberg, K., Gergeleit, M., and Brettel, K. (1998) *Biochemistry* **37**, 9466–9476

Schubert, W. D., Klukas, O., Kraub, N., Saenger, W., Fromme, P., and Witt, H. T. (1997) *J. Mol. Biol*. **272**, 741–769

Sétif, P., and Brettel, K. (1993) *Biochemistry* **32**, 7846–7854

Sieckmann, I., Brettel, K., Bock, C., Van der Est, A., and Stehlik, D. (1993) *Biochemistry* **32**, 4842–4847

Sieckman, I., van der Est, A., Bottin, H., Sétif, P., and Stehlik, D. (1991) *FEBS Lett.* **284**, 98–102

Stehlik, D., Bock, C. H., and Petersen, J. (1989) *J. Phys. Chem*. **93**, 1612–1619

Tang, J., Bondeson, S., and Thurnauer, M. C. (1996) *Chem. Phys. Lett*. **253**, 293–298

Thurnauer, M. C., and Gast, P. (1985) *Photobiochem. Photobiophys*. **9**, 29–38

Timmel, C. R., Fursman, C., Hoff, A., and Hore, P. (1998) *Chem. Phys*. **226**, 271–285

van der Est, A., Bock, C., Golbeck, J., Brettel, K., Sétif, P., and Stehlik, D. (1994) *Biochemistry* **33**, 11789–11797

van der Est, A., Sieckmann, I., Lubitz, W., and Stehlik, D. (1995) *Chem. Phys.* **194**, 349–360

van der Est, A., Prisner, T., Bittl, R., Fromme, P., Lubitz, W., Mobius, K., and Stehlik, D. (1997) *J. Phys. Chem. B* **101**, 1437–1443

van der Est, A., Hager-Braun, C., Leibl, W., Hauska, G., and Stehlik, D. (1998) *Biochim. Biophys. Acta* **1409**, 87–98

van Gorkom, H. (1974) *Biochim. Biophys. Acta* **347**, 439–442

Vassiliev, I. R., Jung, Y. S., Mamedov, M. D., Semenov, A. Y., and Golbeck, J. H. (1997) *Biophys. J.* **72**, 301–315

Vassiliev, I. R., Jung, Y. S., Yang, F., and Golbeck, J. H. (1998) *Biophys. J.* **74**, 2029–2035.,

Vos, M. H., and van Gorkom, H. J. (1988) *Biochim. Biophys. Acta* **934**, 293–302

Vos, M. H., and Van Gorkem, H. J. (1990) Biophys. J. 58, 1547–1555

Yang, F., Shen, G., Schluchter, W. M., Zybailov, B. L., Ganago, A. O., Vassiliev, R., Bryant, D., and Golbeck, J. H. (1998) *J. Phys. Chem. B.* 102, 8288–8299

Zech, S. G., Lubitz. W., and Bittl, R (1996) *Ber. Bunsen-Ges. Phys. Chem*. **100**, 2041–2044

Zech, S. G., van der Est, A., and Bittl, R. (1997*) Biochemistry* **36**, 9774–9779

Zheng, M., and Dismukes, G. C. (1996) *Biochemistry* **35**, 8955–8963

FIGURE LEGENDS

Figure 2.1 Biosynthetic pathway of phylloquinone biosynthesis in *Synechocystis* sp. PCC 6803 (Johnson *et al.*, 2001). The gene products responsible for the biosynthesis of *mena*quinone were initially described in *Escherichia coli* (Sharma *et al.*, 1996).

Figure 2.2 HPLC profiles of pigment extracts from lyophilized PS I complexes. *A*, PS I isolated from wild-type strain of *Synechocystis* sp. PCC 6803. The pigments were separated on a 5.0 mm Ultrasphere C18 reverse phase column. The detection wavelength was 270 nm. The extract from the wild type shows a peak that co-elutes with authentic phylloquinone at 29.7 min. *Top* inset: UV/Vis spectrum of authentic phylloquinone. Bottom inset, near-UV/Vis spectrum of HPLC peak that elutes at 29.7 min. *B*, HPLC of pigment extracts from PS I complexes of the *menB* mutant strain of *Synechocystis* sp. PCC 6803. The pigments were separated on a 5.0- mm Ultrasphere C18 reverse phase column. The peak at 37.2 min in the wild type co-elutes with β-carotene, and shows a spectrum in the visible identical to β-carotene. The peak at 37.2 min in the *menB* mutant shows an additional UV-absorbing component (bottom inset) that co-elutes with plastoquinone-9 and that shows a UV spectrum similar to plastoquinone-9 (top inset) and an m/z of 748. The LC/MS analysis of the PS I complexes from the *menA* mutant was similar.

Figure 2.3 Molecular structures of phylloquinone and plastoquinone-9. A common numbering of the quinone ring positions is used in the text, such that the carbonyl group next to the hydrocarbon chain in position 3 is placed in position 4.

Figure 2.4 Magnetic field versus time versus amplitude of P_{700}^{+} and Q^{-} in whole cells of the *menA* mutant strain. Dark-adapted cells were illuminated for 2.5 s, and the intensity was plotted as a function of time at a given magnetic field. EPR conditions were as follows: microwave frequency, 9.7698 GHz; microwave power, 50 mW; modulation

frequency, 100 kHz; modulation amplitude, 1 G; receiver gain, 4×10^4; conversion time, 327 ms; time constant, 10 ms.

Figure 2.5 Two-dimensional slices (from figure 4) of amplitude versus magnetic field (*top*) and amplitude versus time (*bottom*). The spectra are derived from the time-resolved EPR studies at 0.1 (dotted line), 0.5 (solid line), and 2.7 s dashed line) after the opening of the shutter. The arrows refer to the field settings of the kinetic traces in the bottom panel at 3484.5 G, which corresponds to the time-dependent evolution of P_{700}^+, and at 3475 and 3486 G, which correspond to the time-dependent evolution of Q^-.

Figure 2.6 Photoaccumulated and simulated Q-band CW EPR spectra of A_1^- and Q^- in PS I complexes isolated from wild type, deuterated wild type, and *menA* and *menB* mutants. Experimental data are depicted as solid lines, and simulated spectra are depicted as dashed lines. The vertical dashed line is a visual aid; it is aligned to the low field peak of the *menA* and *menB* mutant samples. The photoaccumulation protocol was carried out for 40 min at 205 K. Instrument settings were as follows: microwave power, 1 mW; microwave frequency, 34.056 GHz; modulation frequency, 100 kHz; modulation amplitude, 1 G; temperature, 205 K; time constant, 10 ms; conversion time, 10 ms. 100 scans were averaged.

Figure 2.7 Spin-polarized transient EPR spectra of PS I from *menA* and *menB* mutants compared with the wild type at three different microwave frequencies (from top to bottom, 95, 35, and 9 GHz). The spectra were recorded at a temperature of 150 K and are the integrated signal intensity in a time window 0.5 to 1.5 ms following the laser flash except for the W-band spectrum of wild-type PS I, which is the two-pulse field-swept echo spectrum reported in van der Est *et al.,* 1997.

Figure 2.8 Comparison at 80 K of the out-of-phase echo modulations of PS I complexes from *menA* (solid curve, top), *menB* (solid curve, bottom), and wild type (dashed curves).

Figure 2.9 Pulsed ENDOR spectra of the P_{700}^{+} Q^{-} state of the *menA* and *menB* mutants (*top*) in comparison to that of the P_{700}^{+} A_1^{-} state in wild-type PS I (*bottom*). The spectral ranges attributable to the CH_3 hyperfine couplings in Q^{-} are shaded. The vertical dashed lines at about 8.3 and 21.1 MHz in the traces of *menA* and *menB* indicate the outer wings of the spectra. Shown is a Davies type ENDOR pulse sequence; temperature, 80 K.

Figure 2.10 Reduction kinetics in PS I complexes isolated from the *menB* mutant. *A*, flash-induced optical transient measured at 810 nm after a single flash. Sample conditions are as follows: 50 mg chlorophyll ml^{-1} in 25 mM Tris, pH 8.3, 0.04% β-DM, 10 mM ascorbate, and 4 mM DCPIP in a 1 3 1-cm fluorescence cuvette. Excitation wavelength was 532 nm, and excitation energy was 1.4 mJ. A 300-MHz bandwidth was used in the preamplifier to recover kinetics in the microsecond time range. *B*, flash-induced EPR transient measured at 3485 G magnetic field position (average of 64 traces recorded at 10 s intervals between flashes). Sample conditions are as follows: 0.4 mg chlorophyll ml^{-1} in 25 mM Tris, pH 8.3, 0.04% β-DM, 10 mM ascorbate, and 4 mM DCPIP in an EPR flat cell. Excitation wavelength was 532 nm, and excitation energy was 14 mJ. Time is plotted on a logarithmic scale in which a deviation from the horizontal represents a kinetic phase. The computer-generated exponential fits are shown as solid lines. Results of the exponential fits are displayed as fit curves (*broken* line) with the lifetimes of each phase depicted by an arrow. Each individual component is plotted with vertical offset relative to the next component (with a longer lifetime) or the base line, the offset being equal to the amplitude of the latter component. The relative contributions of each kinetic phase can be judged by the intersection of the fit line with the abscissa.

Figure 2.11 Global decomposition of optical kinetic spectra of PS I complexes from *menB* mutant in the blue region. *A*, spectrum of flash-induced optical transient measured in the absence of methyl viologen. Solid squares represent a component with a 3.2-ms lifetime; checked boxes represent a long lived component (sensitive to DCPIP concentration); solid circles represent a component with a 13- ms lifetime. *B*, spectrum of flash-induced optical transient measured in the presence of 100 mM methyl viologen.

Open squares represent a long lived component (sensitive to DCPIP concentration); solid diamonds represent a component with a 744-ms lifetime; open circles represent a component with an 18-ms lifetime. *C*, difference between A (solid squares) and B (open squares). The contribution of the spectrum in A (checked boxes) was ignored; hence, the difference spectrum underestimates the amount of FeS cluster reduced on a flash (see text). Sample conditions are as follows: PS I complex isolated from *menB* mutant at 10 mg chlorophyll ml^{-1} in 25 mM Tris, pH 8.3, 0.04% β-DM, 10 mM ascorbate and 4 mM DCPIP.

Figure 2.12 Electron spin-polarized EPR spectra of the PS I complexes from wild type, *menA*, and *menB* mutants at room temperature. *Top* trace, wild-type PS I. The two sequential spin polarized spectra have been extracted from the complete time/field data set as described in detail (van der Est *et al.*, 1994). The solid curve corresponds to the radical pair P_{700}^{+} A_1^{-}, whereas the emissive spectrum is due to P_{700}^{+} FeS^{-}. Middle and lower traces, *menA* and *menB* mutants. The curves are decay-associated spectra extracted from the complete time/field data sets. In the mutants only one kinetic component is observed which we assign to P_{700}^{+} Q^{-}.

Figure 2.13 Electron spin-polarized EPR kinetic transients of the PS I complexes from wild type, *menA*, and *menB* mutants. Kinetic traces corresponding to the spectra shown in Figure 12 taken at the field position indicated by the arrow at the bottom of Fig. 2.12. Top trace, native PS I. Middle trace, PS I from *menA*. Bottom trace, PS I from *menB*. The electron transfer from A_1 to FeS is clearly visible in the upper trace. Note, however, that the decay of the signals is dominated by the relaxation of the spin polarization and not by recombination of the radical pairs involved.

Figure 2.14 Flash-induced absorbance change in the PS I complexes from *menA* mutant in the UV region. *A*, flash-induced difference absorbance changes recorded at times 5 ms (*circles*), 100 ms (*squares*),and 5 ms (*triangles*) after a saturating flash. Sample conditions are as follows: PS I complexes isolated from the *menB* mutant at 10

mg chlorophyll ml^{-1} in 25 mM Tris/HCl, pH 8.3, 10 mM sodium ascorbate, 4 mM DCPIP, and 0.03% w/v β-DM. Each point represents the average of 8 measurements spaced 20 s between flashes minus a dark background taken similarly but without the detecting flash. *B*, spectrum of the plastoquinone-9 anion radical in methanol (*checked circles*) adapted from (Benasson and Land, 1973), and spectrum of Q_A^- minus Q_A in deoxycholate-isolated PS II complexes (checked squares) adapted from (van Gorkom, 1974).

Figure 2.15 Kinetics of Q^- oxidation in the *menA* and *menB* mutants. *A*, flash-induced absorbance changes in *menA* measured at 310 nm. Each point represents the difference between the average of 8 flashes with the measuring flash on and 8 flashes with the measuring flash blocked to both sample and reference cuvettes. Sample conditions 10 mg chlorophyll ml^{-1} in 1 mM Tris, pH 8.3, 0.03% β-DM, 10 mM ascorbate, and 4 mM DCPIP in 4-sided fluorescence cuvette. The experimental data are shown as dots, and the computer-generated exponential fits are shown as solid lines. *B*, flash-induced absorbance changes in *menB* measured at 490 nm. Each point represents the average of 16 flashes using a conventional flash spectrometer. Excitation wavelength was 532 nm, and excitation energy was 1.4 mJ. Sample conditions: 10 mg chlorophyll ml^{-1} in 25 mM Tris, pH 8.3, 0.03% w/v β-DM, 10 mM ascorbate, and 4 mM DCPIP in fluorescence cuvette. The experimental data are shown as dots, and the computer-generated exponential fits are shown as solid lines. *C*, electrometric measurements of oriented PS I complexes from the *menB* mutant. Inset, kinetics of the flash-induced membrane potential generation by PS I-containing proteoliposomes. Deconvolution of the slow phase kinetics is shown in the main figure. Sample conditions are as follows: 25 mM Tris, pH 8.3, 10 mM ascorbate, and 4 mM DCPIP. Excitation wavelength was 532 nm, and excitation energy was 1.4 mJ.

Figure 2.16 Field modulation transient EPR spectroscopy of PS I complexes from the *menA* mutant. Top, spectra extracted from the complete time/field data sets for *menA* and wild-type PS I. Solid curve, wild type, decay-associated spectrum of the 32-ms phase assigned to P_{700}^+ $(FeS)^-$. Dashed curve, *menA*, boxcar spectrum taken in a time window

100 ms to 300 ms following the laser flash. Dotted-dashed curve, *menA*, boxcar spectrum taken in a time window 3 ms to 4 ms following the laser flash. Bottom, transient from the *menA* sample taken at the field position indicated by an arrow in the top part of the figure. The dashed curve is a fit to the data which yields a lifetime for the electron transfer from Q^- to FeS of 300 ms and a recombination lifetime of 5 ms. The offset at long times is due to reduction of P_{700}^+ by an exogenous donor in centers in which the transferred electron is lost from FeS.

Figure 2.17 Energetics of PS I in the wild type (A) and *menA*/B mutants (B). The backreaction rates in the wild type refer to conditions where the succeeding electron acceptor has been removed, either biochemically or genetically. The values in bold represent the dominant kinetic phase. The majority of the forward and back electron transfer times in the *menA*/B mutant have not been characterized. The backreaction pathways are depicted as direct to P_{700}^+ for the sake of clarity; the actual pathway likely proceeds, at least in part, back through the electron acceptor chain.

Figure 2.18 Phylloquinone binding site (PsaA) according to the latest, 2.5 Å resolution X-ray structure (Jordan *et al.,* 2001). The next electron acceptor in the chain, F_X is shown as a yellow spacefill, phylloquinone is shown as thick wireframe (pink); W forming possible π-π intractions with the naphthoic ring is shown in the thin wireframe (blue). Hydrogen bond is evident between Ile residue and the top carbonyl group of the phylloquinone.

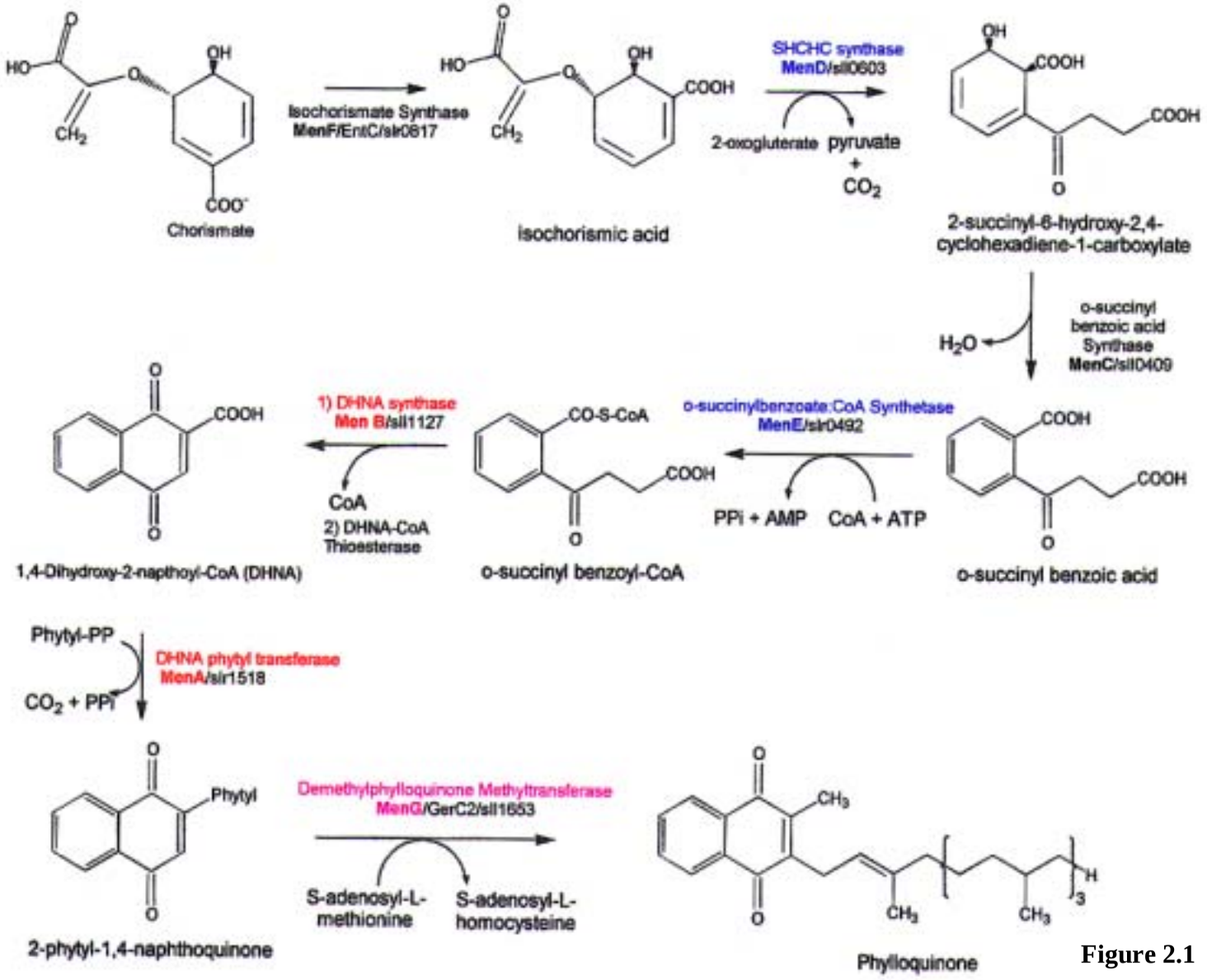
Chorismate
Isochorismate Synthase
MenF/EntC/slr0817
isochorismic acid
SHCHC synthase
MenD/sll0603
2-oxogluterate
pyruvate
+
CO_2
2-succinyl-6-hydroxy-2,4-cyclohexadiene-1-carboxylate
H_2O
o-succinyl benzoic acid Synthase
MenC/sll0409
o-succinyl benzoic acid
o-succinylbenzoate:CoA Synthetase
MenE/slr0492
PPi + AMP
CoA + ATP
o-succinyl benzoyl-CoA
1) DHNA synthase
Men B/sll1127
CoA
2) DHNA-CoA Thioesterase
1,4-Dihydroxy-2-napthoyl-CoA (DHNA)
Phytyl-PP
DHNA phytyl transferase
MenA/slr1518
CO_2 + PPi
2-phytyl-1,4-naphthoquinone
Demethylphylloquinone Methyltransferase
MenG/GerC2/sll1653
S-adenosyl-L-methionine
S-adenosyl-L-homocysteine
Phylloquinone

Figure 2.1

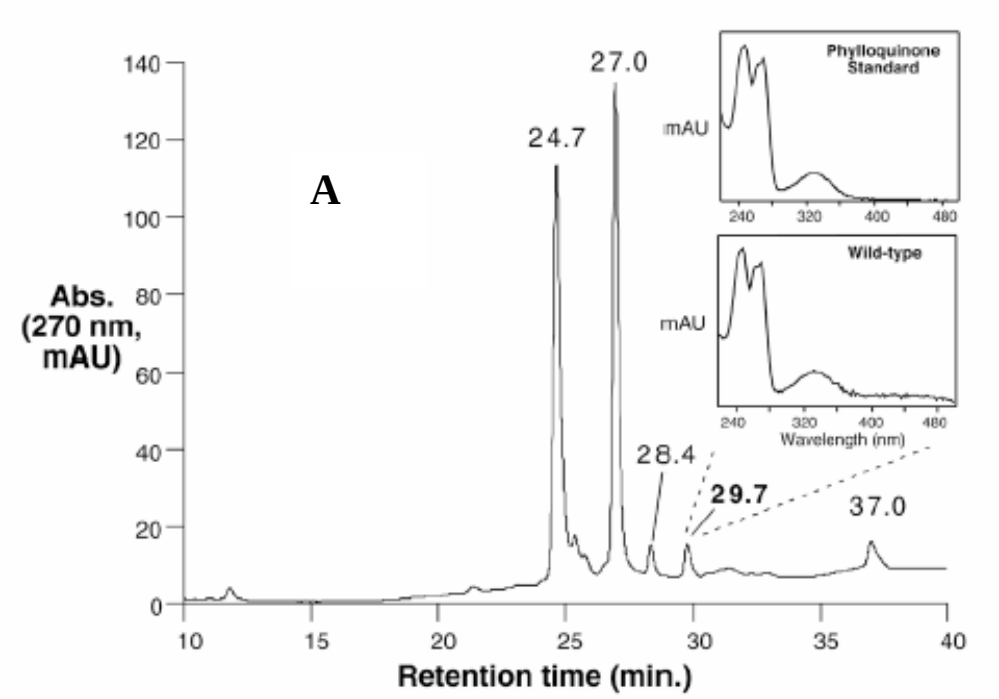
A
Abs. (270 nm, mAU)
Retention time (min.)
24.7
27.0
28.4
29.7
37.0
Phylloquinone Standard
Wild-type
mAU
Wavelength (nm)

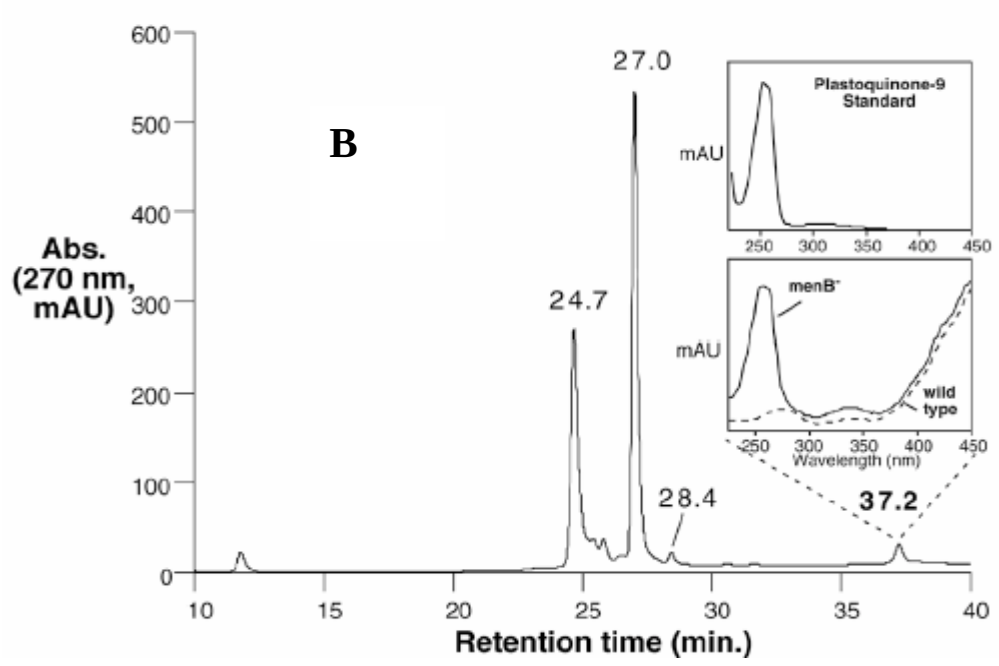
B
Abs. (270 nm, mAU)
Retention time (min.)
24.7
27.0
28.4
37.2
Plastoquinone-9 Standard
menB⁻
wild type
mAU
Wavelength (nm)

Figure 2.2

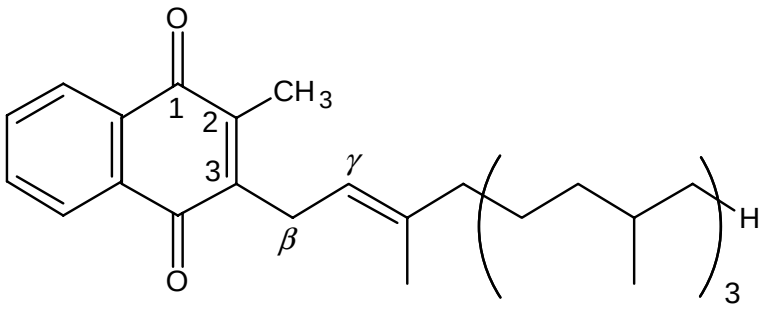

Phylloquinone

C31H46O2

M: 450.35 g

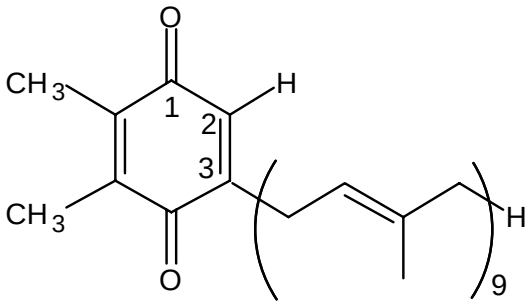

Plastoquinone-9:

$C_{53}H_{80}O_2$

M: 748.64 g

Figure 2.3

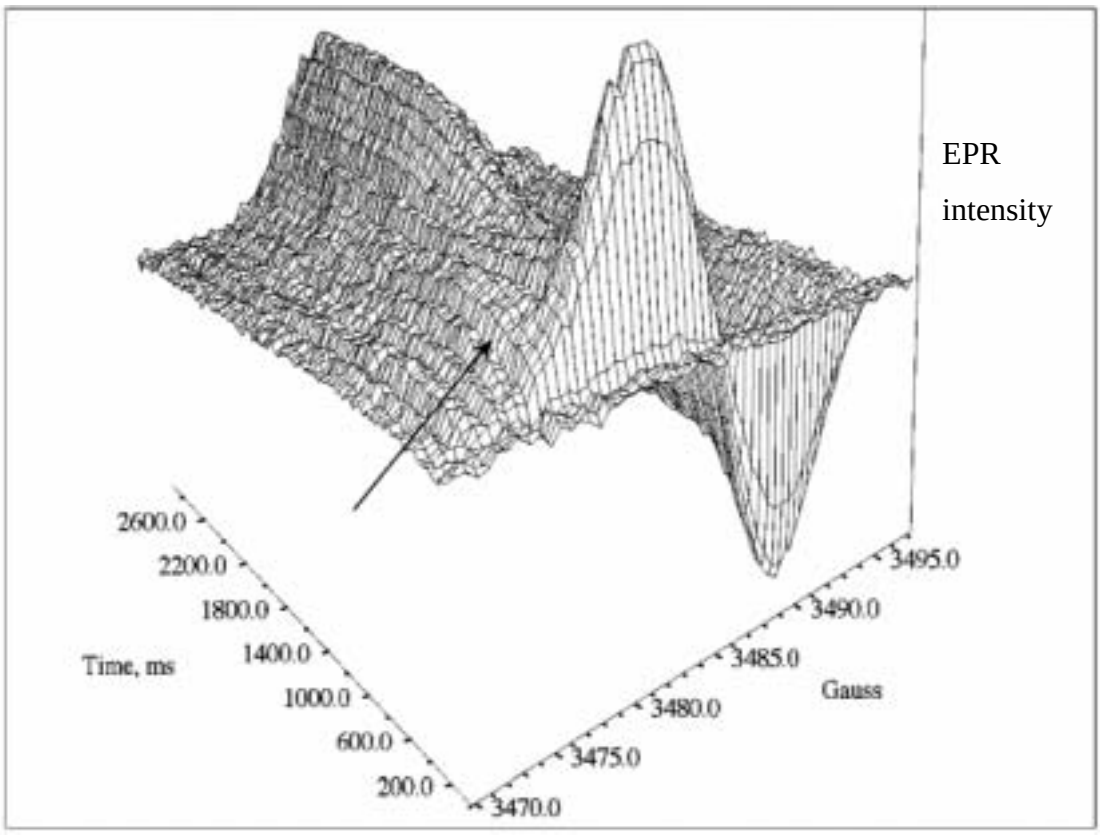
EPR
intensity
2600.0
2200.0
1800.0
1400.0
1000.0
600.0
200.0
Time, ms
3470.0
3475.0
3480.0
3485.0
3490.0
3495.0
Gauss

Figure 2.4

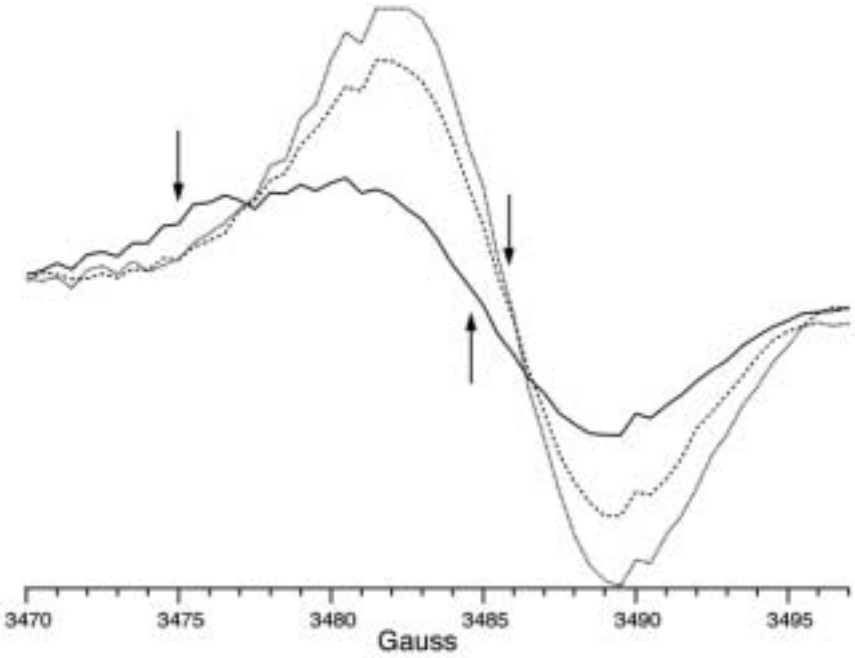
A
3470
3475
3480
3485
3490
3495
Gauss

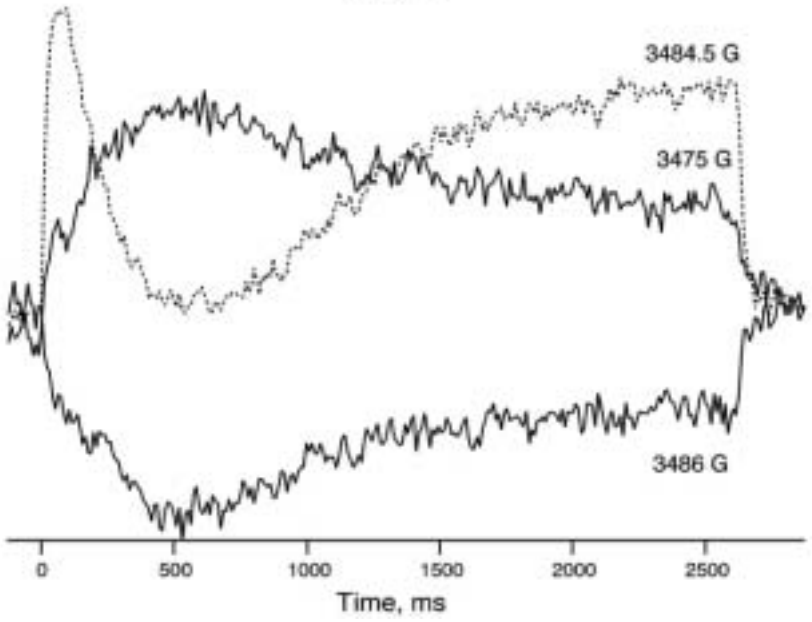
B
3484.5 G
3475 G
3486 G
0
500
1000
1500
2000
2500
Time, ms

Figure 2.5

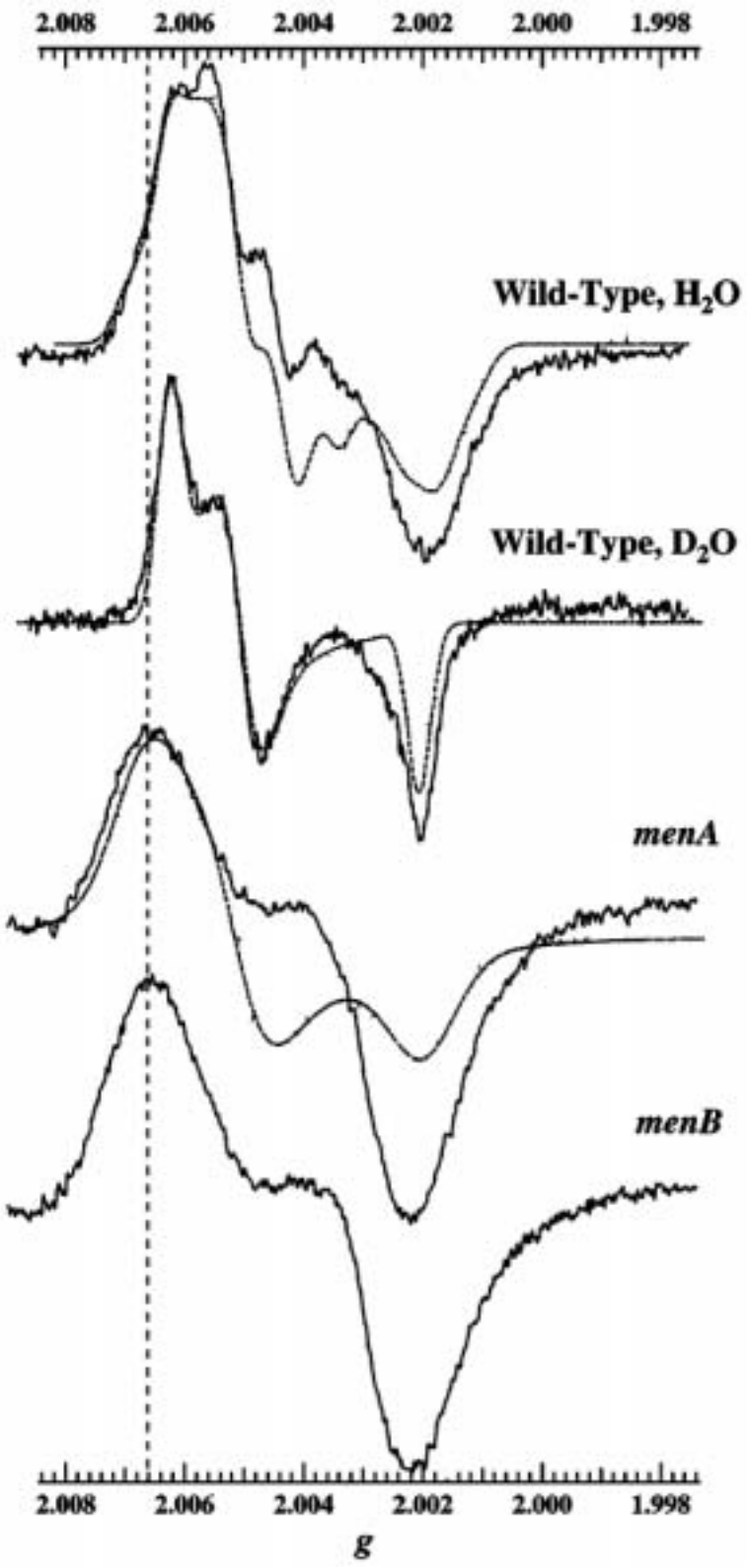
2.008
2.006
2.004
2.002
2.000
1.998
Wild-Type, H2O
Wild-Type, D2O
menA
menB
2.008
2.006
2.004
2.002
2.000
1.998
g

Figure 2.6

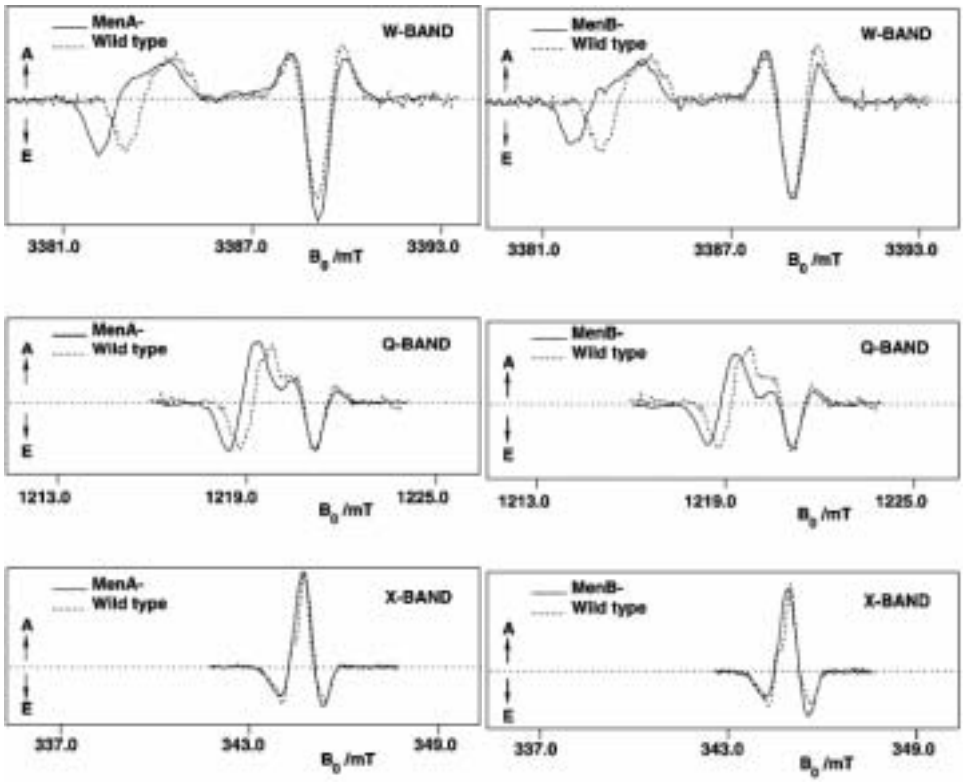
MenA-
Wild type
W-BAND
A
E
3381.0
3387.0
3393.0
B0 /mT
MenB-
Wild type
W-BAND
A
E
3381.0
3387.0
3393.0
B0 /mT
MenA-
Wild type
Q-BAND
A
E
1213.0
1219.0
1225.0
B0 /mT
MenB-
Wild type
Q-BAND
A
E
1213.0
1219.0
1225.0
B0 /mT
MenA-
Wild type
X-BAND
A
E
337.0
343.0
349.0
B0 /mT
MenB-
Wild type
X-BAND
A
E
337.0
343.0
349.0
B0 /mT

Figure 2.7

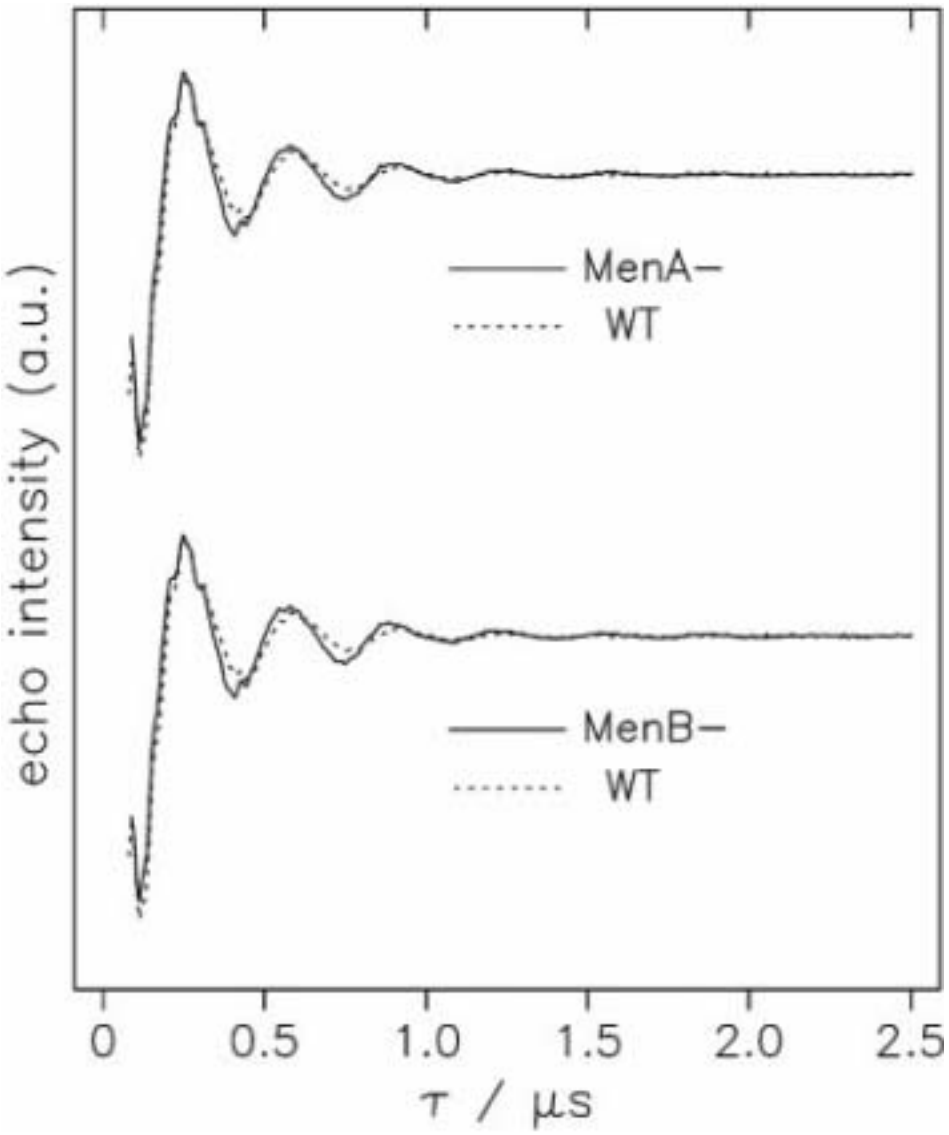

Figure 2.8

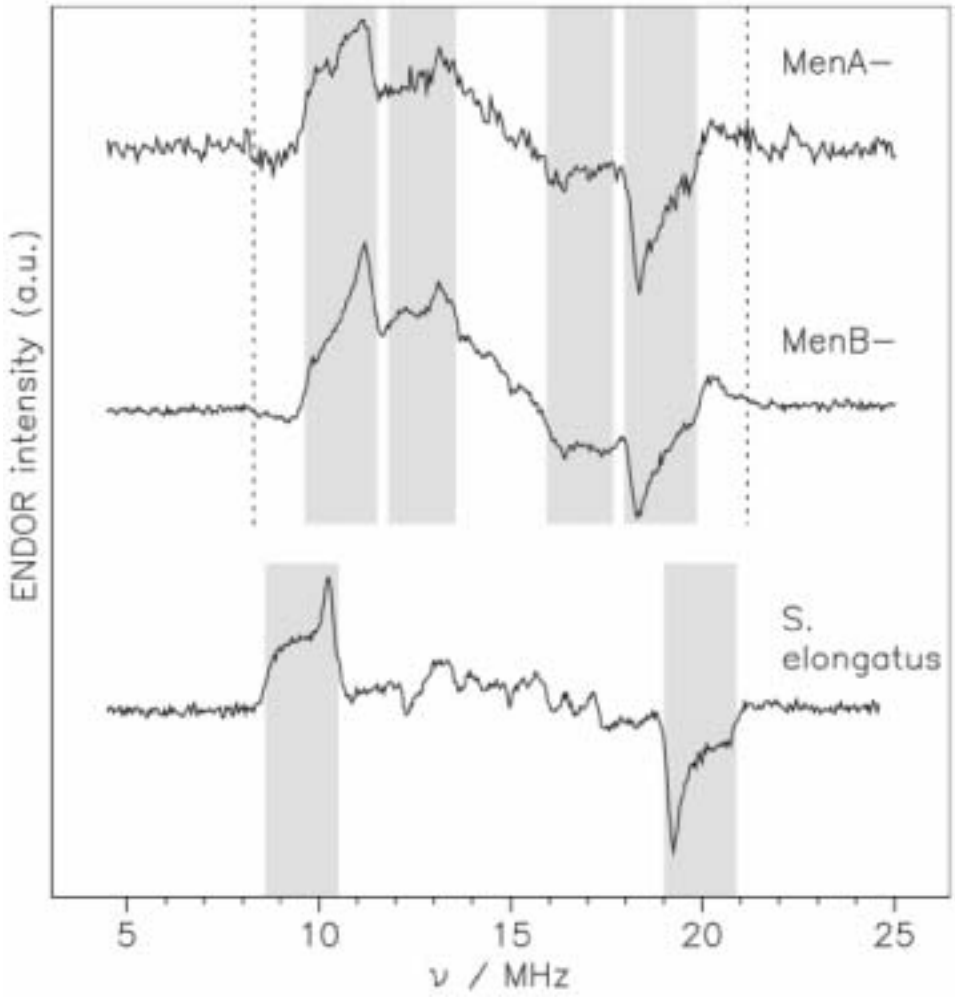

Figure 2.9

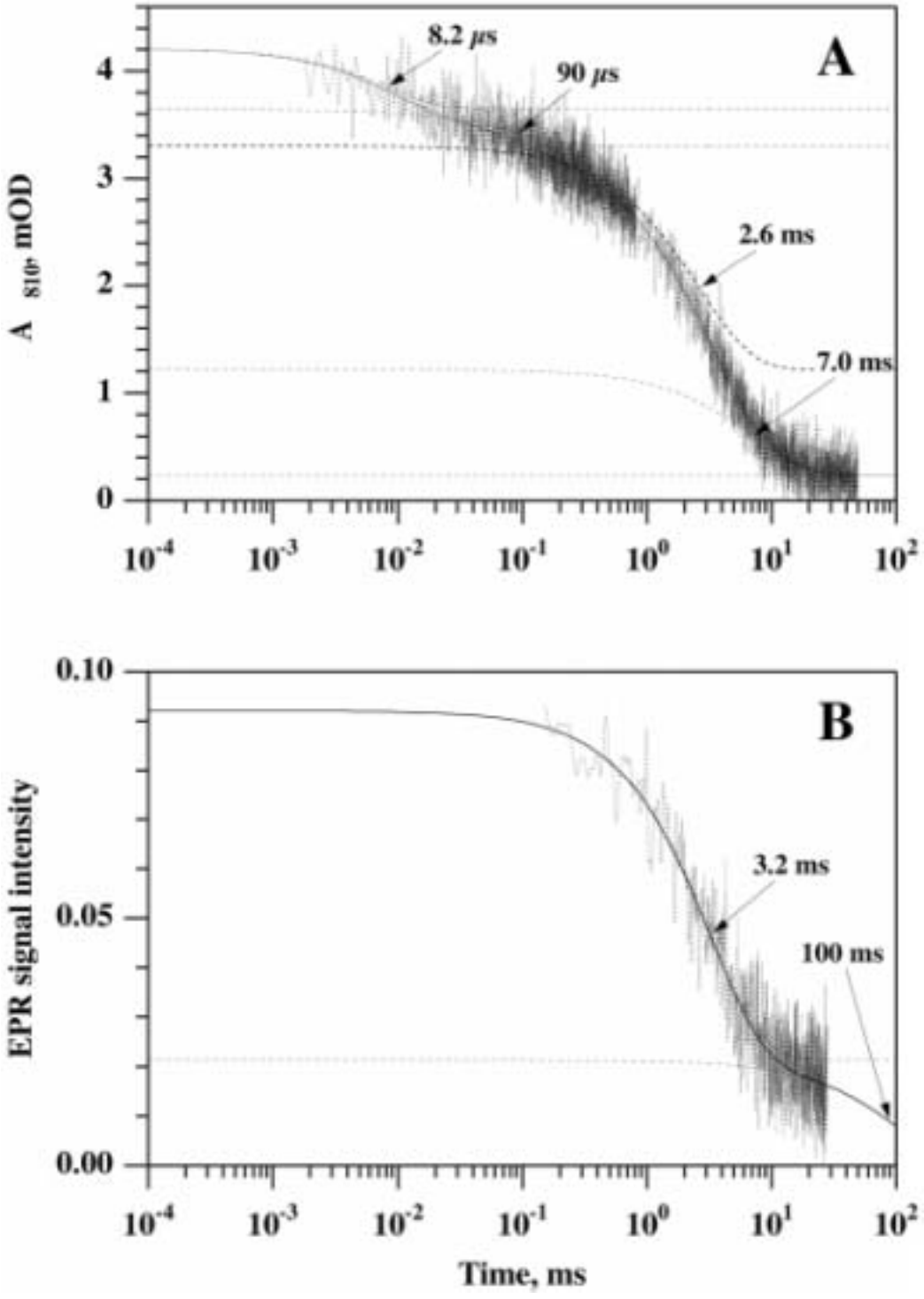
A
8.2 μs
90 μs
2.6 ms
7.0 ms
A 810 mOD
4
3
2
1
0
10-4
10-3
10-2
10-1
100
101
102
B
3.2 ms
100 ms
EPR signal intensity
0.10
0.05
0.00
Time, ms

Figure 2.10

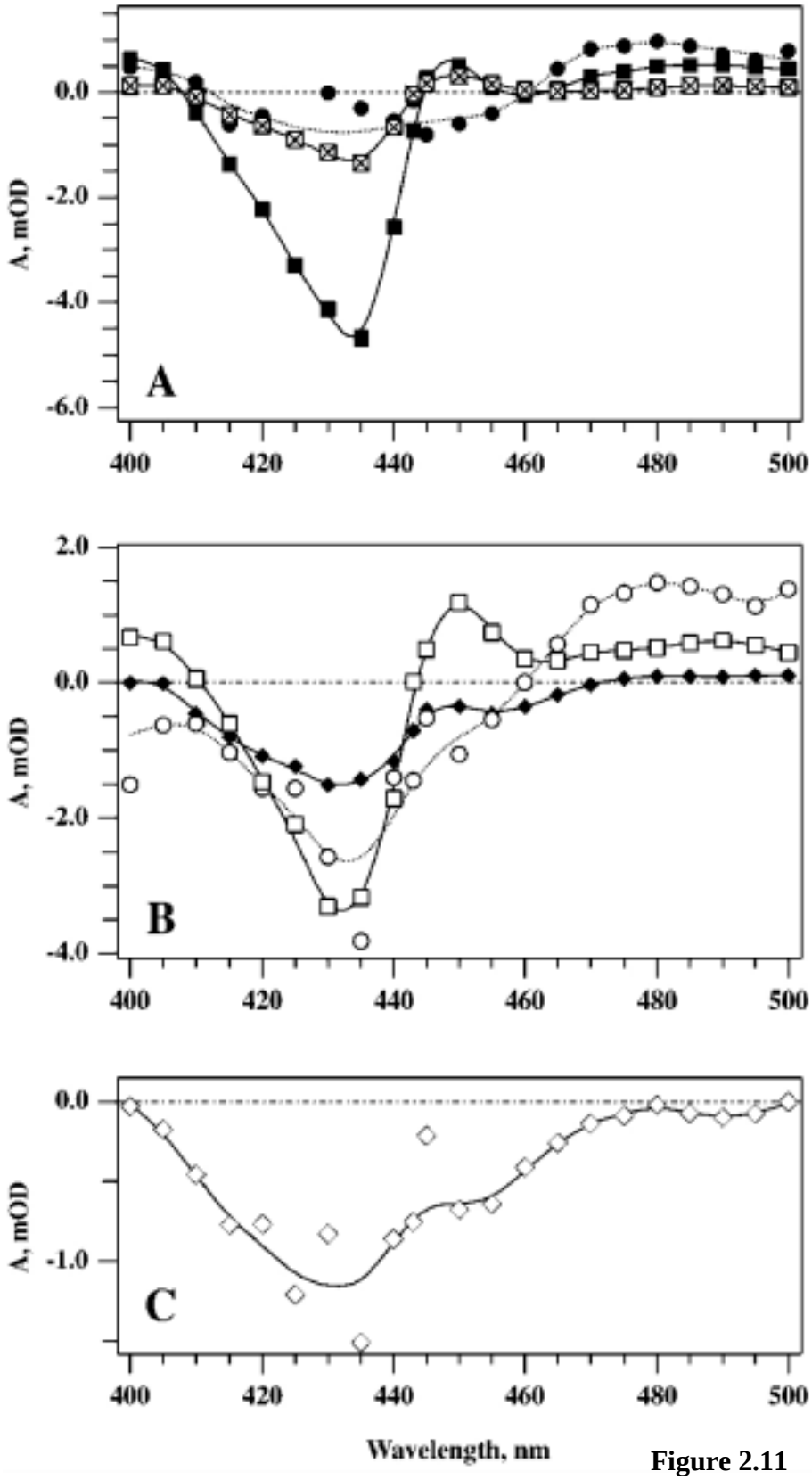

Figure 2.11

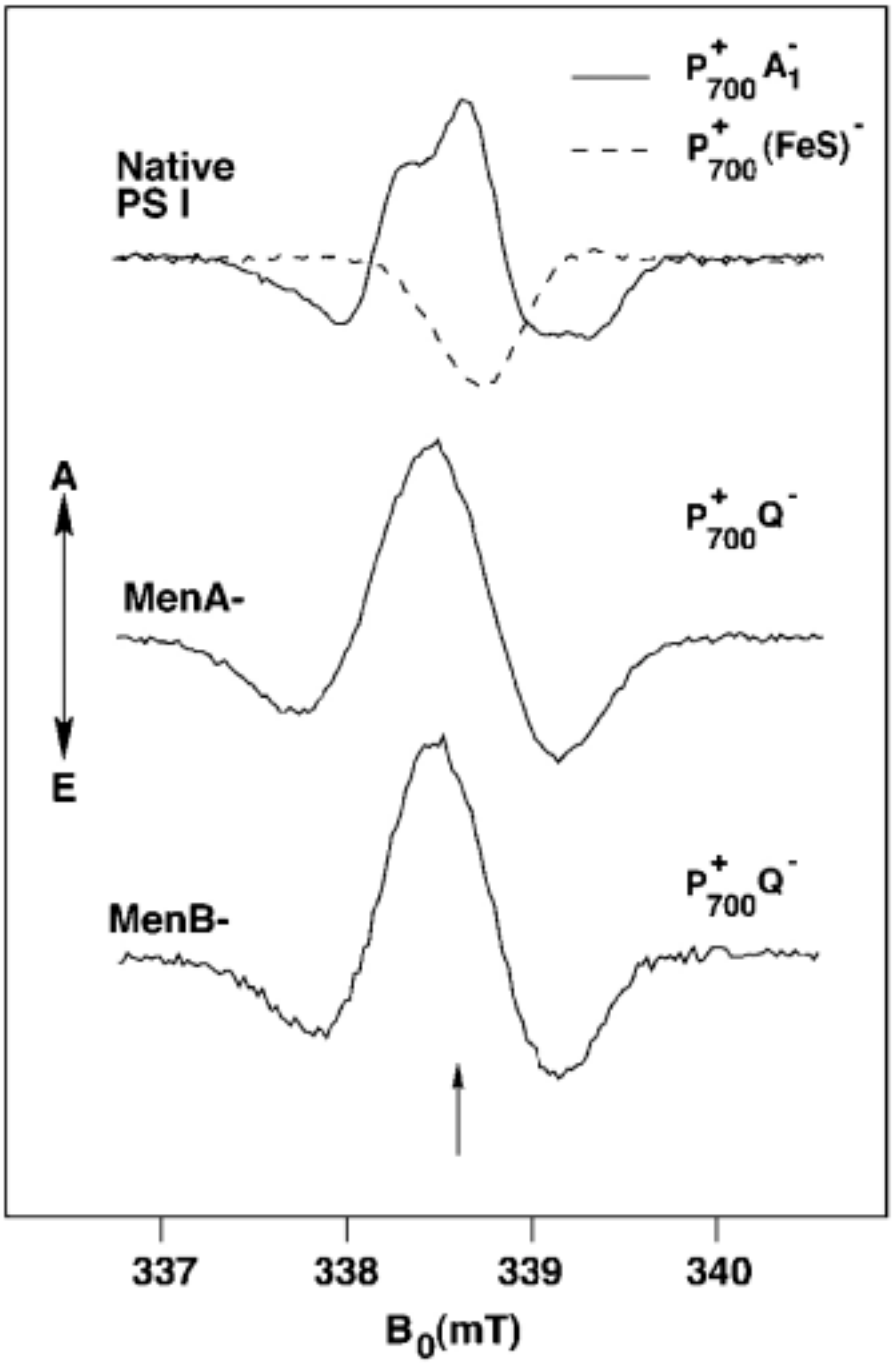
$P_{700}^{+}A_1^{-}$
$P_{700}^{+}(FeS)^{-}$
Native
PS I
A
E
$P_{700}^{+}Q^{-}$
MenA-
$P_{700}^{+}Q^{-}$
MenB-
337
338
339
340
B_0(mT)

Figure 2.12

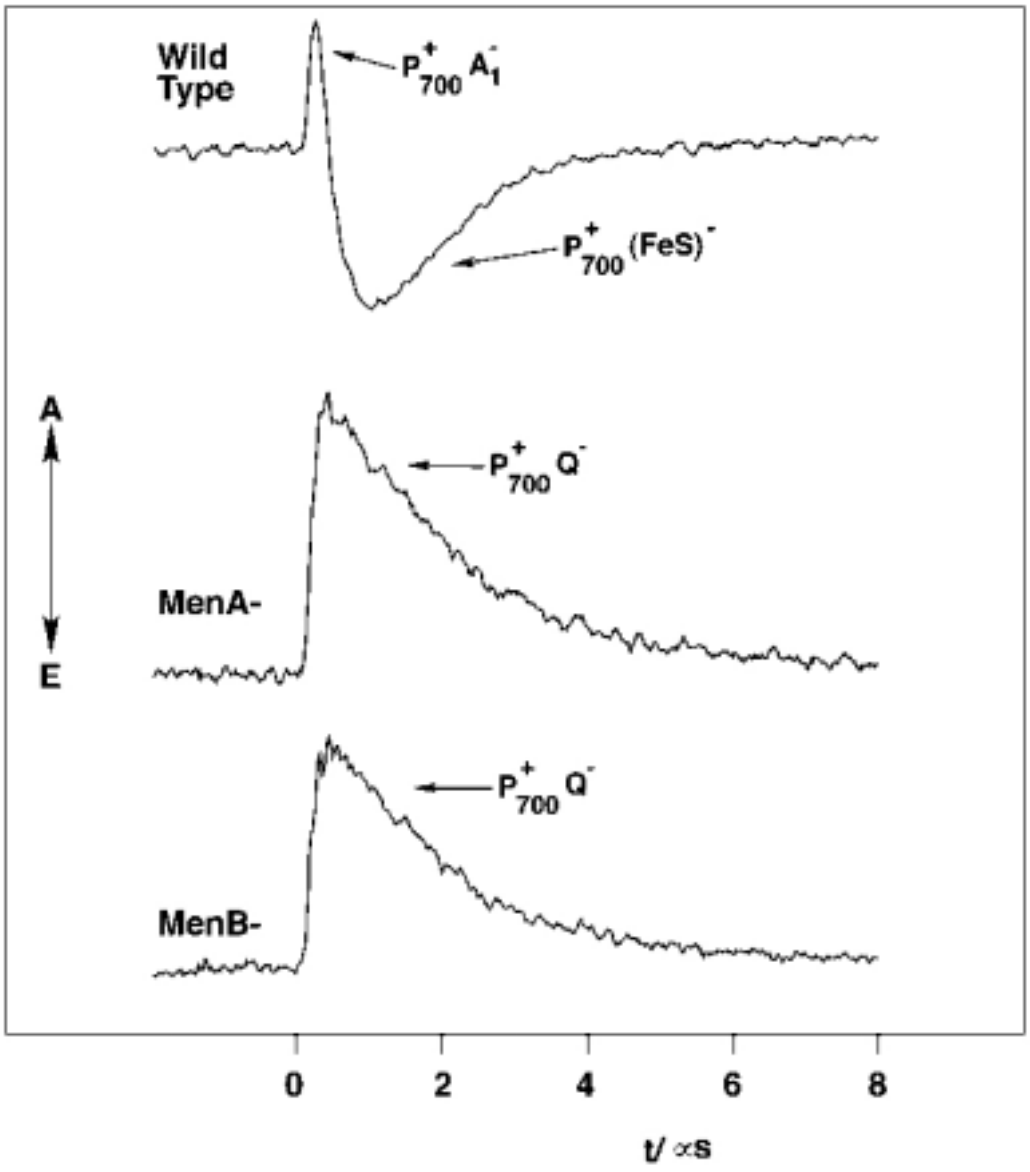

Figure 2.13

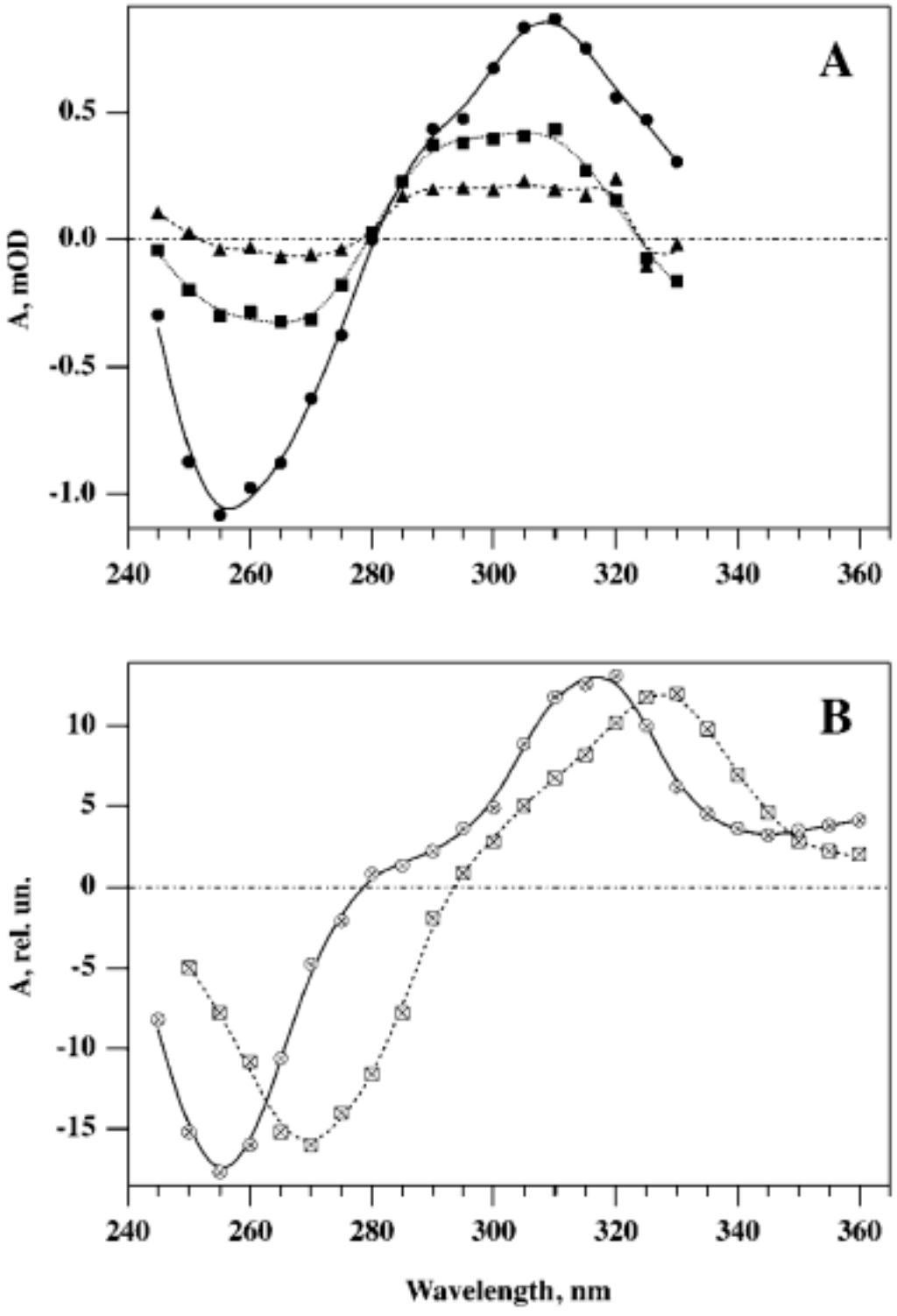
A
0.5
0.0
-0.5
-1.0
A, mOD
240
260
280
300
320
340
360
B
10
5
0
-5
-10
-15
A, rel. un.
240
260
280
300
320
340
360
Wavelength, nm

Figure 2.14

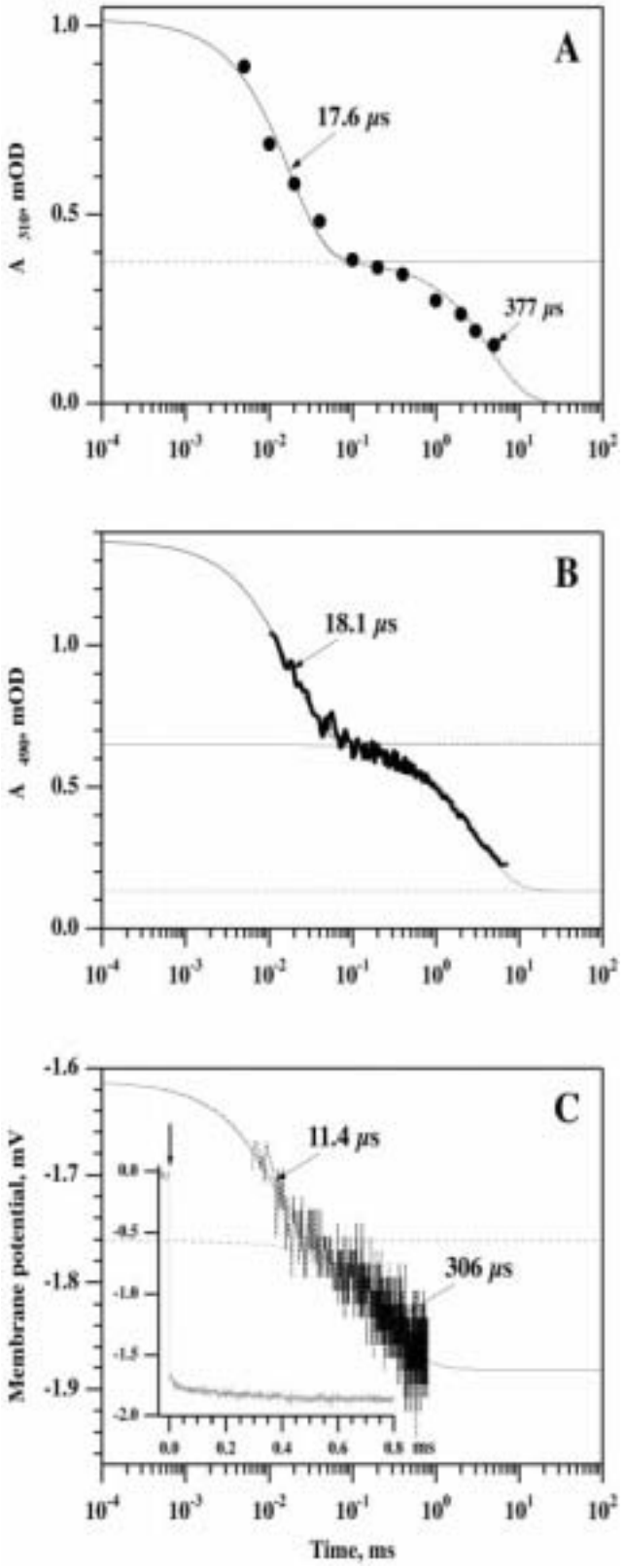
A
17.6 μs
377 μs
A 510, mOD
B
18.1 μs
A 480, mOD
C
11.4 μs
306 μs
Membrane potential, mV
Time, ms

Figure 2.15

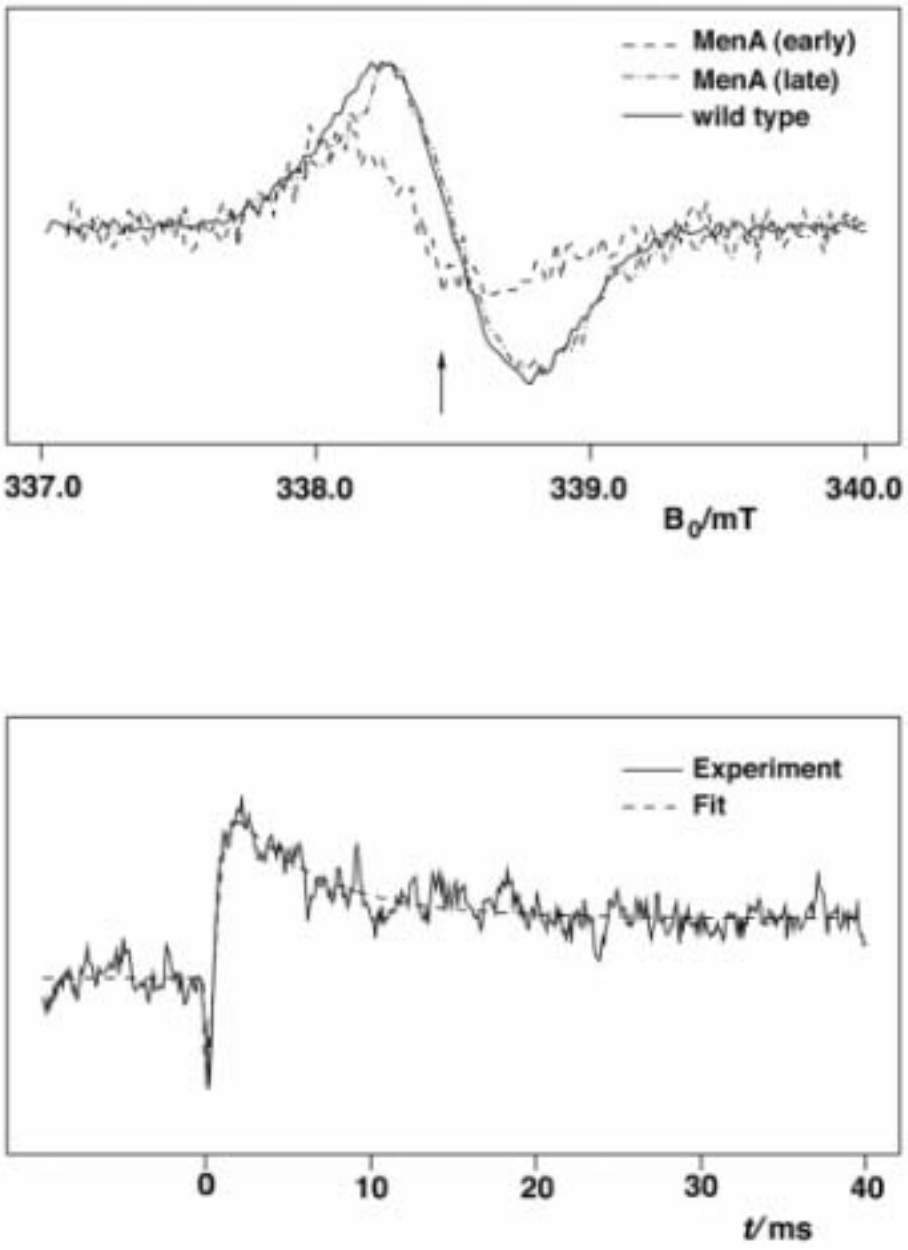
MenA (early)
MenA (late)
wild type
337.0
338.0
339.0
340.0
B0/mT
Experiment
Fit
0
10
20
30
40
t/ms

Figure 2.16

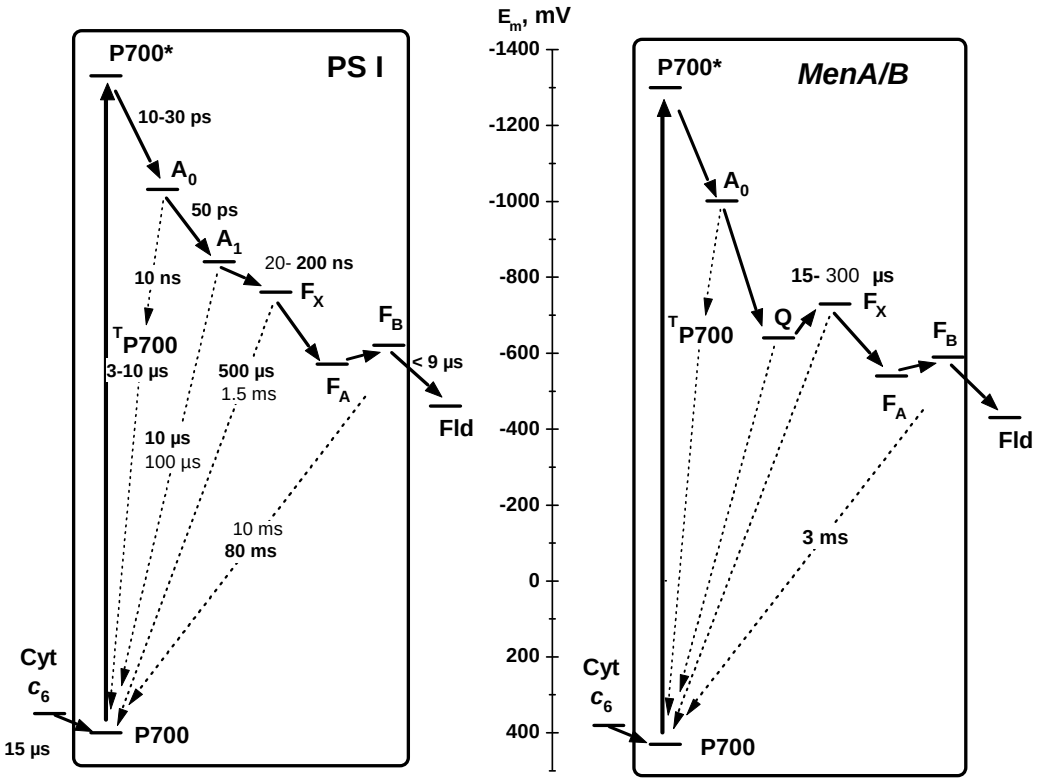
PS I
P700*
10-30 ps
A0
50 ps
A1
20- 200 ns
10 ns
FX
FB
TP700
3-10 µs
500 µs
1.5 ms
< 9 µs
FA
Fld
10 µs
100 µs
10 ms
80 ms
Cyt
c6
15 µs
P700
Em, mV
-1400
-1200
-1000
-800
-600
-400
-200
0
200
400
MenA/B
P700*
A0
15- 300 µs
Q
FX
TP700
FB
FA
Fld
3 ms
Cyt
c6
P700

Figure 2.17

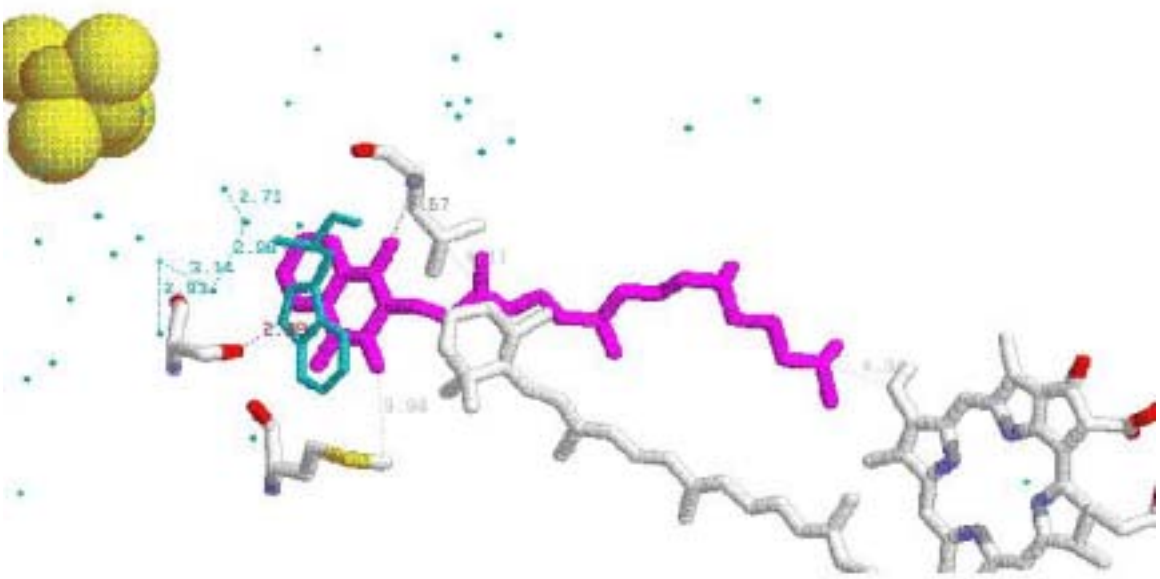

Figure 2.18

Table 2.1 Calculated optimum rates of electron transfer from A_1 to F_X

A_1^-/A_1	F_X^-/F_X	$\Delta G(A_1\text{-}F_X)$	k_{exer}	
$E_{1/2}$, mV	$E_{1/2}$, mV	mV	ns[a]	
			$\lambda = 0.7$[b]	$\lambda = 1.0$[c]
-810[d]	-705[e]	-105	223	1830
-810	-670[f]	-140	148	1180
-810	-650[g]	-150	132	1050
-800[h]	-705	-95	252	2080
-800	-670	-130	166	1340
-754[i]	-705	-49	448	3780
-754	-670	-84	285	2370
-754	-650	-104	223	1830
Mean ± S.D.			223 ± 99	1834 ± 669

[a] ns, nanoseconds

[b] see Moser *et al.,* 1992

[c] see Schlodder *et al.,* 1998

[d] see Vos and Gorkom, 1990

[e] see Chamorovsky and Cammack, 1982

[f] see Parrett *et al.,* 1989

[g] see Shinkarev *et al.,* 2000

[h] see Sétif *et al.,* 1989

[i] see Iwaki and Itoh, 1994

Table 2.2 Deduced values for $E_{1/2}$ of Q

F_X^-/F_X	$\Delta G(Q\text{-}F_X)$		Q/Q^-	
$E_{1/2}$, mV	mV		$E_{1/2}$, mV	
	λ=0.7[a]	λ=1.0[b]	λ=0.7[a]	λ=1.0[b]
-705	+95	+12	-610	-693
-670	+95	+12	-575	-658
-650	+95	+12	-555	-638
Mean ± S.D.			-580 ± 28	-663 ± 28

[a] see Moser *et al.*, 1992

[b] see Schlodder *et al.*, 1998

Chapter 3

Selective Inactivation of the Terminal Acceptors in the Plastoquinone-containing PS I.

ABSTRACT

In the last chapter, it was shown that, when the phylloquinone biosynthetic pathway is altered by interruption of the *menB* gene in *Synechocystis* sp. PCC 6803, plastoquinone-9 occupies the A_1 site in PS I and functions as an electron transfer cofactor from A_0 to the FeS clusters. In this chapter, the redox and kinetic properties of this modified quinone acceptor are described. In order to observe A_1 directly, the terminal FeS clusters F_B, F_A, and F_X were selectively inactivated by various methods: by chemical reduction with dithionite, by physical removal of the PsaC subunit with chaotropic agents, and by genetic interruption of FeS cluster assembly. In the latter case, a *rubA*$^-$ / *menB*$^-$ double mutant of *Synechococcus* sp. PCC 7002 was studied. Inactivation of the particular FeS center was verified by X-band EPR spectroscopy and time-resolved optical spectroscopy in the near-IR region. Through global multiexponential fits of transients in the UV, visible and near-IR regions I obtain the lifetimes of different processes that involve plastoquinone-9 in the A_1 site. Based on spectral analysis of the kinetic components kinetic phases with lifetimes of ca. 10 µs and ca. 500 µs were attributed to the plastoquinone-9$^-$ to P_{700}^+ backreaction. Consequently, two different quinone environments in the *menB* PS I are proposed; each of the environments is caracterized by one of the two lifetimes. Further, the slow kinetic phase with lifetime of ca. 500 µs disappears upon the dithionite treatment, while the fast kinetic phase with lifetime of ca. 10 µs remains unchanged. Thus, the slow kinetic phase is attributed to a high-potential quinone, and the fast kinetic phase, which remains unaffected by dithionite, is attributed to a low-potential quinone.

The *rubA / menB* double mutant of *Synechococcus* sp. PCC 7002 was provided by Yumiko Sakuragi, Gaozhong Shen and Donald Bryant. Optical measurements of the kinetic spectra in the UV were performed in collaboration with Bruce Diner.

INTRODUCTION

The work in this chapter is aimed at understanding the functional chemistry of the quinone acceptor A_1. The general approach to studying A_1 involves replacement of the phylloquinone in PS I with foreign quinones of different redox and structural properties that are nevertheless able to transfer electrons to the FeS clusters. In the previous chapter, I demonstrated that the interruption of the *menB* gene - which codes for dihydroxynaphthoic acid synthase - terminates phylloquinone biosynthesis. As a result, PS I complexes isolated from the *menB* knockouts contain plastoquinone-9 as a functioning A_1 acceptor. For plastoquinone-containing PS I, a global multiexponential analysis of time-resolved optical spectra in the blue showed three kinetic components: i) recombination between P_{700}^+ and FeS^- in the absence of methyl viologen with a 3-ms lifetime; ii) electron transfer to methyl viologen with a 750-μs lifetime; iii) electrochromic shift of a carotenoid pigment with a 15-μs lifetime. Kinetic measurements at 315 nm, along with electrometric measurements showed biphasic kinetics with lifetimes of ca. 15 μs and 250-μs; both of these kinec phases had spectral characteristics of a semiquinone anion radical. Based on these observations, the redox potential of the plastoquinone-9 in the A_1 site was estimated to be more oxidizing than the potential of phylloquinone in the A_1 site and that the electron transfer to F_X is thermodynamically unfavorable.

Selective inactivation of the terminal FeS clusters had been employed successfully for the studies of F_X and A_1 in wild-type PS I (Jung *et al*., 1995; Brettel and Golbeck, 1995; Warren *et al*., 1993). FeS cluster F_B can be inactivated by treatment with mercury chloride (Jung *et al*., 1995). Treatment of wild-type PS I complexes with dithionite results in the reduction of F_A and F_B and, in some cases, F_X. An alternative method of inactivating the FeS clusters is physical removal of PsaC with chaotropic agents, such as urea (Parrett *et al*., 1989). The result of this treatment is a PS I preparation that lacks F_A and F_B (a so-called 'F_X-core'). Addition of an oxidizing agent such as ferricyanide to this preparation in the presence of 2 M urea effectively destroys F_X (Warren *et al*., 1990). In the current study, these methods have been used to selectively

inactivate the FeS centers in order to characterize the redox chemistry of the acceptors in plastoquinone-containing PS I. One possible limitation of this approach is that chemical inactivation can lead to a heterogeneous preparation, which can be more difficult to analyze.

These biochemical methods were complimented with genetic inactivation of FeS assembly. This is achieved by interruption of the *rubA* gene in *Synechococcus* sp PCC 7002 (Shen, Zhao *et al*., 2002; Shen, Antonkine *et al*., 2002). The *rubA* gene is required for the assembly of the F_X iron-sulfur cluster, but F_X is not required for the biosynthesis of trimeric P_{700}-A_1 cores in *Synechococcus* sp PCC 7002 (Shen, Antonkine *et al*. 2002). Following the same approach but inactivating both the *rubA* and the *menB* genes, PS I complexes were isolated that contained plastoquinone-9 and were devoid of FeS centers.

Spectral analyses of the kinetics of backward electron transfer in PS I preparations in which some or all FeS were inactivated, enabled the determination with a high degree of certainty, of which phases in the decay kinetics are associated with oxidation of the semiplastoquinone. In the previous chapter, an intristic relationship between the midpoint potential of the A_1 acceptor and the rates of electron transfer was demonstrated (see also Shinkarev *et al*., 2002 for a detailed analysis of the energetics in plastoquinone-containing PS I). Here, these studies have been expanded by considering the possibility that the two plastoquinones in *menB*$^-$ PS I differ in their midpoint potentials, and thereby give rise to two different kinetic phases in electron transfer.

MATERIALS AND METHODS

Preparation of PS I complexes lacking PsaC

The PS I-F_X core preparations were isolated from the P_{700}-F_A/F_B complexes by treatment with 6.8 M urea at 24 C°, at concentration of 0.2 mg chlorophyll ml^{-1} (Parrett *et al*., 1989). Quality of the preparation was tested by X-band EPR spectroscopy.

Oxidative degradation of F_X

The P_{700}-A_1 cores were produced by treating the P_{700}-F_X cores with 2 M urea and 5 mM potassium ferricyanide at 24 C° at concentration of 0.1 mg chlorophyll ml^{-1} according to (Warren *et al*., 1993). Quality of the preparation was tested by X-band EPR spectroscopy; no EPR signals that could be attributed to the FeS clusters were seen.

Near-IR Spectrophotometry

PS I complexes for the optical measurements were diluted with anaerobic 50 mM Tris/HCl pH 8.3 buffer to the final 50 μg chlorophyll ml^{-1} (ca. 0.5 μM of P_{700}). Sodium ascorbate and DPIP were added to the final concentrations of 2 mM and 5 μM. β-DM was added (0.04%) to reduce light scattering. Dithionite (Sigma, St. Louis, MO) was added before the measurements, as indicated.

Absorbance changes in the near-IR were measured using a laboratory-built differential spectrophotometer (Vassiliev et al., 1997). The HF roll-off amplifier described in the original specification was not used to ensure resolution of the kinetic phases in the sub-microsecond range. The measuring beam was provided by a tunable titanium-sapphire laser equipped with two sets of mirrors, which allowed measurements in the 700nm to 900 nm range.

Excitation flash energy was regulated by a Hewlett Packard delay generator tuning the Q-switch of the YAG laser and the set of neutral filters, which allowed an energy range from 0.5 mJ to 80 mJ. Absorbance transients in the 700 nm to 900 nm region within 5 nm step were obtained at 2 mJ excitation flash intensity, to minimize the antenna chlorophyll contribution. To obtain the dependence of the signal intensity from

the excitation flash energy measuring beam was set to 810 nm and the excitation flash energy was varied from 1 mJ to 80 mJ. The collected transients were analyzed using a global multiexponential fit routine. Point-by-point difference spectra were extracted from the original transients in the 700 nm to 900 nm region and analyzed with *Igor Pro* v 3.1 (Wavemetrics).

Visible Spectrophotometry

Measurements were made with a laboratory-built pulse-probe spectrometer in the blue and green regions on the different preparations of the plastoquinone-containing PS I complexes. Excitation flashes at intervals of 2.5 s were provided by an OPO laser at 685 nm to allow complete reduction of P_{700}^{+}. The measuring light source was a xenon flash-lamp filtered by a monochrometer. The sample was placed in a 10-mm x 10-mm quartz cuvette perpendicular to the direction of the excitation flash. Each data point represents the average of sixteen measurements

UV-spectrophotometry

Optical studies in the UV were conducted using a pulse-probe spectrometer (Diner, B.A., 1998). The monochromator slit was fixed at 4 mm, equivalent to a bandwidth of 8 mm. Measurements in the UV were performed using a xenon flashlamp filtered by a Schott and a Kodak Wratten 34 as the actinic source. The photodiodes were protected with Corion Solar Blind UV-transmitting filters. The optical path length of the cuvette was 1 cm. Each data point represents the average of eight measurements, taken with a flash spacing of 20 s. A background measurement was taken in a similar fashion, except that the sample was shielded from the detecting flash to allow for correction of the actinic flash artifact. The absorbance shown represents the difference between the two measurements.

CW EPR Spectroscopy of the mutant PS I complexes at Q-band

Photoaccumulation experiments were performed using a Bruker ER300E spectrometer equipped with an ER 5106-QT resonator with an opening for in-cavity illumination. Low temperatures were maintained with an ER4118CV liquid nitrogen cryostat and ER4121 temperature controller. The microwave frequency was measured with a Hewlett-Packard 5352B frequency counter, and the magnetic field was measured with a Bruker ER035M NMR Gaussmeter.

Prior to photoaccumulation, the pH of the sample was adjusted to 10.0 with 1.0 M glycine buffer, and sodium dithionite was added to a final concentration of 50 mM. After incubation for 10 min in the dark, the sample was placed into the resonator and the temperature was adjusted to 210 K. The sample was illuminated with a 20 mW He-Ne laser at 630 nm for 30 min. The dark background was subtracted from the photoaccumulated spectra.

CW EPR Spectroscopy of the mutant PS I complexes at X-band

EPR spectra of the photoaccumulated FeS centers in the *menB* and *menA* mutants were obtained using the Bruker ESR 300 instrument equipped with an Oxford temperature controller and liquid helium transfer line. For the measurements of the reduced F_A^- and F_B^- clusters the instrument conditions were set as follows: microwave power, 20 mW, temperature, 15 K, modulation amplitude, 10 G. For the measurements of the reduced F_X^- cluster, the microwave power was set to 80 mW, temperature was set to 6 K, and the modulation amplitude was set to 20 G. The sample conditions were as follows: dithionite, 50 mM; 50 mM Tris buffer, pH 8.3; 0.6 mg chlorophyll ml^{-1}.

Data Analysis

The multiexponential fits of optical kinetic data were performed on a G3/300 Apple computer by the Marquardt algorithm in *Igor Pro* v 3.14 (Wavemetrics). For global analyses in the visible region, individual kinetics were analyzed first. The results of these analyses were used for fitting the whole set of data to global lifetimes, and the

best solution was chosen based on the analysis of χ^2, standard errors of the parameters, and the residuals.

RESULTS

Reduction of the mutant plastoquinone-containing PS I with dithionite

In these experiments, I used the dithionite reduction approach to inactivate the terminal FeS clusters. Previously, in wild-type (phylloquinone-containing) PS I, this method was used successfully to study redox and kinetic properties of the F_X cluster (Shinkarev. *et al*., 2002). Upon addition of dithionite to wild-type PS I complexes, the decay kinetics observed in the near-IR showed a major kinetic phase with a lifetime of ca. 0.5 ms; this is due to the F_X backreaction. Minor kinetic phases with lifetimes 10 µs to 100 µs, which are characteristic of the phylloquinone backreaction, were also usually observed.

Surprisingly, I did not observe the F_X backreaction in the *menB*$^-$ and *menA*$^-$ (plastoquinone-containing) PS I that was treated with dithionite. The expected 0.5 ms phase was absent and fast phases with lifetimes of ca. 100 ns and 5 µs were observed instead. Fig. 3.1 shows a typical result after dithionite reduction. The multiexponential fit in this case resulted in major kinetic phases with lifetimes 100 ns, 3 µs, 8 µs, and a minor phase with a lifetime of 70 µs. The goal was to properly assign these kinetic phases to meaningful physical processes within PS I. Here, I employ spectrophotometry in several regions of the light spectrum - UV, blue, green, and near-IR - to obtain differential spectra of the individual components. The reduction of the PS I acceptors is verified by X- and Q-band EPR spectroscopy.

Excitation flash energy dependence in menB$^-$ PS I *complexes treated with dithionite*

This experiment allowed the identification of relevant processes, namely those that involve P_{700}. It was expected that kinetic phases associated with antenna chlorophyll decay would not saturate at the available excitation flash energies, whereas processes that involve P_{700} would saturate. P_{700} processes include backreactions from each of the PS I acceptors as well as $^TP_{700}$ decay to the ground state. The measurements were taken at 820 nm, a wavelength at which both P_{700} and antenna chlorophyll absorb rather weakly (the extinction coefficient for P_{700} is 6500 M^{-1} cm^{-1} at 830 nm), which would prevent over-

oxidation of the sample. Fig. 3.2 depicts the results of a global multiexponential fit of the transients obtained at several excitation flash energies for the *menB*$^-$ PS I complex treated with dithionite. Major kinetic phases found, were essentially the same as in Fig. 3.1, with the exception that the 3 µs and 8 µs phases merged into one 5 µs phase. The kinetic phase with a lifetime of 44 µs correlates with the 70 µs phase in Fig. 3.1. The slower 476 µs kinetic phase becomes apparent only at higher excitation flash energies.

From Fig. 3.2 it is noted that kinetic phases with lifetimes of 100 ns (open circles), 5 µs (solid circles), 44 µs (solid triangles) show similar saturation behavior; while the 476 µs phase (solid squares) does not saturate as readily. Hence, I concluded that the 476 µs kinetic phase involves relaxation of the antenna chlorophyll triplet. Usually, the 100 ns lifetime is attribute to the A_0^- P_{700}^+ backreaction, as reported in Warren, Parrett *et al*., 1990; the 5 µs lifetime is close to reported values for the $P_{700}/^TP_{700}$ relaxation. To further distinguish between these processes, I performed spectral analysis in the near-IR, using low excitation energy (2 mJ) to minimize the contribution of the slow kinetic phase.

Global Multiexponential Analysis of Optical Spectra in the Near–IR region for the menB$^-$ *PS I reduced with dithionite*

Fig. 3.3 A depicts spectra obtained at 720 nm to 900 nm by global multiexponential analysis of the kinetics in the *menB*$^-$ PS I complexes reduced with dithionite. Four distinct components are present. The spectrum of the fastest component with a 125 ns lifetime (*solid circles*) has a broad maximum at 760 nm to 790 nm and a rapid decline at about 795 nm, which is in good correlation with the spectrum reported in Warren, Parrett *et al*. (1990) for the 30 ns phase of the backreaction in a P_{700}-A_0 core (a PS I complex in which all acceptors but A_0 are deleted). Two components with lifetimes of 2.5 µs and 8 µs show similar spectra with the exception that the spectrum of the 2.5 µs component has a crossover point around 730 nm. Minor kinetic phases with lifetimes of 40 µs to 500 µs are represented by the one component with an average lifetime of 152 µs in this analysis.

Fig. 3.3 B depicts selected individual traces at 815 nm, 730 nm, and 721 nm. The trace at 721 nm definitely shows that the 2.5 µs kinetic phase is different in nature from the 8 µs kinetic phase, in that it has negative absorbance changes (notice the slight "dip" around 3 µs). Therefore, the fit in Fig. 3.1, which shows two components of 3 µs and 8 µs, is closer to reality than the global fit shown in Fig. 3.2. In the latter case, I failed to distinguish between the two components, and they are approximated by the single lifetime of 5 µs.

Based on the three experiments presented above, I can now assign individual phases, the assignments of which are supported by lifetime values and spectral features. The kinetic phase with the 100 ns lifetime represents the P_{700}^{+} A_0^{-} backreaction; kinetic phase with the 2.5 µs lifetime represents the relaxation of the $^{T}P_{700}$ to the ground state; the kinetic phase with the lifetime of 8 µs represents the A_1^{-} P_{700}^{+} backreaction.

The assignment of the major nanosecond kinetic phase to the A_0^{-} P_{700}^{+} backreaction is supported by the observation that the overall amplitude of the signal at 820 nm increases from about 3 mOD in the non-reduced complexes to more than 6 mOD in the dithionite-treated sample. This behavior was expected because A_0/A_0^{-} has significant absorbance changes at 820 nm and that adds to the P_{700}/P_{700}^{+} spectrum. The assignment of the kinetic phase with the 2.5 µs lifetime to the $^{T}P_{700}$ relaxation is based on the previously reported value for this process (3 µs, according to Sétif, 1989). Note also that the spectral shape of the 2.5 µs component is different from the spectral shapes of the 100 ns and 8 µs components. The former crosses over at 730 nm, which is most likely due to the $P_{700}/^{T}P_{700}$ difference spectrum.

Slower kinetic phases with lifetimes of 40 µs to 500 µs are more difficult to assign, because of their relatively weak contribution to the overall signal amplitude. The kinetic phase with a lifetime of 476 µs became prominent only at higher excitation energies, and as was mentioned previously, is probably due to the antenna chlorophyll triplet relaxation. This is close to the value of 0.5 ms reported by Shuvalov for this process (Shuvalov *et al.*, 1976). Kinetic phases with lifetimes 40 µs to 150 µs can be attributed to A_1^{-} and F_X^{-} backreacting with P_{700}^{+}.

EPR characterization of the reduced mutant plastoquinone-containing PS I complexes

Both semiplastoquinone and F_X^- can be photoaccumulated at low temperature in *menB*$^-$ and *menA*$^-$ PS I complexes reduced with dithionite. When strictly dark conditions were maintained during sample preparation, no detectable levels of semiplastoquinone and F_X^- were found. At cryogenic temperatures, the dark sample exhibited a typical F_A^-/F_B^- interaction spectrum. When the sample is illuminated for 10 min to 15 min at 200 K or 7 K, the semiplastoquinone radical or F_X^- can be detected, respectively. This is demonstrated in Fig. 3.4 A, B. Fig. 3.4, A, a shows photoaccumulated spectrum at 7 K, in which the feature at $g = 1.76$ corresponds to F_X^-. The sharp line at $g \sim 2.00$ corresponds to a mixture of P_{700}^+ and the semiplastoquinone anion radical. When the photoaccumulation experiment was performed at 200 K at Q-band, a typical semiplastoquinone anion radical spectrum was observed (Fig. 3.4 B).

Global decomposition of kinetic transients in dithionite-treated menB$^-$ *PS I in the blue region*

Fig. 3.4 shows a global multiexponential fit of the kinetic transients in the 400 nm to 500 nm region. The best fit was obtained using two exponents with 11 µS and 1.2 ms lifetimes, respectively. The major kinetic phase had a lifetime of 11 µs and the spectral shape of an asymmetric derivative; with a minimum at 430 nm, a shoulder around 455 nm, a crossover point at 474 nm and a broad maximum at 480 nm to 495 nm. The contribution of the kinetic phase with a 1.2 ms lifetime is rather minor and its spectral shape resembles the P_{700}/P_{700}^+ difference spectrum, with a minimum around 430 nm and a 450 nm crossover. The question of why the 11 µs kinetic phase does not show a defined P_{700}/P_{700}^+ spectrum in the blue region will be addressed later.

Chaotropic removal of F_A and F_B by urea in plastoquinone-containing PS I complexes

The drawback of the reductive inactivation protocol is that the redox potentials of the preceding cofactors can be altered through electrostatic interaction with reduced F_A and F_B (see Brettel, 1997). The altered potentials would cause altered kinetic properties, and the obtained τ values would not be accurate. Hence, I used an alternative approach in

which the PS I subunit PsaC, which harbors F_A and F_B, was removed by treatment with 7 M urea. This approach has been successfully used for removing PsaC from wild-type PS I complexes (Golbeck, Parrett *et al*., 1988; Golbeck, Parrett *et al*., 1987; Golbeck, Mehari *et al*., 1988; Parrett, Mehari *et al*., 1989). The removal of PsaC is accomplished by incubation of the PS I complexes with 7 M urea, while monitoring the backreaction kinetics in the near-IR.

During the course of the reaction, the ca. 30 ms kinetic phase representing back donation from F_A^-/F_B^- disappears, and the faster phases with lifetimes ranging from 0.1 ms to 1 ms appear (Fig. 3.6). The *men*B-F_X core prepared by this method was treated with dithionite, and the results were quite similar to the results of dithionite treatment of the intact *menB*-PS I complex (Fig. 3.7). When the chemical reduction is performed anaerobically, generally more dithionite is needed to achieve the same result in the *men*B-F_X core. Qualitatively, the results of dithionite reduction in the case of the *menB*-F_X core and the *menB*$^-$ PS I complex were the same. This was somewhat surprising, since the potential of F_X is lower than the potentials of F_A/F_B, and usually this cofactor cannot be reduced with dithionite at pH 8.3. A possible explanation is that dithionite reduces plastoquinone rather than F_X, and this explains the appearance of the A_0 to P_{700}^+ backreaction in the 820 nm measurement. When *menB*$^-$ PS I complexes are treated with dithionite, reduced F_X is barely visible in the dark sample, and becomes apparent only after photoaccumulation (Fig. 3.8). The magnetic properties of the F_X cluster in plastoquinone-containing PS I (Fig. 3.8 A) are somewhat different from wild-type PS I (Fig. 3.8 B), especially in terms of decreased anisotropic linewidths and higher g_y values. This is an interesting finding, and it suggests that the phylloquinone-to-plastoquinone replacement affects the F_X cluster, which is located 14 Å distant.

Global decomposition of kinetic transients in the blue region

Global multiexponential analysis of the kinetic transients of the *men*B-F_X core in the blue resulted in three kinetic components with lifetimes of 10 µs, 81 µs and 473 µs, respectively. Fig. 3.10 A shows kinetic spectra in the 400 nm to 500 nm region. The components with 81 µs and 473 µs lifetimes show typical P_{700}^+/P_{700} difference spectra

with a minimum at 430 nm, a crossover around 442 nm, a small maximum at 445 nm, a small minimum at 460 nm and a broad maximum at 480 nm to 500 nm. The spectrum of the 10 µs kinetic phase shows more of a derivative shape, in which the intermediate maximum at 445 nm is not very prominent and the crossover point is shifted to 460 nm.

Addition of the external acceptor methyl viologen to the *men*B-F_X core preparation results in the kinetic spectrum shown in Fig. 3.10 B. The long-lived component is the P_{700}/P_{700}^{+} difference spectrum and the kinetics are DCPIP concentration-dependent. The component with the lifetime of 220 µs has a derivative-shaped spectrum with a broad 420 nm to 440 nm minimum, a crossover point at 460 nm and a maximum around 480 nm. The component with the lifetime of 11 µs has a crossover point further shifted to 470 nm and an even broader minimum of 420 nm to 440 nm.

Absorbance changes in the UV region of the menB-F_X core

Flash-induced absorbance changes due to semiplastoquinone minus plastoquinone can be observed in the near-UV. Fig. 3.11 shows the absorbance changes at 310 nm for the *menB*-F_X core; these can be fitted to decay kinetics with lifetimes ranging from 15 µs to 1 ms. This indicates that the quinone component contributes to all the kinetic phases observed in the *men*B-F_X core preparation.

Inactivation of the FeS clusters in the plastoquinone-containing PS I by genetic removal

Removal of PsaC with urea often results in heterogeneous preparations, indicating that some parts of the PS I complex may be damaged due to this chaotropic treatment. The finding that rubredoxin is required for the *in vivo* assembly of F_X in cyanobacteria (Shen *et al.,* 2002) provides an alternative method for preparing PS I complexes in which the FeS clusters are absent. The interruption of the *rubA* gene in a *menB* mutant background results in a *menB*-A_1 core *in vivo*. Because of the absence of contributions from F_X, F_A and F_B, it is possible to observe kinetic phases specific to electron transfer processes involving plastoquinone (Figs. 3.12-2.15).

Absorbance changes at 810 nm in rubA⁻ / menB⁻ PS I complexes

Fig. 3.12 B shows decay kinetics measured at 820 nm in *rubA*⁻ / *menB*⁻ PS I complexes. When all three FeS centers are absent, charge recombination occurs between P_{700}^{+} and A_1^{-} after a single turnover flash. The best fit was obtained using a stretched multiexponential routine, which resulted in kinetic phases with lifetimes of 1.3 µs, 10 µs and 315 µs and stretched parameters of 0.92, 0.97 and 0.74, respectively. The kinetic phase with a lifetime 315 µs is the major contributor (ca. 70%) to overall signal amplitude. In several cases, very fast nanosecond phases can be seen, the contribution of which varies from preparation to preparation. The fast nanosecond phases are most probably due to the loss of plastoquinone-9 during isolation. In PS I complexes in which plastoquinone is absent, the P_{700}^{+} A_0^{-} charge recombination is observed.

Global decomposition of kinetic transients at 810 nm, obtained at several excitation flash energies, in the rubA⁻ PS I complexes and rubA⁻ / menB⁻ PS I complexes

In order to rule out possible contributions to the absorbance changes by antenna chlorophyll triplet relaxation, I studied the flash-saturation profile in the near-IR. Lifetimes reported previously for this process range from the tens-of-microseconds (Brettel and Golbeck 1995; Vassiliev, Jung *et al*., 1997) to the hundreds-of-microseconds (Shuvalov, 1976). Fig. 3.13 shows the saturation profile for *rubA*⁻ PS I complexes (panel A) and *rubA*⁻ / *menB*⁻ PS I complexes (panel B).

The results of the global multiexponential fit did not always match the fit obtained just for one transient; certain kinetic phases became apparent at different excitation energies. For the *rubA* mutant, the global fit correlates rather well with the fit shown in Fig. 3.12 A. All three kinetic phases are present, and the lifetimes obtained in this analysis are 11 µs and 81 µs for the major kinetic phases and 905 µs for the minor kinetic phase. All three kinetic phases shows a similar saturation profile, but the kinetic phase with the lifetime of 11 µs saturates at higher flash energies, indicating that antenna chlorophyll triplet relaxation contributes in the tens-of-microsecond region in this mutant. The flash-energy saturation profile for the *rubA / menB* double mutant is presented in Fig. 3.13 B. In addition to the kinetic phases shown in Fig. 3.12 B, kinetic phases with

lifetimes of 136 ns and 800 µs are present. The nanosecond kinetic phase represents the back donation from A_0^- to P_{700}^+ in those complexes from which plastoquinone is lost. All kinetic phases show a similar saturation profile, and there is no apparent contribution from the antenna chlorophyll triplet relaxation.

Global decomposition of optical kinetic spectra of rubA⁻ / menB⁻ PS I complexes in the blue and green regions

Study of the wavelength dependence of absorbance changes in the visible region can show which kinetic phases are derived from the P_{700}/P_{700}^+ difference spectrum, as well as from possible band-shifts of pigments in close proximity to the quinone acceptor. PS I contains 13 carotenoid molecules which function to quench excessive energy. Most probably, quenching occurs by accepting excitation energy from a chlorophyll triplet, forming the metastable carotenoid triplet (^{T}Car). The metastable ^{T}Car was formed with a lifetime of 25 ns and it decayed with a lifetime of 3 µs in whole Chlorella cells and in chloroplasts (Witt, 1971). The spectrum associated with decay of this metastable carotenoid state is characterized by three negative peaks in the blue, at 430 nm, 460 nm and 490 nm, as well as by a large positive peak at 520 nm (Witt, 1971). Study of absorbance changes in the green, therefore, allows one to eliminate any contribution from this decay process.

Fig. 3.14 depicts a two-exponential global fit of the flash-induced kinetic transients in the 380 nm to 600 nm region for the wild-type, *menB* mutant, and *rubA⁻ / menB⁻* PS I complexes. Kinetic spectra of the *rubA⁻ / menB⁻* PS I complexes (Figure 2.14 C) consist of two major components with lifetimes of 10 µs and 580 µs, respectively. The component with a lifetime of 10 µs has a derivative-shaped spectrum with a broad shoulder at 380 nm to 400 nm, a broad minimum at 420 nm to 440 nm, a shoulder around 455 nm, a crossover point at 470 nm and a maximum at 520 nm The low-abundance component, with a lifetime 580 µs, has a derivative-shaped spectrum with a shoulder at 380 nm to 400 nm, a sharp minimum at 425 nm, a crossover point at 440 nm and a maximum at 460 nm; this is typical of the P_{700}/P_{700}^+ difference spectrum. A similar situation is observed in the *men*B mutant PS I complexes, in which two kinetic phases of

different spectral shapes are also present, with 10 µs and 2 ms lifetimes (Fig. 3.14 B) The kinetic phase with lifetime 2 ms reflects the backreaction of the FeS centers; it is an admixture of P_{700}/P_{700}^{+} and $[FeS]^{-}/[FeS]$ difference spectra (Semenov, Vassiliev *et al.*, 2000). The 10 µs kinetic phase is associated with plastoquinone and shows a striking resemblance to the spectrum observed in the *rubA / menB* mutant. It may reflect both forward donation to the FeS clusters and backward donation to the P_{700}^{+} from A_1^{-}.

The absorbance changes in the blue and green for wild-type PS I complex are shown in Fig. 3.14 A. The major kinetic phase has a lifetime of 130 ms and is most definitely associated with the backreaction from F_A^{-} and F_B^{-}. The minor kinetic phase, with lifetime of ca. 400 µs reflects the backreaction from the F_X^{-} cluster. The fast kinetic phase with lifetime of 8 µs has significant absorbance at 520 nm, it is very similar to the ^{T}Car decay spectra reported by Witt (1971). In the intact wild-type PS I complexes, no phylloquinone backreaction is observed, hence the 8 µs phase represents a pure ^{T}Car relaxation. Most likely are three species that contribute to the fast (tens-of-microsecond) process in the case of the *rubA / menB* double mutant: P_{700}/P_{700}^{+}, Car/^{T}Car, and probably a pigment band-shift.

Kinetic spectra of the rubA^{-} / menB^{-} PS I *complexes in the UV region*

If charge recombination occurs between P_{700}^{+} and semiplastoquinone in the *rubA / menB* double mutant, then the kinetics of A_1^{-} oxidation measured in the UV should match that of P_{700}^{+} reduction determined at 820 nm. Measuring the wavelength dependence in the UV should also produce a semiplastoquinone/plastoquinone difference spectrum that matches the one obtained previously for the *men*B mutant in chapter 2. Fig. 3.15 A shows a point-by-point difference spectra of absorbance changes taken 15 µs, 300 µs and 1 ms after a saturating flash. The spectra have a derivative shape with a crossover point at 290 nm, which is more than 10 nm shifted to the red than previously reported for the *men*B mutant (dotted line). This reflect a subtle structural difference in the plastoquinone-containing PS I complex that is also devoid of the FeS clusters. This slight change in the spectral shape might also be attributable to an increase in the hydrophobicity of the quinone binding site upon the loss of the FeS clusters A similar red-shift of the crossover

point is observed between plastoquinone-9 in methanol and plastoquinone-9 in PS II complexes (Fig. 3.15, *B*). Fig. 3.15 *C* shows the decay kinetics at 315 nm fitted to two exponentials. The fit results in two kinetic phases with lifetimes of 15 µs and 390 µs, which correlate well with P_{700}^{+} reduction monitored at 820 nm (Fig. 3.12, *A*).

Description of the kinetic phases in the mutant plastoquinone-containing PS I preparations

The results presented above are summarized in Table 3.1. Since different spectrophotometric techniques with different time resolutions were used for different spectra regions, the number and values of the exponential components vary among experiments. Consequently, the lifetimes reported in Table 3.1 for four types of PS I preparation represent averages of the lifetimes obtained through analysis of their kinetic spectra in the near-IR, UV, and visible regions.

The major components are relatively similar from preparation to preparation. All of the preparations show a fast kinetic phase with lifetime of 10 µs to 15 µs. The visible spectrum is derivative-shaped, has a minimum around 430 nm, a crossover point around 465 nm and a maximum at 520 nm. This spectrum is observed in *menB*$^{-}$ PS I complexes reduced with dithionite, in *menB*-F_X cores and in *rubA*$^{-}$ / *menB*$^{-}$ PS I complexes. The fast kinetic phase contributes significantly to absorbance changes in the UV in the cases of the *menB*-F_X core and the *rubA*$^{-}$ / *menB*$^{-}$ PS I complex. Wavelength-dependent measurements in the UV show a typical semiplastoquinone minus plastoquinone difference spectrum. These kinetic phases are matched in the near-IR, where the P_{700}/P_{700}^{+} difference spectrum contributes to the absorbance change. I therefore attribute it to the A_1^{-} to P_{700}^{+} backreaction. The ^{T}Car relaxation in the visible, which occurs with similar microsecond kinetics, obscures the usual P_{700}/P_{700}^{+} difference spectrum in this region and increases the overall amplitude of the fast kinetic phase.

The slow kinetic phases have lifetimes that vary from 400 µs to 800 µs and are also attributable to the A_1^{-} to P_{700}^{+} backreaction. The slow kinetic phases are present in all preparations except *menB*$^{-}$ PS I reduced with dithionite, and they have a contribution from both semiplastoquinone minus plastoquinone and P_{700} minus P_{700}^{+}. There was

significant heterogeneity associated with the slow kinetic phases. This was especially noticeable in the preparation of the *menB*-F_X core: the contribution of the slow kinetic phase to the total absorbance change varied from sample-to-sample. This might be an indication that plastoquinone can be easily lost from its binding site.

The addition of 100 mM methyl viologen to the *men*B-F_X core resulted in two kinetic phases, with lifetimes 10 µs and 220 µs, that did not show the expected P_{700}/P_{700}^{+} contribution in the blue region (Fig. 3.10, *bottom*). The ^{T}Car relaxation contributes to the fast kinetic decay. I attribute these two phases to electron transfer from A_1^{-} and F_X^{-} to methyl viologen.

DISCUSSION

Biphasic photo-induced oxidation of plastoquinone

The main finding of this work is that there exist two kinetic phases associated with the A_1^- to P_{700}^+ backreaction in plastoquinone-containing PS I. This is not a new finding; the biphasic oxidation of A_1^- has been reported previously in wild-type (phylloquinone-containing) PS I complexes. For example, in a PS I core devoid of FeS clusters, two major decay kinetics associated with the A_1^- to P_{700}^+ backreaction were observed with half-times of ca. 10 µs and ca. 110 µs and an amplitude ratio ca. 2.5:1 (Brettel and Golbeck, 1995). Similarly, in the PS I complexes isolated from the *rubA* mutant, two major kinetic phases representing the A_1^- to P_{700}^+ backreaction were observed with the lifetimes 11 µs and 87 µs at an amplitude ratio ca. 1:1 (Shen *et al.*, 2002, see also Fig. 3.12, *A*). The reason for this heterogeneity remains unknown. In the case of plastoquinone-containing PS I, however, one can speculate that the two kinetic phases appear due to the two different plastoquinones each in a different environment. Specifically, the midpoint potentials of these two quinones may differ.

The reason for the difference in the redox properties becomes clear when we consider results of the dithionite treatment of the plastoquinone-containing PS I complex. The slow (hundreds-of-microseconds) phase of plastoquinone oxidation was observed in all *menB*$^-$ PS I preparations except in the dithionite-treated *menB*$^-$ PS I complex. The fast (tens-of-microsecond) phase, however, is present in all preparations, including the dithionite treated PS I complex (Table 3.1). Hence, I attribute the slow kinetic phase to the oxidation of a high-potential quinone which is reducible with dithionite at pH 8.3, and I attribute the fast phase to the oxidation of a low-potential quinone which can not be reduced with dithionite at pH 8.3. The fact that no semiquinone species were detected in the dark in the dithionite reduced sample by the Q-band EPR must also be considered. This would imply double reduction of the plastoquinone; a doubly reduced quinone is diamagnetic and does not have an EPR signal.

Importantly, the double reduction is irreversible and renders the quinone inactive in subsequent electron transfer reactions. In PS I complexes in which the quinone is

doubly reduced, I expected to find the A_0^- to P_{700}^+ backreaction as the major component, because there exists no suitable oxidized electron carrier to accept electrons from A_0^-. This is exactly the case in the dithionite-treated *menB*$^-$ PS I complex. The major kinetic phase has a lifetime of ca. 125 ns, which is characteristic of the A_0^- to P_{700}^+ charge recombination (Fig. 3.1).

In chapter 2, I demonstrated that in the *menB* mutant forward plastoquinone to F_X electron transfer is biphasic with lifetimes ca. 10 µs and ca. 300 µs. I also proposed that A_1 to F_X electron transfer in the *menB*$^-$ PS I is endergonic by +12 to +95 mV. Further treatment of the data led to the estimate of +35 mV for the A_1 to F_X electron transfer (Shinkarev *et al.,* 2002), which fits well with the estimate that was given in chapter 2. These reports did not take into account the possibility that two plastoquinones with different midpoint potentials may both participate in electron transfer. For example, in the calculations of Shinkarev *et al*. (2002), we used 15 µs for the forward electron transfer A_1 to F_X and 100 µs for the backreaction A_1 to P_{700}. These reports treated rates as the "average of the rates of two quinones" (*i.e.* the high and the low potential quinone). For the low potential quinone, both the backreaction to P_{700} and the forward donation to F_X occur in the tens-of-microseconds time range; for the high-potential quinone these reactions occur in the order of hundreds-of-microseconds time range. Forward donation must be faster than the charge recombination for the electron transfer to be efficient. According to my measurement for the high-potential plastoquinone, this condition holds true; forward donation to F_X has a lifetime of ca. 200 µs, whereas backward donation to P_{700}^+ is preparation-dependent and occurs with a 400 µs to 600 µs lifetime. This is not necessarily true for the low-potential quinone, in which the lifetimes for the forward and backreaction routes are rather similar.

The ca. 500 µs difference between the lifetimes of the backreaction would roughly give a ca. 50 mV difference between the midpoint potentials of the two quinones, with the high-potential one being about 70 mV more electropositive than F_X and the low potential one being 20 mV more electropositive than F_X.

Directionality of the electron transfer in the plastoquinone-containing mutant PS I

In phylloquinone-containing wild-type PS I, two structurally different quinone environments can be identified by examining the 2.5 Å X-ray structure (last section of Chapter 1). However there is no consensus on the functional difference between these two quinones (see also chapter 5).

With the identification of the two different quinone environments in plastoquinone-containing PS I, the idea of asymmetric bidirectional electron transfer is reinforced, if the high and low potential quinones were shown to be located in either the PsaA or PsaB binding sites. However, there is no direct evidence to draw such a conclusion. Furthermore, there exists the possibility that electron transfer is bidirectional in plastoquinone-containing PS I, but unidirectional in phylloquinone-containing PS I. I will return to this issue in the Chapter 5, where I will show that for the phylloquinone-containing PS I (wild type) the forward electron electron transfer proceeds predominately through the PsaA-branch.

SUMMARY

The work presented in this chapter points to the presence of two structurally and functionally different quinone environments in plastoquinone-containing PS I. One quinone has relatively low redox potential and is characterized by lifetimes of ca. 10 µs and 15 µs for the forward and backreaction routes of oxidation, respectively. The second quinone has relatively high redox potential and is characterized by lifetimes of ca. 200 µs and 500 µs for the forward and backreaction routes of oxidation, respectively. The high-potential quinone is doubly-reducible with dithionite in the dark at pH 8.3, as judged by disappearance of the slow kinetic phase in the backreaction kinetics in dithionite-treated *menB*$^-$ PS I complexes.

REFERENCES

Benasson, R., and Land, E. J. (1973) *Biochim. Biophys. Acta* **325**, 175-181

Brettel, K. (1997). *Biochimica Et Biophysica Acta-Bioenergetics* **1318**(3): 322-373.

Brettel, K. and J. H. Golbeck (1995) *Photosynthesis Research* **45**(3): 183-193.

Golbeck, J. H., T. Mehari (1988) *Biophysical Journal* **53**(2): A268-A268.

Golbeck, J. H., K. G. Parrett (1987 *Biochimica Et Biophysica Acta* **893**(2): 149-160.

Golbeck, J. H., K. G. Parrett (1988). *FEBS Letters* **228**(2): 268-272.

Jordan P., Fromme P., Witt H. T., Klukas O., Saenger W., Krauβ N. 2001 *Nature* **411**, 909

Moser, C., and Dutton, P (1992) *Biochim. Biophys. Acta* **1101,** 171-176

Moser, C.C., Keske, J. M., Warncke, K., Farid, R.S., and Dutton, P. (1992) *Nature* **355**, 796-802

Nelson N, Ben-Shem A (2002) *Photosyn. Res.* **73** (1-3): 193-26

Parrett, K. G., T. Mehari (1989). *Biochimica Et Biophysica Acta* **973**(2): 324-332.

Gaozhong Shen, Mikhail l. Antonkine, Art van der Est, Ilya R. Vassiliev, Klauss Brettel, Robert Bittle, Stephan G. Zech, Jindong Zhao, Dietmar Stehlik, Donald A. Bryant, and John H. Golbeck. *J. Biol. Chem*, 2002, **277**, 20355

Shen, G. Z. Zhao, J. D. Reimer, S. K. Antonkine, M. L. Cai, Q. Weiland, S. M. Golbeck, J. H. Bryant, D. A. *J. Biol. Chem*, 2002, **277**, 20343

Shinkarev V.P, Zybailov B. L., Ilya R. Vassiliev, and John H. Golbeck (2002) manuscript in preparation

Shuvalov, (1976) *Biochim. Biophys. Acta* **430**, 113-121

van Gorkom, H. (1974) *Biochim. Biophys. Acta* **347**, 439-442

Vassiliev, I. R., Y. S. Jung. (1997) *Biophysical Journal* **72**(1): 301-315.

Warden, J. T. and J. H. Golbeck (1986) *Biochimica Et Biophysica Acta* **849**(1): 25-31.

Warren, P. V., Parrett K. G. (1990) *Biochemistry* **29**(28): 6545-6550.

Witt, H.T. (1971) *Quartely Rev. of Biophys*. **4**, pp. 365-477

FIGURE LEGENDS

Figure 3.1 Absorbance changes at 810 nm in dithionite-treated *menB*$^-$ PS I complexes. *A*, flash-induced optical transient at 810 nm in the *menB*$^-$ PS I complex. The transient represents average of 4 single-flash experiments. Excitation flash energy is 10 mJ. Sample conditions: 50 µg chlorophyll ml^{-1} in 20 mM Tricine, pH 8.2; 0.02% DM, 2 mM ascorbate. *B*, result of the addition of dithionite (1 mM final concentration) to the *menB*$^-$ PS I complex; the transient represents the average of 16 single-flash experiments, all other conditions are the same as in *A*.

Figure 3.2 Global decomposition of kinetic transients at 810 nm obtained at different excitation flash energies in the *menB*$^-$ PS I reduced with dithionite. *Open circles* represent major component with a lifetime of 100 ns; *solid circles* represent component with a lifetime of 5 µs; solid triangles represent component with a lifetime of 44 µs. *Solid squares* represent component with the lifetime 476 µs. *Solid diamonds* represent the baseline.

Figure 3.3 Global decomposition of optical kinetic spectra of *men*B-PS I reduced with dithionite in the near-IR region. ***A*,** spectra of the flash-induced optical transients. *Open circles* represent major component with a lifetime of 100 ns, scaled by 0.35 for the better view. *Solid triangles* represent component with 8 µs lifetime. *Open triangles* show component with a lifetime 3 µs. *Open squares* represent long-lived components with the average lifetime of 152 µs in this analysis. *B*, Individual transients at selected wavelengths. Sample conditions were as follows: *menB*$^-$ PS I complex at 50 µg chlorophyll ml^{-1} in 20 mM Tris, pH 8.2; 0.02% β-DM, 1 mM sodium dithionite. Excitation flash energy is 2 mJ

Figure 3.4 EPR studies of the photoaccumulated paramagnetic centers in the *menB*$^-$ PS I complexes. *A*, X-band EPR spectrum of the FeS centers in *menB*$^-$ PS I after photoaccumulation. Sample conditions were as follows: concentration 0.5

mg chlorophyll ml^{-1}, dithionite 50 mM, illuminated at 77 K outside the cavity, temperature reduced to 7 K, with illumination continued in the cavity. EPR conditions were as follows: microwave power 40 mW, temperature 7 K, modulation amplitude 20 G. *B*, Q-band EPR spectrum of the semiplastoquinone radical photoaccumulated in the *menB*$^-$ PS I complexes. Sample conditions: concentration 0.7 mg chlorophyll ml^{-1}, dithionite, 50 mM, 15 minutes of illumination at 210 K. EPR conditions: microwave power, 1 mW, modulation amplitude 1 G, temperature 210 K.

Figure 3.5 Global decomposition of optical kinetic spectra of *menB*-PS I reduced with dithionite in the blue. *A*, spectra of the flash-induced optical transients. *Solid triangles* represent the component with a lifetime of 11 µS. *Open squares* represent components with average lifetimes of 1.2 ms. *B*, Individual transients at selected wavelengths. Sample conditions: anaerobic *menB*$^-$ PS I complexes at 10 mg chlorophyll ml^{-1} in 10 mM Tris, pH 8.2, 0.02% β-DM, dithionite, 0.1 mM. Instrument conditions: excitation flash energy, 0.7 mJ; 32 flash-probes taken at logarithmically spaced time intervals; each data point is an average of 32 flashes.

Figure 3.6 Removal of F_A and F_B with 7 M urea in *menB*$^-$ PS I complexes**.** Flash-induced optical transients at 810 nm in the PS I complexes after the addition of urea. Individual time points are labeled on the figure. Sample conditions: concentration of 0.2 mg chlorophyll ml^{-1}, Ascorbate 10 mM, DCPIP, 5 µM, 50 mM Tris buffer pH 8.3 (8.7 after the urea addition). Instrument condition: excitation flash energy 12 mJ, each transient represents an average of 4 acquisitions.

Figure 3.7 Addition of dithionite to *menB*$^-$ PS I whole complex and *menB*-F_X core. *A*, result of the aerobic addition of dithionite to *menB*-F_X core. Optical transients at 810 nm are labeled according to the final concentration of dithionite in the sample. *B*, result of the aerobic addition of dithionite to *menB*$^-$ PS I whole complexes. Optical transients at 810 nm are labeled according to the final concentration of dithionite in the sample.

Figure 3.8 Low-temperature EPR spectra of the photoaccumulated F_X acceptor in the *menB*$^-$ F_X core. *A,* EPR spectra of F_X in wild-type F_X core. *Top trace* represents dark spectrum, *middle trace* represents light spectrum; *bottom trace* represents photoaccumulated spectrum. *B,* EPR spectra of F_X in *menB*-F_X core. *Top trace* represents dark spectrum; *middle trace* represents light spectrum; *bottom trace* represents photoaccumulated spectrum. Sample conditions in *A*, *B* : 0.5 mg chlorophyll ml^{-1}, dithionite, 100 mM, Tris buffer, 50 mM, pH 8.3. EPR conditions: temperature, 6.3 K, microwave power, 126 mW, modulation amplitude, 20 G

Figure 3.9 Global decomposition of kinetic transients at 810 nm obtained at different excitation flash energies in the *men*B F_X core complexes. *Open squares* represent component with a lifetime of 28 µs; *solid triangles* represent component with a lifetime of 3 µS; solid triangles represent component with a lifetime of 44 µS. *Crosses* represent a component with a lifetime of 825 µS and *solid diamonds* represent the baseline

Figure 3.10 Global decomposition of optical kinetic spectra of the *men*B-PS I with F_A and F_B removed by urea. *A,* Spectrum in the absence of methyl viologen. *Open circles* represent component with a lifetime of 10 µS, *Open squares* represent component with a lifetime of 81 µS; *Open triangles* represent component with a lifetime of 473 µS. *B,* spectrum measured in the presence of 100 mM methyl viologen. *Open squares* represent long lived component (sensitive to DPIP concentration); *Open triangles* represent component with a lifetime of 220 µS; *Open circles* represent component with a lifetime of 11 µS.

Figure 3.11 Absorbance changes in the UV region of the *menB*-F_X core. The shown trace represents the decay kinetics at 310 nm

Figure 3.12 Absorbance changes at 810 nm in *rubA*$^-$ / *menB*$^-$ PS I complexes. *A,* flash-induced optical transient at 820 nm in the *rubA*$^-$ PS I complex. The transient represents average of 16 single-flash experiments. Excitation flash energy, 3 mJ. Sample conditions:

50 µg chlorophyll ml^{-1} in 20 mM Tricine, pH 8.2; 0.02% DM, 2 mM ascorbate. *B,* flash-induced optical transient at 810 nm in the *rubA*$^-$ / *menB*$^-$ PS I complex; conditions are the same as in *A.*

Figure 3.13 Global decomposition of kinetic transients at 810 nm obtained at different excitation flash energies in the *rubA*$^-$ PS I complexes and *rubA*$^-$ / *menB*$^-$ PS I complexes. *A*, Flash energy dependency of the *rubA*$^-$ PS I complexes. *Solid circles* represent component with a lifetime of 11 µs; *solid triangles* represent component with a lifetime of 81 µS, *solid squares* represent minor component with a lifetime of 905 µs. *Solid diamonds* represent the baseline. *B,* Flash energy dependence of the *rubA*$^-$ / *menB*$^-$ PS I complexes. *Checked circles* represent components with a lifetime of 136 ns, *solid circles* represent component with a lifetime of 28 µs, *open triangles* represent component with a lifetime of 3 µs, *solid squares* represent component with a lifetime of 300 µs, *open squares* represent the component with a lifetime of 800 µs, *solid diamonds* represent the baseline.

Figure 3.14 Global decomposition of optical kinetic spectra of PS I complexes in the blue and green**.** *A*, kinetic spectra of the wild-type PS I complexes. *Checked squares* represent component with a lifetime of 130 ms, *open triangles*, represent component with a lifetime of 390 µs, *solid circles* represent component with a lifetime of 8 µs. *B,* kinetic spectra of the *menB*$^-$ PS I complexes. *Solid circles* represent component with a lifetime of 10 µs, *checked squares* represent component with a lifetime of 2 ms *C,* kinetic spectra of the *rubA*$^-$ / *menB*$^-$ PS I complexes. *Solid circles* represent component with a lifetime of 9 µs, *checked squares* represent component with a lifetime of 585 µs.

Figure 3.15 Kinetic spectra of the *rubA*$^-$ / *menB*$^-$ PS I complexes in the UV region. *A*, flash-induced absorbance changes recorded at times 15 µs (*circles*), 300 µs (*squares*, 1ms (*triangles*) after a saturating flash. Dotted line shows plastoquinone/semiplastoquinone difference spectrum obtained in Chapter 1. Sample conditions are as follows: PS I complexes isolated from *rubA / menB* double mutant at 10 mg chlorophyll ml^{-1} in 25

mM Tris/HCl, pH 8.3, 1 mM sodium ascorbate, 2 μM DCPIP and 0.03% β-DM. *B,* spectrum of the plastoquinone-9 anion radical in methanol (checked circles) adapted from (Benasson *et al.,* 1973), and spectrum of Q_A^-/Q_A in deoxycholate-isolated PS II complexes (checked squares) adapted from (van Gorkom, 1974). *C*, two-exponential fit of the kinetic transient at 315 nm, sample conditions as in *A*.

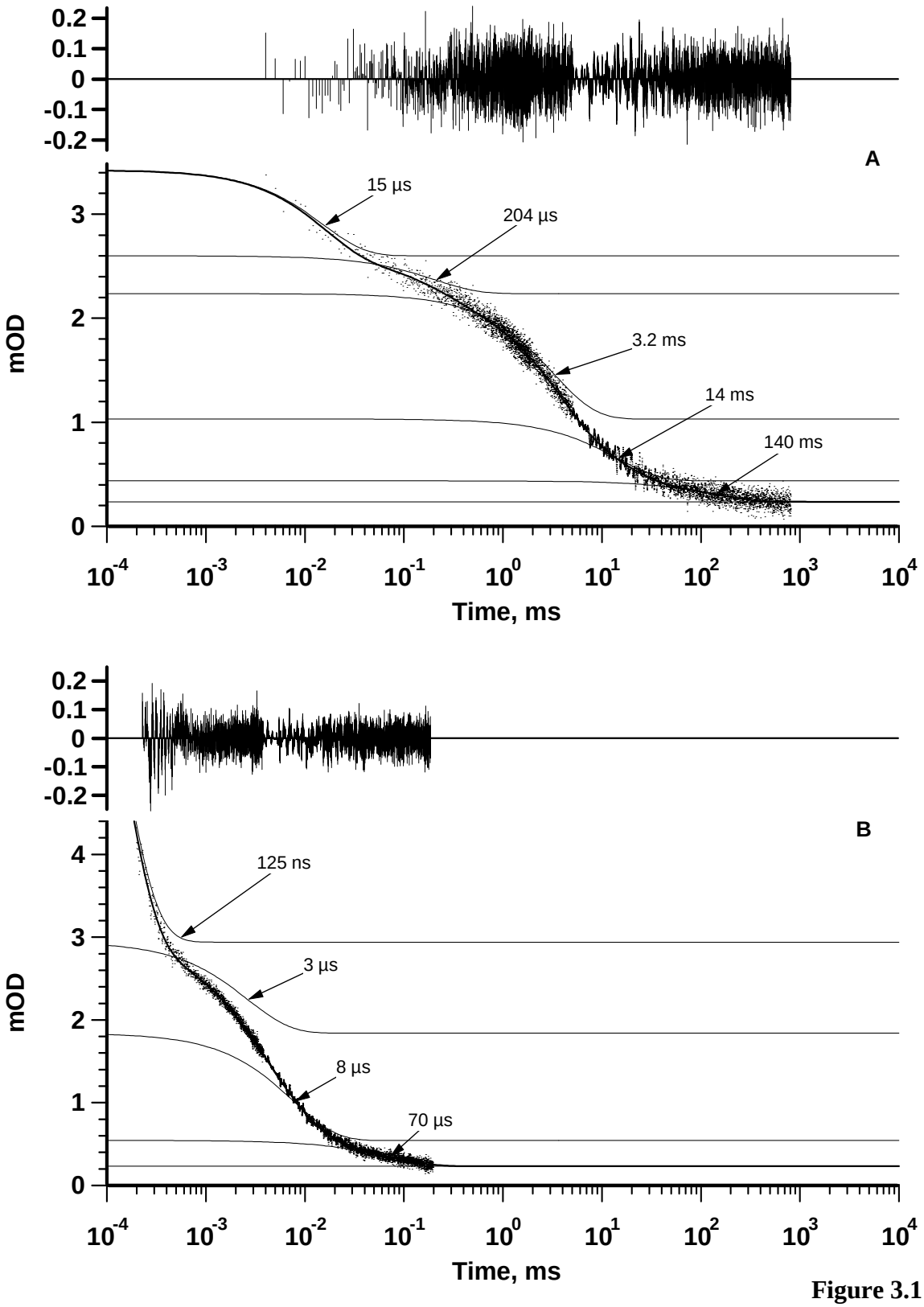
0.2
0.1
0
-0.1
-0.2
A
15 µs
204 µs
3.2 ms
14 ms
140 ms
mOD
Time, ms
B
125 ns
3 µs
8 µs
70 µs

Figure 3.1

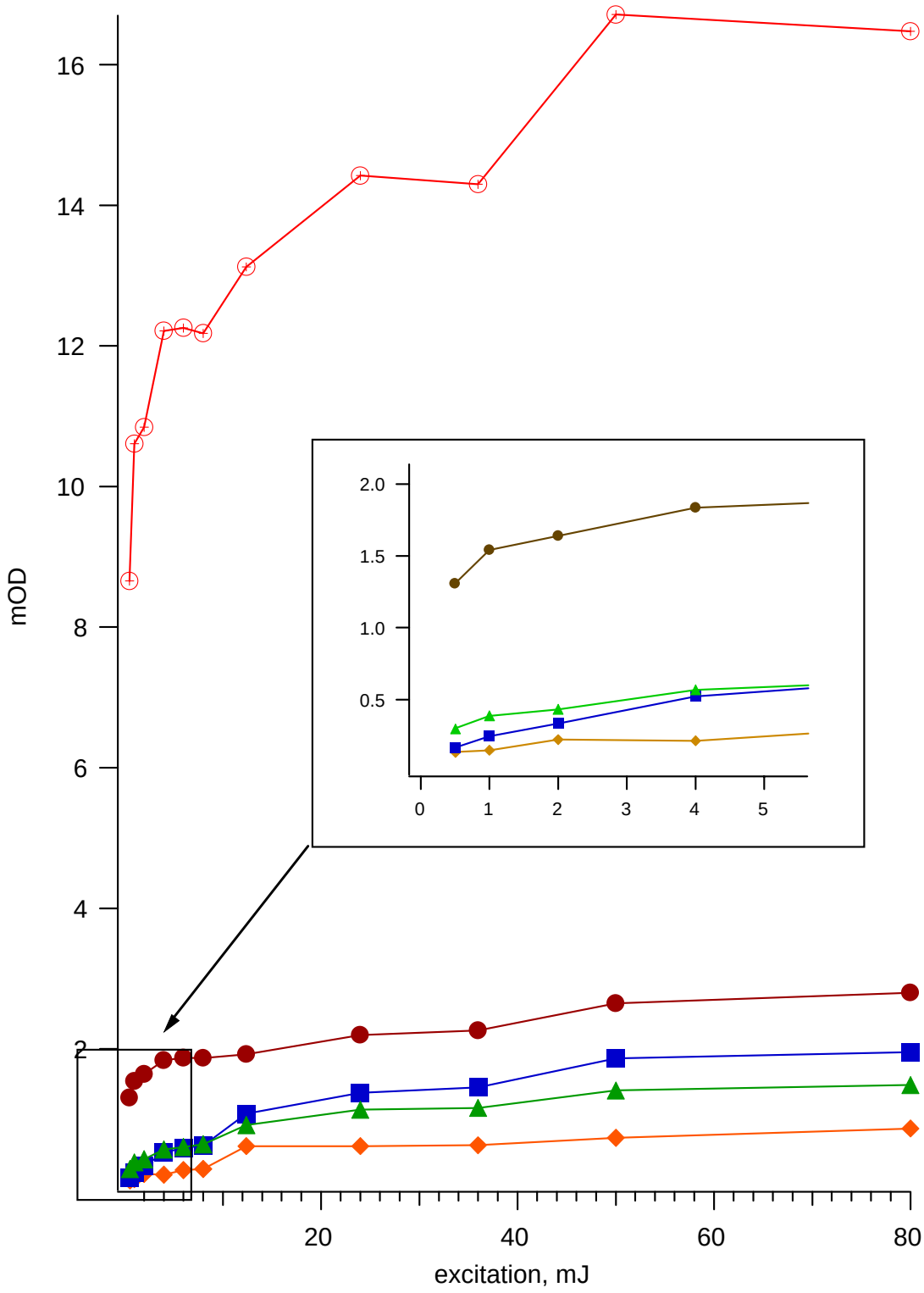

Figure 3.2

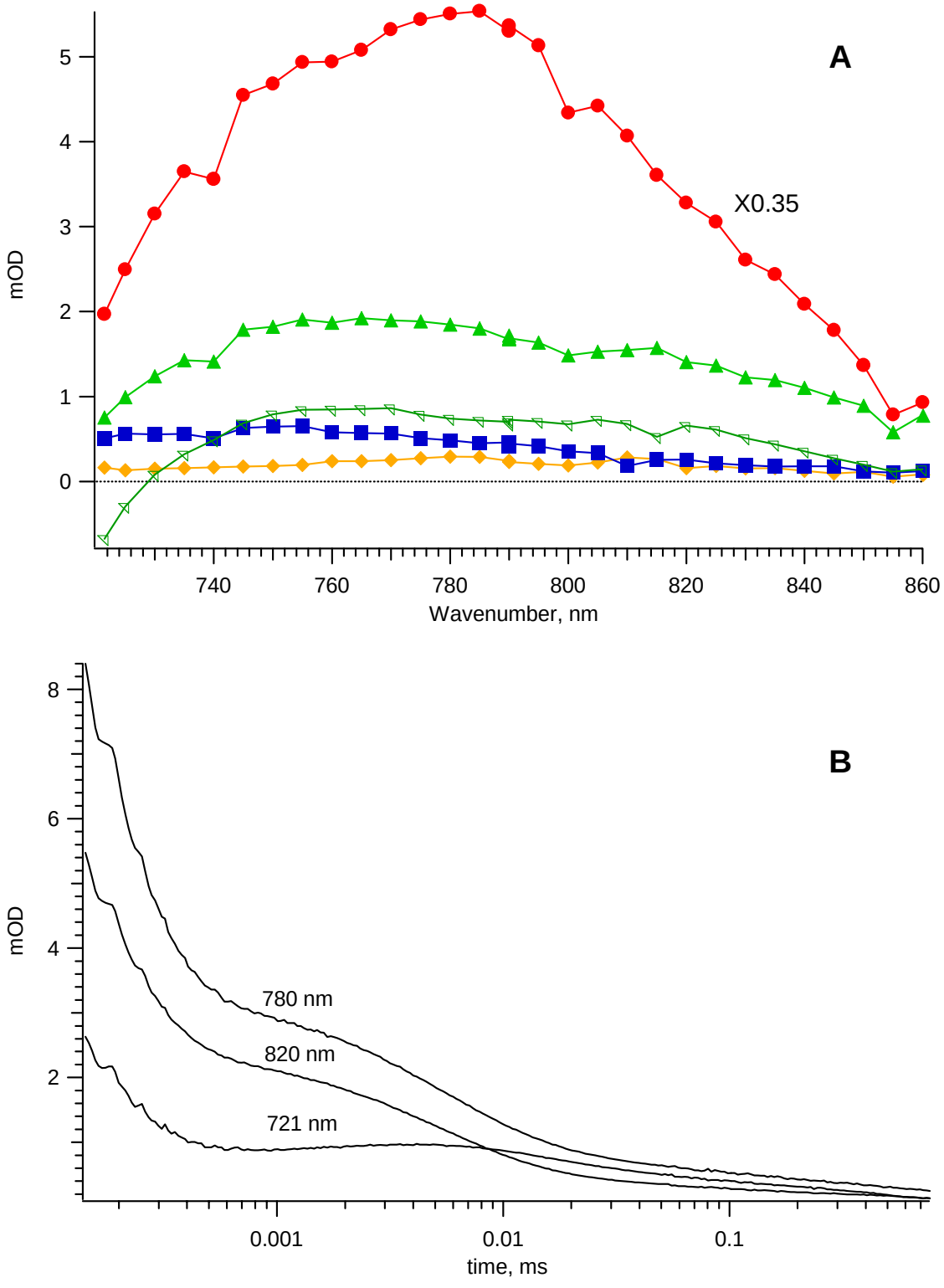
A
X0.35
mOD
5
4
3
2
1
0
740
760
780
800
820
840
860
Wavenumber, nm
B
mOD
8
6
4
2
780 nm
820 nm
721 nm
0.001
0.01
0.1
time, ms

Figure 3.3

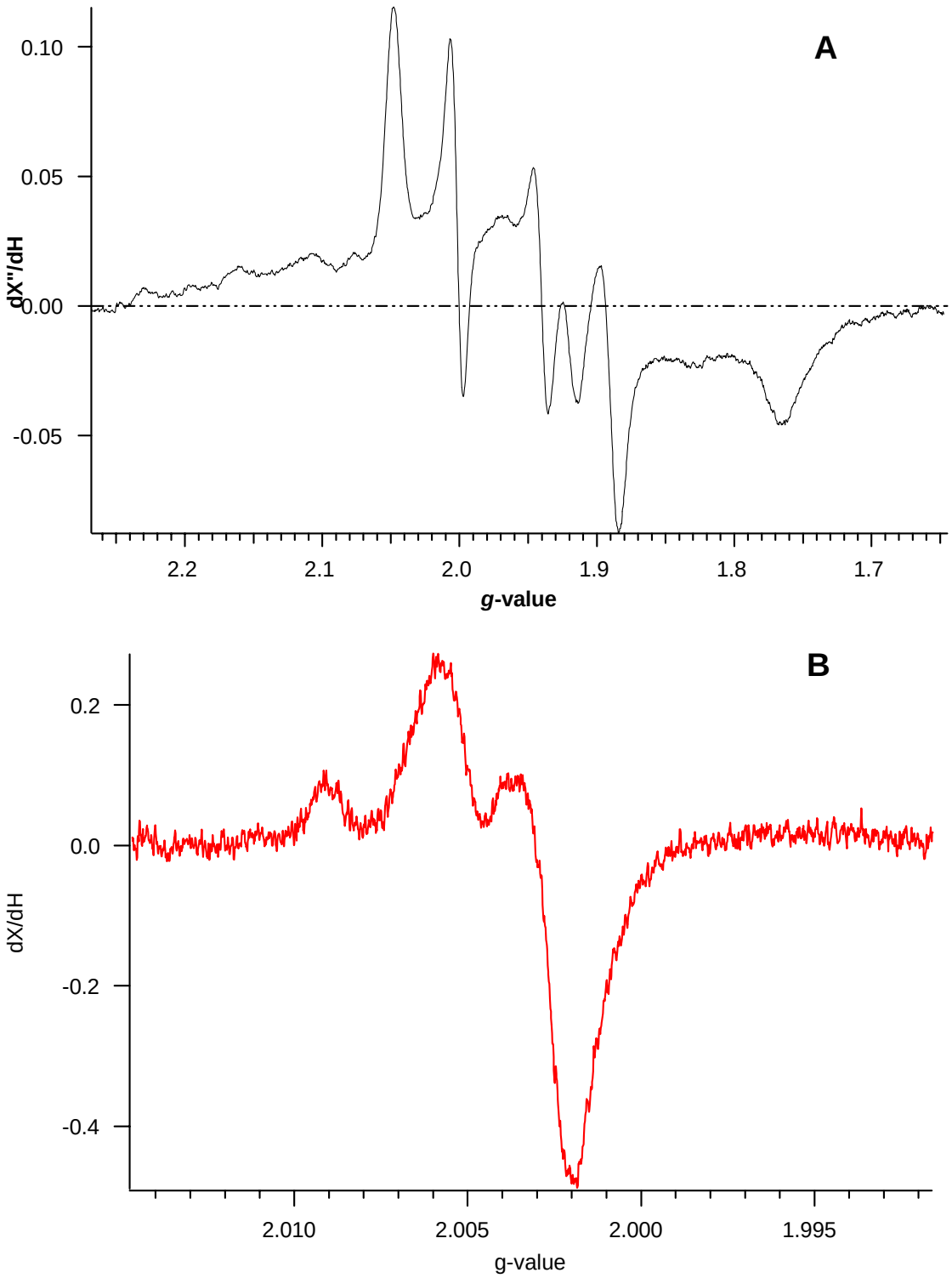
A
0.10
0.05
0.00
-0.05
dX''/dH
2.2
2.1
2.0
1.9
1.8
1.7
g-value
B
0.2
0.0
-0.2
-0.4
dX/dH
2.010
2.005
2.000
1.995
g-value

Figure 3.4

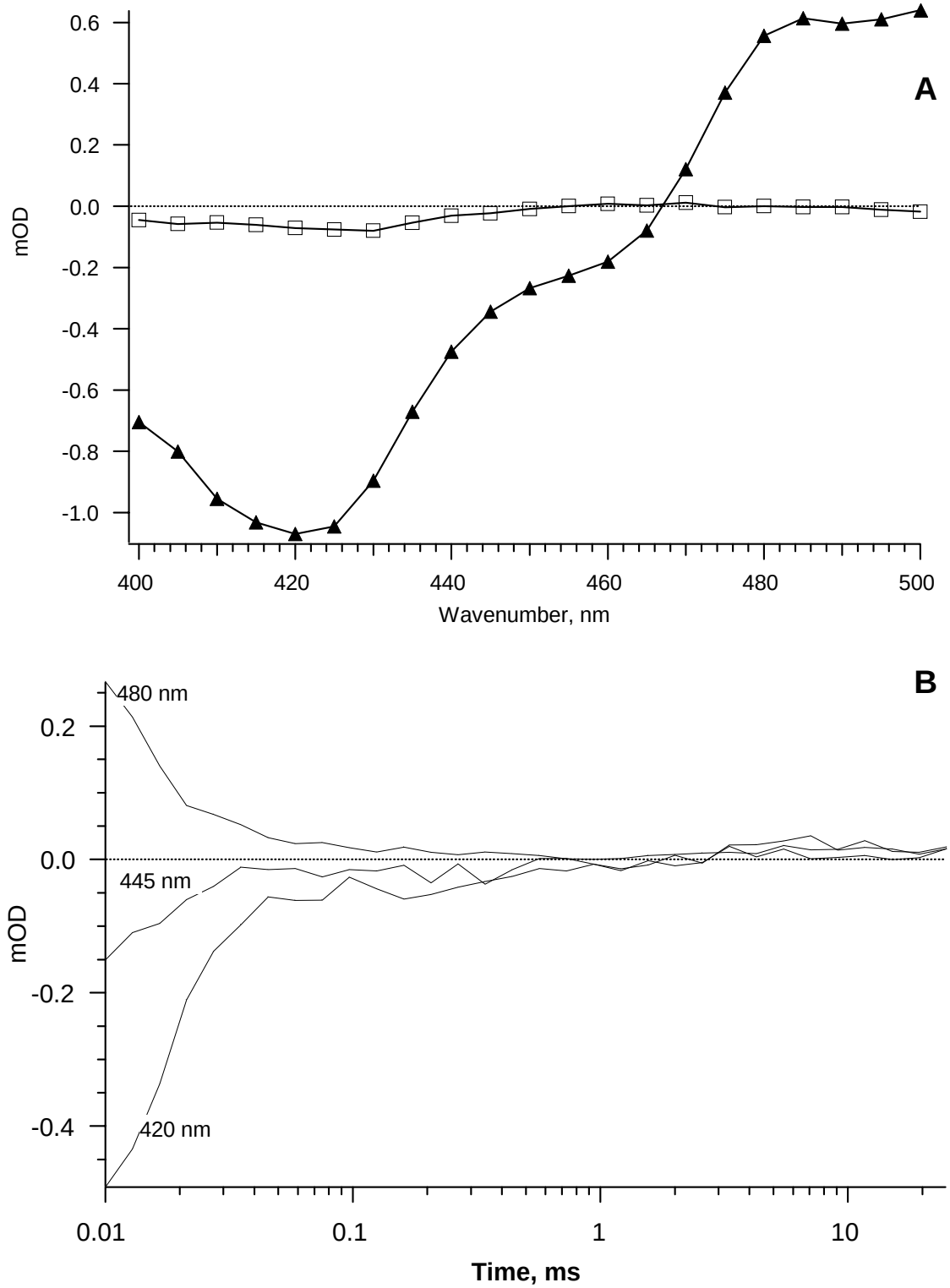
A
0.6
0.4
0.2
0.0
-0.2
-0.4
-0.6
-0.8
-1.0
mOD
400
420
440
460
480
500
Wavenumber, nm
B
480 nm
445 nm
420 nm
0.2
0.0
-0.2
-0.4
mOD
0.01
0.1
1
10
Time, ms

Figure 3.5

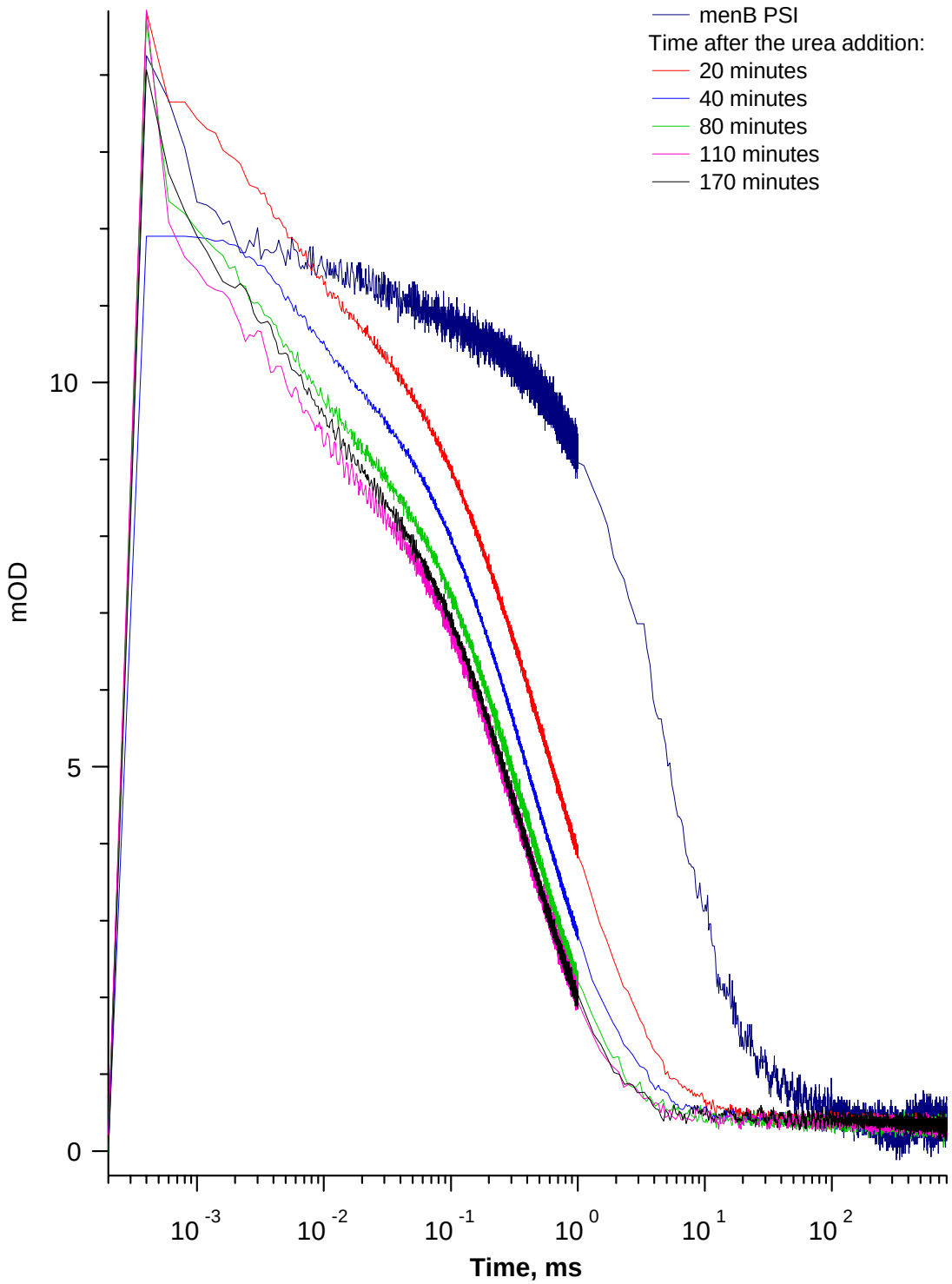
menB PSI
Time after the urea addition:
20 minutes
40 minutes
80 minutes
110 minutes
170 minutes
mOD
10
5
0
10 -3
10 -2
10 -1
10 0
10 1
10 2
Time, ms

Figure 3.6

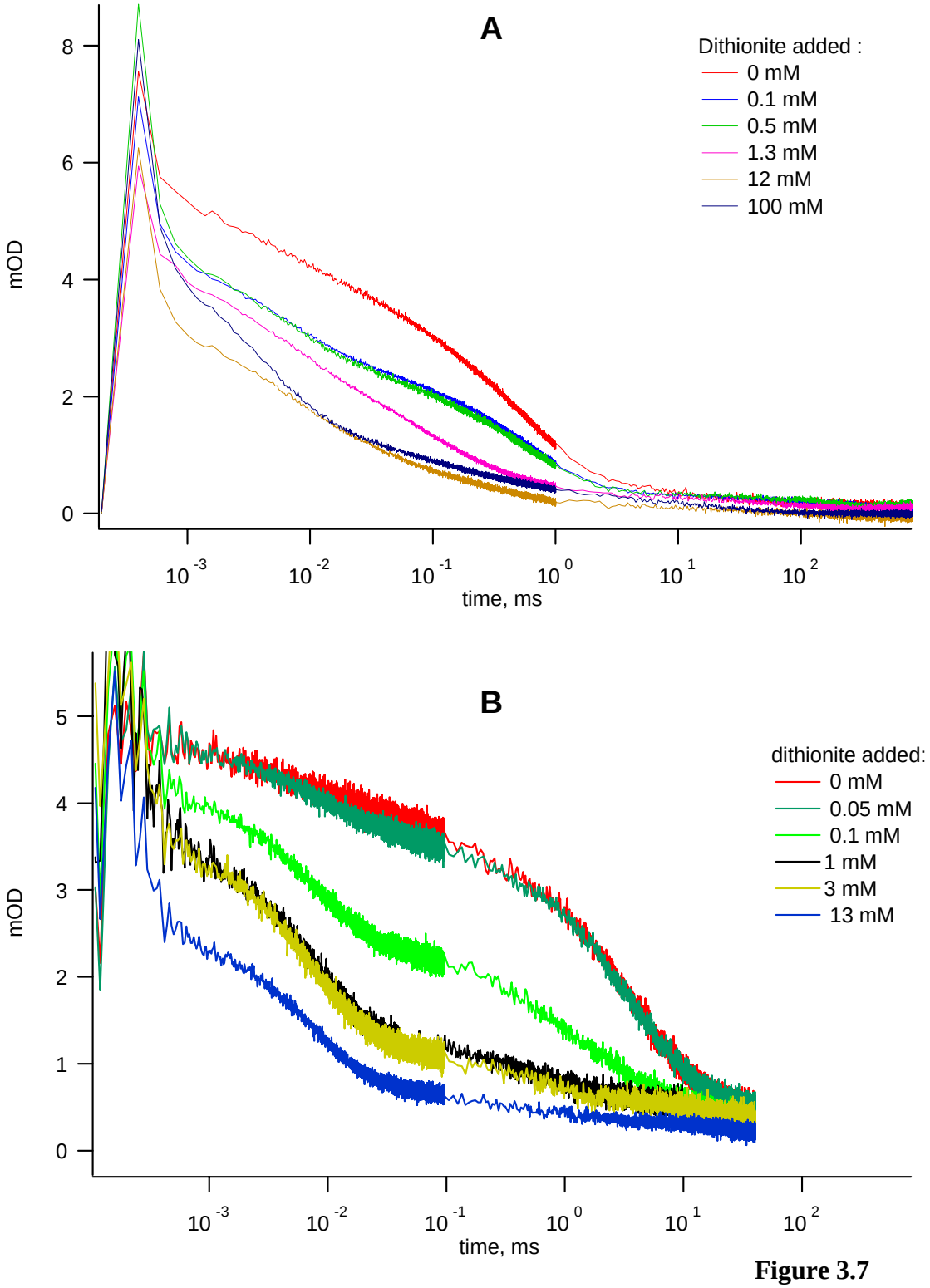
A
Dithionite added :
0 mM
0.1 mM
0.5 mM
1.3 mM
12 mM
100 mM
mOD
time, ms
B
dithionite added:
0 mM
0.05 mM
0.1 mM
1 mM
3 mM
13 mM
mOD
time, ms

Figure 3.7

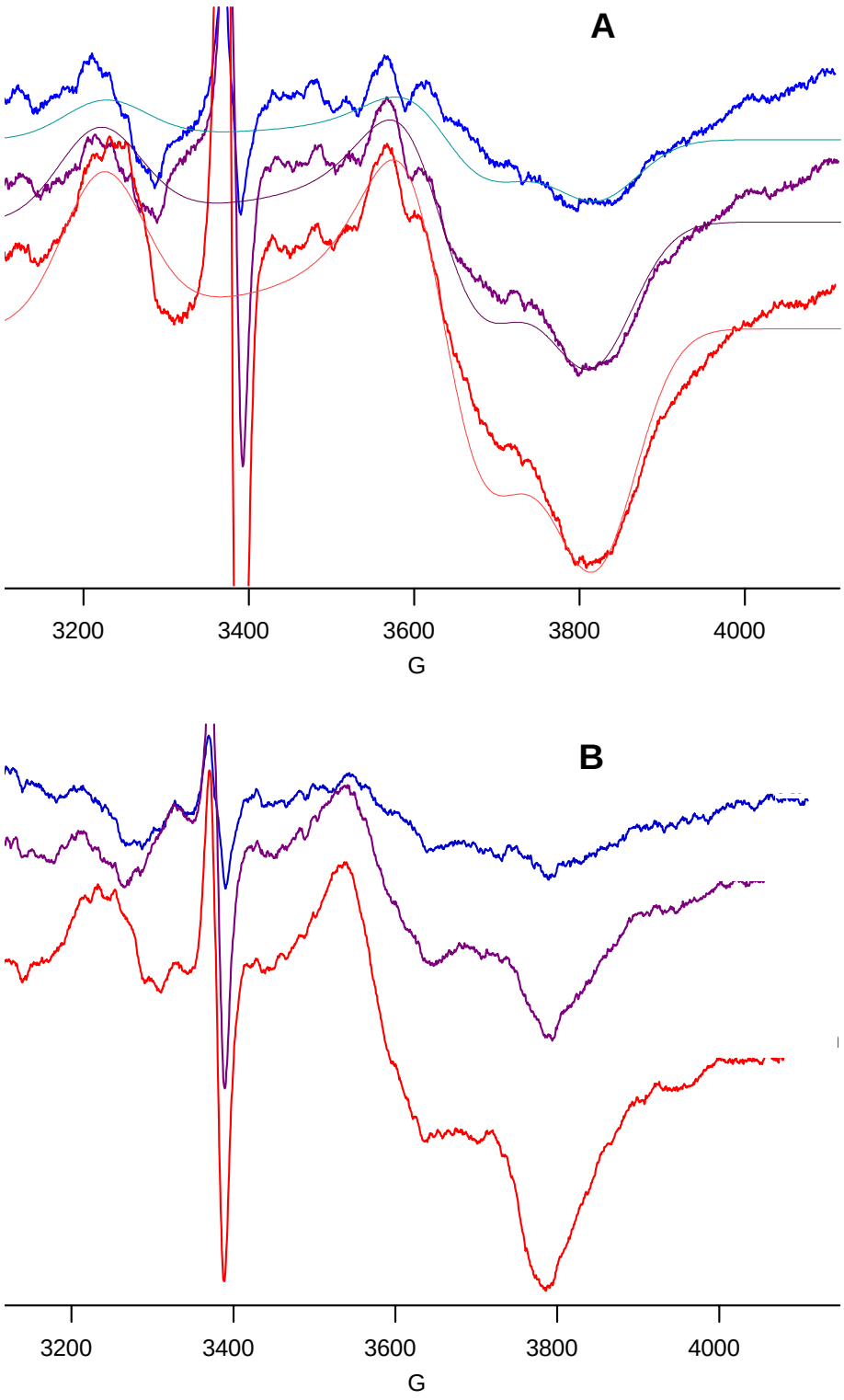

Figure 3.8

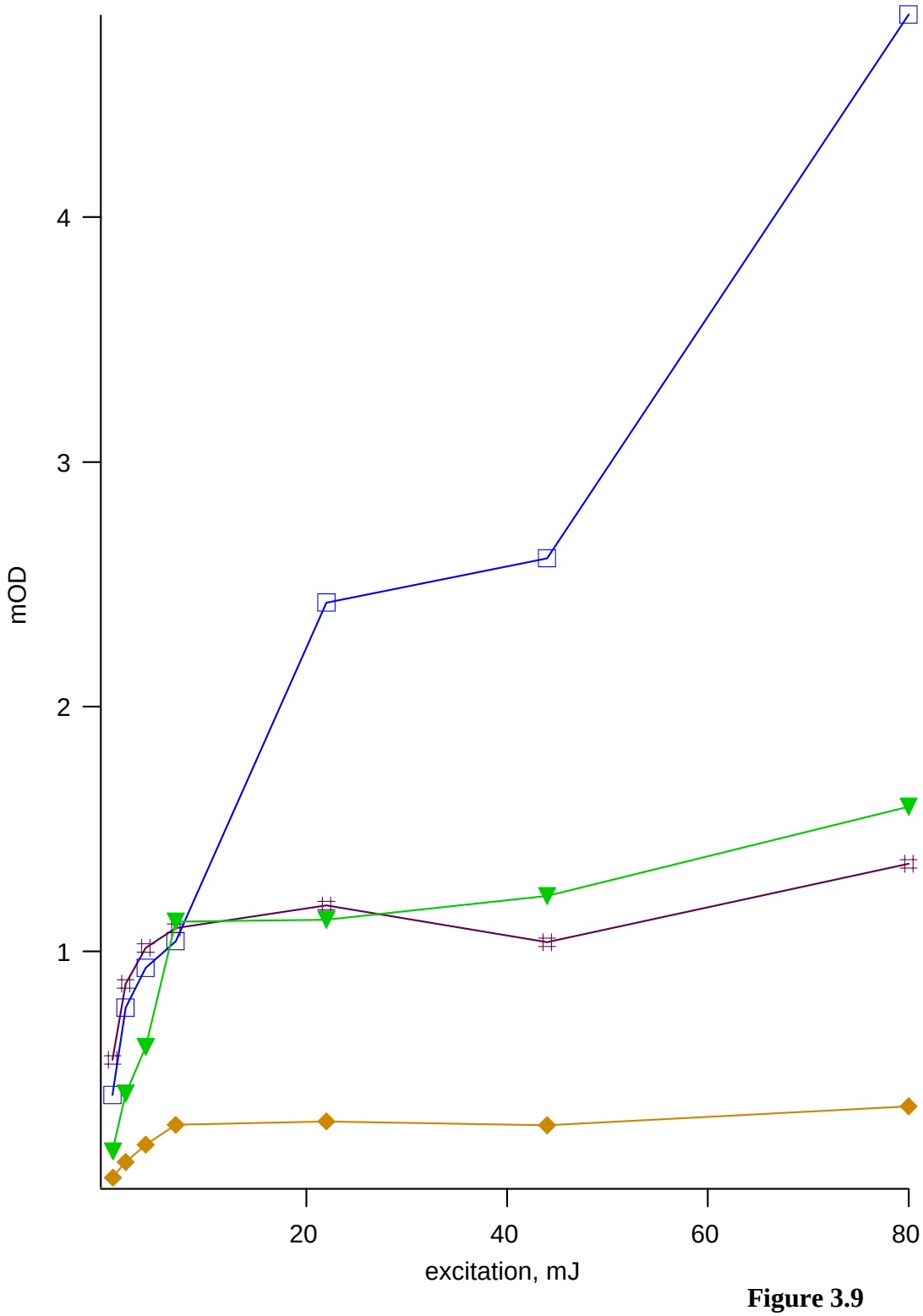

Figure 3.9

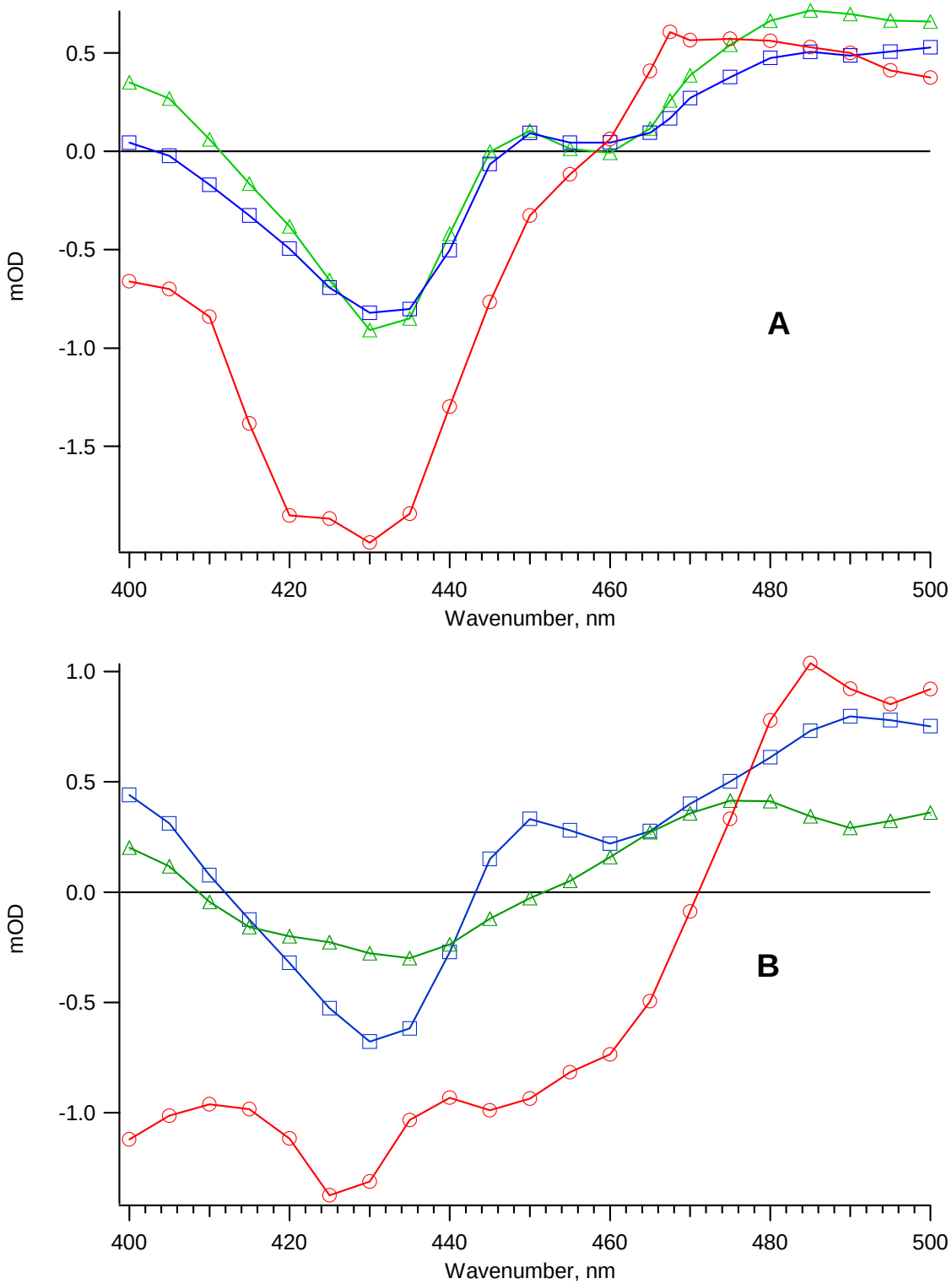
0.5
0.0
-0.5
-1.0
-1.5
mOD
A
400
420
440
460
480
500
Wavenumber, nm
1.0
0.5
0.0
-0.5
-1.0
mOD
B
400
420
440
460
480
500
Wavenumber, nm

Figure 3.10

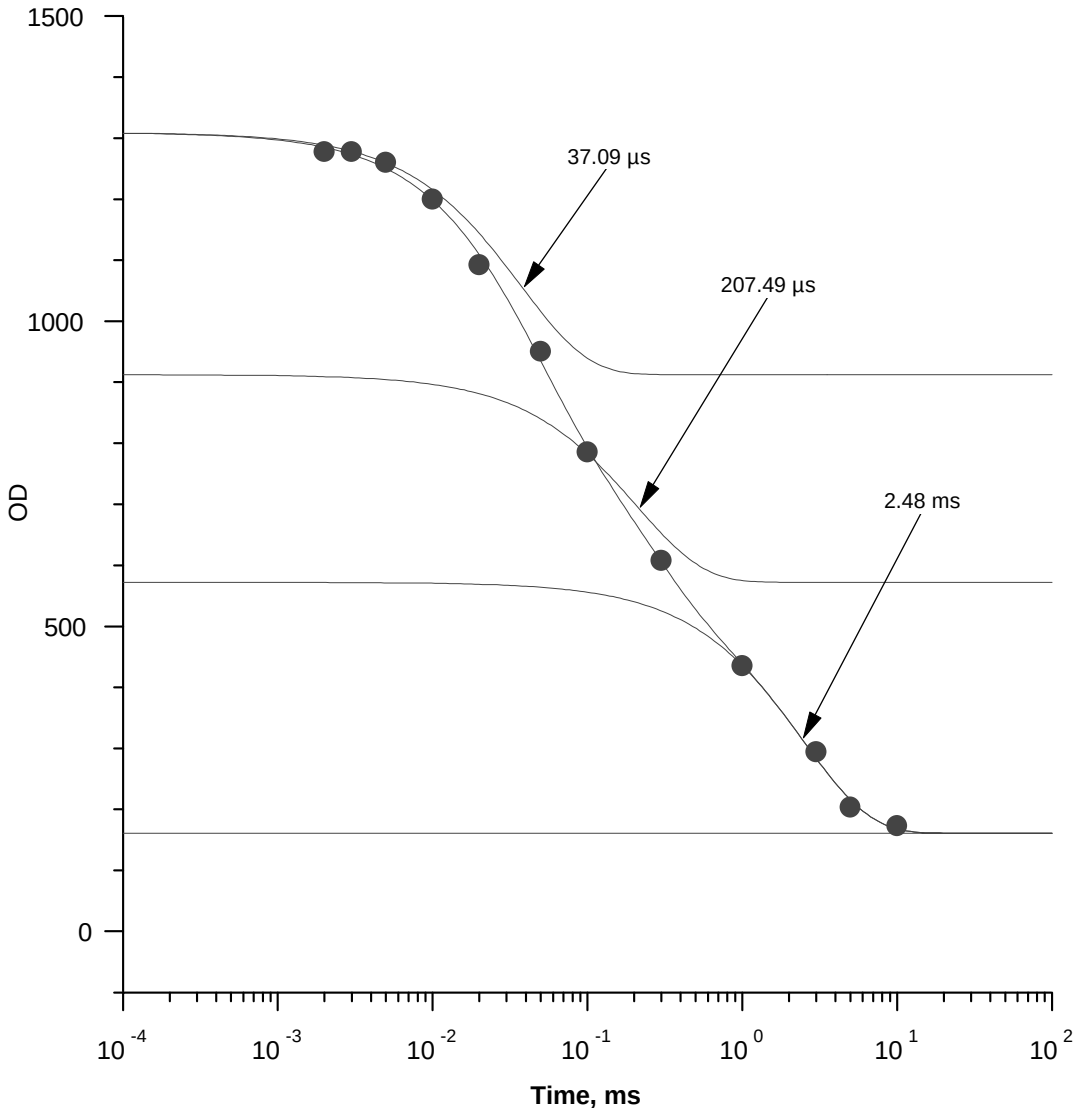
1500
1000
500
0
OD
37.09 µs
207.49 µs
2.48 ms
10 -4
10 -3
10 -2
10 -1
10 0
10 1
10 2
Time, ms

Figure 3.11

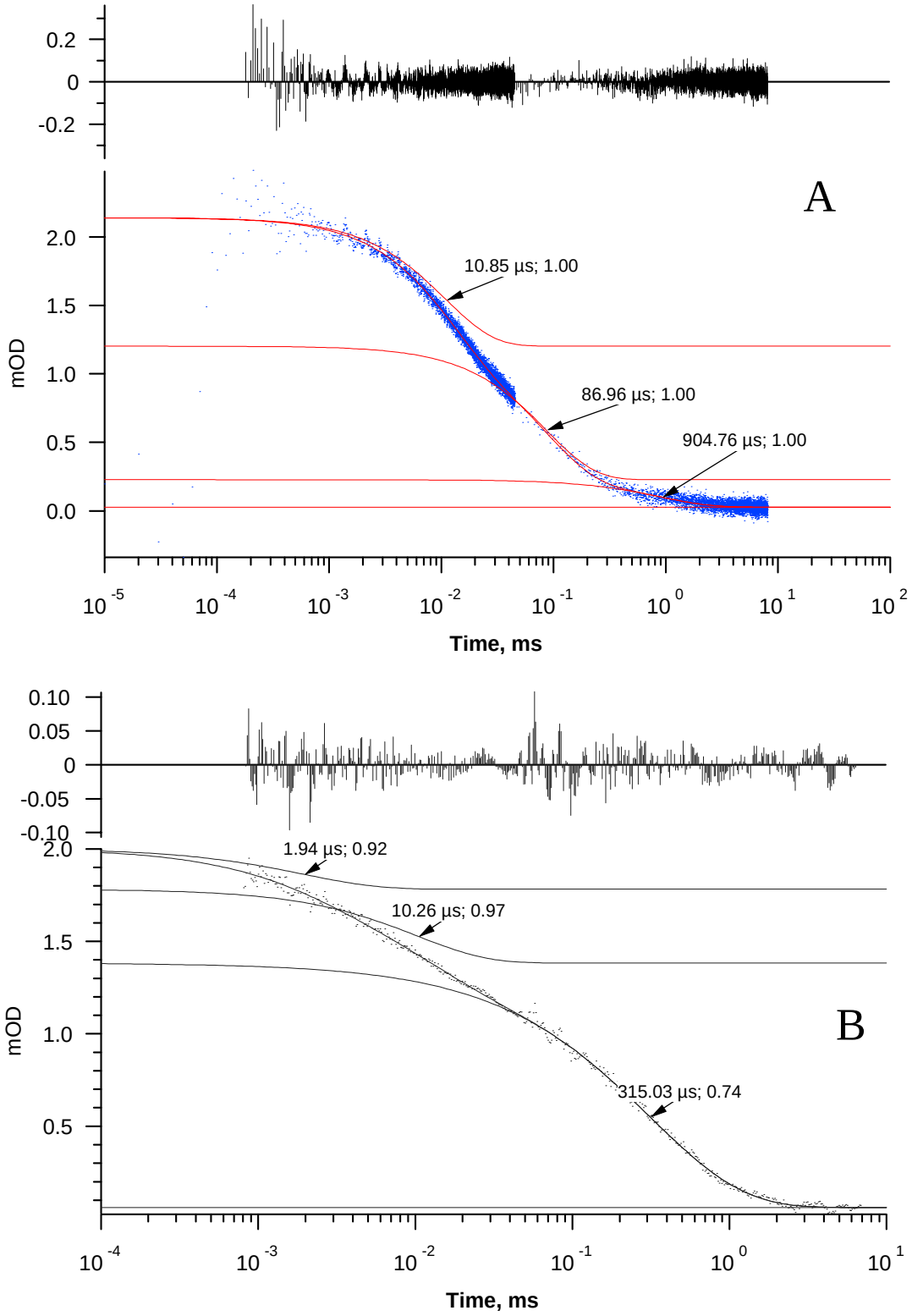
A
10.85 µs; 1.00
86.96 µs; 1.00
904.76 µs; 1.00
mOD
Time, ms
B
1.94 µs; 0.92
10.26 µs; 0.97
315.03 µs; 0.74
mOD
Time, ms

Figure 3.12

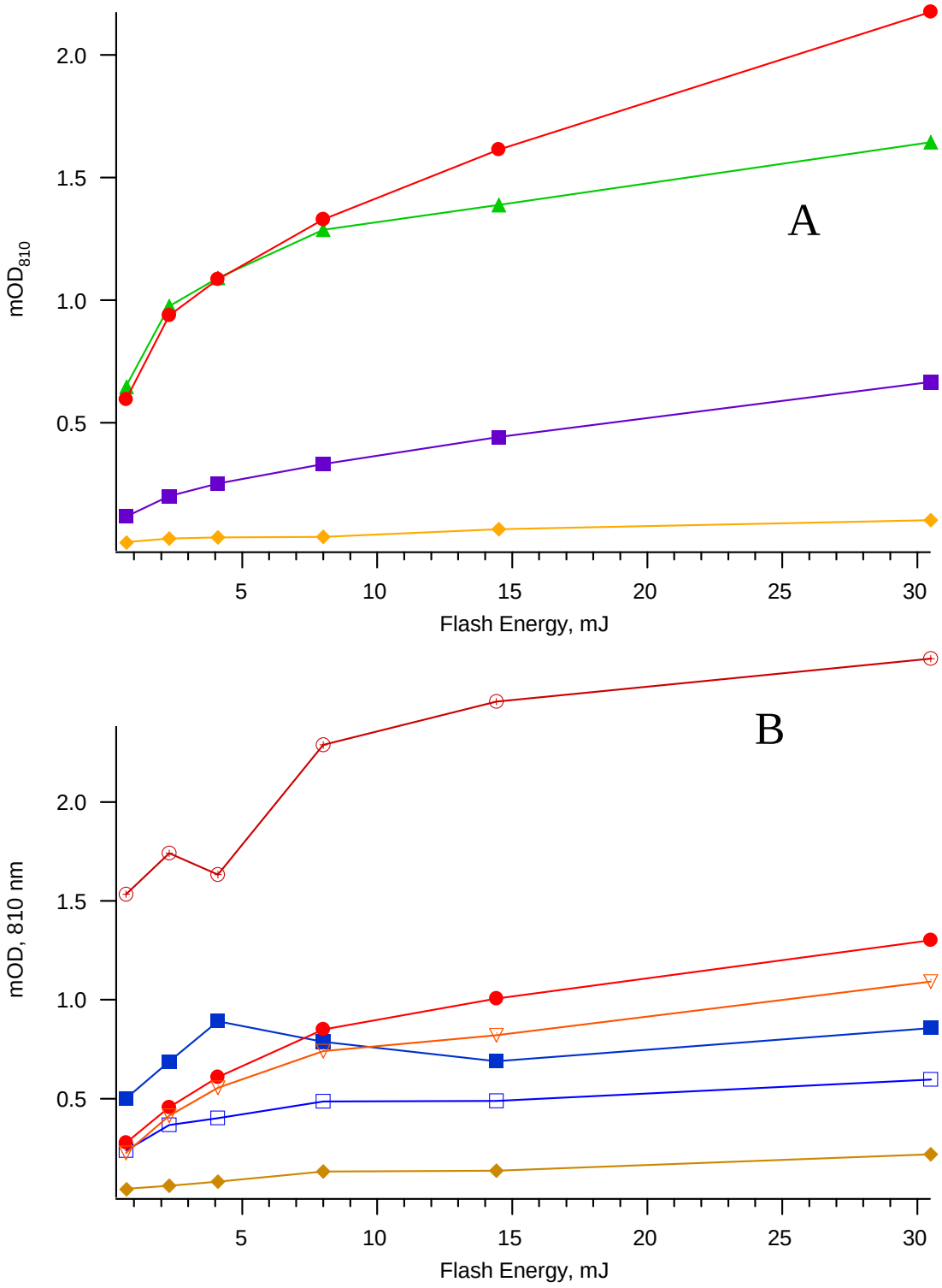
A
mOD810
2.0
1.5
1.0
0.5
5
10
15
20
25
30
Flash Energy, mJ
B
mOD, 810 nm
2.0
1.5
1.0
0.5
5
10
15
20
25
30
Flash Energy, mJ

Figure 3.13

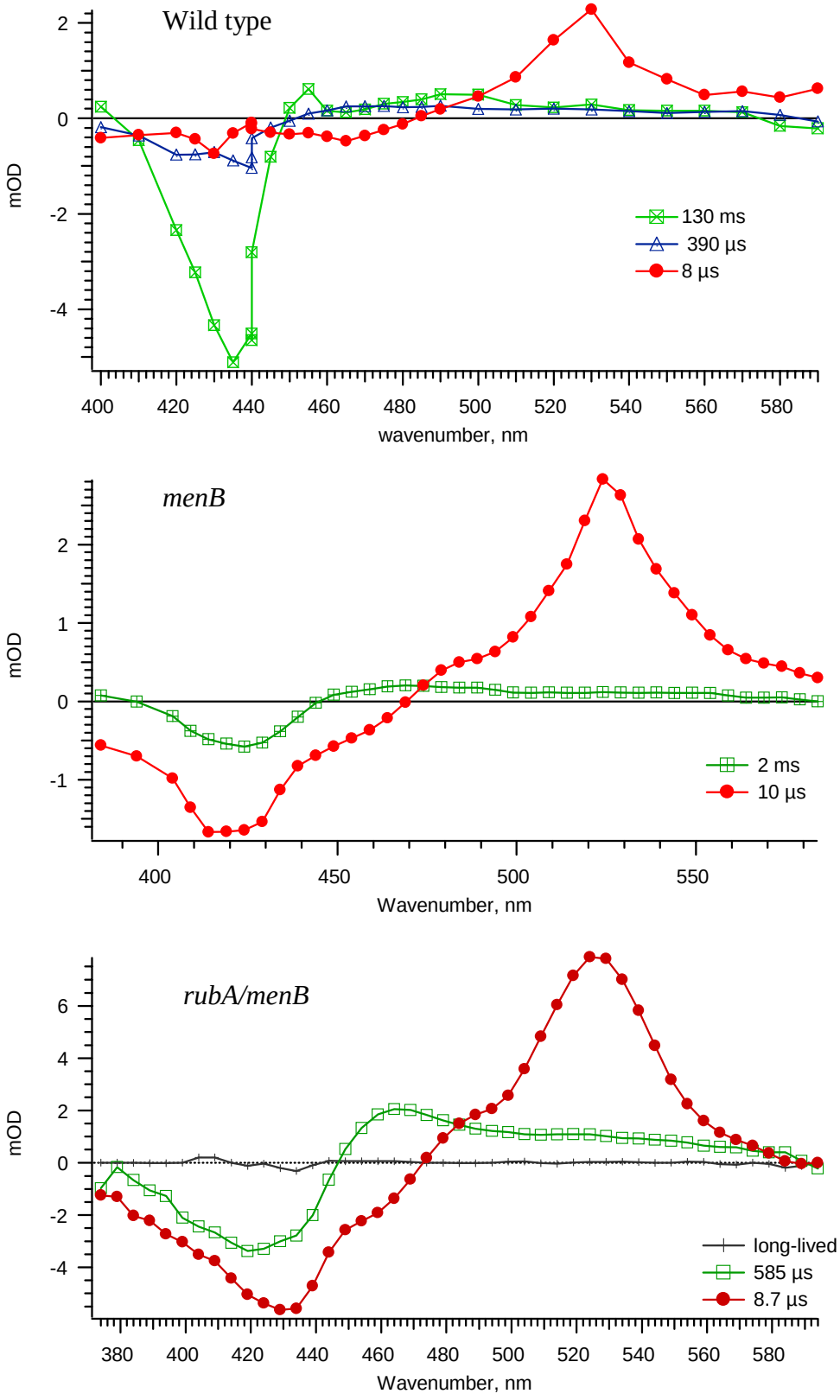
Wild type
mOD
wavenumber, nm
130 ms
390 µs
8 µs
menB
Wavenumber, nm
2 ms
10 µs
rubA/menB
Wavenumber, nm
long-lived
585 µs
8.7 µs

Figure 3.14

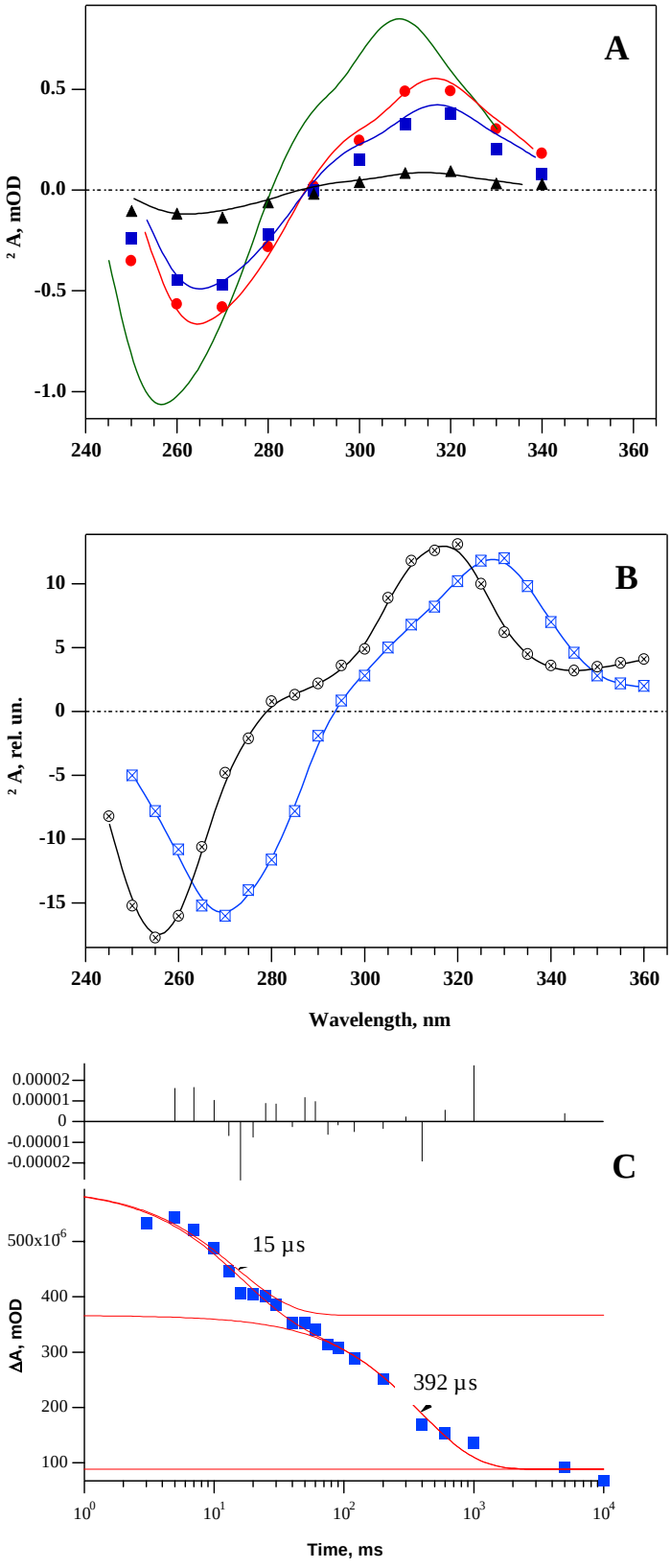
A
0.5
0.0
-0.5
-1.0
240
260
280
300
320
340
360
B
10
5
0
-5
-10
-15
Wavelength, nm
0.00002
0.00001
0
-0.00001
-0.00002
C
500x10^6
400
300
200
100
15 µs
392 µs
ΔA, mOD
Time, ms

Figure 3.15

Table 3.1 Assignment of the kinetic phases in the mutant plastoquinone-containing PS I preparations

menB + dithionite	Major kinetic phases[a]	Process
	125 ns	$A_0 \rightarrow P_{700}$[b]
	3 µs	$^{T}P_{700} \rightarrow P_{700}$
	10 µs	$A_1 \rightarrow P_{700}$[b,c]
	(>50 µs)	$A_1 \rightarrow P_{700}$[d], $^{T}chl_{ant} \rightarrow chl$[e]
menB-F_X core	10 µs	$A_1 \rightarrow P_{700}$
	100 µs	$A_1 \rightarrow P_{700}$
`	500-800 µs[f]	$A_1 \rightarrow P_{700}$, $F_X \rightarrow P_{700}$
menB-F_X core +MV	10 µs	$A_1 \rightarrow F_X \rightarrow MV$[c]
	220 µs	$A_1 \rightarrow F_X \rightarrow MV$
	Slow	$DCPIP \rightarrow P_{700}$
rubA/*menB*	120 ns	$A_0 \rightarrow P_{700}$[g]
	15 µs	$A_1 \rightarrow P_{700}$[c]
	400-600 µs[f]	$A_1 \rightarrow P_{700}$

---

[a] Averaged through different experiments

[b] Contribution of the triplet of state P_{700} is not excluded

[c] Relaxation of ^{T}Car contributes in the visible to the 10 µs phase

[d] minor phase with less than 2% contribution to the total

[e] Becomes apparent only at higher excitation energies, lifetime ca. 500 µs, antenna chlorophyll

[f] Percent contribution and lifetimes vary from preparation to preparation

[g] In the complexes where plastoquinone is lost

Chapter 4

In vivo and *in vitro* Replacements of Plastoquinone-9 in Phylloquinone Biosynthetic Pathway Mutants

ABSTRACT

In previous chapters, I showed that when phylloquinone biosynthetic pathway is altered by interruption of the *menA* and *menB* genes in *Synechocystis* sp. PCC 6803, plastoquinone-9 occupies the A_1 site in PS I, where it functions as an efficient electron transfer cofactor from A_0 chlorophyll to the terminal FeS clusters. In this chapter, I demonstrate that plastoquinone-9 in the mutant PS I complexes can be successfully replaced by a variety of other quinones. Restoration of phylloquinone into the A_1 site is one case of replacement of plastoquinone-9. I monitor the restoration of phylloquinone by optical and EPR spectroscopic methods and show that P_{700}^+ re-reduction kinetics, the quinone orientation in the A_1 site, and the pattern of the 2-CH_3 hyperfine splitting in the *menB* mutant with the restored phylloquinone are indistinguishable from the wild type.

In the *menB* mutant cells supplemented with a set of unsubstituted or substituted anthraquinones, I observe incorporation of the anthraquinone head-group into the A_1 site by CW-EPR and near-IR optical kinetic spectroscopies. In contrast, in the *menA* mutant cells supplemented in the same way, I do not observe incorporation of the anthraquinone head-group into the A_1 site. Based on these observations, I conclude that as with naphthoquinones (Johnson *et al*., 2001), phytylation is required for its incorporation into PS I *in vivo*.

When the quinone replacements were carried out *in vitro*, naphthoquinones and anthraquinones were added directly to *menB*$^-$ or *menA*$^-$ PS I complexes, and both phytylated and unphytylated quinones were able to replace plastoquinone-9 as an A_1 acceptor.

Growth studies of the mutant cyanobacteria cells with anthraquinones were carried out in collaboration with Gaozhong Shen.

INTRODUCTION

Substituted quinones serve as cofactors in electron transport chains, as demonstrated in bacterial reaction centers (Gunner *et al*., 1986; Woodbury *et al*., 1986) and in the two photosystems of plants and cyanobacteria (Nugent, 1996; Golbeck, 1993; Nitschke and Rutherford, 1991). These quinones are comprised of a polar aromatic ring (which is either a benzoquinone or a naphthoquinone head group), and a non-polar isoprenoid tail of various chain lengths and degrees of saturation. Benzoquinones such as plastoquinone-9 and ubiquinone-10 function in membrane-bound protein complexes either as fixed or exchangeable electron/proton carriers during photosynthetic and respiratory electron transport. In (PS II), plastoquinone-9 functions as a bound one-electron carrier in the Q_A site and as an exchangeable 2-electron/2-proton carrier in the Q_B site. The reduced plastoquinone-9 is subsequently displaced from the Q_B site by an oxidized Q, diffuses laterally through the membrane, and becomes oxidized and deprotonated by the cytochrome b_6f complex (see the introductory chapter). Photosynthetic reaction centers of purple bacteria either use ubiquinone-10 (e.g. *Rhodobacter sphaeroides*) in a similar double role or use menaquinone-9 in the Q_A site (e.g. *Rhodosprillulum viridis*).

In PS I, phylloquinone - a substituted 1,4-naphthoquinone (1,4-NQ) with a 20-carbon, largely saturated phytyl tail - functions as a bound one-electron carrier in the A_1 site. There exist two A_1 sites with phylloquinone in PS I, but neither of the two phylloquinones functions in a manner equivalent to Q_B in the bacterial reaction center and in PS II. Instead, the electron is transferred through A_1 to soluble ferredoxin via a chain of three bound FeS clusters. Quinones are extremely versatile: they can function either as the interface between electron transfer involving organic cofactors and electron transfer involving FeS clusters (PS I), or between pure electron transfer and coupled electron/proton transfer involving a second organic cofactor (PS II). Each quinone displays equilibrium binding and redox properties that can be very different for each site of interaction (Trumpower, 1982); these properties are conferred largely by the protein environment.

One of the approaches that I use to understand the structural determinants that allow quinones to function with a low redox potential in the A_1 site of PS I, is biological replacement of the native phylloquinone. The only used method previously used to remove phylloquinone was to extract lyophilized PS I complexes with organic solvents, a method that is efficient at removing one (Malkin, 1986; Biggins and Mathis, 1988) or both (Biggins and Mathis, 1988; Itoh *et al*., 1987; Sétif *et al*., 1987) phylloquinone molecules. Quinone substitution into the A_1 site has been demonstrated for these PS I complexes (Sieckman *et al*., 1991; van der Est *et al*., 1997). However, up to 85 of the 100 chlorophylls and all of the carotenoids and lipids are lost and it is uncertain whether or not the PS I complex has undergone structural changes as a result of solvent extraction.

In previous chapters, I discussed the generation and characterization of phylloquinone-less mutants of the cyanobacterium *Synechocystis* sp. PCC 6803. The method employed was interruption mutagenesis of two genes, *menA*, which codes for phytyl transferase, and *menB*, which codes for 1,4-dihydroxy-2-naphthoate (DHNA) synthase. The goal was to prevent phylloquinone production, with the intent of creating an empty A_1 site. However, through spectroscopic analysis, I found that the A_1 site in the *menA* and *menB* mutants was still occupied by a benzoquinone derivative identified as plastoquinone-9, which is otherwise exclusively associated with PS II. Detailed EPR and optical spectroscopic analyses showed that the plastoquinone-9 occupies the site at the same distance from P_{700}^+ and with the same orientation as phylloquinone in the wild type; it functions as an efficient intermediate electron transfer carrier between A_0 and F_X. The redox potential of plastoquinone-9 in the A_1 site was estimated to be somewhat more oxidizing than phylloquinone, which would render the electron transfer step from Q^- to F_X thermodynamically less favorable. Forward electron transfer nevertheless occurs, because of the large, favorable free energy change from A_0^- to flavodoxin.

Wade Johnson and I (Johnson, Zybailov *et al*., 2000) demonstrated that it is possible to introduce various quinones into the A_1 site *in vivo* by utilizing the unmodified phytyl transferase and methyl transferase enzymes in the existing biosynthetic pathway of the *menB* mutant cells. The interested reader should also refer to Wade Johnson's Ph.D. dissertation, which provides a comprehensive analysis of the results of our experiments

with naphthoquinone supplements. To summarize, when *menA* and *menB* mutant cells were grown in a medium supplemented with phylloquinone precursors, certain 1,4-NQ derivatives become phytylated by the product of the *menA* gene (a phytyl transferase) methylated by the product of the *menG* gene (a methyl transferase) and incorporated into the A_1 site as phylloquinone. For other 1,4-NQ derivatives, the phytyl transferase and methyl transferase appear to be unable to function.

In this chapter, I expand studies of the *in vivo* supplementation strategy and demonstrate that certain anthraquinones can replace plastoquinone-9 in *menB*-PS I *in vivo*. Furthermore, I complement the results of the biological replacement with *in vitro* studies, which demonstrates that plastoquinone-9 is rather loosely bound, and is readily exchangeable with naphthoquinones or anthraquinones.

MATERIALS AND METHODS

Isolation of Thylakoid Membranes and PS I Complexes

Thylakoid membranes were prepared from cells as described in (Sun *et al*., 1997). The membranes were pelleted by centrifugation at 50,000 x *g* for 90 min and resuspended in SMN buffer (0.4 M sucrose, 10 mM MOPS, 10 mM NaCl) for storage. Chlorophyll was extracted from thylakoid membranes and PS I complexes with 80% acetone and determined according to (Arnon, 1949). For the isolation of PS I complexes, thylakoid membranes were incubated in SMN buffer with 20 mM $CaCl_2$ for 0.5 to 1.0 hr at room temperature in the dark to enhance the trimerization of PS I. To this mixture, β-DM was added to a final concentration of 1.5% (w/v) and incubated in the dark on ice with occasional gentle mixing for 0.5 to 1.5 hrs. The non-solubilized material was removed by centrifugation at 10,000 x g for 15 minutes. The trimeric and monomeric PS I complexes and PS II were separated by centrifugation in 10 to 30% (w/v) sucrose gradients with 0.04% DM in 10 mM MOPS, pH 7.0.

Measurement of PS I Activity

Steady-state rates of electron transfer in isolated PS I complexes were measured using cytochrome c_6 as the electron donor and flavodoxin as the electron acceptor, as described in (Yang *et al*., 1998). The measurement of P_{700} photooxidation in whole cells was based on a technique developed by Harbison and adapted to cyanobacteria as described in (Jung *et al*., 1995).

Q-band EPR Spectroscopy of Photoaccumulated PS I Complexes

Photoaccumulation experiments were carried out using the same instrumentation and methods as described in chapter 2

Optical Kinetic Spectroscopy in the Near-IR Region

Optical absorbance changes in the near-IR were measured using a laboratory-built spectrophotometer as described in chapters 2 and 3. To assure resolution of kinetics in the

µs time domain, the high-frequency roll-off amplifier described in the original specifications was not used; instead, the signal was fed directly into the plug-in (11A33 differential comparator, 100 MHz bandwidth) of the Tektronix DSA601 oscilloscope. The sample cuvette contained the PS I complexes isolated from the *menA* or *menB* mutants at 50 µg chlorophyll ml^{-1} in 25 mM Tris/HCl, pH 8.3, 10 mM sodium ascorbate, 4 µM DCPIP, and 0.04% (ß-DM).

In vitro Quinone Reconstitution

Two different methods of reconstitution were used for the *in vitro* replacements of the plastoquinone-9 in the mutant PS I by other quinones. Method one was used to monitor quinone incorporation by Q-band EPR, method two was used to monitor the quinone incorporation by near-IR spectrophotometry.

Method 1: to *menB*$^-$ or *menA*$^-$ PS I complexes resuspended in the Tris pH 8.2 buffer (50 mM), at concentration of 0.8 mg chlorophyll ml^{-1}, was added a solution of the quinone in ethanol (no more than 2% final concentration by volume) to the final quinone concentration of 0.5 mM. The sample was incubated on ice in the dark for 6 to 8 hrs. Soluble quinones were removed by dialysis and the sample volume was brought back to the original by the ultrafiltration with the Amicon YM-100 filters.

Method 2: to the solution of the mutant PS I complexes in the spectroscopic cuvette (Tris buffer, pH 8.2, 25 mM), at concentration of 50 µg chlorophyll ml^{-1}, was added a solution of the quinone in ethanol to the final quinone concentration of 50 µM.

RESULTS

Growth of Cells with Anthraquinone Supplements

Anthraquinone supplementation experiments were performed in a similar manner to naphthoquinone supplementation experiments (Johnson, 2000; Johnson *et al*., 2001), except that the light-sensitive *menB18* strain was used. Fig. 4.2 shows photos of the *menB* (*top*) and *menA* (*bottom*) cells grown for three days with various anthraquinones at high-light intensity. The fact that *menA* mutant failed to grow in these conditions hints that the anthraquinones become phytylated prior to incorporation into the A_1 site. The possibility that anthraquinones are metabolized to naphthoquinone, and only then become phytylated, can be ruled out by the CW EPR experiments presented below.

When the growth medium of the *menB*18 mutant cells is supplemented with anthraquinones, the resulting kinetics of the backreaction to P_{700}^{+} is more complex than either in either *menB* or wild-type PS I complexes (Fig. 4.4). Retention of the fast ms phase indicates that some of the A_1 sites in PS I complexes still may be occupied by plastoquinone-9. Appearance of the hundreds-of-millisecond kinetics phases is due to those A_1 sites that recruited anthraquinones. Slow phases with lifetimes 1 s to 2 s are sensitive to DCPIP concentrations, which indicates that anthraquinone-containing PS I is more prone to oxidation.

When the *menB18* mutant is grown in media supplemented with 9,10-anthraquinone, the EPR spectrum exhibits significantly narrower linewidth (Fig. 4.3). The narrower *g*-anisotropy can be explained by a further delocalization of the unpaired electron spin density. Since 9,10-anthraquinone has a three fused aromatic rings, the spin density on the carbonyl oxygens is lower and the semianthraquinone exhibits smaller g-anisotropy. This result supports the conclusion that 9,10-anthraquinone is recruited in the A_1 site.

Phylloquinone Exchange Experiments

To determine the stability of phylloquinone in the A_1 site over time, two experiments were set up. The first was an *in vivo* pulse experiment (Johnson, 2000;

Johnson *et al.*, 2001). The second experiment, which I report here, was an *in vitro* reconstitution experiment with authentic phylloquinone. The *in vivo* study was performed to determine whether protein synthesis is required for reincorporation of phylloquinone in the A_1 site, *i.e.* whether only newly-synthesized PS I complexes take up exogenously supplied phylloquinone. The *in vitro* study was performed to determine if phylloquinone can directly displace plastoquinone-9 in PS I complexes. These studies are complementary and provide a clue as to the relative binding affinities of phylloquinone and plastoquinone-9 in the A_1 site.

The *in vitro* study involved incubating PS I complexes from the *menB* mutant with phylloquinone and then assaying the replacement of plastoquinone-9 as a function of the added amount of phylloquinone. We used time-resolved flash spectroscopy in the near-IR to determine the backreaction kinetics from $[F_A/F_B]^-$ to P_{700}^+, and EPR spectroscopy to determine the *g*-anisotropy and hyperfine contribution of the quinone in the A_1 site. Fig. 4.7 shows the CW Q-band EPR spectra of the photoaccumulated semiquinones in *menB*$^-$ PS I complexes incubated with phylloquinone for 8 hrs at 4 degrees C°. The spectra are indistinguishable from wild-type PS I complexes, showing the restoration of the *g*-anisotropy and prominent hyperfine couplings characteristic of bound phylloquinone. This shows that phylloquinone has assumed its proper orientation in the A_1 site.

When reconstitution with phylloquinone is performed at room temperature and the PS I concentration is lowered to ca. 50 µg chlorophyll ml^{-1} the quinone replacement happens almost instantly, as can be judged by disappearance in the near-IR of the 3 ms and 9 ms kinetic phases in the P_{700}^+ reduction transients (Fig. 4.8). In this experiment phylloquinone was added stepwise into the spectroscopic cuvette containing the reaction media. Kinetic phases with average lifetimes ranging from 50 ms to 100 ms (the 80 ms and 10 ms kinetic phases were not resolved in these transients) have appeared at the expense of the 3 ms kinetic phase, indicating almost complete reconstitution when about 10:1 molar excess of phylloquinone to P_{700} was added.

An interesting feature of the reconstitution is that the fast kinetic phases disappear more rapidly than the slow kinetic phases recovers, as Fig. 4.12, *bottom* demonstrates. The cause of this behavior has not yet been unambiguously determined at this point. One

interesting possibility is that both plastoquinones (PsaA and PsaB sites) are equally active in the backward electron transfer to P_{700}, but the two phylloquinones differ in their degrees of participation in the backward electron transfer. Thus, when the added phylloquinone occupies the binding site where it is less active, fast kinetic phases associated with plastoquinones are lost, but slower, phylloquinone-related phases are not recovered. However, the other possibility that the observed difference in rate of change of the two phases is due to the artifacts of analysis or experimental error cannot be completely excluded.

In summary, the *in vivo* and *in vitro* experiments show that the phylloquinone to plastoquinone-9 exchange is mediated by diffusion and does not involve the biosynthesis of any new protein, the expenditure of ATP, or the involvement of chaperones. That wild-type PS I contains exclusively phylloquinone in spite of a 20-fold excess of plastoquinone-9 in the membrane (Johnson, 2000; Johnson *et al*., 2001) implies that its affinity for the A_1 site is likely a factor of 10^3 or higher than plastoquinone-9.

In vitro replacement of the plastoquinone-9 with alien quinones in the A_1 site of menB PS I

In these experiments, I explore possible alternatives to either plastoquinone-9 or phylloquinone as acceptors in the A_1 site in PS I, using an *in vitro* reconstitution method. The *menB*$^-$ PS I complexes reconstituted with menaquinone-8 (a naphthoquinone structurally similar to the phylloquinone, with exception of the unsaturated phytyl chain) exhibits backreaction kinetics almost identical to that in the wild type (Fig. 4.6). This result indicates that degree of saturation of the phytyl chain does not significantly alter the function of the A_1 acceptor.

In contrast, *menB*$^-$ PS I complexes reconstituted with naphthoquinones which does not contain a phytyl chain (2-CH_3-NQ and 1,4-NQ) exhibit faster backreaction kinetics (about 15 ms in both cases) coinciding with a likely change in the midpoint potential of the A_1 acceptor. A similar result can be expected when forward electron transfer from A_1 to F_X is affected by a different orientation of the quinone in the A_1 site. For example, *menB*$^-$ PS I complexes reconstituted with 9,10-anthraquinone showed two

distinct kinetic phases in P_{700} reduction kinetics (ca. 16 ms and ca. 400 ms), which may reflect two different orientations of the anthraquinone in the A_1 site.

EPR studies of photoaccumulated PS I complexes were used to assess the incorporation of a foreign quinone into the A_1 site *in vitro*. Fig. 4.5 shows CW Q-band EPR spectra of *menB*$^-$ PS I complexes reconstituted with MQ-8, 2-CH_3-NQ, 1,4-NQ and 9,10-anthraquinone. Distinct hyperfine splittings due to the 2-methyl group were evident in the case of MQ-8 and 2-CH_3-NQ indicating correct orientation of the quinone in the A_1 site. A narrowing of the linewidth was observed in the case of anthraquinone. This was expected for a semianthraquinone radical, as a consequence of a reduced unpaired spin density on the carbonyl oxygen atoms.

Similar studies of quinone reconstitution in the *menA* mutant PS I *in vitro* gave identical results. This was expected, since the incorporation of the foreign quinone is non-enzymatic.

DISCUSSION

Results presented in this chapter demonstrate that plastoquinone-containing PS I complexes can be effectively used for *in vivo* biological and *in vitro* chemical quinone replacements. Previously, Wade Johnson and I demonstrated that certain substituted naphthoquinones supplied during growth of the *menB* mutants result in recovery of phylloquinone in the A_1 site (Johnson *et al*., 2001). EPR and optical properties of the PS I complexes with the recovered phylloquinone fully match the properties of the wild type. Specifically, the phylloquinone orientation, location, and amount of unpaired electron density on the 2-methyl group are the same as in the wild type, as determined by transient EPR, ESE pulsed EPR, and CW EPR spectroscopy, respectively (Johnson *et al*., 2001). Hence, we concluded that the interruption of the phylloquinone biosynthesis does not irreversibly alter the structure of the quinone-binding site. Given this important fact and provided that plastoquinone-9 has very low affinity to the A_1 site, it follows that the *menB* mutant PS I is an ideal system to employ for *in vitro* quinone replacements. This is true regardless of the chemical nature of the quinone; all other features of the A_1 site remain the same, both before and after quinone substitution.

The *menB* mutant cells were also able to assimilate a variety of substituted and unsubstituted anthraquinones supplied to the growth media. Even though HPLC-MS evidence for the methylation or phytylation is lacking, I suspect that phytylation occurs; this is based on the parallel studies of *menB* and *menA* mutant cells grown with supplied anthraquinones (Fig. 4.4). This result, if it can be confirmed by direct detection of phytylated anthraquinones, will broaden the known substrate range of the phytyl transferase.

Even though phytylation is presumably required for the incorporation of the supplemented quinones into PS I, my studies of the plastoquinone-9 reconstitution *in vitro* demonstrate that unphytylated naphthoquinones and anthraquinones can successfully replace plastoquinone in the A_1 site, and that they function as A_1 acceptors when added directly to the *menB*$^-$ PS I complex. This apparent discrepancy between *in vivo* and in *vitro* studies can be explained by considering that constraints on the

hydrophobicity of a given molecule are more strict *in vivo* in order for it to enter the PS I complexes inside the thylakoid membranes.

SUMMARY

Results of supplementations with anthraquinones suggest that three-ring aromatic quinones also serve as substrates for the phytyl transferase. The fact that phytyl transferase knockouts supplemented with naphthoquinones were not able to assimilate naphthoquinones into the A_1 site suggests that phytylation is a necessary step for the quinone incorporation into PS I *in vivo*. However, quinone replacement experiments performed *in vitro* showed that both phytylated and unphytylated quinones can replace plastoquinone-9 and function as A_1 acceptors when added to the *menB*$^-$ PS I complexes. A phytylation requirement for *in vivo* incorporation may indicate that quinones need to pass through a hydrophobic barrier in order to enter PS I in the thylakoid membrane.

REFERENCES

Alegria, A. E., Ferrer, A., Santiago, G., Sepulveda, E., and Flores, W. (1999*) J. Photochem. Photobiol. A* **127**, 57–65

Arnon, D. I. (1949) *Plant Physiol*. **24**, 1–15

Biggins, J., and Mathis, P. (1988) *Biochemistry* **27**, 1494–500

Bittl, R., Zech, S. G., Fromme, P., Witt, H. T., and Lubitz, W. (1997) *Biochemistry* **36**, 12001–12004

Depew, M. C., and Wan, J. K. S. (1988) in *The Chemistry of the Quinonoid Compounds* (Patai, S., and Rappoport, Z., eds) Vol. **II**, pp. 963–1018, John Wiley & Sons, New York

Golbeck, J. H. (1993) *Proc. Natl. Acad. Sci. U. S. A.* **90**, 1642–1646

Gunner, M. R., Robertson, D. E., and Dutton, P. L. (1986) *J. Phys. Chem*. **90**, 3783–3795

Gunner, M. R., Robertson, D. E., Lobrutto, R., McLaughlin, A., and Dutton, P. L. (1987) *Biophys. J.* **51**, A378-A378

Haraguchi, H., Yamano, K., Kusunoki, N., and Fukuda, A. (1997) *J. Agric. Food Chem.* **45**, 2784–2787

Itoh, S., Iwaki, M., and Ikegami, I. (1987) *Biochim. Biophys. Acta* **893**, 508–516

Itoh S, Iwaki M, I Ikegami, I. (2001) *Biochimica et Biophysics Acta* **45073** (2001) 1-24

Iwaki, M., and Itoh, S. (1991) *Biochemistry* **30**, 5347–5352

Johnson, T. W. 2000 *Ph.D. dissertation*

Johnson, T. W. Zybailov B., Jones A. D., Bittl R., Zech S., Stehlik D., Golbeck J. H., and Chitnis P. R.(2001*) Journal of Biological Chemistry* **276**(43), 39512–39521

Jung, Y. S., Yu, L., and Golbeck, J. H. (1995) *Photosynth. Res.* **46**, 249–255

Malkin, R. (1986) *FEBS Lett*. **208**, 343–346

Nitschke, W., and Rutherford, A. W. (1991) *Trends Biochem. Sci*. **16**, 241–245

Nugent, J. H. A. (1996) *Eur. J. Biochem*. **237**, 519–531

Oettmeyer, W., Dostatni, R., and Santel, H. J. (1987) *Z. Naturforsch*. **42**, 693–697

Rippka, R., Deuuelles, J., Waterbury, J. B., Herdman, M., and Stanier, R. Y. (1979*) J. Gen. Microbiol*. **111**, 1–61

Sakuragi Y., Zybailov B., Shen G. Z., Jones A. D., Chitnis P. R., van der Est A., Bittl R., Zech S., Stehlik D., Golbeck J. H., Bryant D. A. (2002) *Biochemistry* **41** (1) 394-405

Sétif, P., Ikegami, I., and Biggins, J. (1987) *Biochim. Biophys. Acta* **894**, 146–156

Sieckman, I., Van der Est, A., Bottin, H., Sétif, P., and Stehlik, D. (1991) *FEBS Lett*. **284**, 98–102

Sun, J., Xu, Q., Chitnis, V. P., Jin, P., and Chitnis, P. R. (1997) *J. Biol. Chem*. **272**, 21793–21802

Thurnauer, M. C., and Gast, P. (1985) *Photobiochem. Photobiophys.* **9,** 29–38

Trumpower, B. L. (1982) *Function of Quinones in Energy Conserving Systems*, Academic Press, New York

van der Est, A., Bock, C., Golbeck, J., Brettel, K., Sétif, P., and Stehlik, D. (1994) *Biochemistry* **33**, 11789–11797

van der Est, A., Prisner, T., Bittl, R., Fromme, P., Lubitz, W., Mobius, K., and Stehlik, D. (1997*) J. Phys. Chem. B* **101**, 1437–1443

van der Est, A., Sieckmann, I., Lubitz, W., and Stehlik, D. (1995) *Chem. Phys*. **184**, 349–360

Vassiliev, I. R., Jung, Y. S., Mamedov, M. D., Semenov, A. Y., and Golbeck, J. H. (1997) *Biophys. J*. **72**, 301–315

Woodbury, N. W., Parson, W. W., Gunner, M. R., Prince, R. C., and Dutton, P. L. (1986) *Biochim. Biophys. Acta* **851**, 6–22

Yang, F., Golbeck, J. H., and Bryant, D. (1998) *J. Phys. Chem*. **102**, 8288–8299

Zech, S. G., van der Est, A. J., and Bittl, R. (1997) *Biochemistry* **36**, 9774–9779

FIGURE LEGENDS

Figure 4.1 Molecular structures of naphthoquinones, benzoquinones and 9,10-anthraquinone. A common numbering of the quinone ring position is chosen in the text, with the carbonyl that is next to longer hydrocarbon chain placed in position 4.

Figure 4.2 Growth of the *menB18* (top) *and menA* (bottom) in the BG-11 media supplemented with various anthraquinones. The photos were taken after 3 days of growth in the high light conditions (ca. 60 μE m^{-2} s^{-1})

Figure 4.3 CW Q-band EPR spectra of photoaccumulated semiquinones in PS I complexes isolated from wild-type cells, *menB* mutant cells, and *menB* mutant cells grown in the media supplemented with 9,10-anthraquinone. EPR settings are the same as in Fig. 4.2

Figure 4.4 P_{700}^{+} reduction kinetics in PS I complexes isolated from the *menB*18 mutant grown in a media supplemented with various anthraquinones. From top to bottom: *menB18* control, *menB* + 9,10-anthraquinone, *menB* + 1-methyl-9,10-anthraquinone, *menB* + 1-amino-9,10-anthraquinone, *menB* + 2,6-diamino-9,10-anthraquinone. Excitation was provided by a xenon flash lamp. All other conditions as in Fig. 4.5

Figure 4.5 *In vitro* replacement of plastoquinone-9 in the *menB* mutant quinones: CW Q-band EPR spectra of the photoaccumulated semiquinones. Quinones were added to the *menB* mutant PS I complexes dissolved in 50 mM Tris pH 8.2 buffer (0.5 mg chlorophyll ml^{-1}) to the final concentration of 1 mM. Soluble quinones were washed out by dialysis and the samples were concentrated to 0.8 mg chlorophyll ml^{-1}.

Figure 4.6 *In vitro* replacement of plastoquinone-9 in the *menB* mutant by various quinones: P_{700}^{+} reduction kinetics. Replacement procedure was the same as described in

the legend to Fig. 4.5, for the optical measurements reconstituted PS I complexes were diluted to 50 µg chlorophyll ml^{-1}.

Figure 4.7 *In vitro* replacement of plastoquinone-9 in the *menB* mutant by phylloquinone - CW Q-band EPR spectra of the photoaccumulated semiquinone radicals in wild-type PS I, *menB*$^{-}$ PS I incubated with phylloquinone, and *menB* PS I. Reconstitution procedure: to PS I preparation at 1 mg chlorophyll ml^{-1} was added the solution of phylloquinone in ethanol, 0.5 mM final concentration. The mixture was illuminated for 10 min at room temperature and left for 8 hrs at 4 degrees °C in the dark. All other conditions were as in Figs. 4.5 and 3.9

Figure 4.8 *In vitro* reconstitution of plastoquinone-9 in *menB*$^{-}$ PS I complex by phylloquinone monitored by the near-IR spectrophotometry at 820 nm. *Top*, P_{700}^{+} reduction kinetics in men PS I complexes treated with increasing amounts of Vitamin K_1. The depicted transients represent average of three different reconstitution experiments for 4, 2 and 1 phylloquinone equivalents, and average of two different reconstitution experiments for the 0.5 and 10 phylloquinone equivalents. *Bottom*, absolute amplitudes of the fast and slow phases were calculated using multiexponential fit routine and plotted against molar ratio of Vitamin K_1 per P_{700}; *solid squares* represent recovery of the slow phase, *checked circles* represent loss of the fast phase.

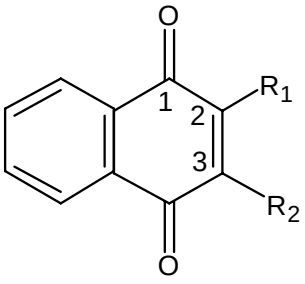

1,4-napthoquinones

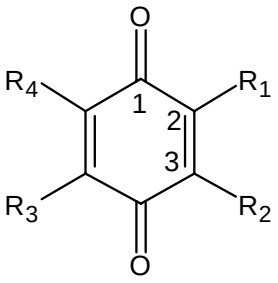

1,4-benzoquinones

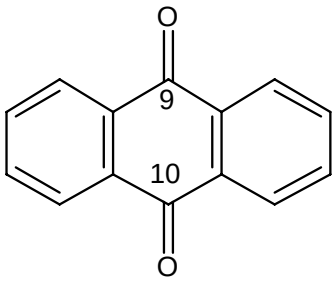

9,10-anthraquinone

Phylloquinone:

$R_1 = CH_3$,

R_2 =

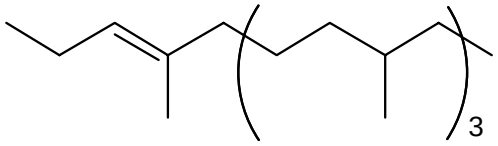

(phytyl)

Plastoquinone-9:

$R_1 = H$; $R_4, R_3 = CH_3$

R_2 =

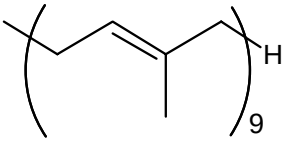

Figure 4.1

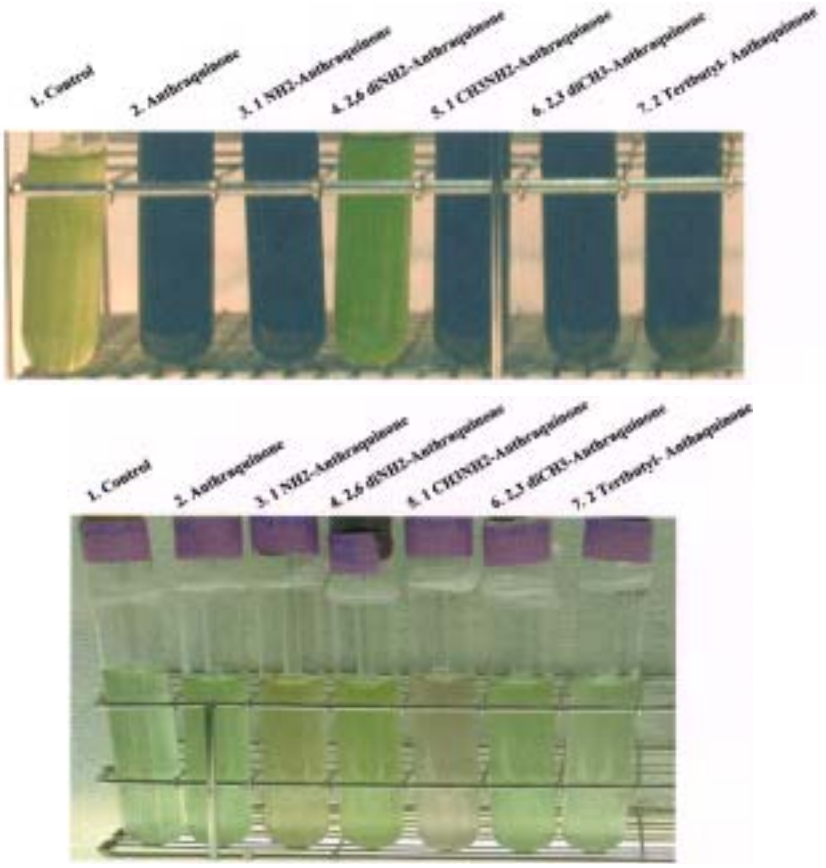
1. Control
2. Anthraquinone
3. 1 NH2-Anthraquinone
4. 2,6 diNH2-Anthraquinone
5. 1 CH3NH2-Anthraquinone
6. 2,3 diCH3-Anthraquinone
7. 2 Terbutyl- Anthaquinone
1. Control
2. Anthraquinone
3. 1 NH2-Anthraquinone
4. 2,6 diNH2-Anthraquinone
5. 1 CH3NH2-Anthraquinone
6. 2,3 diCH3-Anthraquinone
7. 2 Terbutyl- Anthaquinone

Figure 4.2

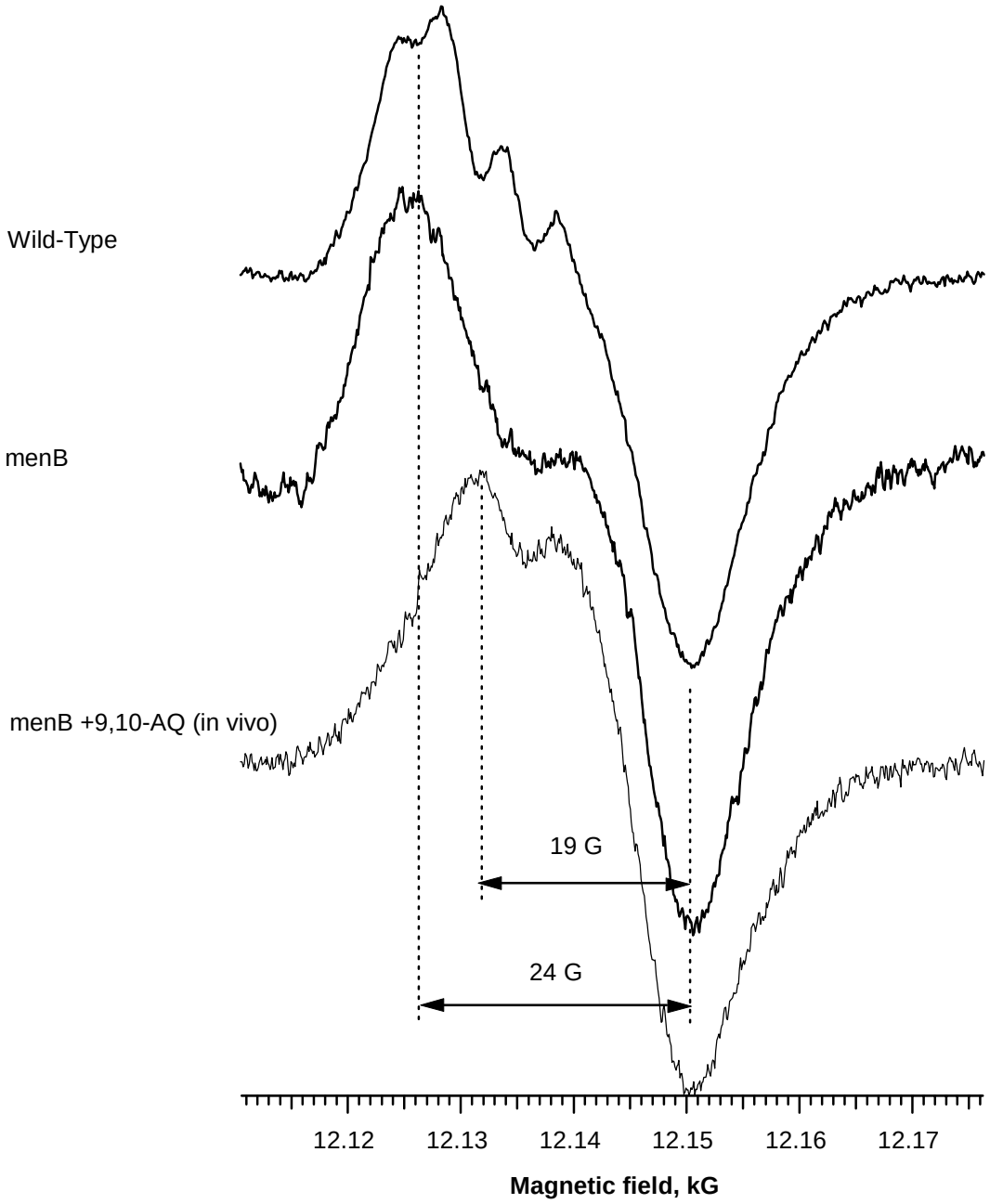
Wild-Type
menB
menB +9,10-AQ (in vivo)
19 G
24 G
12.12
12.13
12.14
12.15
12.16
12.17
Magnetic field, kG

Figure 4.3

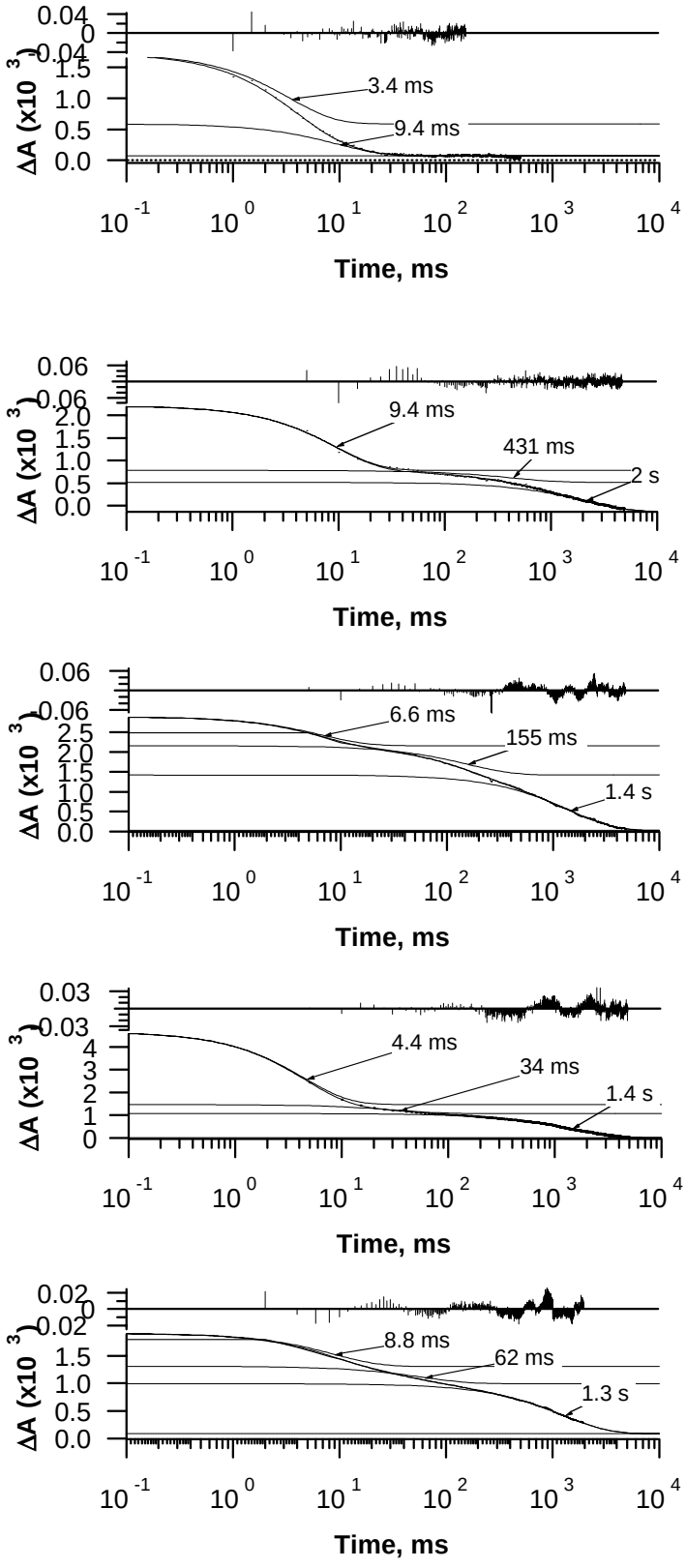
0.04
0
-0.04
ΔA (x10 3)
1.5
1.0
0.5
0.0
3.4 ms
9.4 ms
10 -1
10 0
10 1
10 2
10 3
10 4
Time, ms
menB
Grown in a media supplemented with :
0.06
-0.06
2.0
1.5
1.0
0.5
0.0
9.4 ms
431 ms
2 s
menB + AQ
2.5
6.6 ms
155 ms
1.4 s
menB +1-Me-AQ
0.03
-0.03
4
3
2
1
0
4.4 ms
34 ms
1.4 s
menB + 1-NH 2AQ
0.02
-0.02
8.8 ms
62 ms
1.3 s
menB +2,6-di-NH 2-AQ

Figure 4.4

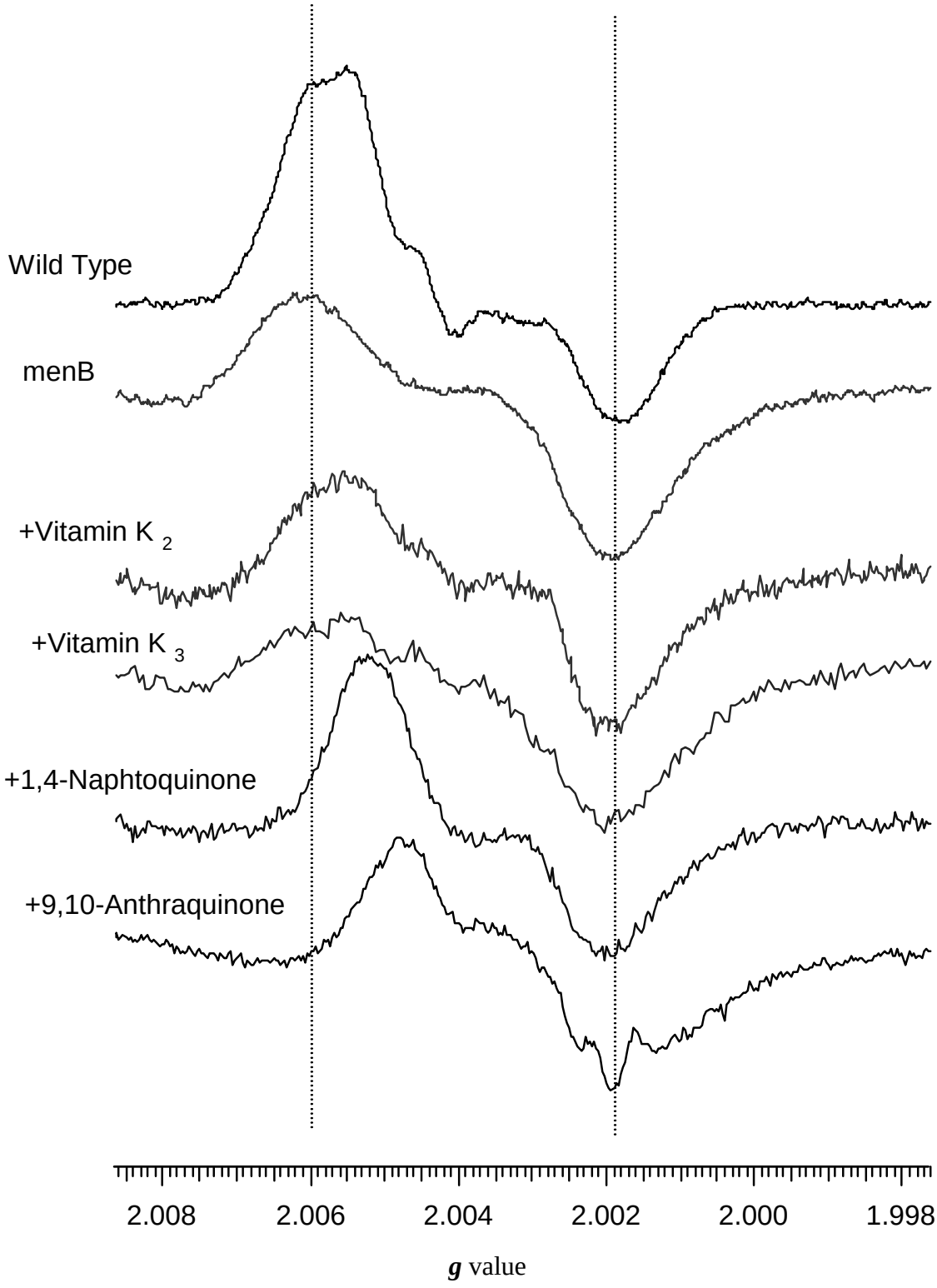
Wild Type
menB
+Vitamin K 2
+Vitamin K 3
+1,4-Naphtoquinone
+9,10-Anthraquinone
2.008
2.006
2.004
2.002
2.000
1.998
g value

Figure 4.5

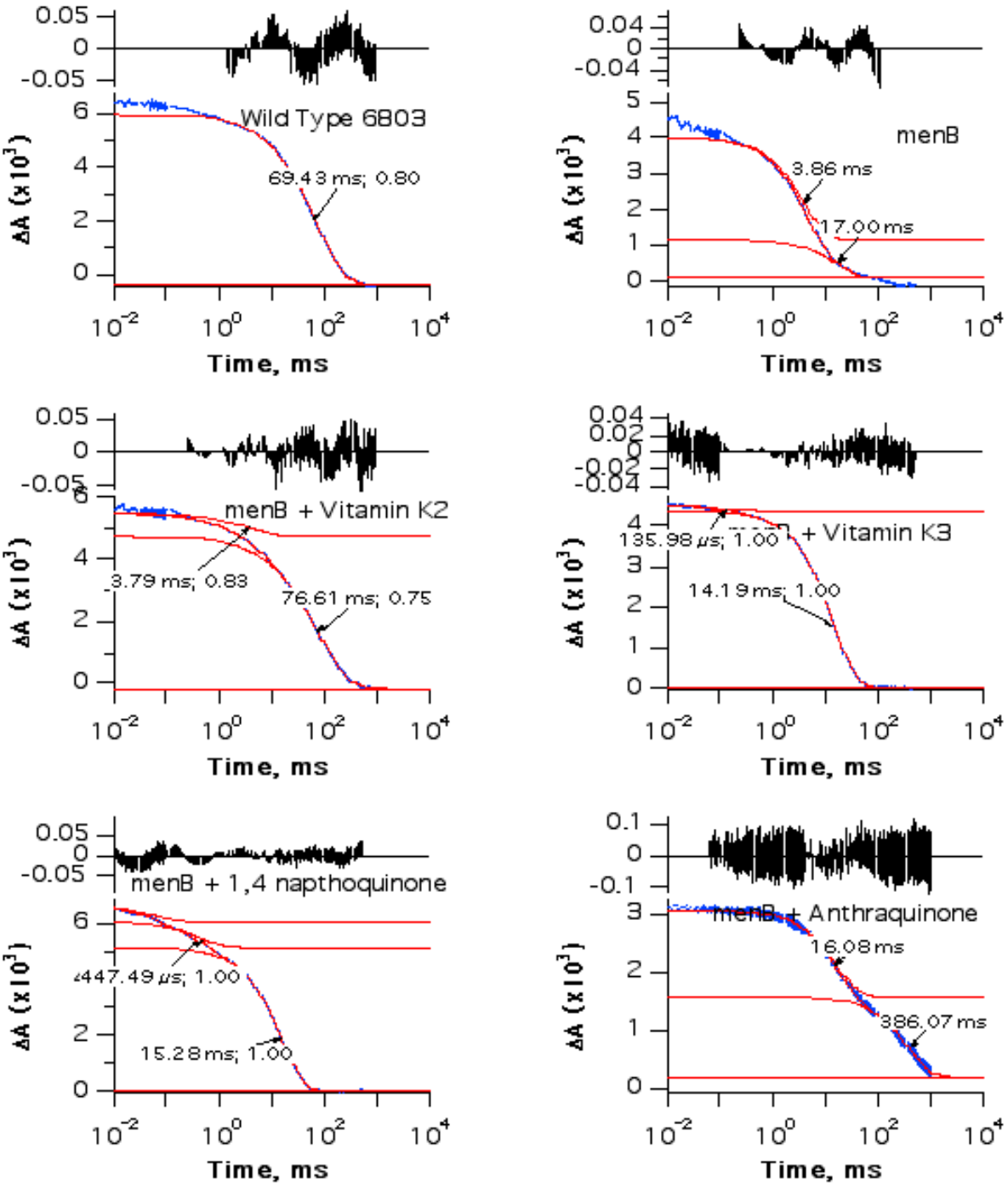
Wild Type 6803
69.43 ms; 0.80
menB
3.86 ms
17.00 ms
menB + Vitamin K2
3.79 ms; 0.83
76.61 ms; 0.75
+ Vitamin K3
14.19 ms; 1.00
menB + 1,4 napthoquinone
447.49 µs; 1.00
15.28 ms; 1.00
+ Anthraquinone
16.08 ms
386.07 ms
ΔA (x10³)
Time, ms

Figure 4.6

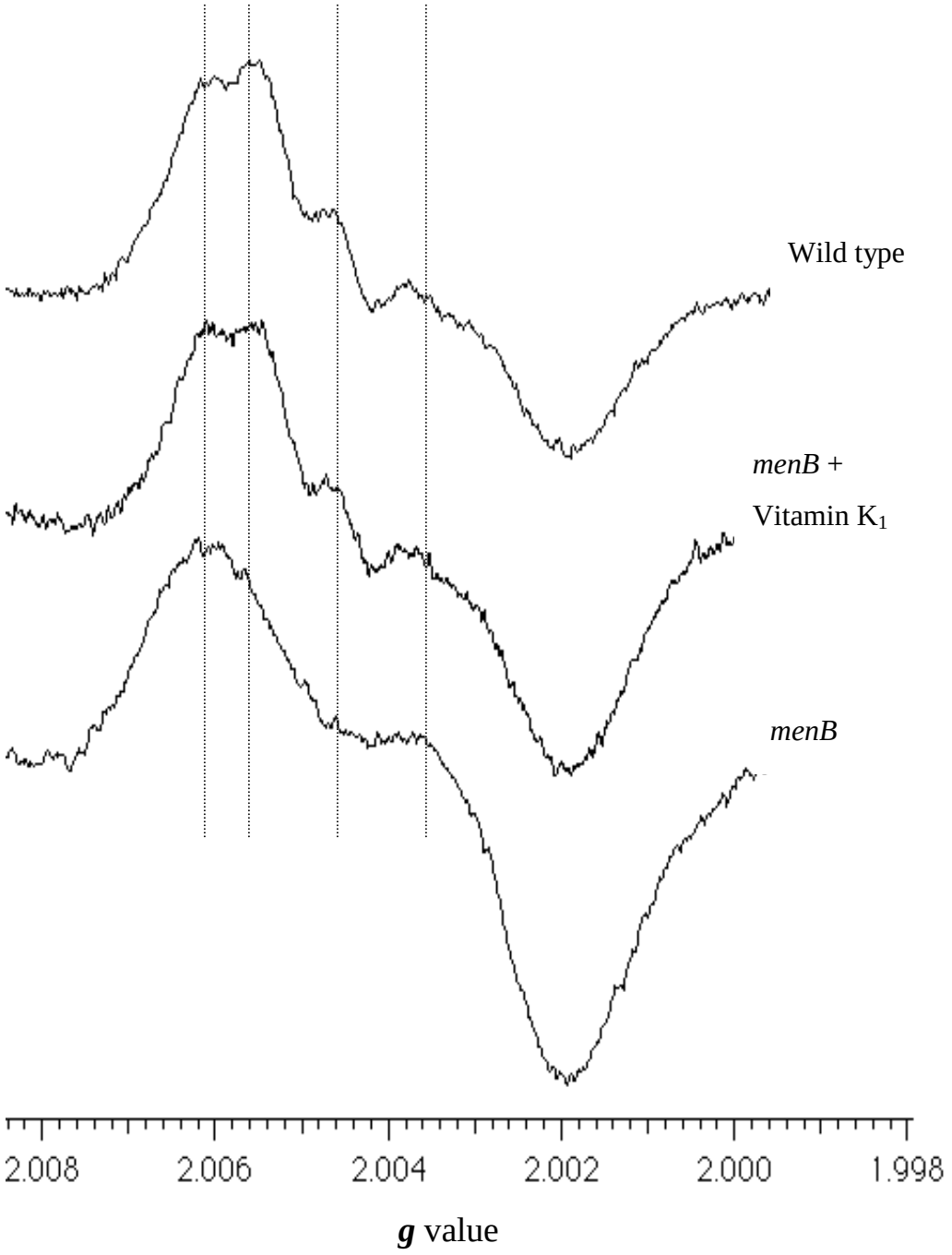
Wild type
menB +
Vitamin K_1
menB
2.008
2.006
2.004
2.002
2.000
1.998
g value

Figure 4.7

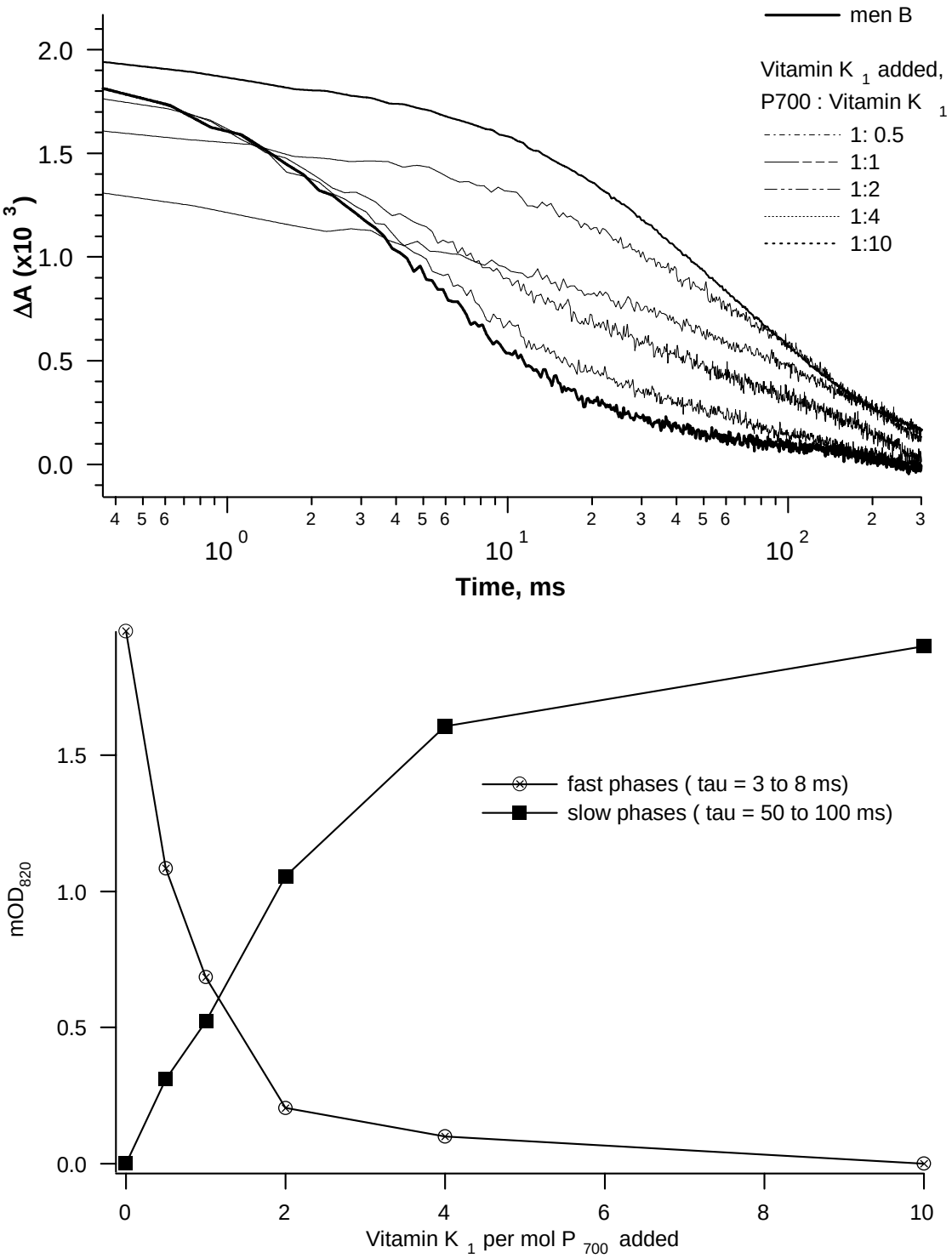
men B
Vitamin K 1 added,
P700 : Vitamin K 1
1: 0.5
1:1
1:2
1:4
1:10
ΔA (x10 3)
2.0
1.5
1.0
0.5
0.0
4 5 6 2 3 4 5 6 2 3 4 5 6 2 3
10 0
10 1
10 2
Time, ms
fast phases (tau = 3 to 8 ms)
slow phases (tau = 50 to 100 ms)
mOD820
1.5
1.0
0.5
0.0
0 2 4 6 8 10
Vitamin K 1 per mol P 700 added

Figure 4.8

Chapter 5

Directionality of Electron Transfer in Type I Reaction Centers

[In preparation, in part as papers: "Electron Transfer in Cyanobacterial Photosystem I. Physiological and Spectral Characterization of Site-Directed Mutants in a Putative Electron Transfer Pathway from A_0 to F_X" by Wu Xu, Boris Zybailov, Gaozhong Shen, Julia Pushkar, Alfia Valieva, Christian Teutloff, Stephan G. Zech, Robert Bittl, Art van der Est, Dietmar Stehlik, Parag Chitnis and John H. Golbeck;

"Evidence for Highly Asymmetrical Electron Transfer in Cyanobacterial Photosystem I: Characterization of Forward Electron Transfer through Q_K-A and Q_K-B in Quinone Binding Site Point Mutants" by Alfia Valieva, Wu Xu, Boris Zybailov, Klaus Brettel, Mariana Guergova-Kuras, Julia Pushkar, Gaozhong Shen, Dietmar Stehlik, Stephan G. Zech,Parag R. Chitnis, John H. Golbeck, Art van der Est;

"Electron Transfer in Cyanobacterial Photosystem I: Characterization of Reverse Electron Transfer through Q_K-A and Q_K-B in Quinone Binding Site Point Mutants" by Boris Zybailov, Oksana Gopta, Wu Xu, Parag Chitnis, and John H. Golbeck]

ABSTRACT

A common structural feature of the photosynthetic reaction centers is the presence of two pseudo-symmetrical branches of electron carries. In Type II reaction centers electron transfer is unidirectional; the electron proceeds through only one branch of cofactors and reduces the terminal acceptor, a soluble quinone, located in the other branch. In PS I there no functional constraint on the directionality of the electron transfer is apparent. Hence, electron transfer from P_{700} to the F_X iron-sulfur cluster can involve one or both branches.

In this chapter, I address the directionality issue by studying the phylloquinone-binding pocket site-directed mutants, W697F (PsaA) and W677 (PsaB), S692C (PsaA) and S672 (PsaB), R694A (PsaA) and R674A (PsaB) using EPR spectroscopy and time-resolved differential spectrophotometry in the UV/Vis region. The recombination kinetics is faster in all of the mutants compared to the wild type. The W to F mutation on the PsaA-side has a less pronounced effect on the backreaction kinetics than the corresponding mutation on the PsaB-side; after an excitation flash, P_{700}^+ is re-reduced in the dark with a ca. 10 ms lifetime in the PsaB-side mutant while the PsaA-side W to F mutant has backreaction lifetimes in the wild-type range (ca. 30 ms to 100 ms).

In the cases of S to C and R to A substitutions, the effect is different; the mutations on the PsaA-side show the fastest backreaction kinetics. These findings imply that the backreaction is bidirectional in PS I, with both quinones capable of mediating the P_{700}^+ re-reduction in the dark. The introduced 'symmetry breaking' via the site-directed mutations forces the backreaction to proceed through the quinone with the highest midpoint potential.

The photoaccumulated semiquinone radicals in the wild-type and mutant PS I complexes is further studied by Q-band (34 GHz) CW-EPR spectroscopy. The strength of the hyperfine splitting due to the 2-CH_3 group of the quinone is reduced in the case of PsaA-side mutant S692C (PsaA), whereas it is strengthened in the case of W to F mutants,. The latter finding is corroborated by the pulsed ENDOR and transient EPR data, which also show that the W697F (PsaA) mutation leads to an increase in the

hyperfine coupling of the methyl group on the phylloquinone ring while the S692C (PsaA) mutation causes a decrease in this coupling.

I conclude that: i) mutation of amino acids in close contact with the PsaA-branch quinone in PS I leads to changes in the spin density distribution of the reduced quinone observed by EPR, either as a result of changes in the electronegativity of the environment and/or changes in the strength of the π-stacking ii) at low temperature, cyclic electron transfer to A_1 occurs along the PsaA-branch (because alteration of amino acids only in the vicinity of the PsaA-branch phylloquinone, Q_K-A, leads to changes in the pulsed ENDOR, CW-EPR and transient EPR spectra); 3) the transient EPR spectra at room temperature are due to radical pairs generated predominantly by electron transfer along the PsaA-branch of cofactors.

At room temperature, the absorption differences in the near UV/blue of whole cells and PS I complexes of wild-type *Synechocystis* sp. PCC 6803 reveal a major, fast kinetic phase with lifetime of ca. 300 ns and a minor, slow kinetic phase with lifetime of ca. 10 ns. Whole cells and PS I complexes from the S692C (PsaA) and W697F (PsaA) of mutants show a significant slowing of the slow kinetic component, while the W677F (PsaB) and S672C (PsaB) mutants show a less significant slowing of the fast kinetic component. Transient EPR studies directly detect the slowing of the slow kinetic component, and given the optically-measured time constants for the mutants, the fast component should slowed, and thus be detectable directly. It should also be detected indirectly by this predicted influence on the spin polarization patterns. The combined effect of temperature and mutation, observed for the PsaA-side and predicted for the PsaB-side, is expected to slow the fast kinetic phase to well within the time window accessible by transient EPR; yet at 260K, the spectra and kinetics of the W677F (PsaB) and S672C (PsaB) mutants remain identical to wild-type PS I.

Simulations of the early time behavior of the spectra show that the signals are due only to $P_{700}^+ A_1^-$ and that no significant population of $P_{700}^+ F_X^-$ is present during the first 100 ns following laser excitation. Together, the results demonstrate that the slow kinetic phase is due to electron transfer from Q_K- in the PsaA-branch to F_X, and that this accounts for most of the electrons being transferred. The assignment of the fast kinetic

phase and its relative amplitude remain uncertain; however, it is clear that the fast kinetic phase accounts for a minor fraction of the electrons being transferred. All of the results point toward a significant asymmetry in the electron transfer in PS I and suggest that the forward transfer in cyanobacterial PS I is predominately along the PsaA-branch.

The transient EPR experiments reported in this chapter were performed in collaboration with Dietmar Stehlik. The optical spectrophotometry in the UV was done in collaboration with Klaus Brettel. The mutant strains of *Synechocystis* sp. PCC 6803 were generated for these studies by Wu Xu and Parag Chitnis. Initial physiological and biochemical characterization of the mutant cells was performed by Gaozhong Shen.

INTRODUCTION

The 2.5 Å structure of PS I complex reveals the presence of two chains of electron carries between P_{700} and F_X which are related to each other by C_2 rotational symmetry in the interface of the PsaA/PsaB heterodimer (*Jordan et al.*, 2001). All reaction centers whose structure has been solved are known to share a motif of symmetrically arranged branches of electron carriers. Recent phylogenetic analysis presented in (Baymann *et al*., 2001) places the type I reaction center as the ancestral photosystem and infers the descendence of PS II from the type I reaction center via gene duplication and gene splitting (see also chapter 1).

Based on the structural and phylogenetic relationships between the reaction centers, unidirectionality of the electron transfer is a reasonable conjecture for PS I complex . Electron transfer in Type II reaction centers is unidirectional since there is no direct electron transfer to Q_B. However, there is still a possibility that unidirectionality is an emergent feature in the Type II reaction centers, and that the ancestral photosynthesis was bidirectional (Baymann *et al*., 2001, Guergova-Kuras *et al*., 2001). Bidirectionality in PS I complex, therefore, is a reasonable conjecture. Additional support for bidirectionality comes from the sequence similarity between PsaA and PsaB, which is ca.60% overall, and almost identical within the heterodimer interface at the quinone binding sites). Moreover, Type I bacterial reaction centers are homodimers (Buttner, *et al*., 1992), hence there is very little room for any structural ambiguity leading to the functional differences between the two possible paths for the electron transfer.

In the PS I, however, I identify certain structural differences that exist between the two branches of the electron carries. As illustrated in Fig. 5.1, amino acid W673 (PsaB) does not have a counterpart on the PsaA-side. The two bound quinones differ in the positions of their hydrophobic side chains; on the PsaB-branch quinone, the phytyl tail is "curved around", making hydrophobic contacts with the PsaB amino acid residues, while on PsaA-branch, the quinone phytyl chain is more linear, making hydrophobic contacts with carotenoids and chlorophylls. Another interesting feature is the arrangement of the structured water between the phylloquinones and F_X, which is

different on the PsaA and PsaB sides (not shown). As a result, the system of hydrogen bonds is asymmetric in the vicinity of the phylloquinones. While it is impossible to resolve the directionality issue from the structural arguments alone, what is apparent is that the two quinones may differ in their functionality (*i.e.* slightly different midpoint potentials or rates of related electron transfer). The experimental data accumulated todate, unfortunately, is still insufficient to arrive at a firm conclusion, and sometimes leads to opposite conclusions.

The experimental evidence supporting unidirectionality comes from EPR experiments in which only one semiphylloquinone can be photoaccumulated under strongly reducing conditions (MacMillan *et al.*, 1997; Yang *et al*., 1998). In this chapter, I address this issue by studying photoaccumulation of the semiphylloquinone in wild-type and mutant PS I complexes. It can be demonstrated that two different quinones are accumulated; which one depends on experimental conditions (*i.e.* the percentage of glycerol in the reaction medium and the time and temperature of the photoaccumulation protocol). Transient EPR experiments can to support of the unidirectionality hypothesis (Sieckmann *et al*., 1991; van der Est *et al*., 1994); the limitation, however, is that this technique cannot resolve lifetimes faster than ca. 20 ns.

Another set of observations that must be considered in terms of a unidirectional or bidirectional model concern the biphasic oxidation of A_1 - as monitored by visible spectroscopy (Sétif and Brettel, 1993; Joliot and Joliot, 1999) - and the biphasic back donation to P_{700}^+(Brettel and Golbeck, 1995). The two kinetic phases of forward electron transfer were explained by a fast redox equilibration of A_1 and F_X (ca. 20 ns kinetic phase) and a slower (ca. 150 ns kinetic phase) decay of this state due to further electron transport to F_A/F_B (Sétif and Brettel, 1993). An alternative explanation of the biphasic kinetics in PS I involve the presence of the two structurally different quinone environments (Joliot and Joliot, 1999). Specifically, the two different kinetics can be attributed to two different quinone environments, one associated with PsaA and the other with PsaB (Guergova-Kuras *et al*., 2001). The studies of W to F site-directed mutants in *Chlamydomonus rheinhardtii* further demonstrated that the mutation of a residue near the quinone on the PsaB-side specifically affects the faster components, while the

corresponding mutation on the PsaA-side affects the slower component (Guergova-Kuras *et al*., 2001). This led the authors to conclude that both branches of cofactors are active. General limitations of the mutagenic approach must, however, be considered: there is always a possibility that the introduced mutation may alter the structure in a manner that has not been predicted. For example, there is a chance that a mutation on the PsaA side, can affect the environment of the PsaB side, and visa-versa. Hence, the results might not reflect function in the wild type. Therefore, while using the mutagenic approach, one must be careful, and consider not a single mutation, but various sets of mutations, to separate different influences and relate the obtained results to the wild type.

In this chapter I use the mutagenic approach and study three different sets of mutants: (W to F mutants, R to A mutants and S to C mutants on PsaA, as well as corresponding mutants on PsaB; Fig. 5.1). I present studies of the kinetics of reverse and forward electron transfer in the mutants W677F (PsaA), W677F (PsaB), S692C (PsaA), S672C (PsaB), R674A (PsaB), R690A (PsaA), using optical absorption difference spectroscopy and transient EPR spectroscopy. I also report photoaccumulation of the phylloquinone in the mutant and wild-type PS I complexes in a search for two different quinone environments.

MATERIALS AND METHODS

Generation of the site-directed PS I mutants

For site-directed mutagenesis of the *psaA* and *psaB* genes, two recipient strains were constructed with deletion of a portion of the *psaA* gene or deletion of the whole *psaB* gene. The *Synechocystis* sp. PCC 6803 pWX3 recipient strain was constructed through deletion of the EagI-EcoRI fragment that contains the 1130-bp 3' part of the *psaA* gene and the whole *psaB* gene, and replacement with a spectinomycin-resistance cartridge gene. The *Synechocycstis* sp. PCC 6803 pCRT□B recipient strain was obtained through deletion of the HindIII-EcoRI fragment that contains the 3' half of the *psaB* gene and replacement with a 1.3 kbp kanamycin-resistance cartridge gene.

Two plasmids pGEM-3C+ and pIBC were constructed as the templates for PCR-based site-specific mutagenesis. To generate mutations in the Q_k-B binding site, the plasmid pGEM-3C+ was constructed through cloning of a1588-bp segment of the *psaB* 3' region and the 760-bp region downstream of the *psaB* into the pGEM7z vector. A chloramphenicol resistance gene was inserted at the *Eco*RI site just downstream of *psaB* gene. To generate mutations in the Q_k-A binding site, the pIBC plasmid was constructed through cloning of a DNA fragment that contained most of the *psaA* gene, the *psaB* gene, and a 760 bp downstream region of the *psaB* gene into a pBluescript II KS vector. A chloramphenicol resistant cassette gene was inserted after the 3' terminator of the *psaB* gene. PCR mutagenesis was carried out using the Transformer^{TM} site-directed mutagenesis kit (CLONTECH Laboratories, Inc). The constructs with specific mutations in the *psaA* gene were generated through PCR mutagenesis using the pIBC plasmid DNA as the template and appropriate primers for W677F (PsaA), R694A (PsaA) and S692C (PsaA). The constructs with specific mutations in the *psaB* gene were generated through PCR mutagenesis using the pGEM-3C+ plasmid DNA as the template and appropriate primers for W677F (PsaB), R674A (PsaB) and S672C (PsaB). All mutation sites were confirmed by DNA sequencing.

The plasmids with the desired *psaA* mutations derived from pIBC were used to transform the *Synechocystis* sp. PCC 6803 recipient strain pWX3. The plasmids with the

desired *psaB* mutations derived from pGEM-3C+ were used to transform the *Synechocystis* sp. PCC 6803 recipient strain pCRT□B. Transformants with chlorophyll-resistance were selected under low light conditions. To verify the full segregation of the transformants, DNA fragments containing the mutation sites were amplified through PCR from the genomic DNA of the mutant strains and sequenced to confirm the desired nucleotide change.

Growth of Synechocystis sp. PCC 6803

Wild-type and mutant *Synechocystis* sp. PCC 6803 cells were grown in medium BG-11 (Rippka *et al.*, 1979). Agar plates for the growth of mutant strains were kept at low light intensity (2 to 5 μE m^{-2} s^{-1}); liquid cultures of wild-type and mutant strains were grown under reduced light conditions (10 to 20 μE m^{-2} s^{-1}) in the presence of 5 mM glucose (Johnson, 2000). Cell growth in liquid cultures was monitored by measuring the absorbance at 730 nm using a Cary-14 spectrophotometer that had been modified for computerized data acquisition by On-Line Instruments, Inc. (Bogart, GA). Cells from liquid starter cultures in the late exponential phase of growth (A730 = 0.8 to 1.2) were harvested by centrifugation and were washed once with BG-11 medium. All cultures were adjusted to the same initial cell density (A730 = 0.1) for growth experiments and bubbled with air as described (Shen *et al.*, 1993).

Isolation of Thylakoid Membranes and PS I Complexes

Thylakoid membranes were prepared from cells in the late exponential growth phase as described (Shen *et al.*, 1993). Cells were broken by two passages through a French pressure cell at 20,000 lb in^{-2} at 4 °C. The thylakoid membranes were pelleted by centrifugation at 50,000 × g for 45 min. The thylakoid membranes were resuspended in buffer (50 mM HEPES/ NaOH, pH 8.0, 5 mM $MgCl_2$, 10mM $CaCl_2$, 0.5% (v/v) dimethyl sulfoxide, and 15% (v/v) glycerol) for storage and/or in 50 mM Tris/HCl, pH 8.0, for further PS I complex preparations. For the isolation of PS I complexes, thylakoid membranes were solubilized in 1% (w/v) β-DM for 2 to 4 h at 4 °C. The trimeric and monomeric PS I complexes were separated by centrifugation on 5 to 20% (w/v) sucrose

gradients with 0.03% β-DMin 50 mM Tris, pH 8.0. Further purification was achieved by a second centrifugation on sucrose gradients in50 mM Tris, pH 8.0, in the absence of β-DM(Johnson, 2000). at 10 ml min-1.

Q-band CW EPR Spectroscopy

Photoaccumulation experiments at Q-band (34 GHz) were carried out using a Bruker ESR300E spectrometer equipped with an ER 5106 QT-W1 resonator with a port for in-cavity illumination. Cryogenic temperatures were maintained with an ER4118CV liquid nitrogen cryostat and controlled by an ER4121 temperature control unit. The microwave frequency was measured with a Hewlett-Packard 5352B frequency counter, and the magnetic field was measured with a Bruker ER035M NMR gaussmeter. The magnetic field was calibrated using γ,γ-bisdiphenylene-β-phenylallyl complexed 1:1 with benzene.

Photoaccumulation protocols on wild-type and mutant PS I complexes were carried out in a manner similar to that described in (Yang *et al.,* 1998). Prior to the measurement, the pH of the sample was adjusted to 10.0 with glycine buffer, and sodium dithionite was added to a final concentration of 50 mM. After incubation for 20 min in the dark, the sample was placed into the resonator, the temperature adjusted to 205 K, and a background spectrum was recorded. The sample was illuminated with a 20-mW He-Ne laser at 630 nm for 40 min, the laser was turned off, and the light-induced spectrum recorded. The spectra reported represent the difference between the two measurements.

For the search of different quinone environment percent glycerol, pH, time and temperature of illumination, were varied and are further discussed in the results section.

Transient EPR spectroscopy

The low temperature X-band (9 GHz) transient EPR experiments were carried out on a laboratory-built spectrometer, using a Bruker ER046 XK-T microwave bridge equipped and an ER-4118X-MD-5W1 dielectric ring resonator and an Oxford CF935 helium gas-flow cryostat (12). The loaded *Q*-value for this dielectric ring resonator was about *Q*=3000, equivalent to a rise time of $\tau_r = Q/(2\pi * \nu_{mw}) \approx 50$ ns. The low temperature

X-band experiments on the R694A (PsaA) and R674A (PsaB) mutants were carried out using the set-up described below for room temperature measurements except that the sample was placed in quartz tube and a liquid nitrogen cryostat was used to control the temperature. Q-band (35 GHz) transient EPR spectra of the samples were also measured with the same set-up except that a Bruker ER 056 QMV microwave bridge equipped with a home built cylindrical resonator was used. All samples contained 1 mM sodium ascorbate (NaASC) and 50 µM phenazine methosulfate (PMS) as external redox agents and were frozen in the dark. The samples were illuminated using a Spectra Physics Nd-YAG/MOPO laser system operating at 10 Hz.

Room temperature X-band experiments were performed using a modified Bruker ESP 200 spectrometer equipped with a home-built, broadband amplifier (bandwidth >500 MHz). A flat cell and a rectangular resonator were used and the samples were illuminated using a Q-switched, frequency doubled Continuum Surelite Nd-YAG laser at 532 nm with a repetition rate of 10 Hz. 1 mM NaAsc and 50 mM PMS were added to mediate cyclic electron transfer.

Optical Kinetic Spectroscopy in the Near IR Region

Optical absorbance changes in the near-IR were measured using a laboratory-built spectrophotometer (Vassiliev *et al.*, 1997). To ensure resolution of kinetics in the microseconds time domain, a high frequency roll-off amplifier described in the original specifications was not used, and the signal was fed directly into the plug-in (11A33 differential comparator, 100-MHz bandwidth) of the Tektronix DSA601 oscilloscope. The sample cuvette contained wild-type or mutant PS I complexes at 50 µg chlorophyll ml^{-1} in 25 mM Tris/HCl, pH 8.3, 10 mM sodium ascorbate, 4 µM DCPIP, and 0.04% β-DM.

Flash-Induced Transient Absorption Spectroscopy in the near UV/Blue region

Flash-induced absorbance changes were measured with a time resolution of about 2 ns with a set-up described previously (Brettel *et al*., 1998) using 300 ps pulses of about 300 nJ/cm^2 at 532 nm for excitation (repetition rate, 1 Hz) and the relatively flat top of a

50 µs Xe flash as measuring light. Stock solutions of PS I complexes were diluted in a buffer containing 50 mM Tris, pH 8.3, 10 mM NaAsc and 500 µM DCPIP, to a final chlorophyll concentration of typically 60 and 150 µM for measurements at 380 and 480 nm, respectively.

The optical pathlength for the measuring light was 2 mm. Between 1024 and 4096 transients were averaged for each sample and wavelength in order to improve the signal-to-noise ratio. A Marquardt least squares algorithm program was used for fitting of the absorbance change transients to a multi-exponential decay. Time zero was defined as the midpoint of the rising edge of the transient, and fitting was started from 2.5 ns after time zero.

Analysis of Kinetic Data

The multiexponential fits of optical kinetics were performed by the Marquardt algorithm in Igor Pro version 4.1 (Wavemetrics Inc., Lake Oswego, OR) on a G3/300 Macintosh computer. The best solution was chosen based on the analysis of χ^2, standard errors of the parameters, and the residuals of the fits.

RESULTS

Backward Electron Transfer Kinetics in the A_1 Mutants

While the pathway taken by the electron in the initial charge separation determines the directionality of forward electron transfer, the pathway of the backreaction is determined at F_X, the point at which the bifurcating pathway converges. Since forward electron transfer originates from P_{700}, and backward electron transfer originates from F_X^-, it is likely that the factors that govern the choice of the pathway are different in each case, and that the behavior of the forward and backreactions may differ with respect to directionality.

The kinetics of P_{700}^+ reduction in PS I complexes can be monitored using the absorbance change at 820 nm, which is depicted in Fig. 5.2 for the wild type, W697F (PsaA) and W677F (PsaB). At 298 K, wild-type PS I shows that the majority of P_{700}^+ is reduced with lifetime of ca. 100 ms. A minor, slow decay phase, with lifetime of ca. 1 s results from the donation by DCPIP in PS I complexes in which the electron has been lost from the acceptor side. The re-reduction of P_{700}^+ in the W697F (PsaA) mutant is faster than the wild type, with lifetime of ca. 22 ms, and the lifetime in the W667F (PsaB) mutant shows a further acceleration in the kinetics of P_{700}^+ reduction to lifetime of ca. 7 ms. The room-temperature optical kinetics of P_{700}^+ reduction in PS I complexes of the wild type, S692C (PsaA) and S672C (PsaB) mutants are also depicted in Fig. 5.5. The lifetime of P_{700}^+ in the S672C (PsaB) mutant is longer than in the wild type, with lifetime of ca. 58 ms, and the lifetime in the S692C (PsaA) mutant shows a further acceleration in the kinetics of P_{700}^+ reduction to lifetime of ca. 8 ms. Therefore, in contrast to the W mutants, in which alteration of the PsaB-branch quinone produces the greatest acceleration in the rate of P_{700}^+ reduction, in the S mutants, the PsaA-side mutation produces the greatest acceleration in the rate of P_{700}^+ reduction. A similar effect is observed with R to A mutants, where the R694A (PsaA) mutant shows the faster backreaction kinetics (lifetime of ca. 20 ms) while the PsaB-side mutant, R674A, barely differ from the wild type.

According to the reasoning outlined in (Semenov *et al*., 2002) and (Shinkarev *et al*., 2001), an acceleration in the backreaction kinetics implies that the quinone in the mutant has more oxidizing redox potential than the quinone in the wild type. The significance of this result is that backward electron transfer from $[F_A/F_B]^-$ to P_{700}^+ may to proceed down the branch of cofactors that confers the more oxidizing environment to the quinone. The break in the kinetic symmetry between the PsaA-side and PsaB-side mutants within the class of W to F mutants and S to C mutants implies that the environment of the two quinones is not identical. Thus, backward electron transfer is likely to be governed by a different set of initial constraints than those that govern forward electron transfer originating in P_{700}. The different rate constants from the PsaA-side and PsaB-side mutants imply that the redox potentials of the PsaA-branch phylloquinone and PsaB-branch phylloquinone are not identical.

CW EPR Spectroscopy at Q-band of Photoaccumulated A_1 in the mutant and wild-type PS I complexes

The CW EPR spectrum of photoaccumulated semiphylloquinone in wild-type PS I complexes, obtained using standard protocol as described in Material and Methods exhibits strong hyperfine splitting due to increased spin-density on the carbon atom of the 2-methyl group (chapter 2, see also Yang *et al*., 1998). The observed pattern of the strong hyperfine splitting is most likely due to the protein environment, since the semiphylloquinone in an alcoholic solution shows significantly weaker hyperfine coupling and the four-line pattern is not observed.

Therefore, by measuring Q-band EPR spectra and estimating strength of the hyperfine interactions of the photoaccumulated semiphylloquinone in the mutant PS I complexes, we can keep track of the structural changes because they lead to variations in the spin density of the 2-methyl group by. Figs. 5.3, 5.5 show the photoaccumulated EPR spectra in the sets of W to F mutants, S to C mutants, respectively. Photoaccumulated semiphylloquinone in the W677F (PsaB) exhibits less prominent hyperfine splitting than does the corresponding PsaA-side mutant, W677F (PsaA). The situation is reversed for the sets of S to C and R to A mutants, where it is the PsaA-side mutants that show the

lack of the hyperfine pattern, while the pattern of hyperfine splitting of 2-CH_3 in the PsaB-side mutants does not differ significantly from that of the wild type. A small amount of A_0^- is also present in the wild type, W697F (PsaA) and S692C (PsaA) spectra, and contributes to the overall spectra in the highfield (g_{zz}) region. Contamination of the semiphylloquinone spectral shape by A_0^- is rather poorly reproducible, and probably is the function of heterogeneity of the PS I complex preparation, in that we expect to get A_0^- photoaccumulated in those centers where A_1 is either missing or doubly reduced (Yang *et al*., 1998).

Both EPR and optical data point to a high degree of functional asymmetry between the two quinones: point mutations at the PsaA or PsaB quinone binding sites produce different effects on the electron transfer rates and the shapes of the photoaccumulated EPR spectra. The implication is that, in principle, we would be able to observe two different quinones in wild-type PS I by varying the conditions of photoaccumulation. The premise behind such an experiment is that, after photoaccumulation and subsequent double reduction of the 'active' quinone, it is possible to photoaccumulate the second quinone and that the two semiphylloquinones have potentially different EPR spectra. Finding appropriate conditions for such photoaccumulation is not a straightforward task, since one of the quinones must be completely doubly reduced prior to the accumulation of the second quinone; hence, photoaccumulation of A_0^- is likely.

Fig. 5.7 demonstrates that it is indeed possible to observe two different quinones in PS I by varying the conditions of photoaccumulation. Using the standard photoaccumulation protocol (see Materials and Methods) - and illuminating the wild-type PS I complexes containing of ca. 15% to 30% sucrose or glycerol at 210 K - we obtain the usual EPR spectrum with four prominent hyperfine lines (Fig. 5.7 *A*). If after that we illuminate the same sample at room temperature for ca. 5 minutes (supposedly doubly reducing one of the quinones) and bring the temperature back to 210 K, we obtain a spectrum that lacks the hyperfine pattern (Fig. 5.7 B). However, the possibility that this effect may be due to the conformational changes during freezing/unfreezing, and not to the differentiation of the two inherently present quinone environments can not be

completely excluded. Nevertheless, in combination with our other data this result further demonstrates inherent asymmetry between the two quinones.

Spin Polarization patterns of $P_{700}^{+}A_1^{-}$ at X- and Q-bands

The spin polarization patterns of $P_{700}^{+}A_1^{-}$ are sensitive to the orientation of A_1 and toits environment (see van der Est *et al*., 2001). Thus, they provide a good method for probing the effects of the mutations on the quinone. Fig. 5.8 presents X-band and Q-band spectra of $P_{700}^{+}A_1^{-}$ in the W677F (PsaA) and W677F (PsaB) mutants, together with the corresponding wild-type spectra taken at low temperature. The same comparison for S692C (PsaA) and S672C (PsaB) is shown in Fig. 5.9, and corresponding X-band spectra of the R694A (PsaA) and R674A (PsaB) mutants are shown in Fig. 5.10. The overall polarization patterns for the R694A (PsaA) and R674A (PsaB) mutants are very similar to those of the wild type, but subtle differences in the partially resolved methyl hyperfine structure are observable in the W677F (PsaA) and S692C (PsaA) mutants.

The effect of the hyperfine couplings is most pronounced in X-band spectra, while the *g*-anisotropy plays a more important role in the Q-band spectra which makes the latter more sensitive to the quinone orientation. Because the Q-band spectra are virtually identical with those of the wild type, we conclude that the mutations do not induce any significant change in either the orientation of the observed quinone or in its *g*-anisotropy. Careful inspection of the X-band spectra (Figs. 5.8 *A*, 5.9 *B* and 5.10 *A*, 5.10 *B*) shows that while the spectra of the PsaB mutants are almost indistinguishable the wild type, the methyl hyperfine splitting pattern is slightly more pronounced for the W677F (PsaA) mutant (Fig. 5.8 *A*) and less pronounced for the S692C (PsaA) mutant (Fig. 5.9 *A*). This is seen most clearly on the low field shoulder of the central absorptive peak; it suggests that mutations in PsaA affect the strength of the methyl hyperfine coupling, probably due to changes in the spin density distribution and binding of the quinone. There is also a slight shift of the low-field emission in the Q-band spectrum of the W677F (PsaA) mutant relative to that of the wild type, which is also consistent with an increase in the methyl hyperfine coupling.

Pulsed ENDOR of $P_{700}^{+}A_1^{-}$

Fig. 5.12 compares the pulsed ENDOR spectra of $P_{700}^{+}A_1^{-}$ in the W697F (PsaA), W677F (PsaB), S692C (PsaA) and S672C (PsaB) mutants with that of the wild-type PS I. The ENDOR spectra are taken at a field position for which the spectra appear approximately symmetric with respect to the proton Larmor frequency. ENDOR lines occur in absorption (positive features) and emission (negative features), depending on the electron spin polarization of the radical pair. Two clearly resolved powder patterns of an axially-symmetric tensor are observed at the extremities of the spectra in the range 8.6 MHz to 10.6 MHz and 18.9 MHz to 20.9 MHz. These features are assigned to the 2-CH_3 group of phylloquinone, and the shift of corresponding features in the two powder patterns indicates the change in the corresponding hyperfine tensor components, $A_{\|}$ and $A_{\perp}$.

A qualitative comparison shows that the spectra of the PsaB mutants are virtually identical to wild type while those of the PsaA mutants display systematic changes. The edges of the methyl hyperfine powder patterns shift by about 5% compared to wild type for both PsaA mutants, but the direction of the shift is opposite in the two cases with larger couplings observed for the $W679F_{PsaA}$ mutant and smaller couplings in the S692C (PsaA) mutant. If we set the hyperfine tensor components of wild type and both PsaB mutants to $A_{\|}$=12.1±0.1 MHz, $A_{\perp}$=8.9±0.1 MHz, we evaluate $A_{\|}$=12.7±0.1 MHz, $A_{\perp}$=9.4±0.1 MHz for W697F (PsaA) and $A_{\|}$=11.5±0.1 MHz, $A_{\perp}$=8.4±0.1 MHz for S692C (PsaA). These changes in the strength of the hyperfine splitting for the PsaA and not the PsaB mutants are consistent with the changes in the spectra of photoaccumulated A_1^{-} (Figs. 3 and 5) and with the spin polarization patterns of $P_{700}^{+}A_1^{-}$ (Figs. 5.8 and 5.9).

Clearly, only mutations in the PsaA protein lead to a change in the hyperfine couplings; while PsaB mutations do not, which shows that only the quinone in the PsaA-branch is being observed in the EPR and ENDOR experiments. Keeping in mind that for the low temperature spin polarization patterns and pulsed ENDOR experiments, only the fraction of reaction centers in which cyclic electron transfer to A_1 takes place are observed, we conclude that for this fraction electron transfer occurs along the PsaA-branch. However, the low temperature results do not rule out the possibility that the

PsaB-branch might represent the pathway that leads to stable charge separation to the FeS clusters. It is conceivable that the behavior at low temperature or under the strongly reducing conditions used for the photoaccumulation experiments might be different from the behavior under physiological conditions. Therefore it is important to combine these experiments with measurements at room temperature, in which forward electron transfer past $P_{700}^{+}A_1^{-}$ can be observed.

Room temperature electron spin polarized EPR spectra at X-Band

Electron spin polarized EPR spectra from the wild type and the mutants, measured at room temperature, are depicted in Fig. 5.11. Temperature dependence of the spectra was also measured, and no significant differences were observed between the spectra at 250 K versus those at room temperature. The spectra were extracted from the complete time/field data sets using the fitting procedure described in (van der Est *et al.*, 1994 and Kandrashkin 2002); positive signals correspond to absorption (A) and negative signals correspond to emission (E). As the electron is transferred to the FeS clusters, the initial E/A/E polarization pattern due to $P_{700}^{+}A_1^{-}$ changes into the primarily emissive P_{700}^{+} contribution to the P_{700}^{+} $(FeS)^{-}$ spectrum. Again, the mutations in the immediate vicinity of the PsaA-branch quinone lead to small but significant changes in the spectra (top left and middle left) while no difference is detectable within experimental error between the PsaB-side mutant data and wild-type data. Moreover, the spectral differences induced by the W677F (PsaA) and S692C (PsaA) mutations are the same as observed at low temperature, and are consistent with the pulsed ENDOR data. The hyperfine structure due to the methyl group ortho to the phytyl tail of phylloquinone is more pronounced in the $P_{700}^{+}A_1^{-}$ spectrum of the W677F (PsaA) mutant, whereas it is less pronounced in the spectrum of the S692C (PsaA) mutant. The correspondence of the low temperature spectra and those at physiological temperatures is significant because it shows that conclusions based on low temperature data are relevant for the function of PS I under physiologically-relevant conditions.

In contrast to the W and S mutants, which only show an effect when the mutation is on the PsaA side, both the R694A (PsaA) and R674A (PsaB) mutants (Fig. 5.11

bottom), show significant differences from the wild type. The fact that both mutations cause a change at room temperature when electron transfer to F_X is observed, while they are identical to wild-type PS I when it is blocked at low temperature, indicates that the mutations affect the properties of F_X rather than A_1.

Forward Electron Transfer - Time-Resolved Optical Measurements in Whole Cells

Table 5.1 summarizes the lifetimes and amplitudes of the fast and slow kinetic phases measured at 390 nm and 400 nm in wild-type and mutant cells. At 390 nm, two kinetic phases are found in the wild type with lifetimes of ca. 10 ns and ca. 300 ns. At 390 nm, the lifetime of the slow kinetic phase is increased by a factor of ca. 3.5 in the PsaA-side mutant W697F (PsaA) and at both wavelengths by an average factor of 4 in the PsaA-side mutant S692C (PsaA). However, the lifetime of the slow kinetic phase does not change significantly at either wavelength in the PsaB-side mutants W677F (PsaB) and S672C (PsaB). In comparison to the slowing of the slow phase in PsaA-side mutants, the slowing of the fast phase is not as pronounced in the PsaB-side mutants. At 390 nm, the lifetime of the fast kinetic phase is increased by a factor of 2.6 in the PsaA-side mutant W677F (PsaB) and at both wavelengths by an average factor of only 1.3 in the PsaA-side mutant S692C (PsaA). However, the latter may not be significant, in so much as the S692C (PsaA) mutant also shows a similar increase in its lifetime. Note, however, that the S692C (PsaA) mutant has the largest effect on the slow kinetic phase; hence, a similarly large effect on the fast kinetic phase in the S672C (PsaB) mutant might have been expected. However, the precision of the data is limited to (probably) ± 50% so that it may not be possible to draw firm conclusions.

Nevertheless, the scatter in the data, and the relative change in the values indicates that more weight should be given to the to the PsaA-side values than the PsaB-side values. Consistent with the expectation that the R mutants should affect the redox potential of F_X, and thus electron transfer in both branches, the slow kinetic phase becomes slower in the R674A (PsaB) mutant (even though the mutation is in the PsaB side). Surprisingly, however, the fast kinetic phase is not altered significantly. Again, due to the limited number of data points collected which restrict the precision of the

measurement, the values of the fast kinetic phase need to be considered with caution. Nevertheless, the data are sufficiently reliable to show that in the R674A (PsaB) mutant there is no correspondingly large increase in the fast phase. Together the data show that for all mutations expected to influence electron transfer in the PsaA-branch, the slow kinetic phase is slowed significantly. It is less clear whether such a trend holds for the fast kinetic phase. The lifetimes for the W mutants suggest that the fast phase is only affected by mutations on the PsaB side. However, the R and S mutants do not confirm this.

Room temperature and 260 K electron spin polarized EPR signals at X-Band

The lifetime values determined from the room temperature transient EPR experiments summarized in Table 5.2 (*left* column). In the room temperature experiments, fit of the data yields a lifetime for the electron transfer of 520 ± 50 ns in the W697 (PsaA) mutant compared to lifetime of 240 ± 50 ns in the wild type. In contrast, the transients and spectra from the W677 (PsaB) mutant are indistinguishable from wild-type PS I. the S692 (PsaA) and S672C (PsaB) mutants, which have similar kinetic behavior to the W mutants, except that the effect of the PsaA mutation is even greater. A fit of the data set yields a lifetime of 920 ± 50 ns in the S692 (PsaA) mutant and again the PsaB mutant is indistinguishable from the wild type. Thus, consistent with the optical data a slowing of the slow phase as a result of the mutations in the PsaA-branch quinone binding site is observed. However, the corresponding PsaB-branch mutations do not produce a noticeable effect.

For the R to A mutants at room temperature the analysis of the transient EPR datasets yields almost identical lifetimes of 460 ± 50 ns and 410 ± 50 ns for the forward electron transfer confirming that the mutations primarily affect F_X. The values of the optically determined lifetimes for the mutants shown in Table 4.1 are consistently longer than the values determined from the transient EPR experiments in Table 4.2. It is possible that the spin relaxation can also influence the lifetimes obtained from EPR transients. Relaxation effects are microwave power dependent (van der Est *et al*., 1994) and since no significant dependence on the microwave power was found for the electron transfer

lifetimes; temperature is the more likely cause of the difference in the lifetimes determined optically and from EPR. These data suggest that electron transfer occurs only along the PsaA-branch. The room temperature transient EPR data show no clear influence from the fast kinetic phase observed optically.

When wild-type PS I complex is cooled to a temperature of 260 K, charge separation between P_{700} and F_A/F_B remains reversible, yet the slow phase of forward electron transfer, as measured by transient EPR and absorbance changes at 380 nm (Schlodder, 1998), slows down, which hints at a temperature activation of the forward electron transfer process. When measured by transient EPR, the kinetics of A_1^- reoxidation in the W697F (PsaA) and S692C (PsaA) mutants is also slowed by a factor of three as compared with kinetics at room temperature (see Table 4.2, *right* column). Yet, at 260 K the kinetics of A_1^- oxidation in the W677F (PsaB) and S672C (PsaB) mutants remains identical to that of wild-type PS I complexat 260 K, and show no indication of a fast kinetic phase. If we assume that the fast kinetic phase has the same temperature coefficient as the slow phase, and if we further assume the room temperature optically-determined rates are similar to those as listed in Table 4.1, then we would expect the fast phase to slow to ca. 75 ns to 90 ns, which is within the kinetic window of transient EPR for direct detection of a $P_{700}^+ A_1^-$ signal from the PsaB-branch. In addition, the spin polarization pattern of this spectrum, as well as that of the subsequent $P_{700}^+ (FeS)^-$ state, would be characteristically different as predicted from the theoretical description of sequentially populated radical pairs (Kandrashkin, 1998). In a detailed analysis of the transient EPR spectra of the PsaB mutants with respect to both kinetic behavior and polarization pattern, there is no indication for the existence of a fast kinetic phase of A_1 oxidation (in either wild-type or mutant PS I complexes - van der Est, personal communication). Thus, there is no evidence of a contribution by a fast kinetic phase in the electron transfer between A_1^- and the FeS clusters. Based on the experimental error in both the simulation parameters and net polarization, I estimate that the slow kinetic phase accounts for at least 90% of the observed transient EPR signals.

DISCUSSION

The EPR and ENDOR spectroscopic data for the site-directed mutants can be interpreted in terms of changes in the local environment of the quinones. It is generally accepted that, for photosynthetic reaction centres that asymmetry in the H-bonding to the two carbonyl groups of the quinone acceptor results in an alternating spin density distribution over the quinone ring (Lubitz and Feher, 1999). This can also explain the relatively large hyperfine coupling of the phylloquinone methyl group in PS I. The 2.5 Å resolution X-ray structure (1JB0) shows that the carbonyl meta to the methyl group is H-bonded to L722 (PsaA) or to L706 on PsaB, while the carbonyl ortho is not H-bonded. The electron withdrawing effect of the single H-bond changes the distribution of the electron and leads to a high spin density on the ring carbon to which the methyl group is bound. This in turn leads to a large methyl hyperfine coupling. Exact interpretation of the changes in the hyperfine couplings induced by the mutations is difficult, because they are sensitive to a number of factors. However, if we assume that the distortion of the spin density caused by the H-bonds is the dominant factor, then the W677F (PsaA) mutation appears to increase the asymmetry while the S692C (PsaA) mutation appears to decrease it. S692 on PsaA is 3.27 Å distant from the carbonyl ortho to the methyl group of Q_K-A and S672 on PsaB is 3.37 Å distant from the carbonyl ortho to the methyl group of Q_K-B. The S is H-bonded to the π-stacked residues W677F (PsaA) and W677F (PsaB). A second H-bond is present from the serine -OH to the M688 (PsaA) backbone C=O, located 2.6 Å distant. Because of the proximity of these H-bonds to the quinone carbonyl oxygen, changes in the electron withdrawing ability of the residues or the presence or absence of the S-W H-bond can be expected to influence the spin density on the quinone carbonyl oxygen. The hyperfine couplings suggest that replacement of W697 (PsaA) by F leads to a greater asymmetry between two carbonyl oxygens. Replacement of S692 (PsaA) by C leads to a smaller asymmetry. In both cases the change in the hyperfine couplings can be related to changes in the environment of the quinone near the carbonyl ortho to the methyl group. In the W677F (PsaA) mutant the H-bond between the S692 (PsaA) and W697 (PsaA) is disrupted since the phenylalanine side group cannot

participate in H-bonding. It is reasonable to expect that this results in a stronger H-bond between S692 (PsaA) and M688 (PsaA) and in a decrease in the electronegativity of the surroundings of the quinone carbonyl group. Replacement of S692 (PsaA) with a C will also affect this region of the quinone environment. Although S and C differ only by the substitution of the hydroxyl group in serine by a thiol group in C, the van der Waals radius of the sulfur is larger than that of oxygen. The effect of this change on the environment is difficult to predict, since there will be a subtle balance between the lower electronegativity of the sulfur (which will tend to weaken the H-bond to the W) and the larger radius (which will place the shared hydrogen atom closer to the W and quinone carbonyl). The hyperfine couplings suggest that the environment of the carbonyl oxygen ortho to the methyl group becomes less electronegative in the W677F (PsaA) mutant, resulting in a larger asymmetry in the electron withdrawing effect of the two carbonyl oxygens and hence a larger spin density on the ring carbon next to the methyl group. In the S692C (PsaA) mutant, on the other hand, the weaker methyl hyperfine coupling is consistent with an increase in electronegativity of the environment of the carbonyl oxygen ortho to the methyl group resulting in a lower asymmetry in the spin density distribution on the quinone.

Other factors - such as changes in the strength of the H-bond from the quinone to L722 (PsaA), and of the π-π interaction with the W - undoubtedly also contribute to the changes in the hyperfine couplings. The π-stacking is known to diminish the H-bond asymmetry effect. Thus, changes in the interaction between the quinone and W or F are also expected to influence the hyperfine couplings. In the W677F (PsaA) mutant, it is likely that the strength of the π-stacking is weaker than in the wild type, and hence the H-bond asymmetry effect should be increased. Similarly, the decreased methyl hyperfine couplings in the S692C (PsaA) mutant can be explained by an increase in the strength of the π-stacking. However, the location of the H-bond between the S and W suggests that the environment of the carbonyl ortho to the methyl group probably plays the dominant role in altering the hyperfine couplings. Based on the values of the couplings the magnitude of the change in the spin density distribution can be estimated to be of the

order of ca. 10%, thus the change in the electronic structure of the quinone is rather subtle but nonetheless clearly visible in the spectra.

The photoaccumulation experiments show that the electron-active quinone is located in the PsaA-branch. The same conclusion was reached previously (Yang *et al*., 1998) from studies of PsaE/PsaF double deletion mutants, which showed complete loss of the A_1^- spectrum and appearance of an A_0^- spectrum. This effect requires double reduction and protonation of the quinone. Because PsaE and PsaF are located on the PsaA side of the PS I complex, it was suggested that removal of these subunits facilitates protonation of the quinone via a water channel.

The ability to photoaccumulate A_1^- rests largely on a favorable combination of kinetic rates, particularly in that forward electron transfer between the sulfite ion, and P_{700}^+ outcompetes the backreaction between P_{700}^+ and A_1^-. This condition is clearly met for the PsaA-branch quinone; however, it is not clear whether or not this condition can be met for the PsaB-branch quinone, which may have different forward and backward kinetics. If electron transfer along the PsaB-branch occurred to any significant extent, it would require that either (i) no accumulation of Q_K-B^- occurs or (ii) the point mutations have no effect on Q_K-B while removal of the PsaE and PsaF has the same effect on both quinones. Clearly, neither of these assumptions is physically reasonable.

At low temperature, the photoaccumulated A_1^- spectra, the spin polarization patterns, and the pulsed ENDOR spectra all show an effect when mutations are made in PsaA, but the corresponding spectra from the PsaB mutants are identical to those from the wild type. Thus, we conclude that only the phylloquinone bound to PsaA (Q_K-A) contributes to these spectra; Q_K-B does not. Because the observed changes in the properties of the quinone are small, it is reasonable to extrapolate to the conclusion that the electron cycle between P_{700} and A_1 at low temperature is unidirectional along the PsaA-branch. This is consistent with the conclusion reached in (Boudreaux *et al*., 2001) from point mutation studies in the eukaryotic organism, *Chlamydomonas reinhardtii.* However, it must be kept in mind that cyclic electron transfer involving P_{700} and A_1 only occurs in roughly 50% the reaction centers in frozen solution, while stable charge separation to the FeS clusters takes place in the remainder. Therefore, we need to

consider the pathway taken by the fraction that is involved in non-cyclic electron transfer. An important feature of the two fractions is that their relative amplitudes does not change under prolonged illumination.

This behavior rules out the possibility that they are due to two competing pathways, since if all reaction centers had even a low probability for the non-cyclic pathway, prolonged illumination would lead to complete non-cyclic charge separation. The two fractions clearly have different activation energies for forward electron transfer past A_1 presumably as a result of a structural difference. Therefore, if we postulate that the non-cyclic pathway is via the PsaB-branch, the activation energy of A_1 to F_X electron transfer would have to be different in the two branches, and since the acceptor F_X is common to both branches, the difference in activation energy would have to be associated with differences in the two quinones.

Moreover, at low temperature there would have to be two populations of reaction centers in which the initial charge separation was biased exclusively towards the PsaA-branch and PsaB-branch, respectively. The fraction biased towards the PsaA-branch would lead to cyclic electron transfer, while the fraction biased towards the PsaB-branch would lead to non-cyclic charge separation. Alternatively, if we postulate that the non-cyclic pathway is also along the PsaA-branch, the two fractions would have to be associated with differences in either A_1 or F_X in the PsaA-branch, and the electron transfer would be biased strongly towards the PsaA-branch. At present, we cannot distinguish between these two possibilities, however, the “freezing out” of directionality of the initial charge separation into two fractions as required by the bi-directional model seems unlikely given that this reaction is almost certainly activationless. On the other hand the two activation energies for the A_1 to F_X electron transfer in the unidirectional model might be associated with different distributions of the charge among the four iron atoms of F_X. It is known from NMR experiments that the dynamics of the charge distribution is strongly temperature dependent, and simple calculations of the electrostatic energy suggest that changes in the charge distribution could have a significant impact on the rate of electron transfer from A_1 to F_X.

At room temperature the changes in the spectra from the W and S mutants (Fig. 5.11) mirror those at low temperature, *i.e.*, mutations in PsaB have no effect on the patterns, while those in the PsaA result in clearly visible changes. Therefore we conclude that the spectra at room temperature are also dominated by radical pairs generated by electron transfer along the PsaA-branch. Optical experiments reveal a component of electron transfer from A_1 to F_x with a lifetime of ca. 10 ns, and it has been proposed that this corresponds to electron transfer in the PsaB-branch (Brettel and Leibl, 2001). Thus, it is important to consider the influence of such a kinetic phase would have on the room temperature transient EPR data.

Although the nominal time resolution of our transient EPR spectrometer is in the range of tens of nanoseconds, the spin dynamics of short-lived precursors has a significant effect on the transient EPR spectra of subsequent radical pairs. Indeed, the influence of singlet-triplet mixing in the primary radical pair on a timescale as short as 600 ps has been observed in reaction centers of green sulfur bacteria, heliobacteria and purple bacteria (van der Est *et al*., 1998; Tang *et al*., 1999; Hulseboshc *et al*., 1999). In PS I complex, the lineshapes and relative amplitudes of the early and late spectra are sensitive to the presence of a fast kinetic phase of electron transfer to the FeS clusters (van der Est *et al*., 2001) and recently, the contribution to the spin polarization patterns of such a phase was calculated (Kandrashkin 2002). The simulations indicate that although a minor fraction of fast electron transfer as observed optically cannot be ruled out, the experimental spectra from wild-type cyanobacterial PS I complex show no clear evidence for the presence of the 10 ns phase. Thus, the room temperature spin polarization patterns presented in Fig. 5.11 suggest that the majority of electrons proceed along the PsaA-branch under physiological conditions.

SUMMARY

Data presented in this chapter support the hypothesis that forward electron transfer in wild-type PS I occurs predominately through the PsaA-branch of cofactors under physiological conditions. In contrast, backward electron transfer proceeds through both branches. The presence of the two quinones in different environments results in functional asymmetry of electron transfer.

REFERENCES

Bittl, R., and Zech, S. G. (2001) *Biochim Biophys Acta* **1507**, 194-211.

Boudreaux, B., MacMillan, F., Teutloff, C., Agalarov, R., Gu, F., Grimaldi, S., Bittl, R., Brettel, K., and Redding, K. (2001) *J Biol Chem* **276**, 37299-37306

Brettel, K., Golbeck, J.H., (1995) *Photosyth. Res*. **45**, 183-193

Brettel, K., and Leibl, W. (2001) *Biochim Biophys Acta* **1507**, 100-114

Deisenhofer, J., Epp, O., Miki, K., Huber, R., and Michel, H. (1984) *J Mol Biol* **180**, 385

Frauke Baymann, Myriam Brugna, Ulrich Mühlenhoff, Wolfgang Nitshke (2001), *Biochim Biophys Acta* **1507**, (291-310)

Fromme, P. (1999) in *Concepts in Photobiology: Photosynthesis and Photomorphogenesis* (Singhal G.S., R. G., Sopory S.K., Irrgang K.D. and Govindjee, ed), pp. 181-220, Narosa Publishing House/India, New Delhi

Guergova-Kuras, M., Boudreaux, B., Joliot, A., Joliot, P., and Redding, K. (2001) *Proc Natl Acad Sci U S A* **98**, 4437-4442.

Hanley, J., Deligiannakis, Y., MacMillan, F., Bottin, H., and Rutherford, A. W. (1997) *Biochemistry* **36**, 11543-11549

Hastings, G., and Sivakumar, V. (2001) *Biochemistry* **40**, 3681-3689.

Hulsebosch, R. J., Borovykh, I. V., Paschenko, S. V., Gast, P., and Hoff, A. J. (1999) *J. Phys. Chem. B* **103**, 6815-6823

Joliot, P. and Joliot, A., (1999) *Biochemistry* **38**, 11130-11136

JordanP, Fromme P, Witt H. T., Klukas O, Saenger W, Krauβ N. 2001 *Nature* **411**, 909

Kamlowski, A., Altenberg-Greulich, B., van der Est, A., Zech, S. G., Bittl, R., Fromme, P., Lubitz, W., and Stehlik, D. (1998) *J. Phys. Chem. B* **102**, 8278

Kandrashkin, Y. E., and van der Est, A. (2002) *RIKEN Review* **44**, 124-127

Koradi, R., Billeter, M., and Wuthrich, K. (1996) *J Mol Graph* **14**, 51-55, 29-32

Lubitz, W., and Feher, G. (1999) *Appl. Magn. Reson.* **17**

Nitschke, W., and Rutherford, A. W. (1991) *TIBS* **16**, 241-245
Purton, S., Stevens, D. R., Muhiuddin, I. P., Evans, M. C., Carter, S., Rigby, S. E., and Heathcote, P. (2001) *Biochemistry* **40**, 2167-2175.

Rigby, S. E., Evans, M. C., and Heathcote, P. (2001) *Biochim Biophys Acta* **1507**, 247-259.

Sétif P., Brettel, K. (1993) *Biochemistry* **32**, 7846-7854

Shen, G., Zhao, J., Reimer, S. K., Antonkine, M. L., Cai, Q., Weiland, S. M., Golbeck, J. H., and Bryant, D. A. (2002) *J Biol Chem* **25**, 25

Sieckman, I., Van der Est, A., Bottin, H., Sétif, P., and Stehlik, D. (1991) *FEBS Lett*. **284**, 98–102

Stehlik, D. (1997) *J. Phys. Chem*. B **101**, 1437–1443

Tang, J., Utschig, L. M., Poulektov, O., and Thurnauer, M. C. (1999) *J. Phys. Chem. B* **103**, 5145-5150

van der Est, A., Bock, C., Golbeck, J., Brettel, K., Sétif, P., and Stehlik, D. (1994) *Biochemistry* **33**, 11789-11797

van der Est, A., Hager-Braun, C., Leibl, W., Hauska, G., and Stehlik, D. (1998) *Biochim Biophys Acta* **1409**, 87-98

van der Est, A., Prisner, T., Bittl, R., Fromme, P., Lubitz, W., Mobius, K., and

Yang, F., Shen, G., Schluchter, W. M., Zybailov, B., Ganago, A. O., Vassiliev, I. R., Bryant, D. A., and Golbeck, J. H. (1998) *J. Phys. Chem.* **102**, 8288-8299

FIGURE LEGENDS

Figure 5.1 Two phylloquinone binding sites in the interface of PsaA/PsaB heterodimer. The quinone molecules are depicted in yellow sticks, left side corresponds to the PsaB-branch, right site corresponds to PsaA-branch. Amino acid residues discussed in the text are W677 (PsaB), Sr672(PsaB), R674(PsaB); W697(PsaA), S692(PsaA), R694(PsaA). Amino acid residue W673 (PsaB), which does not have a counterpart on PsaA-side is also shown. (pdb entry - 1JB0)

Figure 5.2 Absorbance changes at 820 nm in the PS I isolated from W677F (PsaB) and W697F (PsaB) mutants and wild-type *Synechocystis* sp. PCC 6803. The decay kinetics were fitted to the multiexponential decay, the residuals of the fits are shown on top of the each transient Sample conditions were as follows: 50 µg chlorophyll ml^{-1} in 25 mM Tris, pH 8.2; 0.02% DM, 10 mM sodium ascorbate, 4 µM DCPIP

Figure 5.3 Q-band CW EPR spectra of photoaccumulated A_1 in W677F (PsaB) and W697F (PsaA) mutants and wild-type *Synechocystis* sp. PCC 6803. EPR settings: microwave power, 1 mW, modulation amplitude, 1G, modulation frequency, 100 kHz, temperature 205 K. Dark-adapted PS I complexes were illuminated for 40 min inside the Q-band resonator (see Materials and Methods), dark background was subtracted from the resulted spectrum.

Figure 5.4 Absorbance changes at 820 nm in the PS I isolated from S692C and S672C mutants and wild-type *Synechocystis* sp. PCC 6803. The decay kinetics were fitted to the multiexponential decay, the residuals of the fits are shown on top of the each transient. Sample conditions were as follows: 50 µg chlorophyll ml^{-1} in 25 mM Tris, pH 8.2; 0.02% DM, 10 mM sodium ascorbate, 4 µM DCPIP

Figure 5.5 Q-band CW EPR spectra of photoaccumulated A_1 in S692C and S672C mutants and wild-type *Synechocystis* sp. PCC 6803. EPR settings: microwave power, 1

mW, modulation amplitude, 1G, modulation frequency, 100 kHz, temperature 205 K. Dark-adapted PS I complexes were illuminated for 40 min inside the Q-band resonator (see Materials and Methods), dark background was subtracted from the resulted spectrum

Figure 5.6 Absorbance changes at 820 nm in the PS I isolated from R674A (PsaB) and R694A (PsaA) mutants and wild-type *Synechocystis* sp. PCC 6803. The decay kinetics were fitted to the multiexponential decay, the residuals of the fits are shown on top of the each transient The decay kinetics were fitted to the multiexponential decay, the residuals of the fits are shown on top of the each transient. Sample conditions were as follows: 50 µg chlorophyll ml^{-1} in 25 mM Tris, pH 8.2; 0.02% DM, 10 mM sodium ascorbate, 4 µM DCPIP

Figure 5.7 Q-band CW EPR spectra of photoaccumulated semiquinone in wild-type PS I complex. *A,* semiquinone spectrum obtained by photoaccumulating at 205 K using standard protocol. *B, solid line* represents semiquinone spectrum obtained by re-illumination of the same sample at room temperature for 5 minutes (see text); *dotted line* represents spectrum of semiphylloquinone radical in methanol (reductant - $NaBH_4$).

Figure 5.8 X-band (top) and Q-band (bottom) spin polarized EPR spectra of PS I complexes from the W697F (PsaA), W677F (PsaB) mutants (solid spectra) compared with wild type (dashed spectra) at 80 K. The spectra are due to $P_{700}^{+}A_1^{-}$ and have been extracted from the full time/field datasets by integrating the signal intensity in a time window from 152 ns to 1520 ns following the laser flash. Note that the field axes are different for the X-band and Q-band spectra and that the spectral width at Q-band is much larger. The experimental conditions are given in the Materials and Methods section.

Figure 5.9 X-band (top) and Q-band (bottom) spin polarized EPR spectra of PS I complexes from the S692C (PsaA), S672C (PsaB) mutants compared with wild type at 80 K. All other conditions are as for Figure 9

Figure 5.10 X-band spin polarized transient EPR spectra of PS I complexes from the R694A (PsaA) and R674A (PsaB) mutants compared with the wild type at 135 K. The spectra are due to $P_{700}^{+}A_1^{-}$ and are the integrated signal intensity in a time window 0.8 µs to 1.6 µs following the laser flash. The experimental conditions are given in the Materials and Methods section.

Figure 5.11 Room temperature transient EPR spectra of PS I with point mutations in PsaA (left) and PsaB (right). The spectra are due to $P_{700}^{+}A_1^{-}$ (E/A/E pattern) and $P_{700}^{+}FeS^{-}$ (emissive spectrum) and have been extracted from the time/field datasets by fitting the individual transients. The solid curves are from the mutants and the dashed curves are the corresponding spectra from wild-type PS I. Top left W667F (PsaA), top right W677F (PsaB), middle left S692C (PsaA), middle right S672C (PsaB), bottom left R694A (PsaA), bottom right R674A (PsaB).

Figure 5.12 Pulsed ENDOR of $P_{700}^{+}A_1^{-}$ state in PS I point mutants. Top (a): The W697F (PsaA) (solid spectrum) and W677F (PsaB) (dashed spectrum) mutants compared with wild-type PS I (dotted spectrum). Bottom (b): S692C (PsaA) (solid spectrum), S672C (PsaB) (dashed spectrum) mutants compared with the wild type (dotted spectrum). See Materials and Methods for details of the pulse sequences and other experimental conditions.

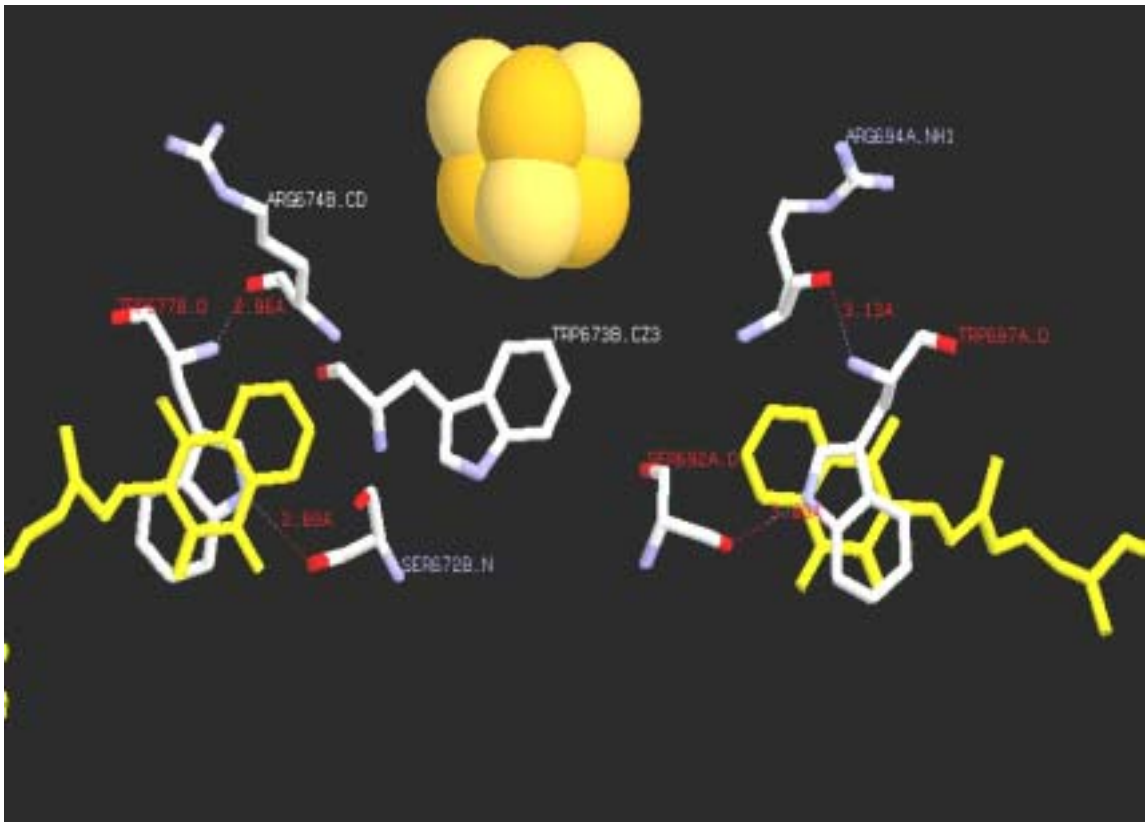

Figure 5.1

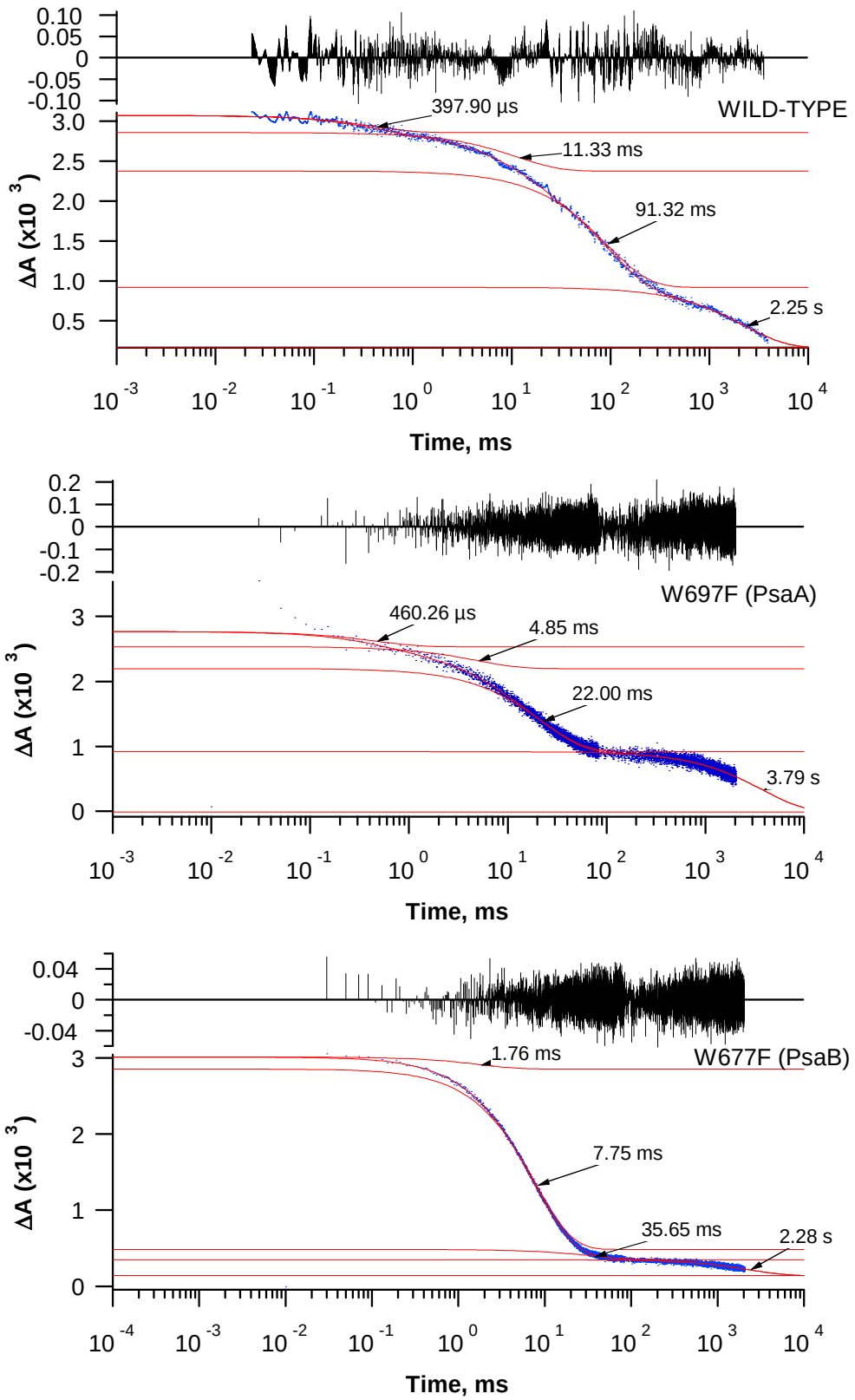
0.10
0.05
0
-0.05
-0.10
397.90 µs
WILD-TYPE
11.33 ms
91.32 ms
2.25 s
ΔA (x10 3)
3.0
2.5
2.0
1.5
1.0
0.5
10 -3
10 -2
10 -1
10 0
10 1
10 2
10 3
10 4
Time, ms
0.2
0.1
0
-0.1
-0.2
W697F (PsaA)
460.26 µs
4.85 ms
22.00 ms
3.79 s
3
2
1
0
Time, ms
0.04
0
-0.04
1.76 ms
W677F (PsaB)
7.75 ms
35.65 ms
2.28 s
10 -4
Time, ms

Figure 5.2

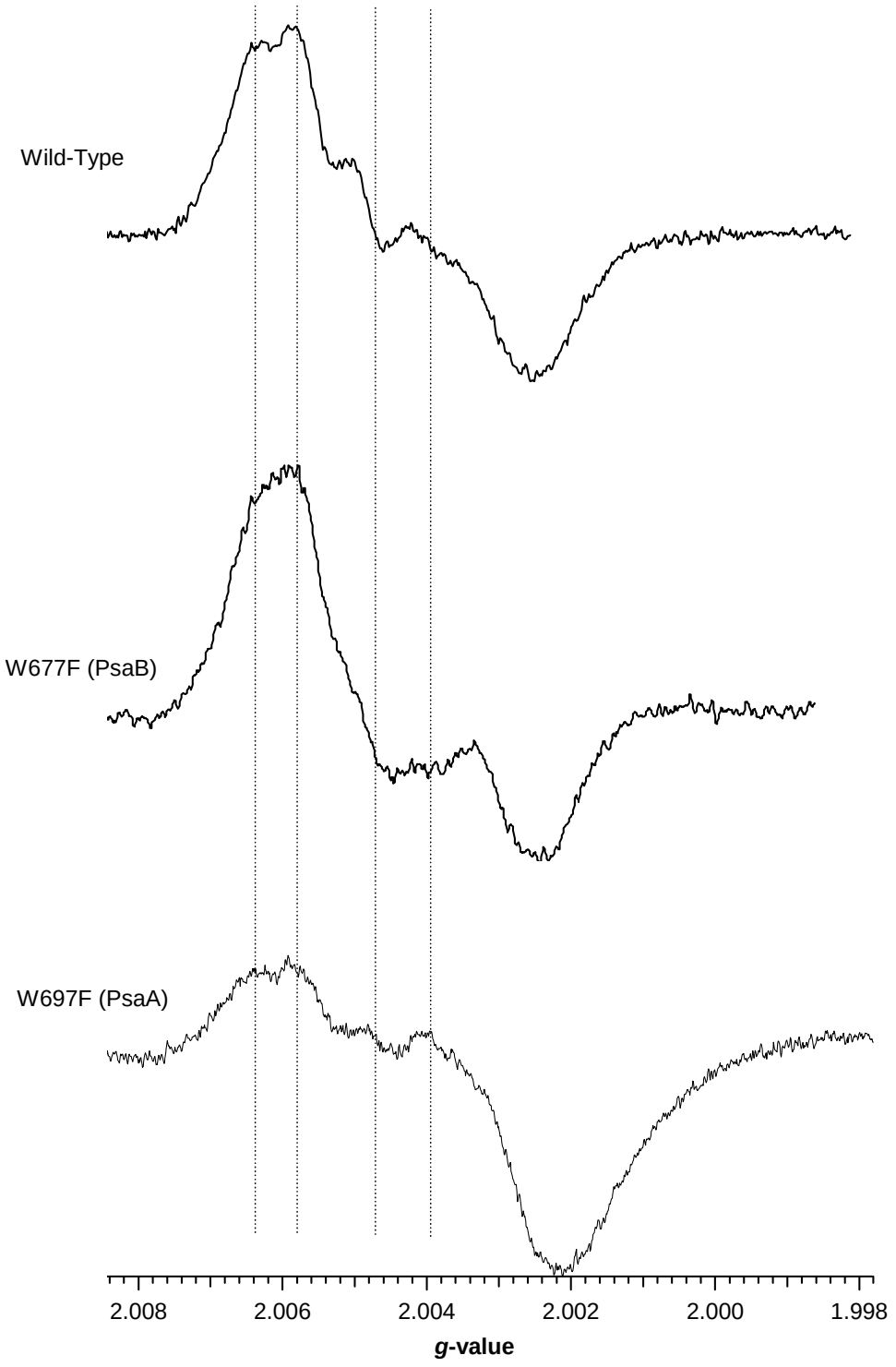
Wild-Type
W677F (PsaB)
W697F (PsaA)
2.008
2.006
2.004
2.002
2.000
1.998
g-value

Figure 5.3

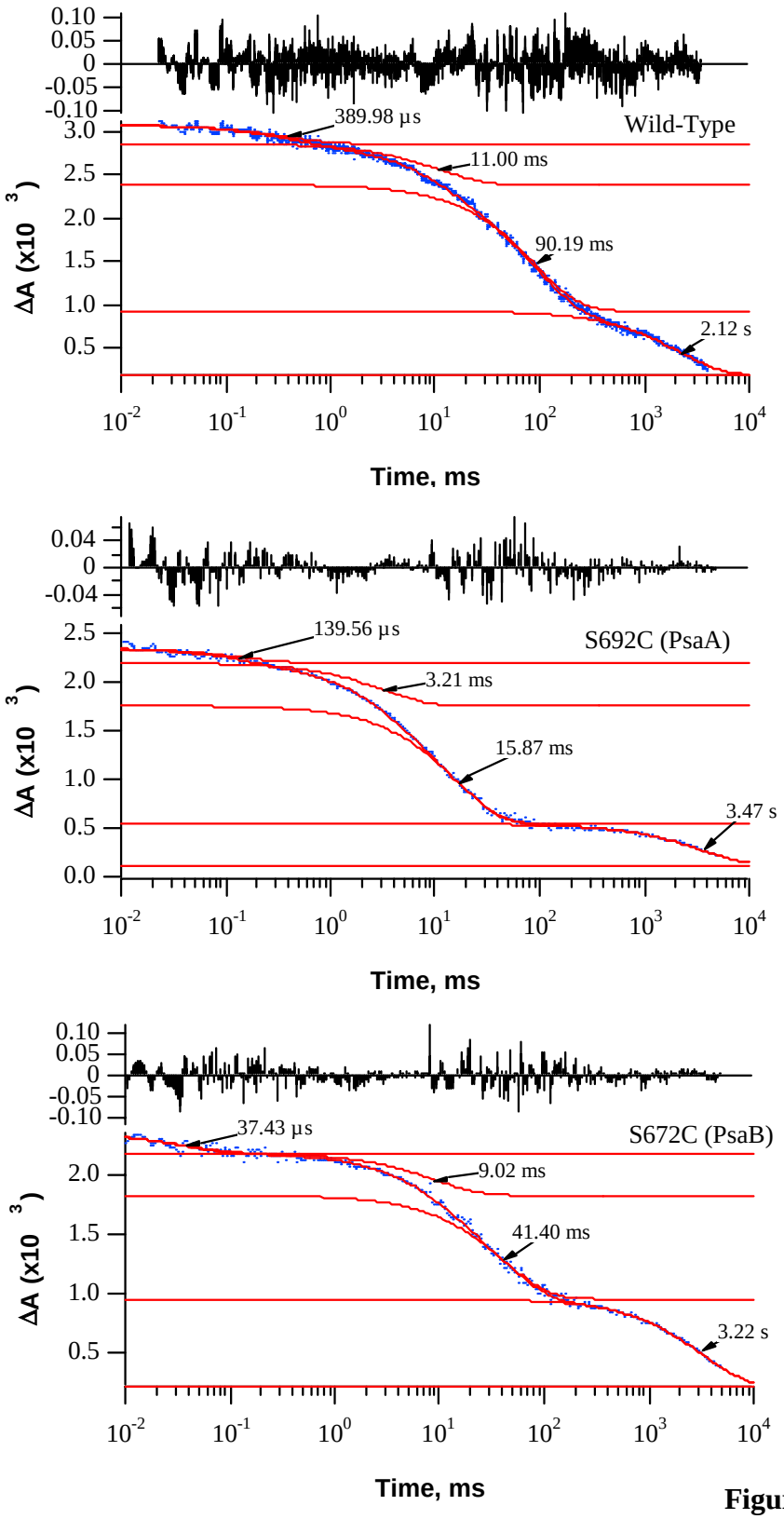
0.10
0.05
0
-0.05
-0.10
389.98 µs
Wild-Type
11.00 ms
90.19 ms
2.12 s
ΔA (x10 3)
3.0
2.5
2.0
1.5
1.0
0.5
10-2 10-1 100 101 102 103 104
Time, ms
0.04
0
-0.04
139.56 µs
S692C (PsaA)
3.21 ms
15.87 ms
3.47 s
2.5
2.0
1.5
1.0
0.5
0.0
ΔA (x10 3)
10-2 10-1 100 101 102 103 104
Time, ms
0.10
0.05
0
-0.05
-0.10
37.43 µs
S672C (PsaB)
9.02 ms
41.40 ms
3.22 s
2.0
1.5
1.0
0.5
ΔA (x10 3)
10-2 10-1 100 101 102 103 104
Time, ms

Figure 5.4

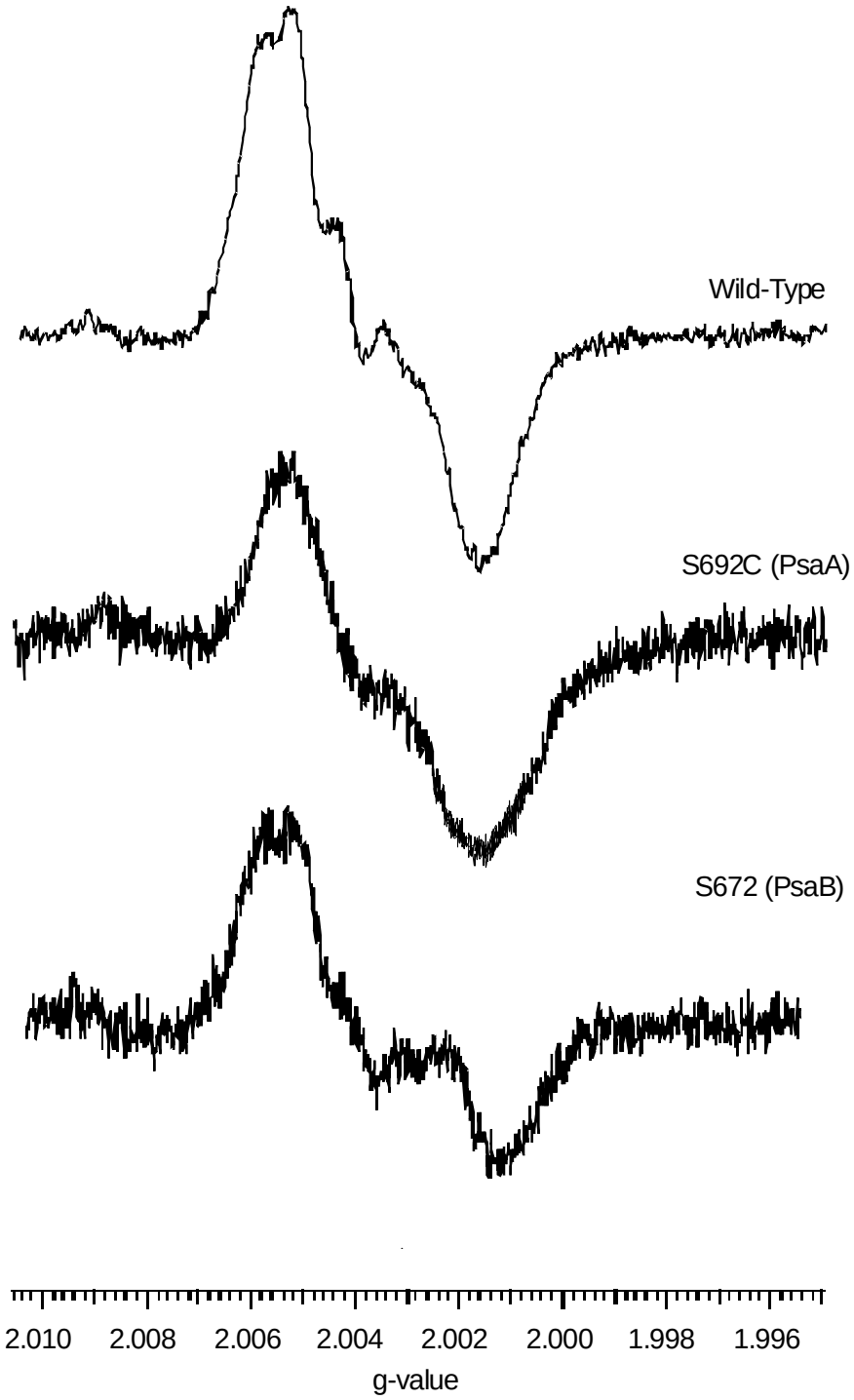
Wild-Type
S692C (PsaA)
S672 (PsaB)
2.010
2.008
2.006
2.004
2.002
2.000
1.998
1.996
g-value

Figure 5.5

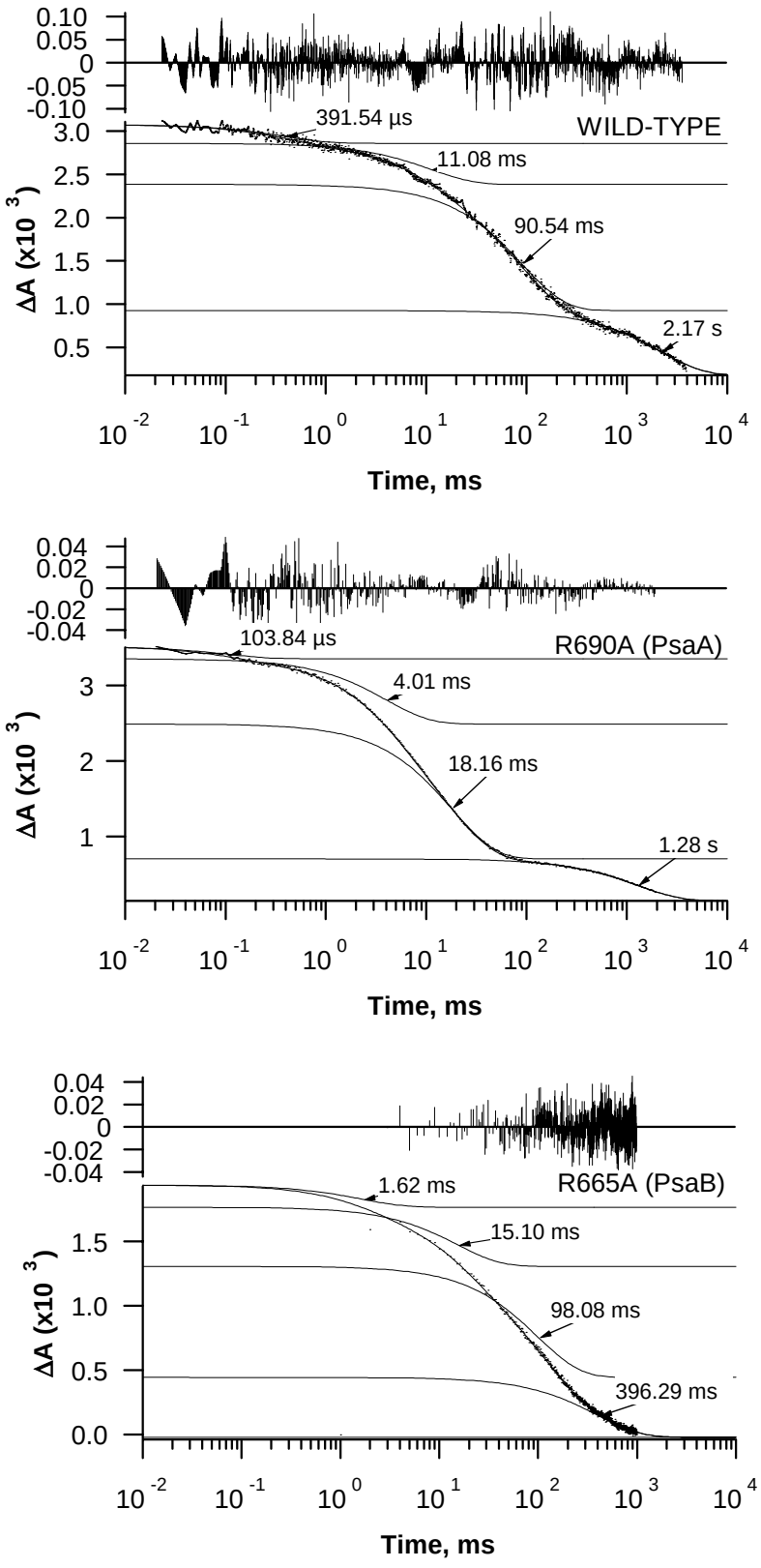
0.10
0.05
0
-0.05
-0.10
391.54 µs
WILD-TYPE
11.08 ms
90.54 ms
2.17 s
ΔA (x10 3)
3.0
2.5
2.0
1.5
1.0
0.5
10 -2
10 -1
10 0
10 1
10 2
10 3
10 4
Time, ms
0.04
0.02
0
-0.02
-0.04
103.84 µs
R690A (PsaA)
4.01 ms
18.16 ms
1.28 s
ΔA (x10 3)
3
2
1
Time, ms
0.04
0.02
0
-0.02
-0.04
1.62 ms
R665A (PsaB)
15.10 ms
98.08 ms
396.29 ms
ΔA (x10 3)
1.5
1.0
0.5
0.0
Time, ms

Figure 5.6

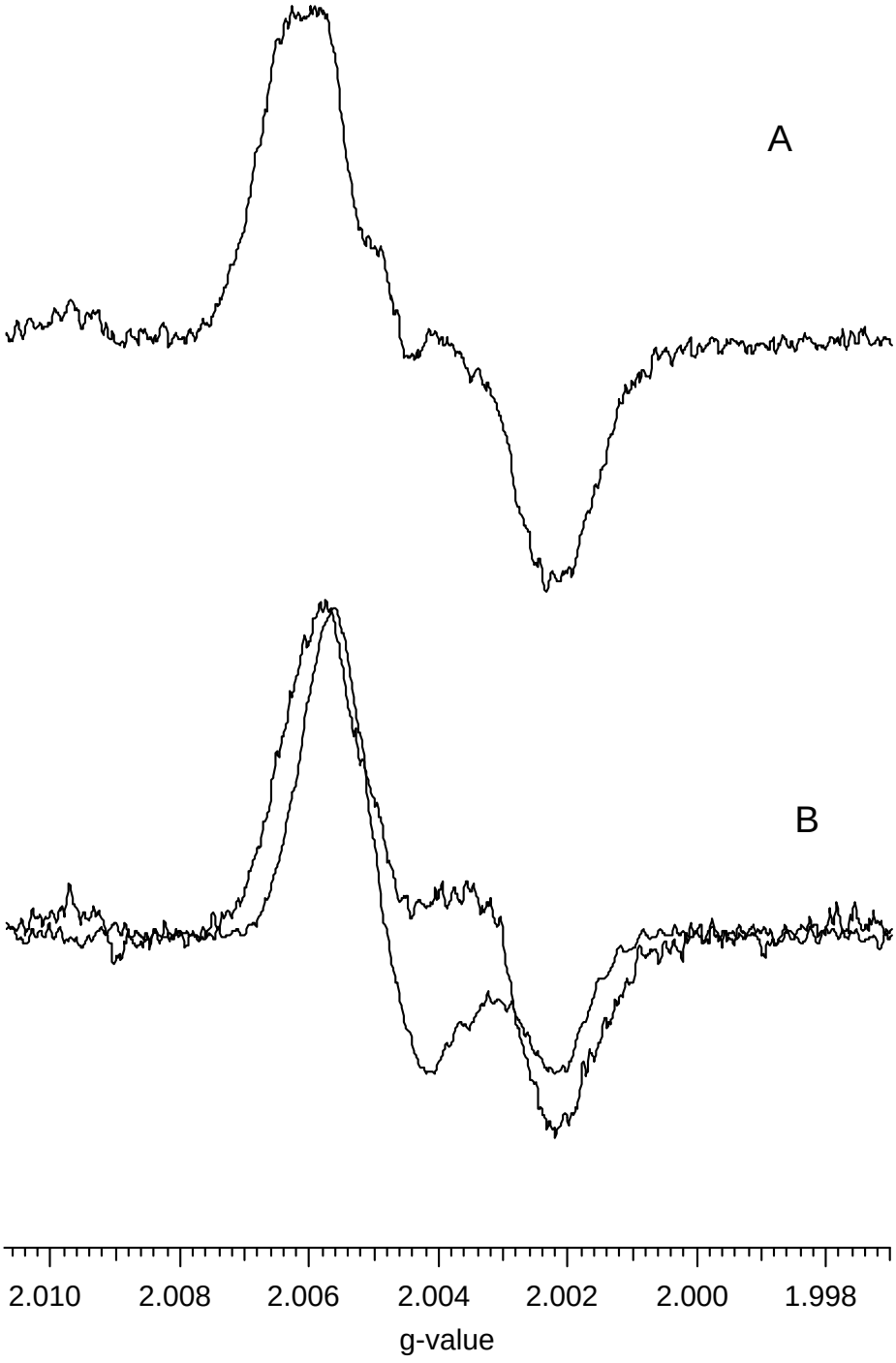

Figure 5.7

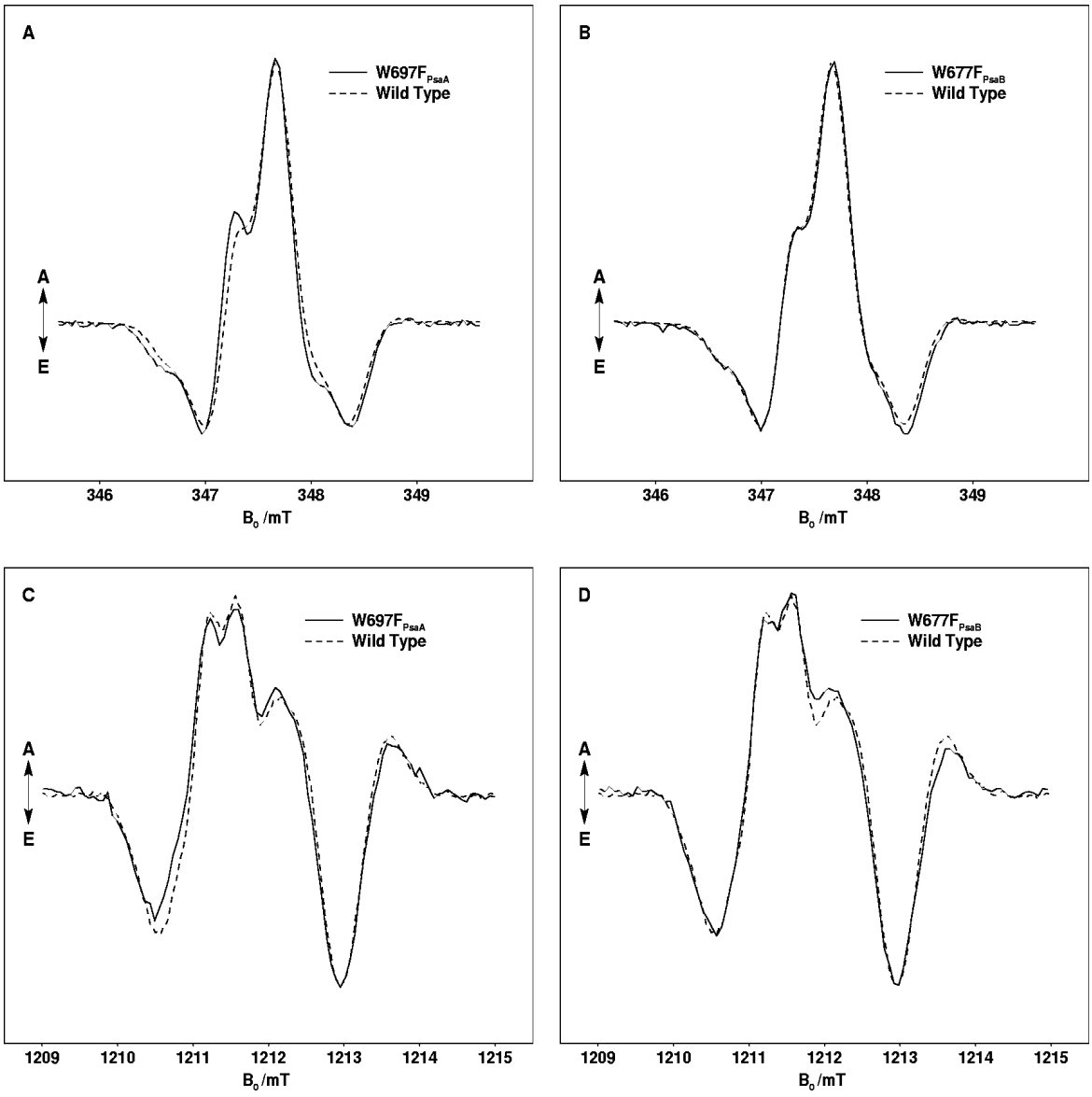
A
W697F PsaA
Wild Type
A
E
346
347
348
349
B0 /mT
B
W677F PsaB
Wild Type
A
E
346
347
348
349
B0 /mT
C
W697F PsaA
Wild Type
A
E
1209
1210
1211
1212
1213
1214
1215
B0 /mT
D
W677F PsaB
Wild Type
A
E
1209
1210
1211
1212
1213
1214
1215
B0 /mT

Figure 5.8

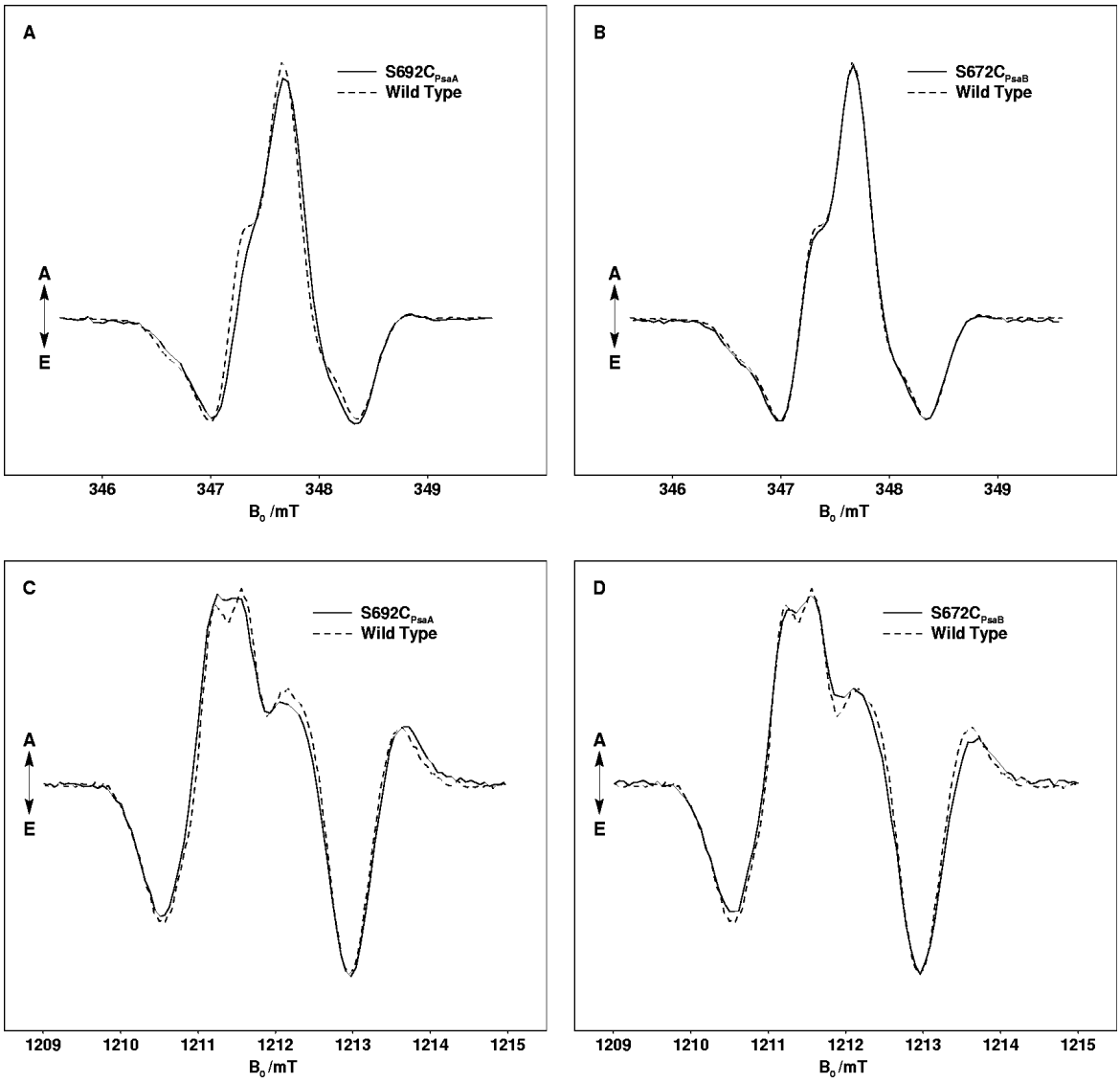
A
S692C PsaA
Wild Type
A
E
346
347
348
349
B0 /mT
B
S672C PsaB
Wild Type
A
E
346
347
348
349
B0 /mT
C
S692C PsaA
Wild Type
A
E
1209
1210
1211
1212
1213
1214
1215
B0 /mT
D
S672C PsaB
Wild Type
A
E
1209
1210
1211
1212
1213
1214
1215
B0 /mT

Figure 5.9

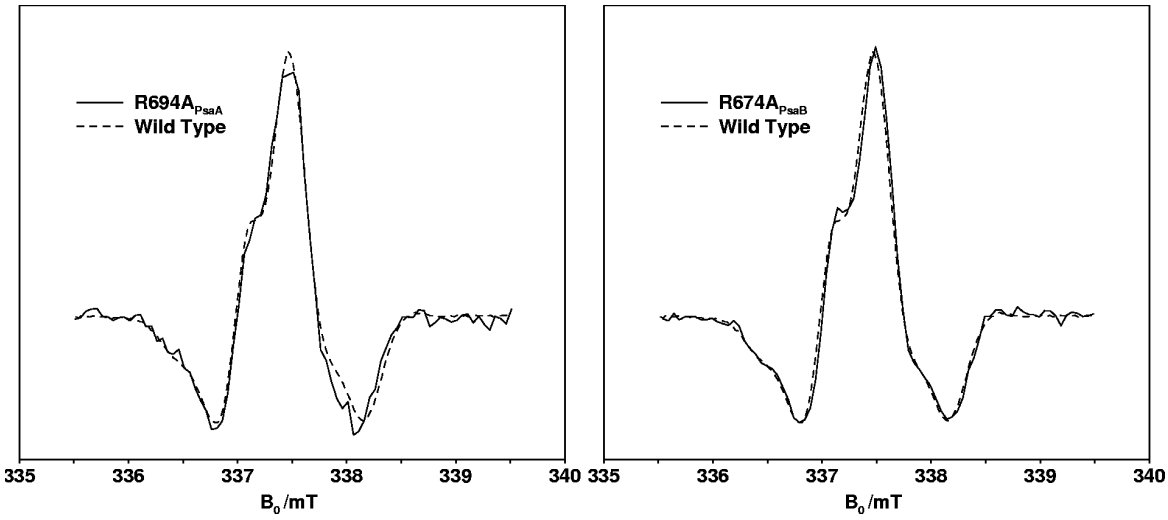
R694A PsaA
Wild Type
335
336
337
338
339
340
B0 /mT
R674A PsaB
Wild Type
335
336
337
338
339
340
B0 /mT

Figure 5.10

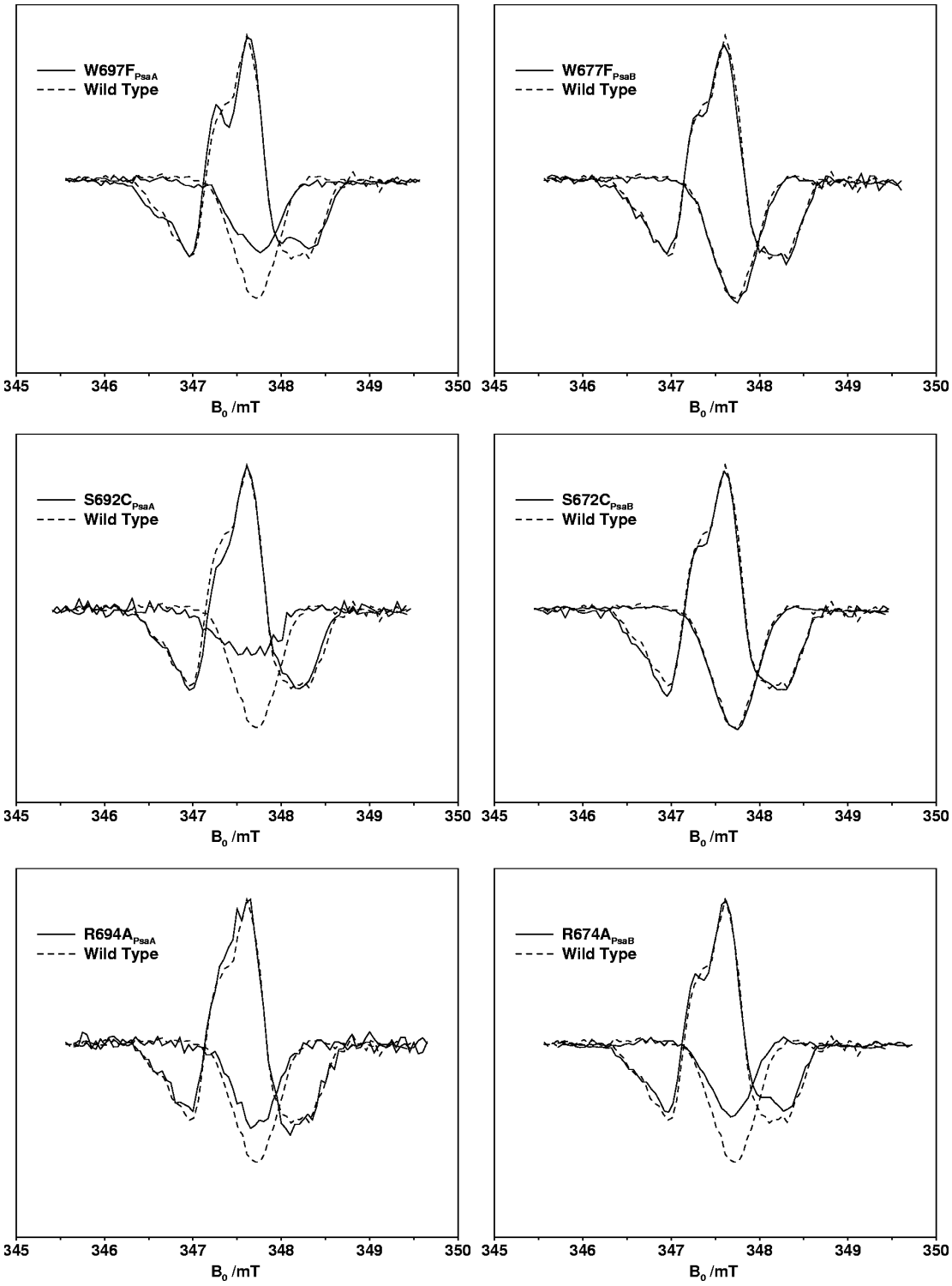
W697F PsaA
Wild Type
W677F PsaB
Wild Type
S692C PsaA
Wild Type
S672C PsaB
Wild Type
R694A PsaA
Wild Type
R674A PsaB
Wild Type
345
346
347
348
349
350
B0 /mT

Figure 5.11

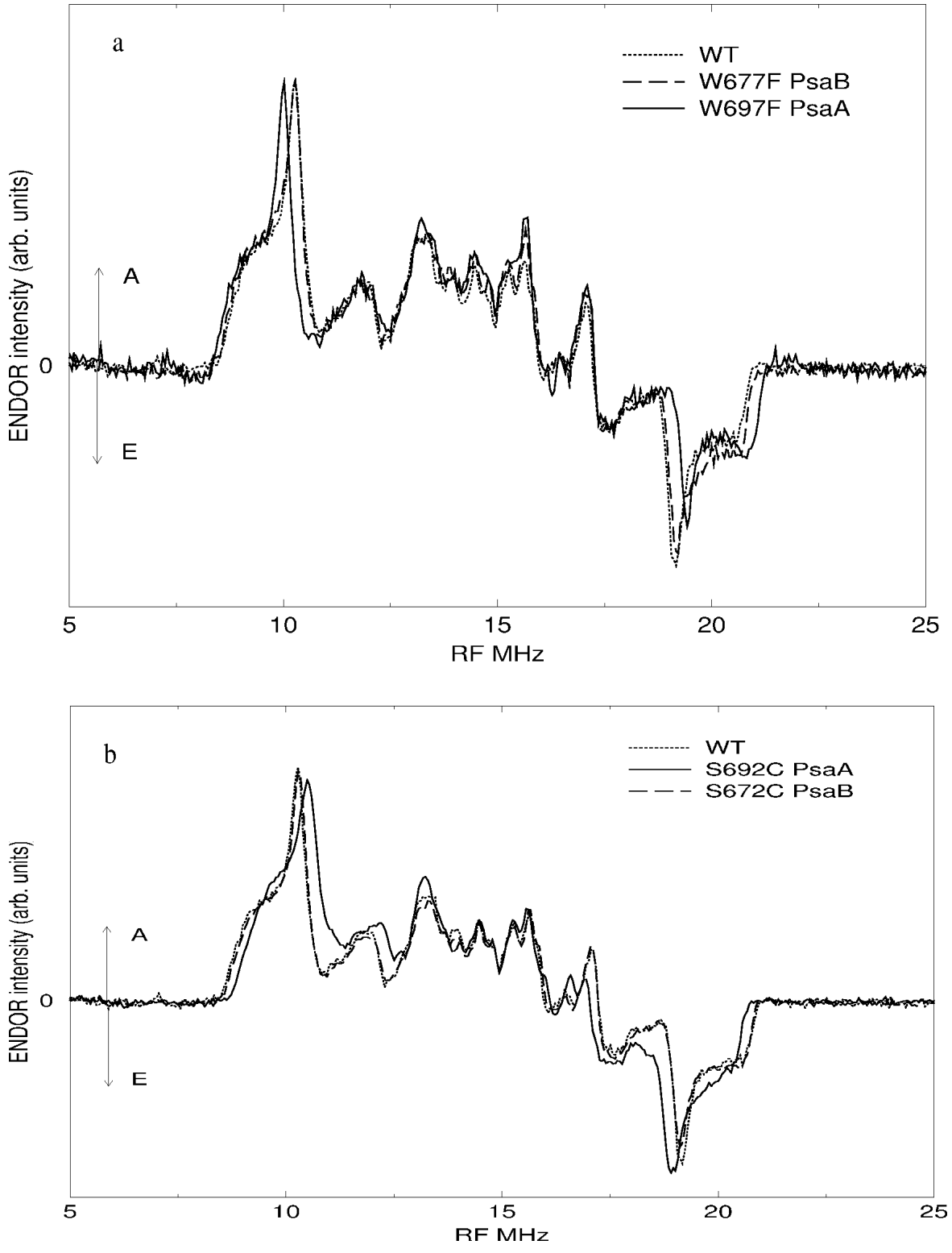
a
WT
W677F PsaB
W697F PsaA
ENDOR intensity (arb. units)
A
0
E
5
10
15
20
25
RF MHz
b
WT
S692C PsaA
S672C PsaB
ENDOR intensity (arb. units)
A
0
E
5
10
15
20
25
RF MHz

Figure 5.12

Table 5.1 Kinetic Analysis of Flash-induced Absorbance Changes Attributed to A_1^- Reoxidation in Whole Cells

	390 nm		400 nm	
	tau(rel.ampl.)	tau(rel.ampl.)	tau(rel.ampl.)	tau(rel.ampl.)
WT	10 ns (0.400)	300 ns (0.600)	11 ns (0.335)	340 ns (0.664)
PsaA W697F	n.d.	n.d.	12 ns (0.268)	1200 ns (0.732)
PsaB W677F	n.d.	n.d.	29 ns (0.382)	384 ns (0.618)
PsaA S692C	15 ns (0.350)	1340 ns (0.650)	14 ns (0.375)	1140 ns (0.625)
PsaB S672C	13 ns (0.380)	214 ns (0.620)	15 ns (0.414)	240 ns (0.586)
PsaB R674A	14 ns (0.298)	1300 ns (0.702)	12 ns (0.320)	910 ns (0.680)

n.d. : not determined

Table 5.2 Kinetic Analysis of Transient EPR spectra at 260K and room temperature

	Room temperature	**260 K**
WT	240±50 ns	840±50 ns
PsaA W697F	520±50 ns	1820±50 ns
PsaB W677F	240±50 ns	840±50 ns
PsaA S692C	920±50 ns	3020±100 ns
PsaB S672C	240±50 ns	840±50 ns
PsaA R694A	410±50 ns	n.d.
PsaB R674A	460±50 ns	1100±50 ns

n.d. - not determined

Chapter 6

Concluding Remarks

The work presented in this dissertation expands understanding of the electron transfer in PS I. Specifically, the structure and function of the A_1 acceptor of cyanobacterial PS I are studied in detail. Experiments in chapters 3, 4, and 5 firmly establish a functional difference between the two quinone molecules. Investigation of the plastoquinone-containing PS I (chapters 2 and 3) determines unambiguously that plastoquinone-9 functions as an A_1 acceptor in the absence of phylloquinone. Furthermore, quinone substitution experiments (chapter 4) demonstrate that a variety of naphthoquinones and anthraquinones can successfully bind to the A_1 sites and function as efficient electron acceptors.

Results of chapter 4 also demonstrate that various quinones can be directly assembled into the A_1 site *in vivo*. However, only a small fraction of the potential substrates of the phytyl transferase has been explored. It can be expected that more comprehensive work will be done in this area, because the broad substrate range of the phytyl (and potentially methyl) transferase provides an attractive opportunity for biogenic synthesis of exotic, substituted quinonoid compounds.

Findings presented in chapter 5 support the hypothesis that electron transfer in cyanobacterial PS I is asymmetric. Specifically, results of EPR and optical spectroscopic measurements demonstrate that most of the electron flow proceeds through the PsaA-branch of the cofactors.

Firstly, to establish definitely the directionality of the electron flow in cyanobacterial PS I it is necessary to look at the electron transfer at the onset of charge separation. Part of this work is ongoing in professor Golbeck's laboratory through the generation of the site-directed mutants in the vicinity of A_0 and the connecting chlorophylls.

Secondly, even more caution needs to be exercised when we one discusses the directionality of the electron transfer in Type I reaction centers in general. Although

substantial evidence is presented here that electron transfer is highly asymmetric in cyanobacterial PS I, this might not be the case for heliobacterial or *Chlorobium* (Type I) reaction centers. To investigate directionality fully, a model which assigns functional and physiological significance to bidirectional versus unidirectional electron transfer is required. Construction of such a model would involve cross-species studies of the origin and evolution of the reaction centers.

VITA
Boris L. Zybailov

EDUCATION
B.S. in Chemistry, The Higher Chemical College of Russian Academy of Sciences, Moscow, Russia, June 1997, G.P.A.: 3.5/4.0**.**

EXPERIENCE
Graduate Student, Penn State University, University Park, August 1998 to present
Prof. **J. H. Golbeck** research group
Research Assistant, Penn State University, August 1996-August 1998
Prof. **J. H. Golbeck** research group
Visiting Research Assistant, Iowa State University, Ames, Iowa, Summer 1995
Prof. **R. Angelici** research group

TEACHING EXPERIENCE
Teaching Assistant, Penn State University. Fall, Spring 1999
Course: General Biochemistry and Microbiology Lab.

RECENT PUBLICATIONS

Boris Zybailov, Yumiko Sakuragi, Mahir D. Mamedov, Alexey Yu. Semenov Gaozhong Shen, Donald A. Bryant, Julia Pushkar, Dietmar Stehlik, Bruce A. Diner, Parag R. Chitnis, **and** John H. Golbeck Recruitment of a Foreign Quinone into the A_1 Site of Photosystem I. V. Spectroscopic Evidence for an Endothermic Electron Transfer Step Between Plastoquinone-9 and the F_X Iron-Sulfur Cluster (2003) *in preparation*

Yumiko Sakuragi, **Boris Zybailov**, Gaozhong Shen, A. Daniel Jones, Parag R. Chitnis, Art van der Est Robert Bittl, Stephan Zech, Dietmar Stehlik, John H. Golbeck, and Donald A. Bryant Insertional Inactivation of the menG Gene, Encoding 2-Phytyl-1,4-Naphthoquinone Methyltransferase of *Synechocystis* sp. PCC 6803, Results in the Incorporation of 2-Phytyl-1,4-Naphthoquinone into the A_1 Site and Alteration of the Equilibrium Constant between A_1 and F_X in Photosystem I; *Biochemistry* 2002, 41, 394-405

Johnson, T. W., **B. Zybailov**, A. D. Jones, J. H. Golbeck, and P. R. Chitnis, Recruitment of a foreign quinone into the A_1 site of photosystem I. IV. *In vivo* replacement of the native quinone in the phylloquinone-less mutants of *Synechocystis* sp. PCC 6803 by externally supplied naphthoquinones, accepted to *J. Biol. Chem* 2001

Vassilieva, E. V., Antonkine, M. L., Zybailov, B. L., Yang, F., Jakobs, C. U., Golbeck, J. H. and Bryant, D. A. Electron transfer may occur in the chlorosome envelope: The CsmI and CsmJ proteins of chlorosomes are 2Fe-2S ferrodoxins (2001) *Biochemistry* 40, 464-473